

LENS-FREE HOLOGRAPHIC MICROSCOPY WITH DEEP LEARNING IMAGE
CLASSIFICATION FOR BIOSENSING AND DISEASE DIAGNOSIS

by

Colin J. Potter

Copyright © Colin J. Potter 2024

A Dissertation Submitted to the Faculty of the

JAMES C. WYANT COLLEGE OF OPTICAL SCIENCES

In Partial Fulfillment of the Requirements

For the Degree of

DOCTOR OF PHILOSOPHY

In the Graduate College

THE UNIVERSITY OF ARIZONA

2024

THE UNIVERSITY OF ARIZONA
GRADUATE COLLEGE

As members of the Dissertation Committee, we certify that we have read the dissertation prepared by **Colin Jacob Potter**, titled *Lens-Free Holographic Microscopy with Deep Learning Image Classification for Biosensing and Disease Diagnosis* and recommend that it be accepted as fulfilling the dissertation requirement for the Degree of Doctor of Philosophy.

Euan McLeod Date: 2/2/24
Professor Euan McLeod

David Brady Date: 2/2/2024
Professor David Brady

Rongguang Liang Date: 02/02/2024
Professor Rongguang Liang

Final approval and acceptance of this dissertation is contingent upon the candidate's submission of the final copies of the dissertation to the Graduate College.

I hereby certify that I have read this dissertation prepared under my direction and recommend that it be accepted as fulfilling the dissertation requirement.

Euan McLeod Date: 2/2/24
Professor Euan McLeod
Dissertation Committee Co-Chair
Wyant College of Optical Sciences

ACKNOWLEDGMENTS

I would like to acknowledge my Advisor, Euan McLeod for his support of myself and of the work presented in this Dissertation. His feedback and ideas helped to solve many problems that arose and to open new avenues of investigation throughout the research presented here. I also acknowledge Shriniketh Sreevatsan, who contributed to the research presented in the fourth Chapter of this Dissertation. Finally, I acknowledge the other members of the Soft Nanophotonics Laboratory for their support.

LAND ACKNOWLEDGMENT

We respectfully acknowledge the University of Arizona is on the land and territories of Indigenous peoples. Today, Arizona is home to 22 federally recognized tribes, with Tucson being home to the O'odham and the Yaqui. Committed to diversity and inclusion, the University strives to build sustainable relationships with sovereign Native Nations and Indigenous communities through education offerings, partnerships, and community service.

DEDICATION

for my Family, my Partner, and for Banjo and Jupiter

TABLE OF CONTENTS

LIST OF FIGURES	10
LIST OF TABLES	12
ABSTRACT	13
INTRODUCTION	14
Goals and Motivation	14
Overview	15
CHAPTER 1 Principles of Biological Sensing and Imaging	17
1.1 Basics of Biosensing	17
1.2 Biosensor Impact	20
1.3 Common Biosensors	22
1.3.1 <i>Polymerase chain reaction</i>	22
1.3.2 <i>Enzyme-linked immunosorbent assay</i>	25
1.3.3 <i>Lateral flow assay</i>	28
1.4 Nanophotonic Biosensors	30
1.4.1 <i>Surface plasmon resonance</i>	30
1.4.2 <i>Simple SPR biosensor</i>	32
1.4.3 <i>Nanohole arrays</i>	34
1.4.4 <i>Nanorod biosensors</i>	34
1.5 Agglutination Assay	35
1.6 Lens-Free Holographic Biosensors	35
1.7 Fundamentals of Biological Microscopic Imaging	36
1.7.1 <i>Source</i>	36
1.7.2 <i>Source field conditioning</i>	37
1.7.3 <i>Sample</i>	39
1.7.4 <i>Field shaping</i>	39
1.7.5 <i>Sample field conditioning</i>	40

1.7.6	<i>Sensor</i>	40
1.8	Common Microscopy Techniques	41
1.8.1	<i>Fluorescence microscopy</i>	41
1.8.2	<i>Polarization microscopy</i>	41
1.8.3	<i>Phase microscopy</i>	41
1.8.4	<i>Other microscopy techniques</i>	42
CHAPTER 2 Lens-Free Holographic Microscopy		43
2.1	Introduction	44
2.2	Compelling and versatile aspects of lensless holographic microscopy	46
2.2.1	<i>Typical LFHM system design</i>	46
2.2.2	<i>LFHM reconstruction</i>	48
2.2.3	<i>Pixel super-resolution</i>	51
2.2.4	<i>Approaching the twin-image term</i>	53
2.2.5	<i>Sample delivery in LFHM</i>	54
2.2.6	<i>Deep learning and machine learning approaches</i>	54
2.2.7	<i>Advantages of LFHM</i>	56
2.3	Clinical applications of lensless holographic microscopy	57
2.3.1	<i>Pathological analysis of tissues and fluids</i>	57
2.3.2	<i>Cytometric analysis of cells and blood</i>	63
2.3.3	<i>Infectious disease monitoring and diagnosis</i>	68
2.3.4	<i>Molecular diagnosis and biosensing</i>	73
2.4	Use of lens-free holographic microscopy in biomedical research	76
2.4.1	<i>Live-cell imaging and cell culture analysis</i>	76
2.4.2	<i>Pharmacological testing</i>	80
2.4.3	<i>Basic biological science</i>	81
2.5	Conclusions and Outlook	83
CHAPTER 3 A Biosensor for SARS-CoV-2 Diagnosis		87
3.1	Introduction	87
3.2	Experimental Methods	90
3.2.1	<i>Quantitative large-area binding sensor</i>	90
3.2.2	<i>Novel modifications to the QLAB sensor</i>	91
3.2.3	<i>SARS-CoV-2 pseudovirus</i>	95
3.2.4	<i>Particle preparation and SARS-CoV-2 agglutination assay</i>	95
3.2.5	<i>Image processing and analysis</i>	96

3.2.6	<i>Residual convolutional neural network</i>	101
3.3	Experimental Results and Discussion	103
3.3.1	<i>SARS-CoV-2 biosensing assay</i>	106
3.3.2	<i>Quantitative and unambiguous assay readout</i>	110
3.4	Summary	114
CHAPTER 4 Deep Learning Algorithms for LFHM Image Classification		115
4.1	Introduction	115
4.2	Materials and methods	119
4.2.1	<i>Portable lens free holographic imaging</i>	119
4.2.2	<i>Training dataset generation</i>	120
4.2.3	<i>Convolutional Neural Network Architectures</i>	122
4.2.4	<i>CNN training and validation</i>	127
4.3	Results and discussion	129
4.3.1	<i>Dropout layer</i>	130
4.3.2	<i>Convolutional layers</i>	131
4.3.3	<i>Normalization layers</i>	132
4.3.4	<i>Pooling layers</i>	133
4.3.5	<i>Padding for Convolutional and Pooling layers</i>	135
4.3.6	<i>L2 regularization</i>	136
4.3.7	<i>Activation layer</i>	137
4.3.8	<i>Final Optimized Network</i>	138
4.4	Conclusions	139
CHAPTER 5 A Novel Polarization- and LSPR-Based Lens-Free Micro- scope and Biosensor		141
5.1	Introduction	141
5.2	Methods	143
5.2.1	<i>AuNR scattering</i>	143
5.2.2	<i>Polarization-based LFHM design</i>	147
5.2.3	<i>AuNR agglutination assay</i>	152
5.3	Results	154
5.3.1	<i>P-LFHM sensor response</i>	154
5.3.2	<i>Image benchmarking analysis</i>	154
5.4	Summary	155
CHAPTER 6 Conclusions and Future Directions		158

APPENDIX A	Appendix A: 3D CAD models of LFHM housing	161
A.1	Portable QLAB designs	161
A.2	P-LFHM designs	161
APPENDIX B	Appendix B: Operating Python code for P-LFHM	165
B.1	Serial illumination and capture	165
B.2	Multiprocessing parallel illumination and capture	168
APPENDIX C	Appendix C: Laser diode array circuit schematics	172
C.1	Circuit design	172
C.2	PCB layout	174
REFERENCES	175

LIST OF FIGURES

1.1	qPCR principles	24
1.2	ELISA principles	26
1.3	LFA schematic	29
1.4	Excitation of SPPs	31
1.5	Kretschmann configuration	33
1.6	Nanophotonic biosensors	34
1.7	Brightfield microscope	37
1.8	Brightfield microscope schematic	38
2.1	Basic in-line LFHM schematic	47
2.2	Twin image example	50
2.3	U-Net architecture	55
2.4	3D LFHM reconstruction of organoids	58
2.5	On-chip LFHM cytometry	64
2.6	LFHM quantification of viral plaques	69
2.7	LFHM biosensor for SARS-CoV-2	74
2.8	In-incubator LFHM for cell culture monitoring	78
3.1	QLAB sensor configuration	91
3.2	Portable QLAB sensor	92
3.3	Fully assembled portable QLAB sensor	93
3.4	Imaging chip assembly	94
3.5	SARS-CoV-2 agglutination assay procedure	97
3.6	Hologram reconstruction and PSR	99
3.7	Threshold-based binding quantification algorithm	100
3.8	Residual CNN architecture	102
3.9	Results of CNN training	105
3.10	Results of SARS-CoV-2 agglutination assay	108
3.11	Two-measurement assay	112

3.12	Comparison of filtered and unfiltered samples	113
4.1	LFHM and CNN schematics	117
4.2	Data generation and CNN training workflow	120
4.3	Key CNN layers and parameters	122
4.4	Training outcomes with dropout	130
4.5	Convolutional layer training effects	132
4.6	Normalization layer training effects	133
4.7	Pooling parameter training effects	134
4.8	Effect of padding on training outcomes	136
4.9	L2 regularization training effects	137
4.10	Activation layer training effects	138
5.1	Gold nanorod characteristics	146
5.2	Gold nanorod simulated scattering response	147
5.3	Polarization-LFHM schematic	149
5.4	Fully assembled P-LFHM device	150
5.5	Comparison of two LFHM devices	151
5.6	Agglutination assay of AuNRs	153
5.7	PiHawk sensor channel response at 850 nm	155
5.8	Single low-resolution hologram USAF reconstruction	156
6.1	Next steps for the P-LFHM system	160
A.1	Portable QLAB CAD designs	162
A.2	P-LFHM CAD designs	164
C.1	Constant current source	172
C.2	Full circuit wire diagram	173
C.3	Laser diode board schematics	174

LIST OF TABLES

1.1	Gold standard and common biosensors.	19
3.1	Network output results for test data sets	106
3.2	Network confidence values	106
4.1	Baseline CNN architecture	121
4.2	Optimized CNN architecture	139

ABSTRACT

Novel biosensing approaches are essential to the improvement and advancement of health and medicine. Many diseases have unique biomarkers that can be used to diagnose, guide treatment, and monitor treatment progress for the disease. In addition, biosensing for infectious diseases is essential for mitigating the impact of pandemics like the COVID-19 pandemic. To this end, lens-free holographic microscopy (LFHM) has emerged in recent years as a novel biosensing platform for a variety of targets and diseases. In this dissertation, a novel LFHM-based biosensor was developed to diagnose COVID-19 in response to the pandemic. Additionally, deep learning algorithms were explored to improve the sensor's performance in real-world and point-of-care conditions. A variety of these deep learning approaches were investigated and characterized, providing an in-depth resource for construction, fine-tuning, and debugging of similar deep learning algorithms. Finally, a second novel LFHM device was constructed that utilizes polarization and localized surface plasmon resonance of gold nanorods to detect single rods. This device was characterized using a resolution test target as a first step towards a biosensing study utilizing this novel device. This work provides a strong foundation for the use of this LFHM-based biosensor in the field for clinical diagnostic procedures, and represents an advancement in LFHM imaging.

INTRODUCTION

Goals and Motivation

The goals of this dissertation are to: (1) apply a portable, lens-free holographic microscope (LFHM) and novel quantification workflow to address a pressing biosensing need in biomedicine and (2) develop a novel LFHM-based biosensor to address limitations facing LFHM biosensors and improve performance as a biosensor. As will be discussed in-depth throughout this dissertation, LFHM is an emerging technology with the potential to have significant impact on clinical and biomedical applications, including those involving microscopic imaging and biosensing. The motivation behind this research is to utilize LFHM's benefits to these applications while resolving some of its limitations through the construction of a biosensor and to provide a basis for eventual translation of this LFHM device into clinical medicine and biomedical research. To this end, an LED-based LFHM biosensor is tested and applied to sense severe acute respiratory syndrome coronavirus 2 (SARS-CoV-2) virus, the virus responsible for the COVID-19 pandemic, and a novel laser diode-based LFHM microscope was invented to improve upon this previous LFHM configuration and improve its performance.

Overview

In Chapter 1, the principles of biological sensing and imaging are explored. Here, modern sensing approaches for biomolecules and for infectious diseases are described, in particular their strengths and weaknesses. Microscopic imaging fundamentals are also explored here, including basic components necessary for conventional microscopes to operate successfully.

Chapter 2 describes the fundamental optics, physics, and mathematics underpinning LFHM imaging and image reconstruction. Additional methods commonly used with LFHM, such as pixel super-resolution (PSR) and deep learning (DL) are also described here. Then, examples of LFHM in a wide variety of clinical and biomedical applications are covered, with special attention paid to the advantages and drawbacks of this method in each application. The purpose of this is to provide a compelling basis for the use of LFHM in biomedicine, to give examples of LFHM devices and where they commonly fall short, and to show that the systems invented in this dissertation are novel and not replicated by any existing devices.

In Chapter 3, a brief characterization of the LFHM system used for the biosensor is covered, followed by details on how it was altered to be optimized for point-of-care COVID-19 diagnosis. Then, results from a biosensing study are shown, and a novel quantification workflow involving a DL algorithm is described that gives evidence for this device's successful application to COVID-19 diagnosis.

Chapter 4 delves deeper into the optimization process for this DL approach. This chapter answers lingering questions on what the alteration of hyperparameters and network architecture does to affect training and network performance of a simple convolutional neural network (CNN). This chapter is meant to provide guidance in CNN construction and

improvement for this and similar types of applications.

In the final experimental chapter, Chapter 5, a novel LFHM device is built to address some of the limitations described in Chapter 3. The physical principles underpinning this device are explained, and the components of the device and key metrics such as resolution are tested and quantified. This device represents a novel contribution to the fields of LFHM and biosensing.

Lastly, the final chapter provides a summary of the aims accomplished in this dissertation and some proposed future directions for this work that would extend its impact.

CHAPTER 1

Principles of Biological Sensing and Imaging

This chapter provides background on modern biosensing technologies and biological imaging basics. These two fields are highly relevant to the LFHM devices invented and tested in this dissertation.

1.1 Basics of Biosensing

Modern biosensors come in many shapes and forms but generally adhere to a few basic principles. Primarily, biosensors must be ideally both sensitive to the target and specific. Additional consideration must of course be paid to the target identity, being careful to select a target that, in itself, is sensitive and specific for the disease process the biosensor is trying to diagnose, however this chapter will be limited to a discussion of biosensors, rather than the target identity, and the target will be assumed to be a good one for a given disease. In this case, sensitivity refers to the false negative rate and limit of detection (LOD) of a biosensor, with a higher sensitivity corresponding to a lower false negative rate and a lower LOD, enabling detection of very low target concentrations [1]. Specificity refers to the false positive rate, where high specificity indicates a low false positive rate. Producing a biosensor that balances these two characteristics is quite difficult to accomplish, and extensive

testing is needed to confirm sensitivity and specificity. Often, increasing sensitivity reduces specificity, while increasing specificity means decreasing sensitivity. This logically makes sense, as setting a lower positive signal threshold for the biosensor can result in a lower LOD, but would also result in more false positive results simply due to sample variation, similar to the effect raising the p-value has in tests of statistical significance.

Biosensors or tests that provide both high sensitivity and specificity compared to other tests for the same disease are termed a “gold standard” test. All new biosensors tend to be compared to these “gold standard” tests and they are typically the ones sought out in a clinical setting for definitive diagnosis. Examples of these can be found in Table 1.1, which also includes information on their typical LOD ranges (which vary for each biosensor depending on the specific target), costs, and other key information. Most biosensors can only be used for the detection of a single molecule type, such as nucleic acids like DNA and RNA in the case of polymerase chain reaction (PCR), so are only the gold standard for a specific type of analyte. Others, like the lateral flow assay (LFA), are not a gold standard at all but are commonly used in point-of-care (POC) settings due to their cost and size.

Another key aspect of biosensors relates to the signal they produce, in that they must produce one in the presence of a target. Gold standard biosensor platforms tend to produce a signal that is quantitative rather than qualitative, such as PCR or enzyme-linked immunosorbent assay (ELISA). These tend to be the “best” types of biosensors, but the context in which they are used and the specific disease process can mean that the gold standard methods may not always be best. For example, the presence of any bacteria in the blood indicates sepsis, so a quantitative measure of this may not be needed to make clinical decisions, and only high levels of human chorionic gonadotropin (hCG), which is

Table 1.1: Gold standard and common biosensors. Provided below is a list of the biosensing techniques and platforms discussed in this dissertation, including relevant information pertaining to their operation and use cases.

Type	Molecules	Typical LOD	Cost	Size	Training
PCR	DNA and RNA only	$10^2 - 10^3$ copies per mL [2]	~\$10,000 device, \$7.50 per test [3]	Benchtop	Moderate training requirement
ELISA	Protein only	0.1 - 10 ng per mL [4]	~\$10,000 device, \$120 - \$500 per assay with 12 tests maximum per assay [5]	Benchtop	Extensive training requirement
SiMoA [6]	Protein only	10 - 20 target analytes per 100 μ L	>\$10,000 for equipment, individual test are expensive	Benchtop	More training than ELISA required
LFA	Protein, DNA, RNA	$10^2 - 10^3$ ng per mL (1 - 10 M) [7]	A few dollars per test [8]	Portable, fits in a pocket	No training required
SPR	Protein, DNA, RNA	Single molecule possible, 1 - 100 ng per mL typical (1 - 100 nM) [9]	>\$10,000 for equipment, >\$50 per test in some cases	Benchtop, elaborate setup and large equipment	Extensive training requirement
Agglutination	Protein, DNA, RNA, Infectious	60 - 500 ng per mL [10]	A few dollars per test, only sample prep equipment needed which varies	Portable test, non-portable sample preparation equipment	Low training requirement
LFHM	Protein, DNA, RNA, Infectious	0.5 - 100 ng per mL [11, 12]	~\$300 device, \$0.05 - \$0.15 per test	Portable, tabletop device	Low training requirement

always present in the blood, are useful for diagnosing pregnancy, so quantitative readout is also unnecessary for pregnancy tests. These signals can be in the form of a color change like in ELISA and LFAs, or the production of light through luminescence like in PCR. Other

methods include microparticle agglutination, which produces a visual change in the sample, and even surface plasmon resonance shifts.

The final key principle that affects biosensor usability and translation into clinic is the cost and form factor of the device. As a general rule, inexpensive and small biosensors are ideal for use in POC and low-resource settings, whereas expensive and bulky biosensors are best suited for major hospitals. This is why MRIs are not found in everyone's home and often aren't available in low-resource communities, whereas a pregnancy test, which is a type of LFA, can be purchased at every drugstore in every community. One is massive and costs millions of dollars to produce, and the other is a few dollars and can fit in the palm of your hand. These factors also relate to the operability of the device. If a device takes two trained full-time technicians to operate and a trained physician to interpret the results while another can be operated after reading three steps of instructions and can be read by anyone who can see, they will be used optimally in very different environments and for very different diseases. Again, Table 1.1 gives information of cost, size, and relative training requirements for each of the listed biosensors.

1.2 Biosensor Impact

When discussing the potential impact biosensors can have, one needs to look no further than the recent COVID-19 pandemic caused by the SARS-CoV-2 virus. COVID-19 challenged countries around the world as governments and health systems struggled to contain the spread of the disease and to mitigate its impact. The worldwide response was remarkable, with nations implementing policies to limit human-to-human spread, distribute and manufacture hospital resources, and ensure that citizens' basic needs were met. Of all the

measures implemented to combat the COVID-19 pandemic, possibly the most impactful early on was the rapid and early detection of SARS-CoV-2, which informed the need for quarantine, treatment, and contact tracing of infected individuals [13].

The scarcity of available test kits, their accuracy and sensitivity, the delay in receiving results, and the relative complexity of the tests themselves all stood as barriers to widespread testing at the desired scale. The development of new, more sensitive, and specific diagnostic technologies and their mass production has enabled better testing now than was available at the beginning of the outbreak in 2020, which, in combination with the vaccine, significantly slowed the spread of the virus and prevented transmission. Adequate rapid POC tests would have alleviated the strain that the healthcare system faced early on and could have saved many lives through rapid diagnosis of COVID-19, ensuring appropriate quarantine and treatment measures could be implemented to prevent transmission and severe illness.

Other trends in healthcare also motivate interest in biosensing technologies. The move towards personalized medicine is based on the idea that unique levels of hormone and biomolecules, as well as genetic makeup, should motivate and guide treatment methods in patients [14]. Powerful POC tools that are both sensitive and quantitative will be necessary to make this type of precision medicine practical and available to patients in the future.

In the field of oncology, biomolecules are already used to aid in cancer diagnosis for pancreatic cancer [15–18], and are even now being considered for the diagnosis of other cancers too. These include gastric cancer and colon cancer, among others [19, 20]. Highly sensitive biosensors with quantitative readouts will be essential for the widespread use of biomarkers for cancer diagnosis.

Even in neurology, biomarkers for Lewy body disease, frontal temporal dementia, Parkin-

son's disease, Alzheimer's disease, and progressive supranuclear palsy are becoming more widely used [21, 22]. These diseases are particularly difficult to differentiate clinically, so benefit greatly from biomolecule sensing. Development of effective quantitative and sensitive biosensors for these biomarkers would have a great impact on this field, and enable simple diagnosis of a great deal of other neurological diseases much more efficiently and rapidly.

1.3 Common Biosensors

1.3.1 *Polymerase chain reaction*

The type of PCR discussed here is often referred to as real time quantitative PCR (qPCR), with a variation on this being "reverse-transcriptase" qPCR (RT-qPCR). In qPCR, DNA is first isolated from a sample, then mixed with enzymes, short DNA primers, reporter molecules, and single nucleotides [23]. The mixture is then loaded into a qPCR device where it is heated to denature the DNA, separating the two DNA strands. The temperature is lowered to allow the short primer sequences to anneal to the separated DNA strands, and enzymes use the nucleotides to synthesize new DNA, using the original strand as a template. The process repeats, doubling the amount of DNA present with each cycle until the primers are used up and the process saturates. To detect a signal, a fluorescent probe or DNA binding dye is used as a reporter molecule so that signal increases proportionally to the amount of synthesized DNA present. The fluorescent probe remains quenched until it binds to double-stranded DNA or is unquenched by cleavage resulting from DNA synthesis, depending on the type of qPCR performed. Regardless, fluorescent signal is produced as more double stranded

DNA is synthesized. By keeping track of the signal and number of cycles needed to reach saturation, the initial concentration of DNA can be determined. RT-qPCR functions in exactly the same way, however a reverse transcriptase protein is used in the initial synthesis step to transcribe a single strand of DNA from the target RNA before the DNA can be amplified like in qPCR. Figure 1.1 shows details on how qPCR functions and the readout of a dilution series.

Theoretically, this process means that qPCR can detect just a single target DNA or RNA molecule in a 30 μL sample, or around 33 copies per mL. Practically, however, this tends not to be the case, and the LOD of qPCR is typically on the order of 100s to 1000s of copies per mL. SARS-CoV-2 RT-qPCR for example has a LOD of $10^2 - 10^3$ copies per mL [2].

qPCR is currently the gold standard for DNA and RNA biosensing, but it may not be the ideal test in every circumstance. This is due to the medium-complexity sample preparation procedures and the bulky and expensive devices needed to perform it [23, 24]. Trained technicians and laboratory spaces are needed to perform qPCR, which is not always possible. Additionally, it typically takes days to get samples to a lab capable of performing qPCR, prepare those samples, test them, and provide a readout to a patient. In a setting like the COVID-19 pandemic, for example, this presented a serious barrier to widespread use of this biosensor in low-resource and POC settings and may have contributed to the health disparities that were observed during the pandemic. In this sense, despite high sensitivity and specificity, qPCR has some drawbacks as well.

Some PCR-based techniques have been developed to address these limitations, particularly from a device portability and cost standpoint. Devices such as ID NOW™ and

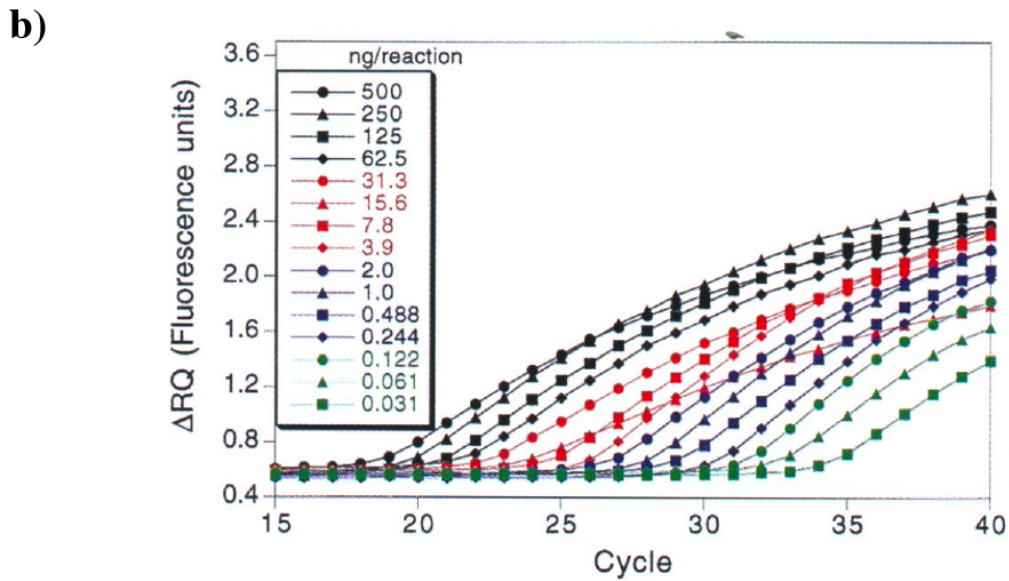
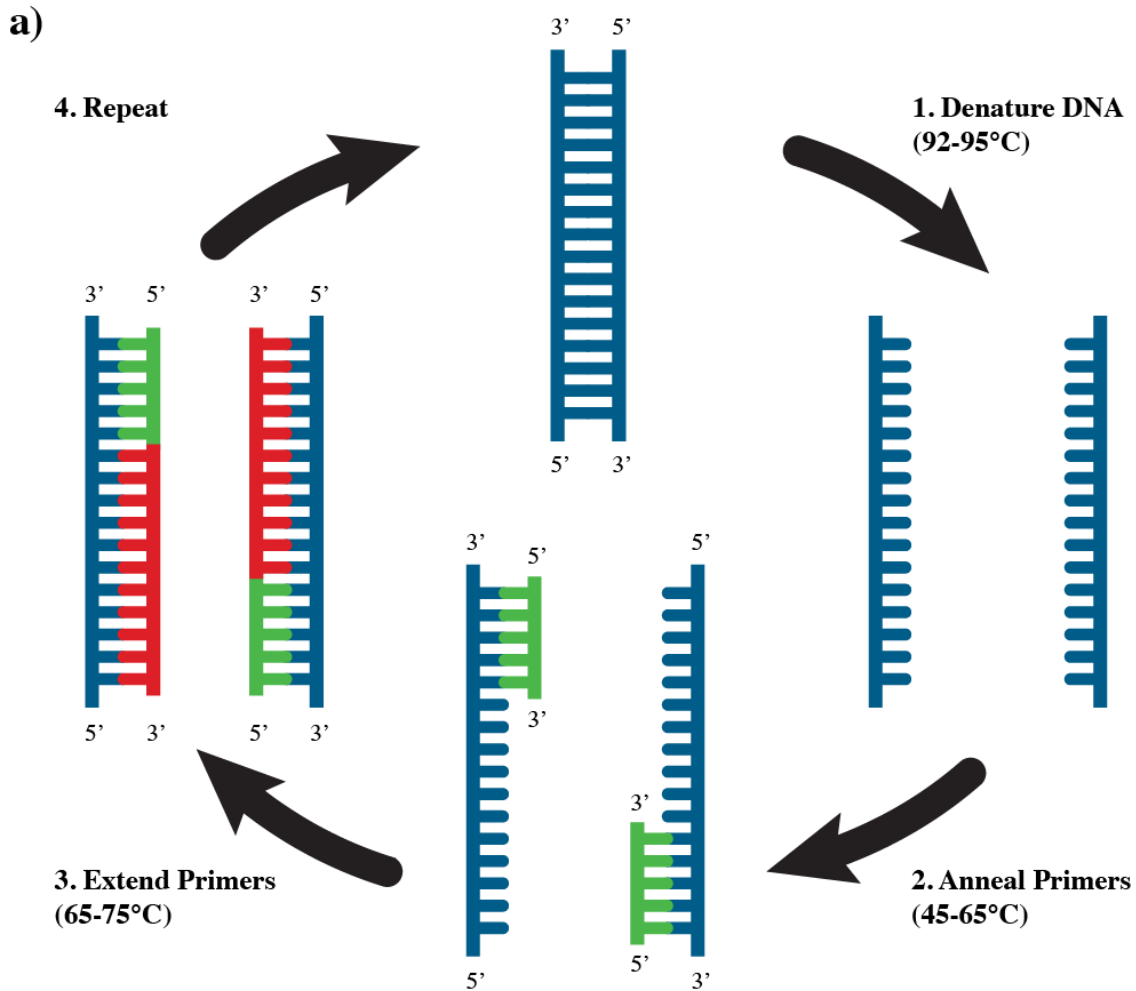


Figure 1.1: qPCR principles. (a) The process by which a single DNA strand is amplified and detected through multiple qPCR cycles. (b) Reproduced from [23]. Depicts the fluorescence signal achieved through qPCR amplification at different initial DNA loads.

POCKIT™ are relatively new technologies that utilize insulated isothermal polymerase chain reaction, or iiPCR, to qualitatively detect the presence of pathogen RNA [25]. In these devices, the sample is heated from the bottom, creating a convection current where it cools as it moves up in the chamber, effectively providing the heating and cooling cycles of traditional PCR. While this has enabled rapid, point-of-care diagnostic PCR testing to become a reality, it can only give a qualitative result (the presence or absence of the target molecule) and is 10-100 fold less sensitive than conventional qPCR [26]. As with all PCR-based biosensors however, they are still incapable of sensing proteins or any other type of biomolecule.

1.3.2 Enzyme-linked immunosorbent assay

ELISA is considered the gold standard biosensing platform for the detection of proteins [27]. In this method, antibodies, rather than DNA primers and enzymes, are the primary functional molecule. First, antibodies are used to coat the bottom of a well and excess antibody still floating in the well is washed off. These antibodies function as a capture molecule, binding the target protein and immobilizing it at the base of the well when the sample is added into the well. Unbound protein is then removed when the sample is washed away. A second antibody binding step is performed, where more antibodies are added to the well, sandwiching the captured target. Another wash step, then the final antibody binding step is performed. This time, the antibody binds to the second antibody and is conjugated with an enzyme. After a fourth wash, a colorless dye is added to the well and the conjugated enzymes convert the dye into a colored dye. Each enzyme can change the color of many dye molecules, resulting in signal amplification which makes this test quite sensitive. The typical LOD for conventional ELISA tends to be around 0.1 - 10 ng per mL [4]. The resulting

color change in the well is then measured using a specialized spectrophotometer device that provides a quantitative readout of protein concentration. Dye conversion only occurs when the third antibody and therefore the protein is present, so this test is specific for any given target protein. Figure 1.2 illustrates this process.

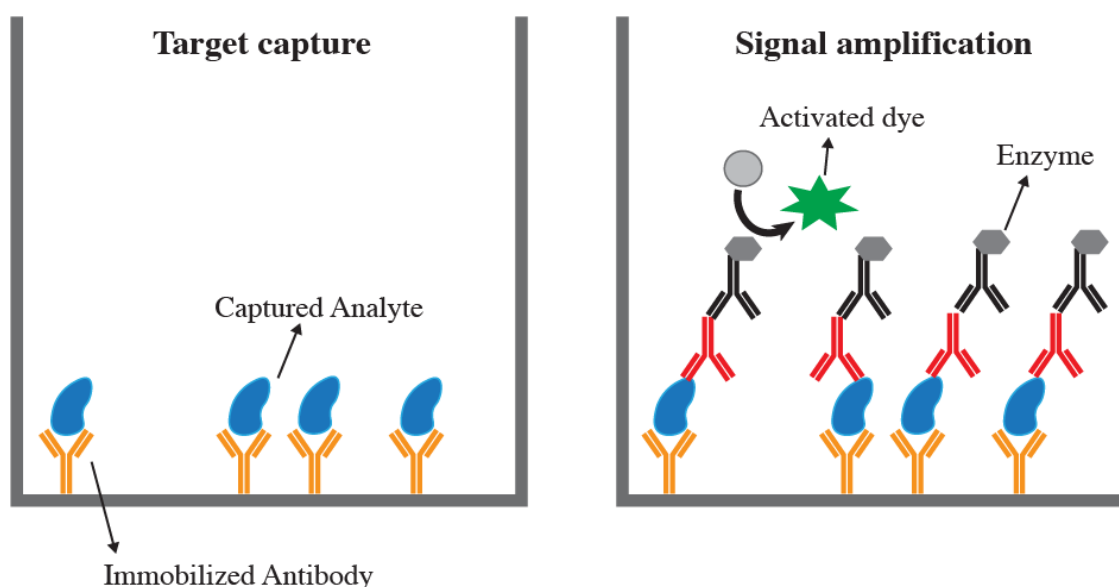


Figure 1.2: ELISA workflow consists of a capture phase, and a signaling phase. During target capture, an analyte is immobilized within a well using an antibody. Signaling occurs when an enzyme attached to the antibody shown in black bound in the final antibody binding phase activates a dye.

There are two main disadvantages to ELISA. First, the extensive sample processing steps required to perform a single assay. With the inclusion of no less than four wash steps, four binding steps, and a dyeing step before a sample can be read, this is one of the more complex assays performed in biosensing. A skilled technician can multiplex different ELISA targets in a single well plate to improve efficiency, but each of the steps still must be performed properly. Second, the antibodies and measurement device, a spectrophotometer, used to perform ELISA are expensive, and the device itself is large and bulky. This means that ELISA is not a practical biosensing platform to use in POC settings or low-resource

settings. The requirement of a skilled technician also limits ELISA's portability.

Similar to PCR, some variations on traditional ELISA have been developed to address these disadvantages. A technique called plasmonic ELISA has been tested to eliminate the need for a specialized device to quantify the color change [28, 29]. Gold nanoparticles function as a reporter molecule, with their plasmonic scattering giving rise to a particular color hue in a negative sample. Instead of activating a dye, the enzyme here alters the surface charge of the nanoparticles, resulting in aggregation which changes the hue. The guiding principle behind plasmonic ELISA's effectiveness is that a hue change is easier to detect with the human eye than a saturation change, which enables positive results to be read without a specialized device. Sensitivity is affected in this case by how well tuned nanoparticle sizes and concentration are so that they begin to aggregate at very low concentration. This, however, means that this technique is not qualitative unless specialized imaging is again performed.

A relatively recent iteration of ELISA called SiMoA improves on the sensitivity of ELISA, reducing the LOD to 10 – 20 target analytes per 100 μL of sample [6]. This technique utilizes an array of femtoliter-sized reaction chambers, each of which can contain only a single 2.7 μm microbead. Beads are coated with a capture antibody and the bound complexes are labelled with an enzyme, just as in conventional ELISA. The confinement of these complexes to a very small volume enables even single complexes (one enzyme) to produce enough signal to detect it. This technique uses a fluorescent fluorophore rather than a dye, thus fluorescent signal is detected. SiMoA improves on ELISA in its sensitivity, however it still requires a device to image the assay result, which limits the assay's use as a POC test.

1.3.3 Lateral flow assay

LFAs are the first biosensing platform discussed in this subsection that are not a gold standard technique. Similar to ELISA, LFAs also rely on antibodies to perform protein biosensing [8], while DNA primers can be used for DNA and RNA biosensing [30]. To perform an LFA, a sample is simply loaded onto one end of a porous membrane. Capillary action pulls the fluid sample from the loading pad through a conjugate pad which contains antibodies or DNA conjugated to a reporter molecule or particle. If the target is present in the sample, it will bind to antibodies or DNA in the conjugate pad as it passes through. The purpose of the reporter is to be invisible to the naked eye unless they are grouped together densely. Capillary action continues to pull the target-antibody/DNA-reporter complex through the membrane until it reaches a region of the membrane called the test zone. Antibodies or DNA are immobilized in this region that also bind the target. Should the target be present, the antibodies or DNA here will sandwich the target, increasing the density of the reporter molecule and creating a visible line that can be seen with the naked eye. Any remaining antibodies or DNA from the conjugate pad unbound to the target protein continue to the control zone of the membrane through capillary action, where they themselves are captured by antibodies or DNA respectively, forming a second line visible to the naked eye. This marks the conclusion of the test. A positive result occurs when both test and control lines are present, while a negative result is when only the control line is present. These types of tests are used in at-home pregnancy tests and now are common for COVID-19 tests as well. Figure 1.3 depicts each of the components of the LFA.

While the LFA is not a gold standard biosensing platform, it is the pinnacle of portabil-

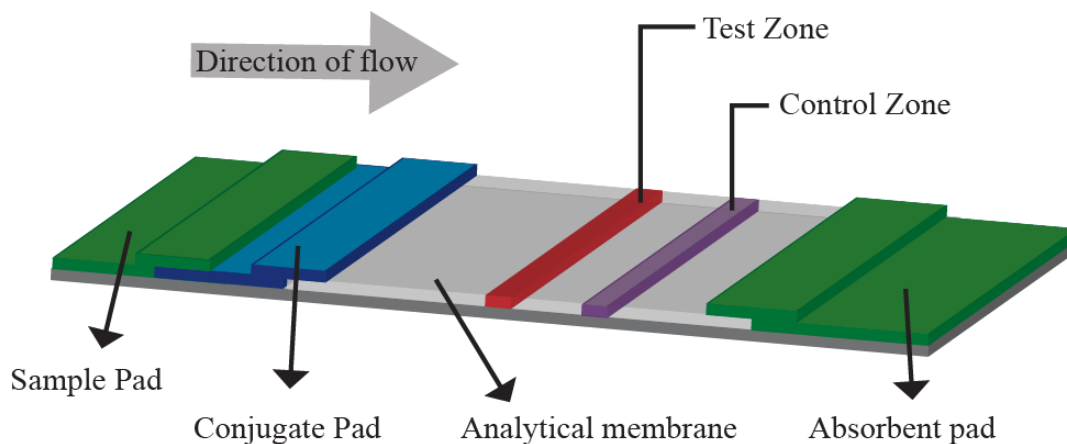


Figure 1.3: LFA schematic. Liquid sample is loaded onto the sample pad where it flows left-to-right driven by capillary action. Reporter molecules or particles are bound to the target molecules in the sample in the conjugate pad, and then are immobilized in the test strip. Unbound reporter is collected in the control strip. Visualization of both strips indicates a positive test.

ity. These tests can be manufactured very cheaply and are small and compact, fitting easily in the palm of a hand. Its reliance on capillary action as the driving mechanism means that these tests can be implemented in any environment and in any orientation, regardless of the effects of gravity. This means it is one of the few sensing technologies that would be practical for use in space as well. Finally, results can be obtained in around 10 minutes, making it the most rapid technique of those discussed in this dissertation. The major drawback of LFAs, however, is its sensitivity. LFAs have a LOD on the order of $10^2 - 10^3$ ng per mL (1 - 10 M), several orders of magnitude higher than either ELISA or PCR [7]. Furthermore, LFAs are not quantitative.

One of the drawbacks of LFAs are their low sensitivity. Restricting the flow path of LFAs has shown the capability to reduce LOD for these assays down by up to 30x, from 150 ng per mL (3.5 M) for c-reactive protein down to 5 ng per mL [31]. Additionally, coupling LFAs with a technique for RNA amplification similar to iPCR, termed reverse transcription loop-mediated isothermal amplification (RT-LAMP) enables an LFA to detect low levels of

RNA, significantly improving zika virus biosensing sensitivity in the LFA [32].

1.4 Nanophotonic Biosensors

In this section, a new class of biosensors is discussed. This class of sensors has emerged in the last decade or two as a compelling platform, particularly in terms of sensitivity. The guiding principle behind these biosensors is nanophotonics and the interaction of nanoscale particles, photonic structures, and thin metals with light. It is necessary, therefore, to briefly discuss the optical principles underlying these techniques before discussing the individual sensing platforms themselves and how they can be used to accomplish molecular biosensing.

1.4.1 *Surface plasmon resonance*

For a majority of nanophotonic biosensors, the principle of surface plasmon resonance (SPR) lies at the core of the technique. When light at optical frequencies interacts with a metal, particularly a thin metal, several things occur. One is that photons are reflected off of the metal due to electrons in the metal's free-electron gas oscillating 180° out of phase with the incident electromagnetic field, a result of the metal's negative relative permittivity [33]. Another is that an evanescent field is produced that will penetrate through the surface on the other side of a sufficiently thin metal. Finally, at specific resonant frequencies and incidence angles, there can be strong coupling from the incident beam into surface charge density oscillations that are bound to the surface (evanescent in the direction perpendicular to the surface), but can travel laterally along the metal. These oscillations are called surface plasmon polaritons (SPPs) and can give rise to strongly enhanced evanescent fields confined to the metal surface. Classically, SPPs are particular solutions of Maxwell's equations that

appear at certain boundaries, for example at the interface of a metal and dielectric like gold and glass, and at specific incident k -vectors.

For SPPs to exist at a given photon energy (freespace wavelength), the lateral component of the wavevector, k_x must be larger than the wavevector of light in free space at that same energy. A visualization of the plasmon dispersion curve would find it to the right of the free-space dispersion curve (Fig. 1.4). To achieve this, utilization of materials like glass whose refractive index is dissimilar to the refractive index of free space is useful since it increases the wavevector component of the exciting light. The combination of the appropriate interface conditions, incidence angle, polarization (p-polarized only), and wavelength results in excitation of surface plasmons.

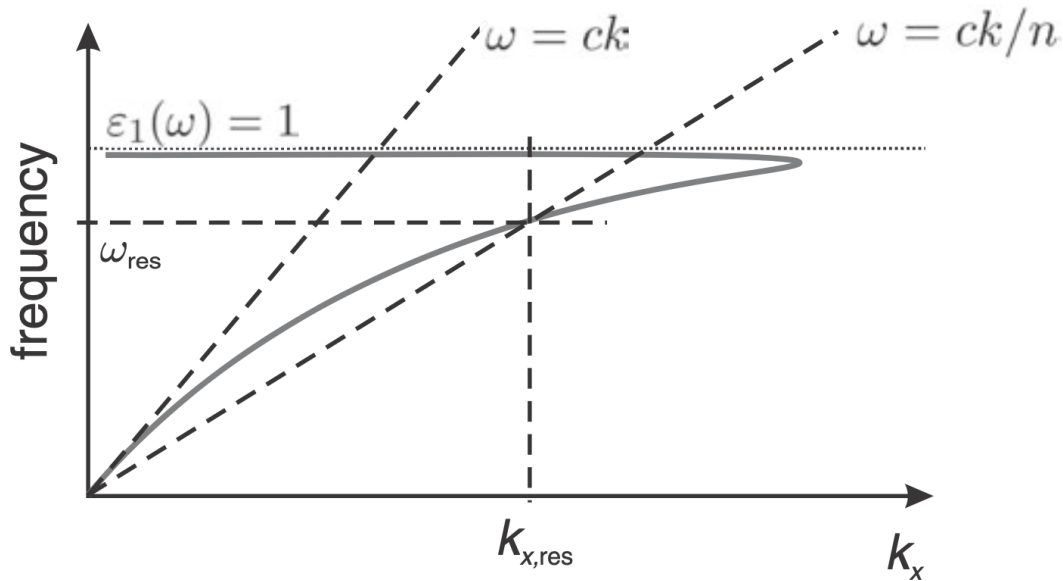


Figure 1.4: Excitation of SPPs. A close-up sketch of the surface plasmon dispersion relation with the light-lines in air and in glass. Glass shifts the dispersion curve to the right, enabling more easily excited surface plasmons. Reproduced from [33].

One example system that satisfies these constraints is the Kretschmann configuration (Fig. 1.5). In this configuration, a glass prism base is coated with a thin metal film. If the

film is too thick, the surface plasmons cannot be excited due to absorption by the metal and reflection at the glass-metal interface. At angles just beyond the critical angle where total internal reflection occurs within the glass, and with an appropriately thin coating of gold or silver, the SPR condition is achieved and surface plasmons can be excited. As a result, the measured reflectivity drops significantly. The thickness of the metal plays a major role on this resonant condition, and small changes to surface thickness are detectable through SPR resonance peak shifts at a different incidence angle.

Metallic nanoparticles or photonic structures composed of metal can exhibit *localized* SPR (LSPR). For these applications, spatial constraints imposed by the size and shape of the structure restrict the freedom of movement of surface charges and start to play a significant role in the formation of surface plasmons, in addition to the index of the medium and wavelength that were seen with a thin metal sheet. The main difference is that the polarizability of the structure, which results from the structure's shape and size, plays a dominating role in the excitation of surface plasmons. LSPR resonance can be observed in the scattered or the transmitted spectrum, where the resonance peak will be located at the wavelength with the highest scattering cross-section or the wavelength with the lowest transmission.

1.4.2 Simple SPR biosensor

One SPR biosensor is based on the aforementioned Kretschmann configuration. Using the same setup, the metal is functionalized with a capture molecule, typically an antibody for protein sensing [34]. The resonance peak is then measured for the system and recorded. Upon the introduction of a sample containing the target analyte, the analyte will bind to the

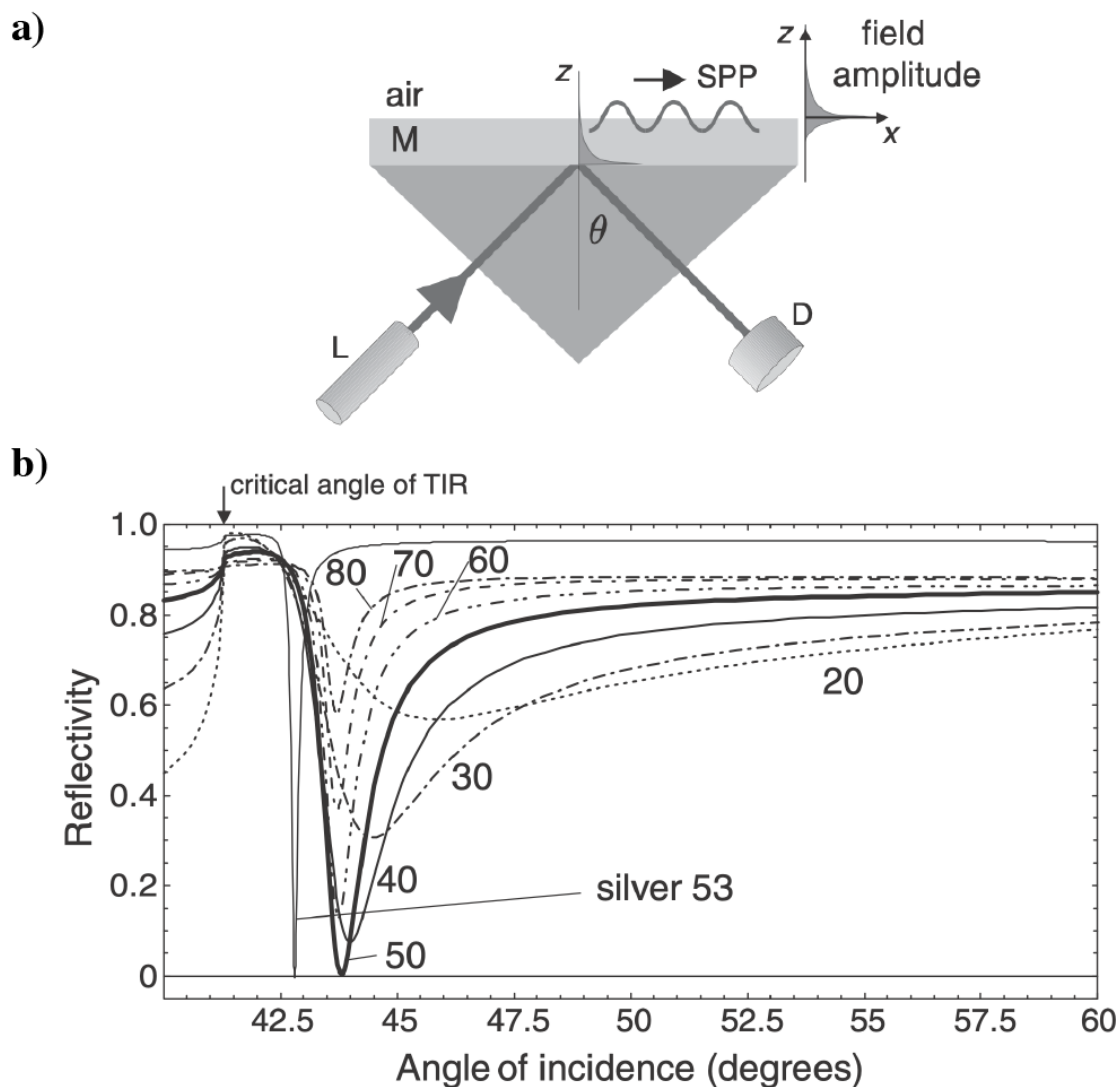


Figure 1.5: (a) Kretschmann configuration of thinly plated metal on a glass prism. Light undergoes total internal reflection in the prism, enabling surface plasmon excitation and propagation along the metal surface. (b) Reflectivity as a function of incidence angle for this configuration. Resonance peak location shifts as metal thickness changes. Reproduced from [33].

antibody on the surface of the thin metal sheet. The interaction with this now thicker film on top of the metal with the evanescent field of the surface plasmon results in a resonance peak shift, which can be recorded and used to determine the concentration of the analyte present in the sample (Fig. 1.6). The earliest implementation of this sensor achieved a LOD of less than 2 μg per mL.

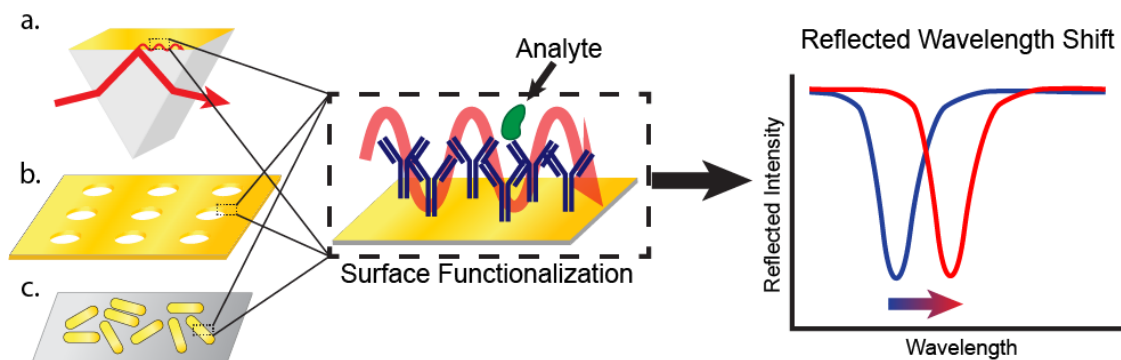


Figure 1.6: Nanophotonic biosensors. SPR peak conditions are a function of metal surface properties, which enables all nanophotonic biosensors discussed here to function. Binding of a target analyte affects these properties, leading to a detectable shift in the SPR peak and sensing of the target.

1.4.3 Nanohole arrays

Another SPR biosensor type leverages the LSPR effect. Arrays of nanoholes in a gold-dielectric layered sheet support spectrally isolated LSPR [35]. The exact spectral wavelength of this peak is quite sensitive to binding of target analyte, resulting in a shift of the LSPR peak (Fig. 1.6). This configuration enabled the detection of binding events at sub-1 ng per mL levels, producing a highly sensitive biosensor. Other work creating a grid of separate nanohole arrays, each functionalized for a different molecule, forms the basis for a biobarcode assay, which can detect and differentiate a variety of biomolecules through their unique signature at different locations on the biobarcode [36].

1.4.4 Nanorod biosensors

Biosensors that use metallic nanorods also operate based on their ability to support LSPR (Fig. 1.6). Using arrays of nanorods functionalized with antibodies has been shown to achieve a LOD on the order of 1 nM (150 ng per mL) [37]. The molecule used for biosensing is particularly large (IgG), so the molarity value is slightly misleading. Since LSPR relies

on physical size changes to impact the resonance peak, larger molecules will require fewer binding events to cause a size change, so weight per volume measurements are a slightly better comparison to the other biosensing methods discussed here. A single-nanorod biosensor has even achieved single-molecule sensing, a feat which no other biosensing method discussed here is capable of [38].

1.5 Agglutination Assay

An agglutination assay is a fairly simple biosensing test. Micro- or nanoscale particles are functionalized with a capture molecule, either antibodies or DNA, such that they bind to the target analyte [10]. Typically, these assays are used for POC sensing applications, however they can require target amplification or purification to retrieve a signal. Basic food-safety applications of agglutination assays involve first culturing a target food pathogen before introducing dyed microparticles. Agglutination occurs if the target bacteria is present, resulting in a bead clumps precipitating out of suspension that can be seen with the naked eye. In other biosensing applications, agglutination can be imaged with a microscope so can be coupled with LFHM. Examples of this are discussed in Chapter 2.

1.6 Lens-Free Holographic Biosensors

This is the final class of biosensors that will be discussed in this chapter. In an effort to limit redundancy, only a brief introduction to the guiding principles of these devices from a biosensing perspective will be given here, and a more in-depth description and analysis of LFHM-based devices will be provided in Chapter 2. In essence, biosensors employing LFHM technology are often paired with some sort of micro or nanoparticle reporter particle which

acts as a proxy for imaging the protein or infectious target itself. While LFHM systems can achieve an impressive resolution and field-of-view, these particles can greatly improve the throughput and specificity of these devices. Micro or nanoparticles are often coated with an antibody for protein detection, but can be coated with DNA to sense DNA and RNA as well with impressive sensitivity and specificity. In some cases, these particles form the basis for an agglutination assay. The wide range of procedures employed in these assays, along with their particular advantages and disadvantages are again detailed in Chapter 2. Suffice it to say here that LFHM biosensors are emerging as a novel class of biosensors with unique and robust characteristics.

1.7 Fundamentals of Biological Microscopic Imaging

Biological microscopic imaging has taken on a variety of forms but all methods rely on the presence of some basic imaging components. In this section, each of these necessary components is explored in the context of a conventional benchtop brightfield microscope like the one depicted in Figure 1.7 before examples of significant biological imaging methods are described.

1.7.1 Source

In all microscopes, regardless of imaging methodology, there must be some form of a light source. In conventional microscopy this source is in the form of an incandescent bulb. This source is a broadband white light source, typically centered slightly more in the red spectrum. Other common sources are laser sources, which are narrowband and precisely tuned and tend to be coherent, and light-emitting diodes or LEDs which have



Figure 1.7: Brightfield microscope. This is the Olympus BX53 microscope. It acts as a bright-field, darkfield, and fluorescence imaging microscope. Of note are its large size which makes this microscope non-portable, and its cost which is \$6,300.

a small bandwidth centered on a particular frequency but are not coherent. The source illuminates the sample, generating either transmitted, scattered, or emitted light that then passes through the rest of the imaging system and results in a final image. Figure 1.8 depicts each of the components discussed in this section in the context of conventional brightfield microscopy.

1.7.2 Source field conditioning

After the source produces light, there are often additional components between the source and sample that condition the light to produce a good image. In conventional microscopy this is a condenser, which focusses the light into a collimated beam before reaching the sample. Also present within the condenser is an aperture which affects the area of the

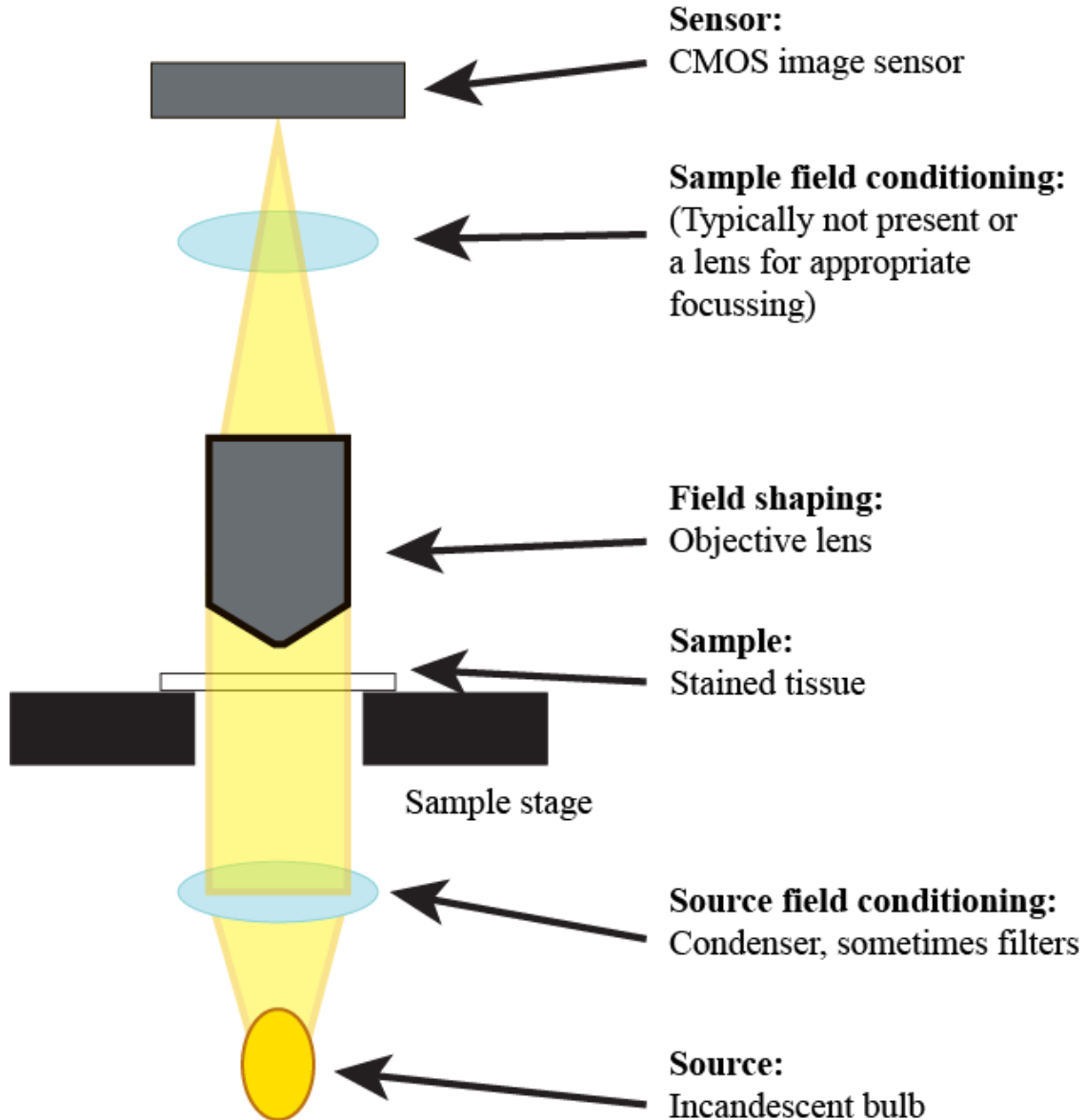


Figure 1.8: Brightfield microscope schematic. This schematic of a basic brightfield microscope can show each component necessary to produce an image of the sample focussed at the plane of the image sensor. Each type of component is labelled and insertion or removal of different specific components enables this setup to perform other types of imaging.

sample that is illuminated. Alignment of a conventional microscope involves positioning of the condenser such that the beam is centered around objective lenses placed after the sample. Other source conditioning methods involve spectral filtering such that only a narrow wavelength of light reaches the sample, field shaping so that the light is focused down to a

small region of the sample, polarization such that light is given a specific polarization state, and spatial field filtering so only specific spatial regions of the emitted field reach the sensor. Each of these conditioning methods is useful and necessary for a specific kind of microscopic imaging.

1.7.3 Sample

As the light passes through the system, it eventually reaches the sample. Samples can be prepared in a wide variety of ways or not at all, and nearly anything can serve as the sample depending on the application. Common sample processing in biological microscopy include sectioning tissue into slices 1 – 20 μm thick, chemical staining which uses chemicals and dyes to stain specific parts of cells and tissues different color based on their chemical makeup, immunolabelling which relies on antibodies to target specific proteins of interest and can either be brightfield or fluorescence-based, or nothing at all. The identity of the sample and the processing it underwent are crucial and oftentimes unique to each different imaging method.

1.7.4 Field shaping

After light interacts with the sample, it then must be collected and prepared for image formation. This is most often accomplished by an objective lens placed close to the sample. The role of the lens is to collect light and shape the field as it passes through it. A number of glass elements inside the lens enables it to bend light by retarding its phase at various points along the light's path, eventually enabling the light to be focused and produce an image on the other side of the objective. The unique composition of each lens determines

its magnification, numerical aperture, and aberrations. Mechanisms in the stage holding the sample of the microscope allow the sample or objective to be positioned appropriately so that focusing is achieved in the correct place to enable imaging to occur.

1.7.5 Sample field conditioning

Beyond the field shaping element of a microscope, there can be additional field conditioning elements. These can be the same elements that are present between the source and sample, but can also be different. The most common is a spectral filter, especially relevant for fluorescence imaging, but additional polarization filters or even spatial filters like ring and pinhole filters can be placed here as well. Again, which conditioning element is used will depend on the type of imaging being performed. In conventional brightfield microscopy, often nothing is required here.

1.7.6 Sensor

The sensor is the final component of any microscope imaging system. The sensor can either be a human eye, which is a sensor that relies on cells in the retina to detect light and the brain to process it, or an image sensor which relies on an array of semiconductors to detect light and a computer to process an image from it. Two common image sensors are CCD and CMOS sensors, with color CMOS sensors found in nearly all modern microscopes. Figure 1.8 depicts each of the components discussed in this section in the context of conventional brightfield microscopy.

1.8 Common Microscopy Techniques

1.8.1 *Fluorescence microscopy*

Fluorescence microscopy is very common in biomedical imaging and is often used to visualize several different subpopulations of cells in a single image through immunolabelling. Its source is often a laser that passes through the objective before interacting with the sample [39]. Emitted fluorescence returning through the objective passes through a filter on the way to the sensor, filtering out the excitation wavelength.

1.8.2 *Polarization microscopy*

Polarization microscopy is useful for the diagnosis of gout and diseases that involve crystal-like aggregation of protein like amyloidosis. It relies on the insertion of 2 polarization filters in each of the field conditioning steps that are used to detect birefringence of the sample [40].

1.8.3 *Phase microscopy*

Phase microscopy is highly useful when dealing with samples that need to be visualized but kept alive, like cells in culture. No sample processing is required, so the sample can be kept intact. An annular filter is added before the condenser of a normal brightfield microscope in the source field conditioning region, followed by a phase plate ring that enables the visualization of phase retardance in the sample [41].

1.8.4 Other microscopy techniques

These are by no means the only microscopic imaging techniques available, but the ones listed above are particularly relevant for LFHM applications, as LFHM has been used to replicate images created by each of these techniques. Dark field imaging for visualizing scattered fields only, confocal microscopy for achieving imaging of a very tight plane of focus only, and other more advanced techniques enable the visualization of a wide variety of samples and at sub-cellular resolutions.

CHAPTER 2

Lens-Free Holographic Microscopy¹

Many clinical procedures and biomedical research workflows rely on microscopy, including diagnosis of cancer, genetic disorders, autoimmune diseases, infections, and quantification of cell culture. Despite its widespread use, traditional image acquisition and review by trained microscopists is often lengthy and expensive, limited to large hospitals or laboratories, precluding use in point-of-care settings. In contrast, lensless or lensfree holographic microscopy (LFHM) is inexpensive and widely deployable because it can achieve performance comparable to expensive and bulky objective-based benchtop microscopes while relying on components that cost only a few hundred dollars or less. Lab-on-a-chip integration is practical and enables LFHM to be combined with single-cell isolation, sample mixing, and in-incubator imaging. Additionally, many manual tasks in conventional microscopy are instead computational in LFHM, including image focusing, stitching, and classification. Furthermore, LFHM offers a field of view hundreds of times greater than that of conventional microscopy without sacrificing resolution. Here, the basic LFHM principles as well as recent advances in artificial intelligence integration and enhanced resolution are summarized. A discussion in detail how LFHM has been applied to the above clinical and biomedical applications is also

¹This chapter is currently under review by Laser & Photonics Reviews

provided. Finally, emerging clinical applications, high-impact areas for future research, and some current challenges facing widespread adoption are identified.

2.1 Introduction

Many clinical diagnostic procedures and biomedical research workflows rely on microscopic images of specimens. For instance, hematology and cytometry rely on images of individual cells and can be used to diagnose infections and diseases including malaria and cancer, as well as genetic disorders like hereditary anemias [42, 43]. Cancer researchers and pharmacological scientists rely on cell culture imaging to determine cell growth and viability [44]. Pathologists use stained and sectioned tissues to diagnose a variety of cancers, genetic disorders, and autoimmune diseases [45]. The use of microscopy is truly ubiquitous in clinical medicine and biomedical research and underpins our current understanding of the human body and medical treatments. Despite its widespread use, traditional image acquisition and review by trained microscopists is often lengthy and expensive, and limited to large hospitals or laboratories, precluding use in point-of-care or low-resource settings [46]. On the other hand, lensless or lensfree holographic microscopy (LFHM) is an inexpensive and widely deployable technology because it can achieve performance comparable to expensive and bulky objective-based benchtop microscopes while relying on components that cost only a few hundred dollars or less [47]. Due to the size and simplicity of the hardware, lab-on-a-chip integration is practical and enables LFHM to be combined with single-cell isolation, sample mixing, and in-incubator imaging. Additionally, many tasks that are performed manually in conventional microscopy are instead computational in LFHM, including image focusing, image stitching, and feature identification and classification. Furthermore, LFHM

offers a field of view (FOV) hundreds of times greater than that of conventional microscopy without sacrificing resolution, a combination quantified as *space-bandwidth product*.

To date, several reviews of LFHM techniques have been written. Reviews on LFHM have provided excellent overviews of technological advances in LFHM, including basic LFHM theory and reconstruction methodologies [47–49], novel resolution enhancement techniques [50, 51], and more advanced image processing and backpropagation algorithms [52, 53], but these reviews have missed some key recent developments. Primarily, no review published to date has made its focus to enumerate biomedical applications of LFHM in adequate depth so as to fully convey the current state of LFHM prevalence and impact on any given biomedical application. Reviews that have addressed biomedically relevant applications have done so sparingly and often at the end of a technical section, where applications are given as examples rather than as the driving factor behind particular technological advances best suited for the particular application. Furthermore, advances in LFHM directed at biomedical applications that have occurred in the last five years are largely absent. Due to the rapidly evolving nature of the field, many high-impact LFHM advances have indeed occurred in the last five years and often their development has been driven by the need to address a specific imaging problem presented by a clinical and biomedical application, including pathology, cellular cytometry, infectious disease, biosensing, live cell and cell culture analysis, pharmacological testing, and basic biological science.

Here, a brief summary of basic principles shared across many LFHM systems as well as some recent technological advances such as artificial intelligence integration and enhanced resolution techniques, and detailed discussion of the ways in which these systems have been applied to the areas mentioned above is provided. In each section, LFHM systems are dis-

cussed that have been developed for use in a specific clinical medicine or biomedical research application, and a commentary is provided on the aspects of LFHM that make it advantageous or disadvantageous for each application as well as design principles that are necessary or are shared by most LFHM systems for success in each application. In providing this additional information, I hope to aid in the identification of effective strategies for targeted technological advancement of LFHM and LFHM translation in these fields. Finally, emerging areas or applications of LFHM in clinical diagnostic medicine and biomedical research, interesting advances in LFHM technology that have not yet seen use in clinical or biomedical applications to date or that remain not fully explored, and the current challenges in the widespread adoption of LFHM in clinical and biomedical fields are identified.

2.2 Compelling and versatile aspects of lensless holographic microscopy

2.2.1 Typical LFHM system design

Holography was coined to reflect that Gabor's work [54] captured both the amplitude and phase field information. The design Gabor used is often called in-line holography since both the reference wave (light passing through the transparent sample unperturbed) and the object wave (light scattered by objects that are being imaged) have the same optical axis.

A typical LFHM system is illustrated in Figure 2.1. Key components includes a light source, which can be a laser diode (LD) [55], a light-emitting diode (LED) [56], or an array of LDs or LEDs [57]; a charge-coupled device (CCD) or complementary metal-oxide-semiconductor (CMOS) image sensor to capture holographic images digitally; spectral filters and/or pinholes/conical optical fiber ends to meet optical coherence requirements specific to each design;

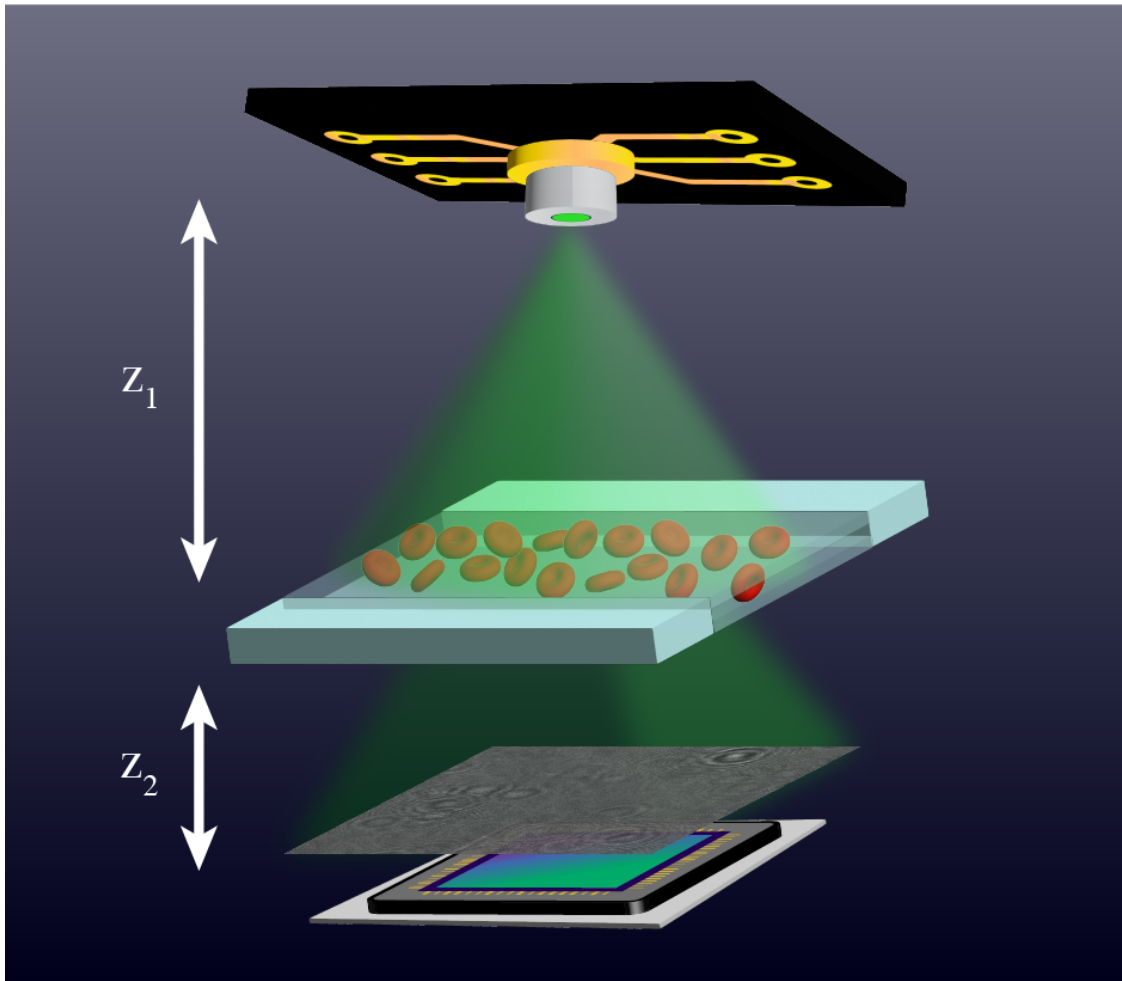


Figure 2.1: Basic in-line LFHM schematic based on Gabor’s initial in-line design with a light source, a sample (depicted here as red blood cells in a microfluidic channel, but this varies depending on the application), and an image sensor, a configuration shared across nearly all LFHM devices [54].

and holders or microfluidic chips for sample delivery [11, 58–60].

The distance between the sample plane at z_s and the light source is denoted as z_1 , which typically ranges from 5–30 cm. Therefore light at z_s can be approximated as plane waves, since the light source is approximately a point source. The separation between the image sensor plane z_i and z_s is denoted as $z_2 = |z_s - z_i|$, typically on the order of 10 μm to 1 mm. Since $z_2 \ll z_1$, the FOV in a LFHM system is equal to the active area of the image sensor, rather than limited by a lens field number. Commercially available modern CCD or CMOS

image sensors have active areas ranging from a few square millimeters to $> 100 \text{ mm}^2$.

Unlike in lens-based microscopy, where FOV is sacrificed to improve optical resolution, in LFHM, resolution is mainly limited by image sensor pixel size and the optical coherence. In order to record a hologram digitally at the image sensor with strong fringe contrast, a LFHM system must meet the coherence requirements, which are stated in Section 3.1 from [47]. Bandpass filters and pinholes are commonly utilized to improve temporal and spatial coherence respectively. In LFHM systems with pixel size limited optical resolution, pixel super-resolution techniques [57] can be used to computationally meld multiple partially redundant sample images with subpixel shifts, achieving optical resolution finer than the image sensor pixel size. In lens-based microscopes, numerical aperture (NA) is commonly used to characterize optical resolution:

$$R \approx \frac{\lambda}{2 \text{ NA}} = \frac{\lambda}{2n \sin \theta_{max}}, \quad (2.1)$$

where λ is wavelength, n represents refractive index, and, in the case of LFHM, θ_{max} denotes the greatest angle where the reference and object waves meet temporal and spatial coherence requirements to exhibit interference effects at the image sensor plane z_i [47].

2.2.2 LFHM reconstruction

As illustrated in Figure 2.1, a hologram $I(x, y, z_i)$ is recorded digitally at the image sensor since sensors can only record intensity information. Our goal is to computationally reconstruct the object wave $E_O(x, y, z_s)$ at the sample plane with both amplitude and phase information.

The recorded intensity image can be expressed as:

$$\begin{aligned}
I(x, y, z_i) &= |E(x, y, z_i)|^2 \\
&= |E_R(x, y, z_i) + E_O(x, y, z_i)|^2 \\
&= |E_R(x, y, z_i)|^2 + E_R^*(x, y, z_i)E_O(x, y, z_i) \\
&\quad + E_R(x, y, z_i)E_O^*(x, y, z_i) + |E_O(x, y, z_i)|^2 \\
&= B_R^2 + B_R e^{-ikz_2} \mathcal{P}_{z_2} \{E_O(x, y, z_s)\} \\
&\quad + B_R e^{ikz_2} [\mathcal{P}_{z_2} \{E_O(x, y, z_s)\}]^* \\
&\quad + |\mathcal{P}_{z_2} \{E_O(x, y, z_s)\}|^2
\end{aligned} \tag{2.2}$$

where $*$ is the complex conjugate operator, $k = \frac{2\pi n}{\lambda}$ is the wavenumber, B_R is a constant, the reference wave $E_R(x, y, z_i) = B_R e^{ikz_2}$ is a plane wave, and \mathcal{P}_z is an operator denoting the forward propagation of light over a distance z , where $E(x, y, z) \equiv \mathcal{P}_z \{E(x, y, 0)\}$ can be calculated using the angular spectrum method [61] as:

$$E(x, y, z) = \mathcal{F}^{-1} \{ \mathcal{F} \{ E(x, y, 0) \} H(\xi, \eta, z) \}, \tag{2.3}$$

with the transfer function in terms of spatial frequencies ξ and η defined as,

$$H(\xi, \eta, z) = \begin{cases} 0, & \text{for } \xi^2 + \eta^2 \geq \frac{n^2}{\lambda^2} \\ e^{2\pi iz \sqrt{\frac{n^2}{\lambda^2} - \xi^2 - \eta^2}}, & \text{otherwise.} \end{cases} \tag{2.4}$$

When the object wave is weak compared to the reference wave, which is generally valid except for dense or thick samples, $|\mathcal{P}_{z_2} \{E_O(x, y, z_s)\}|^2$ in Equation 2.2 can be neglected. To

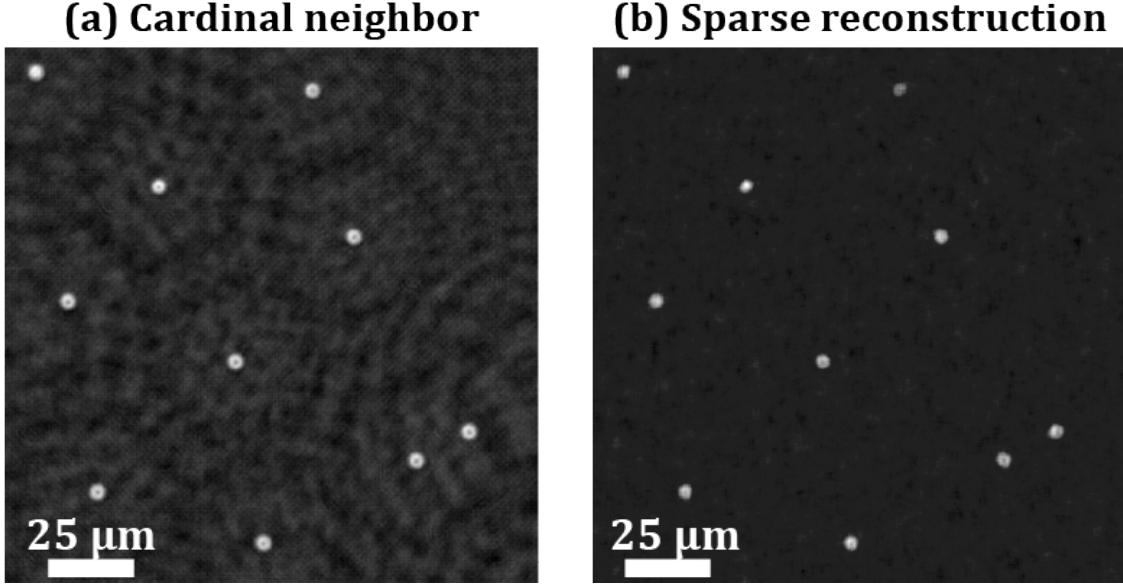


Figure 2.2: Twin image example. a) PSR holographic reconstruction with cardinal neighbor regularization. The ring shape features around 5- μm microspheres are from the twin-image term. b) PSR holographic reconstruction with sparse reconstruction regularization, where twin-image term is suppressed. Figure reproduced with permission from [57].

reconstruct an object image from the captured hologram, one can then back-propagate the recorded intensity image $I(x, y, z_i)$ over a distance of z_2 to the sample plane:

$$\begin{aligned}
 \mathcal{P}_{-z_2}\{I(x, y, z_i)\} &= B_R^2 e^{-ikz_2} \\
 &+ B_R e^{-ikz_2} E_O(x, y, z_s) \\
 &+ B_R e^{ikz_2} \mathcal{P}_{-z_2}\{[\mathcal{P}_{z_2}\{E_O(x, y, z_s)\}]^*\} \\
 &\equiv E_{rec}(x, y, z_s).
 \end{aligned} \tag{2.5}$$

Since $\mathcal{P}_{-z}\{\mathcal{P}_z\{E\}\} = E$, therefore Equation 2.5 can be simplified as:

$$\begin{aligned}
 E_{rec}(x, y, z_s) &= B_R^2 e^{-ikz_2} + B_R e^{-ikz_2} E_O(x, y, z_s) \\
 &+ B_R e^{ikz_2} \mathcal{P}_{-2z_2}\{E_O^*(x, y, z_s)\}.
 \end{aligned} \tag{2.6}$$

By back-propagating the recorded hologram, the reconstructed field $E_{rec}(x, y, z_s)$ is obtained that contains our goal $E_O(x, y, z_s)$ along with a twin-image term. The twin-image term in Equation 2.6 can be thought of as the diffraction pattern from a “twin object” located also at a distance z_2 away from the image sensor, but on the opposite side of the sample. Various approaches towards eliminating artifacts from twin-image term are discussed in Section 2.2.4.

Equation 2.6 provides a way to compute $E_O(x, y, z_s)$ from a recorded hologram $I(x, y, z_i)$. In practice, fast Fourier transforms (FFTs) and inverse FFTs are used to efficiently implement Equation 2.3. Typically, reconstructions can be completed in ~ 1 s with a typical consumer laptop [47]. In addition, graphics processing units (GPUs) can be used to significantly reduce computation time since FFTs can be implemented more efficiently on GPUs [62]. Over the years, the cost of computation has continued to decline rapidly [63], which benefits LFHM both in performance and accessibility.

2.2.3 *Pixel super-resolution*

Pixel super-resolution (PSR) techniques have been frequently deployed to improve optical resolution beyond image sensor pixel size and to also improve the signal-to-noise ratio (SNR) of reconstructed images [57, 64, 65]. Multiple frames of the same scene with slight shifts between the frames are captured, providing a denser sampling of the electric field than image sensor pixel size.

In PSR, an LED array can be used as the light source, where each LED is turned on and off sequentially, illuminating the sample from slightly different angles. Multiple images of the same scene are captured, providing partially redundant information about the scene. Though PSR assumes a static scene, it was successfully used to image microspheres

undergoing Brownian motion in solution [11].

Computationally, the process of synthesizing a high-resolution (HR) hologram from multiple low-resolution (LR) partially redundant holograms is an optimization problem. Denoting the HR hologram estimate as \hat{I} , then:

$$\hat{I} = \arg \min_I C(I), \quad (2.7)$$

where $C(I)$ is the cost function:

$$C(I) = e\{\text{HR, LR}\} + \kappa C_{reg}. \quad (2.8)$$

$e\{\text{HR, LR}\}$ denotes the error term between the HR hologram estimate and measured LR holograms. Since this optimization is an ill-posed problem, typically a regularization term C_{reg} is added to stabilize the PSR algorithm, with κ being the regularization weight. Various regularization methods are compared and a guide on choosing proper regularization methods is provided in [57].

Cardinal neighbor regularization and sparse reconstruction regularization methods are pertinent to most applications, as most samples are naturally smooth and/or sparse. Cardinal neighbor regularization penalizes nearest neighbor fluctuations in the HR hologram, while sparse reconstruction regularization promotes sparsity in the sample plane. PSR holographic reconstruction of 5- μm microspheres using cardinal neighbor and sparse reconstruction regularization methods are shown in Figure 2.2(a) and (b) respectively.

The best demonstrated resolution in LFHM systems used a synthetic aperture recon-

struction approach to achieve a smallest resolvable feature size of approximately $\lambda/2.8$, or 250 nm, equivalent to the resolution of a 1.4 NA objective lens [66]. Future improvements to resolution may be possible by more accurately considering the light-matter interaction at the nanoscale [67].

2.2.4 *Approaching the twin-image term*

Equation 2.6 states that the reconstructed field contains both the object term and the twin-image term. In off-axis holographic microscopy [68], the twin-image is spatially separated from the diffraction from the object and can be digitally removed with relative simplicity; however, for an in-line setup such as that shown in Figure 2.1, the twin image overlaps with the object image that one wishes to recover, making twin-image elimination more challenging.

In these in-line geometries, the twin-image term can be numerically suppressed using iterative algorithms [56]. If the hologram is naively reconstructed to the sample plane at $z = z_s = z_i - z_2$, as shown in Figure 2.2, then the twin image is apparent in the ring-shaped features around the 5- μm microspheres. If instead, the hologram was reconstructed to the $z = z_i + z_2$ plane, then the twin-image term would become in focus while the object term in Equation 2.6 would spread out in a wider ring around the object. By spatially filtering out the in focus twin-image terms, and then propagating the spatially-filtered field a distance of $2z_2$ back to the original object plane, the twin-image term can be greatly suppressed without significantly corrupting the object term. This process can be improved further with multiple propagations back and forth between the object and twin image planes, enforcing the spatial filter at the twin image plane each time. For this approach to be successful, the objects must

be relatively sparse such that the twin image from one object does not significantly overlap with the image of another nearby object.

Another approach to suppress the twin-image term for sparse samples is shown in Figure 2.2(b), where PSR with sparse reconstruction regularization demonstrates ability to suppress the twin-image term [57]. Compared to the iterative filtering algorithm, the sparse reconstruction regularization method is more computationally intensive. However, for larger objects, the iterative filtering algorithm could corrupt the object term, resulting in poorer performance compared to the sparse reconstruction regularization method.

When the sample is not sparse, twin image artifacts can be removed by phase recovery techniques that rely on multiple raw frames, either with different z_2 distances [69] where two holograms captured at two different distances are used to iteratively retrieve phase information, or with different wavelengths [70], where wavelength scanning enables pixel super-resolution along with phase recovery.

2.2.5 Sample delivery in LFHM

As shown in Fig 2.1, samples are placed in between the image sensor and light source. Microscope slides can be used to prepare dried samples [71, 72]. Simple microfluidic chips are utilized for sample delivery for imaging samples in solution [11], on-chip cytometry [58], tracking of micro-swimmers [59], and automated cell counting [60].

2.2.6 Deep learning and machine learning approaches

In recent years, deep learning and machine learning algorithms have been coupled with LFHM techniques with increasing frequency and in an increasing number of ways. Nearly

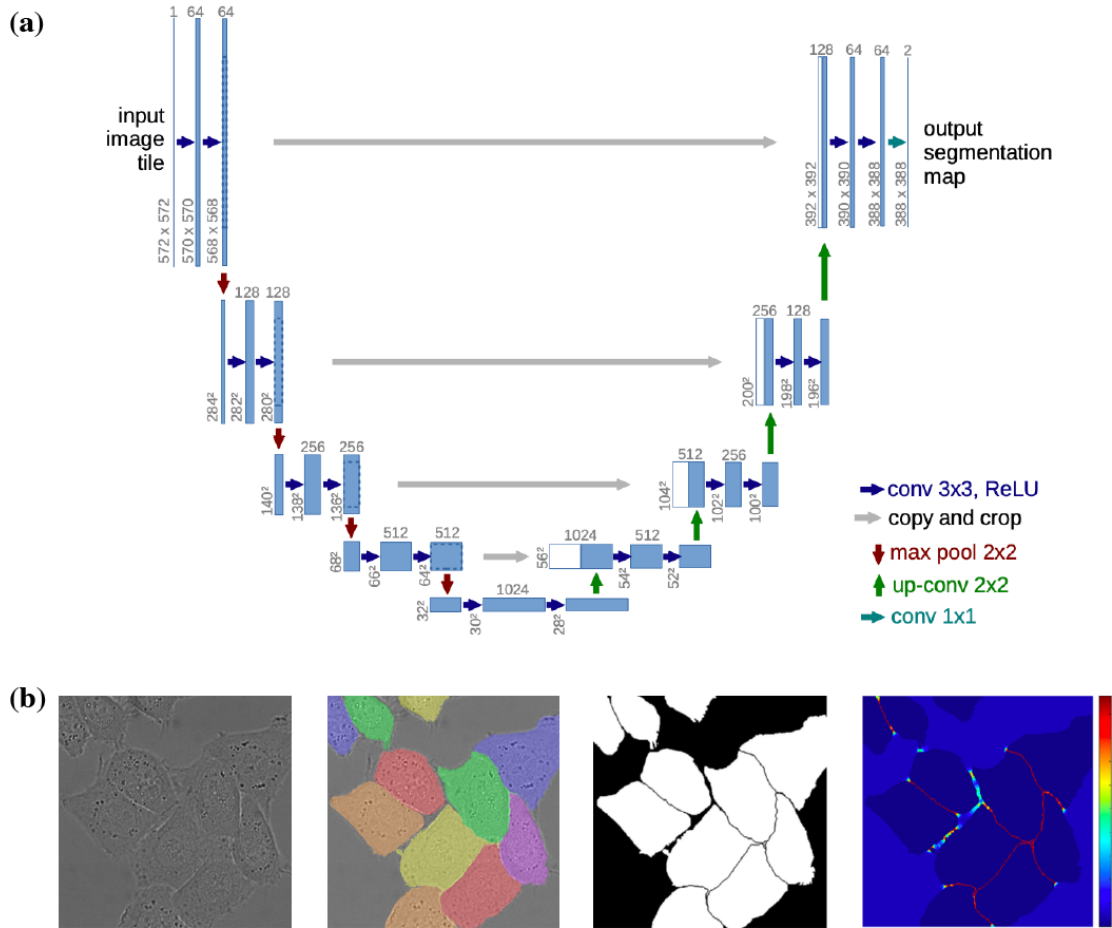


Figure 2.3: U-Net architecture. a) U-net architecture commonly used in LFHM image processing applications. Blue “conv” arrows denote convolutional layers, which perform a convolution operation using 3×3 kernels or filters followed by a ReLU or rectified linear unit activation layer. Red “max pool” arrows denote a max pooling operation which reduces data size. Green “up-conv” arrows denote “up-convolutions” where the data is up-sampled using a sparse transposed kernel matrix. Copy and drop arrows indicate skip connections where information from the contracting or down-sampling side of the network is preserved and passed to the expansive or up-sampling side via concatenation after a center crop. This is necessary for effective network training. b) Image segmentation results of original U-Net architecture. Differential interference contrast (DIC) images of HeLa cells (left) and ground truth segmentation (left center) with U-Net produced segmentation mask (right center) and pixel-wise loss (right). Figure reproduced with permission from [73].

all of these approaches use a type of network called a convolutional neural network or CNN to perform image processing. This type of network performs convolution operations across input images. Like all neural networks, as data passes through it, the network self optimizes to reproduce a training dataset assembled by a human operator. CNNs have been used in

LFHM for focus prediction [74] and image classification [75, 76], among other uses.

One particularly useful network architecture, depicted in Figure 2.3, is the U-net, which enables the network to output images from either an input image or a set of input images [73, 77]. This has been used for PSR reconstructions of holograms [78], phase reconstructions of holograms [79], virtual staining [80], and more. The advantage of using this approach is that it significantly reduces the computational cost and processing time compared with conventional approaches, and it can be more robust when used for a variety of sample types.

Simple, non-CNN networks and machine learning have also been used with LFHM, generally preceded by some form of image processing to produce a one-dimensional vector of input data containing object image characteristics, similar to principal component analysis. This has been applied to LFHM for cell imaging [81] and for nanoparticle agglutination [12].

Complete image processing pipelines have been developed using a combination of neural networks to perform phase unwrapping, reconstruction, and cell metric estimation for cell analysis, showing that deep learning approaches can be applied at each step of an LFHM imaging workflow with great success [82]. Many more examples of deep learning in LFHM have been demonstrated and will be discussed in the context of the relevant clinical or biomedical application to provide a better sense of the problems these approaches solve and their impact.

2.2.7 Advantages of LFHM

LFHM has various advantages over lens-based systems. First, the elimination of objective lenses in LFHM decouples resolution from FOV, resulting in large space-bandwidth product. This enables LFHM to offer equivalent resolution over hundreds or even thousands

times larger FOVs compared to benchtop microscopes [57, 64]. Second, LFHM consists of low-cost components that are often either commercial off-the-shelf or fabricated at low cost by 3D printing and laser cutting [11, 12]. Therefore a typical LFHM can be built with a few hundred dollars in lab settings. LFHMs can be even more cost-effective when manufactured at high volume. Third, unlike typical benchtop microscopes which are bulky and heavy, LFHM can be compact and lightweight, making it a suitable solution for field applications [83, 84].

With these advantages, LFHM systems have many applications in clinical applications, especially point-of-care and low-resource settings. As a whole, the above advantages empower LFHM as a great platform for various applications.

2.3 Clinical applications of lensless holographic microscopy

LFHM has been successfully applied to many clinical applications in recent years. The unique characteristics of LFHM enable this technology to be deployed in more locations, including at the point-of-care, at a lower cost than conventional microscopy. LFHM also offers additional functionality, and in some ways improves on conventional microscopy. In this section, recent applications of LFHM to clinical medicine are explored.

2.3.1 Pathological analysis of tissues and fluids

For clinical medicine, perhaps no field is more reliant on microscopy than pathology. In recent years, LFHM-based devices and techniques have been successfully applied to the imaging of pathological samples for disease diagnosis, including stained and unstained sectioned tissue, thick tissue sections or bulk tissue, cell aspirates, synovial fluid, and cerebrospinal

fluid, as described below.

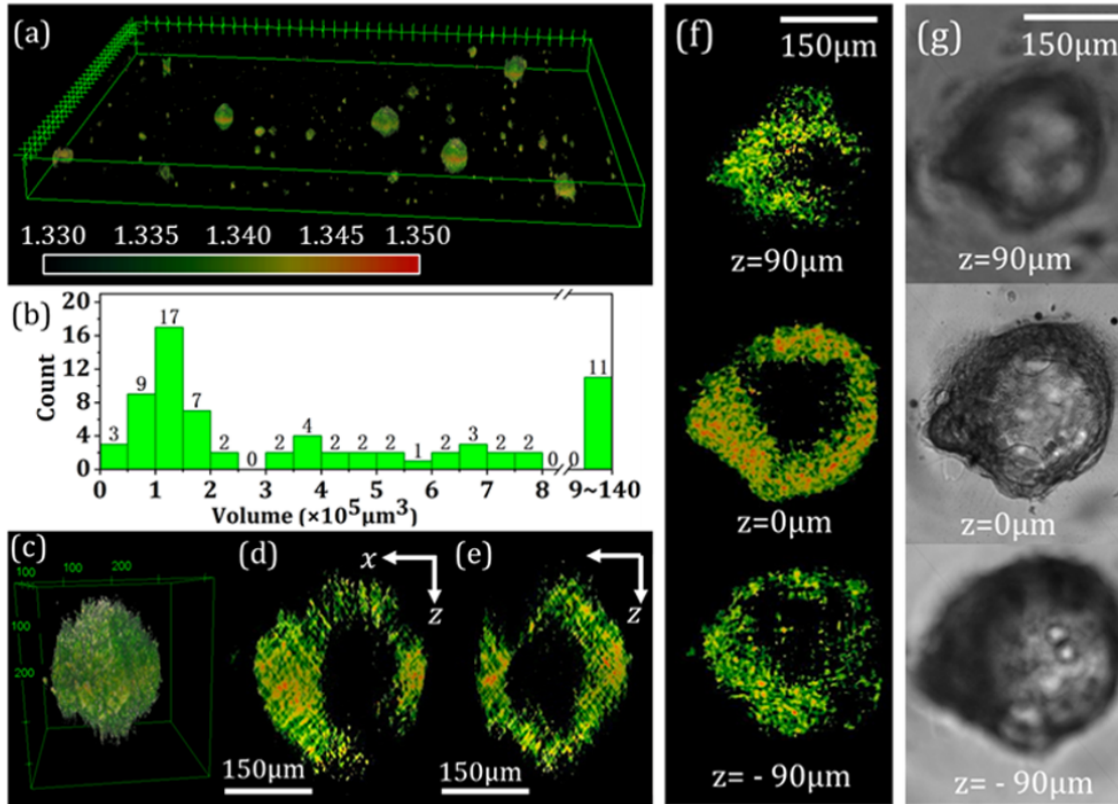


Figure 2.4: 3D reconstruction of organoids. a) Visualization of 3D refractive index reconstructions of salivary gland tumor organoids from a LFHM system. b) Volume calculations from 71 analyzed organoids. c) 3D visualization of single organoid and (d-e) longitudinal sections of this organoid. f) Cross sections of organoids at various z heights, and (g) corresponding bright-field microscope images. Figure reproduced with permission from [85].

Color imaging in pathology is key for sectioned and stained tissue analysis, and there are numerous recent examples of color LFHM. Systems incorporating a single-wavelength partially coherent source (similar to what is shown in Fig. 2.1) and pseudocoloration post-processing are able to generate color images of stained tissue [86]. Recently, multiple wavelength LFHM systems that operate in red, green, and blue domains have shown promise in the reconstruction of color images from stained tissue. Additional wavelengths can be used to reduce color error, but three are sufficient to produce accurate images of stained pathology slides since human eyes also rely on three types of color sensors [87]. Novel computational

denoising algorithms have helped to significantly improve reconstructed image quality and color accuracy of bone marrow smear samples with this type of LFHM configuration [88]. Deep learning methods have also been developed to produce color pathological images from LFHM systems. One method combined a three-wavelength LFHM configuration with deep learning to reduce phase artifacts and balance and combine color into a final image [89]. In one study, pseudocolored images were generated with deep learning from phase reconstructions of LFHM holograms that closely mimic a number of stains including H&E stain, Jones' stain, and Masson's trichrome for unstained skin, kidney, and liver tissue respectively [80]. Another deep learning coloration method used simple greyscale images from a single green 550 nm wavelength to generate color images of H&E stained samples [90].

Several algorithmic approaches have been developed to aid in data volume reduction and LFHM image processing and hologram reconstruction. For example, a phase retrieval algorithm that enables reconstructions with only two z-height holograms has been demonstrated for stained and unstained samples [91]. This simplifies the data acquisition process usually required for other multi-height phase retrieval methods. Image quality and resolution of kidney and intestine pathological slides can be improved significantly by background noise removal, image registration of multi-height and sample scanning holograms, and twin image elimination through multi-height phase retrieval and a quasi-3D reconstruction technique [92]. Novel PSR algorithms have been shown to reduce data volume and even achieve 780 nm resolution in intestine pathological slides [93]. Other computational approaches perform autofocusing for amplitude and phase reconstructions of holograms, either by algorithmic approaches [94] or deep learning approaches [79, 95] which have enabled fast autofocusing for Papanicolaou smear, stained lung tissue, and breast tissue. These deep learning approaches

can also produce phase images from holograms since they used phase information from a multi-height phase recovery approach to train the deep learning algorithm, similar to dedicated phase recovery neural networks [96]. A novel deep learning network termed a Fourier Imager Network incorporates Fourier transforms and has been shown to reconstruct phase and amplitude holograms with superior generalization for pathological tissue reconstructions of tissue outside of the training dataset of lung tissue (prostate, salivary gland, and pap smear samples) [97]. Finally, deep learning has shown the capability to produce superresolution images from low-resolution hologram reconstructions to improve pap smear and lung tissue section image resolution without extensive computational costs [98]. Faster data processing times enabled by algorithms such as these can enable immediate diagnostic results. When paired with the POC-nature of lensfree imaging hardware, fast computational processing can lead to significantly better patient outcomes in time-sensitive situations, such as for sepsis diagnosis, during surgery, or for screening in a rural clinic, where patient followup visits are burdensome due to long travel distances.

One of the most compelling applications of LFHM in this field is in the 3D imaging of bulk tissue, without the need for staining or sectioning. Since the 3D information of a sample is preserved by LFHM holograms, LFHM can fully reconstruct 3D samples and provides a significant improvement on conventional microscopy, enabling the imaging of tumors or tissue without the distortions or time and labor cost created by sectioning and staining. Figure 2.4 shows a 3D reconstruction of a salivary gland tumor organoid made possible by LFHM [85]. This technique collects 61 holograms using on-axis and off-axis LED sources such that the light field propagates at a variety of axial and rotational angles towards the sample. Using a modified 3D form of the angular spectrum method described in section 2.2.2

and the Fourier diffraction theorem, researchers were able to reconstruct the 3D refractive index of the object in a method not dissimilar from tomography. While this does not enable imaging of microstructures or individual cells and cell assemblies, it nevertheless shows that 3D information can be obtained from unprocessed bulk tissue, which would be helpful for clinicians wishing to understand tumor morphology to differentiate various tumor types and staging in different cancers, even during surgery. A similar technique used to image prostatic RWPE1 organoids achieved mesoscopic resolution with the ability to resolve single cells if they are separated from the larger organoid structures [99]. True cellular-level resolution in 3D LFHM imaging has been achieved for thick samples (200 μm) of mouse brain [100]. These samples had to be cleared with the CLARITY method and underwent DAB staining to visualize neurons, but 2D reconstructions using a single LED source and multi-height holograms could be produced at any plane in the tissue.

The 3D imaging capability of LFHM makes it especially suitable for the imaging of fluids or aspirates of cells collected in clinical settings. LFHM configurations have been successfully applied to suspensions of cells in solution [101]. The insertion of a polarization generator or filter between the light source and sample and a polarization state analyzer or second filter between the sample and image sensor of a LFHM setup enables the microscope to image polarization-state sensitive samples. The most clinically relevant use of this setup is to image synovial fluid for detection of gout, whose crystals exhibit negative birefringence under conventional polarization microscopy imaging conditions. The polarization-specific characteristics of needle-shaped monosodium urate (MSU) crystals from gout and oxaloacetate crystals found in urine have been successfully imaged by LFHM using a linearly polarized source [102] and circularly polarized source [103] with pseudocoloring to produce a recogniz-

able color image. Additionally, MSU crystals imaged with left-hand circularly polarized light produced holograms that have been colored using a deep learning algorithm so as to quantify polarization state changes in these samples [104]. Urinalysis has been performed using a single-source LFHM system to detect and track *Trichomonas vaginalis* in urine [105]. A novel reconstruction method termed adaptive sparse reconstruction, which estimates a point spread function directly from data to perform hologram reconstruction, was shown to image urine with blood cells, crystals, and casts [106]. A recent translational study of LFHM in urinalysis with urine phantoms showed that it was sensitive to hematuria and pyuria, correlating strongly to hemocytometer measurements of the same samples by detecting blood cells, bacteria, crystals, and casts [107]. Cerebrospinal fluid analysis using LFHM for diagnosis of meningitis has been successfully demonstrated as well, with an LFHM configuration that imaged erythrocytes and leukocytes in 215 samples [108]. This device also implemented automated cell counting, which enabled it to achieve 100% sensitivity and 86% specificity compared to confirmed diagnostics, which can help eliminate human error in meningitis diagnosis.

A unique application of LFHM in pathology is the ex-vivo analysis of tissues for anatomical research. One LFHM system paired acoustic and electromagnetic waves into a single imaging experiment, where a pulsed laser source captured holograms at specific points on a sound wave as it passed through an ex-vivo tympanic ring and tympanic membrane [109]. Two wavelengths were used to map the surface height of the sample interferometrically. This application is unlikely to be performed in a clinical setting as an intervention or used as a treatment, but is nonetheless relevant to pathological biomedical research so is included here.

For pathological imaging, LFHM has already shown extensive results replicating and

even improving on images achieved with conventional microscopy. The large space bandwidth product enables LFHM to function particularly well when looking for disease pathology which may only be present in a small portion of a very large tissue section, as is sometimes the case in cancer pathology. LFHM is generally incompatible with fluorescence microscopy, which is also used in biomedical research, due to the incoherent nature of fluorescent imaging. However, other labels such as nanoparticles are often just as effective, and serve as coherent scattering labels [58]. Recently, lensfree (non-holographic) fluorescent microscopy has been demonstrated that typically has lower resolution than its holographic counterparts, but research is underway to improve this and this could enable lensless fluorescent imaging in the future [110]. LFHM emerges as a superior technique for pathology in the imaging of 3D samples. While 3D reconstructions of thick, unprocessed tissue with cellular-level resolution have not yet been achieved, various LFHM imaging techniques have achieved either bulk, unprocessed tissue reconstruction or cellular resolution of processed tissues separately. This is due to a current limitation in LFHM where phase modulations to the incident field created by tissues composed of cells, fluids, and extracellular matrix generate too much interference or too little light penetration to effectively reconstruct images from bulk tissues. However, LFHM has achieved cellular resolution of 3D samples when cells are dispersed in a 3D medium, as is discussed in the following section, showing that LFHM may be on the cusp of achieving high-resolution 3D unprocessed tissue imaging in the near future.

2.3.2 Cytometric analysis of cells and blood

Cytometry and hemocytometry applications of LFHM have been quite common in recent years. For cells floating in fluid such as blood, no other imaging technique can retain infor-

mation at any focal plane in 3D as efficiently as LFHM, making this application an obvious choice for researchers to investigate. Additionally, hematological samples are highly relevant to clinical medicine through hematology, oncology, infectious disease, and immunological biomedical research. These are convenient samples for benchmarking studies of novel LFHM configurations due to their availability to researchers. As a result, many recent technological advances in LFHM include some form of hematological analysis. For image processing and hologram reconstruction, hematological samples or cell suspensions satisfy a sparsity assumption that can be leveraged to computationally remove twin-image artifacts [57]. Alternatively, some novel methods have been able to remove twin image artifacts through novel hardware configurations that include two light sources, one of which is off axis [111].

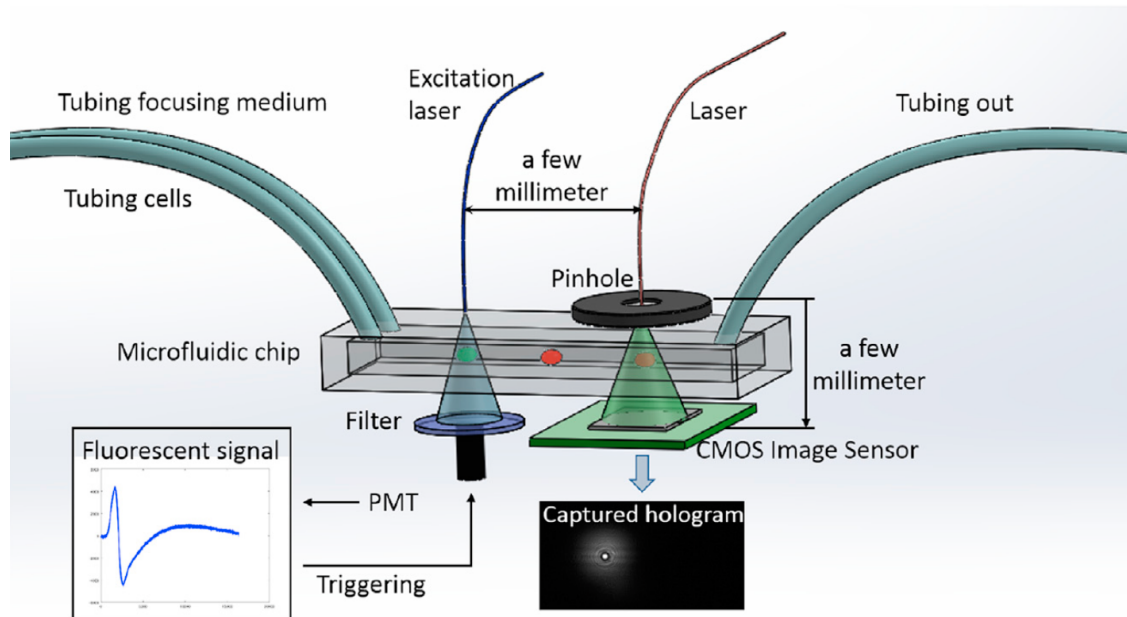


Figure 2.5: Schematic of an on-chip LFHM cytometer with an example measured fluorescent signal and hologram from a single cell. This system uses fluorescent signal detection to trigger hologram acquisition and it uses cell characteristics extracted from holographic reconstructions as inputs to a machine learning algorithm to classify immune cells into three leukocyte types: granulocytes, monocytes, and lymphocytes. Figure reproduced with permission from [112].

Portable LFHM configurations have become more robust and powerful in recent years.

3D printed designs enable cost-effective, point-of-care (POC) implementation in sizes as small as $55 \text{ mm} \times 55 \text{ mm} \times 40.5 \text{ mm}$ ($W \times L \times H$) [113] to image buccal swabs and blood smears [114]. The replacement of a pinhole filter with a cone-shaped optical fiber tip has been shown to be viable in portable and non-portable LFHM configurations for imaging blood smear samples, improving device stability and robustness compared to a pinhole filter [115, 116]. A benchtop holographic point-source configuration has been described for buccal swab and blood smear imaging which also achieves improved device stability (and therefore improved portability) by using off-axis light to illuminate a photopolymer holographic film that encodes a transmission hologram of a point source [117].

Computational techniques, like PSR, have been applied to cytometric samples as well. PSR has been demonstrated in a portable LFHM setup for platelet imaging with $1.55 \text{ }\mu\text{m}$ lateral resolution through a stationary light source and shifting pinhole [118]. Other pixel super resolution techniques have been effectively implemented to improve single-cell resolution in benchtop setups. Arrays of diodes have been understood for over a decade to be effective for this task [119], and additional processing using algorithms for motion estimation have recently enabled pixel super resolution to be performed on free-floating samples undergoing Brownian motion [120]. Gradient-descent phase retrieval methods have been shown to resolve twin-image artifacts and achieve a depth resolution of 50 nm in red blood cell images with a single illumination source [121], while additional registration steps have been tested to determine precise z -positions of holograms for more effective phase retrieval [122].

LFHM's ability to image cells in suspension due to its resolution, FOV, and 3D imaging characteristics enables it to perform superior motility analyses of sperm cells compared to conventional methods. Early methods using multi-illumination and multi-wavelength con-

ditions tracked sperm in 3D using on-chip integration and revealed sperm cells travelling in helical trajectories [59]. However, a simple single-illumination and single-wavelength LFHM can also perform 3D imaging of sperm cells by employing more standard reconstruction and focusing techniques [101, 118]. A technique called MISHELF (multi-illumination single-holographic-exposure lensless Fresnel) microscopy, which uses three distinct wavelengths that are combined before sample illumination and a novel fast converging algorithm for image reconstruction, similarly tracked sperm in 2D and 3D for motility and morphological analysis [123–125].

Cytometric samples can be easily integrated into LFHM systems with on-chip processes to further expand device functionality. As in conventional flow cytometers, cell sorting and counting algorithms are typically part of these modern LFHM systems. Simple configurations with a single illumination source have captured intensity reconstructions of diluted cells flowing through an S-channel microfluidic chip and have used a thresholding-based image segmentation approach to count cells with reasonable success [126]. A Fourier domain-based classification algorithm has recently been shown in a similar on-chip LFHM setup with a straight channel for classifying white blood cells into three subtypes using a raw hologram without image reconstruction [127]. Other methods use deep learning algorithms to count, classify, and even distinguish different cell populations [128, 129]. This approach has been translated into a 3D printed device [130]. These counting methods have shown success when working with multi-height phase reconstructions and with intensity reconstructions. Moving closer to the functionality of modern flow cytometers, one LFHM-based method used nanoparticles bound to target cells to increase scattering and enhance LFHM imaging performance [58]. The specific plasmon resonance characteristics of the particles allowed for the

classification of immune cell populations based on the cell's CD4 and CD8 expression. Magnetic beads functionalized for specific cell detection have been used on-chip to detect target cells in blood on-chip by applying a periodic magnetic field which enables a simple LFHM system to distinguish rare cells in blood [131]. This is relevant for diagnosis of leukemia and other cancers. One particularly sophisticated method combines on-chip microfluidic cell separation, automated cell counting, and fluorescence imaging in a single platform to distinguish 3 different types of leukocytes [112, 132]. Figure 2.5 shows a schematic of this method, in which cells flow through a microfluidic chip where a fluorescence signal is detected and recorded, then used to trigger acquisition of a hologram [112]. This pairs high-resolution imaging of a cell with its fluorescence signature for every cell that passes through the microfluidic chip, a new feature found in expensive modern flow cytometers, but replicated here in a low cost, compact, and portable platform.

LFHM has several advantages over conventional methods of cytometric analysis involving conventional microscopy and even flow cytometry. Firstly, LFHM can easily achieve the same resolution and reproduce the same images for these samples as conventional microscopy. This enables LFHM to be used in low-resource, POC, and large hospital settings where hemotological analysis would be instrumental to clinical decision making. LFHM also preserves the 3D information in a sample, allowing a technician to perform fewer sample processing steps and track cells in real-time for clinical information. However, this does come at the cost of some training on the particular LFHM system. Additionally, LFHM systems are more sensitive to dust and impurities in the sample in question, which can place additional burden on a trained technician in the sample processing steps. On-chip functionality also enables LFHM to replace other techniques like flow cytometry for cell expression

analysis and cell counting in a low cost and portable device. One LFHM system, NaviCell, has reached the commercial stage and has shown high accuracy when compared with conventional, dye-based hemocytometers, and can even perform cell viability testing functions (see Section 2.4.2) [133]. Another commercial system, Cellytics, has shown effective cell sorting of blood cells and cancer cells when images produced with this system are passed through a deep learning classification algorithm [76]. These devices successfully combine on-chip functionality, cell counting and sorting algorithms, and the inherent 3D imaging characteristics of LFHM. The advances of LFHM devices in pathology demonstrated in recent years illuminates LFHM as a compelling emerging technology in clinical cytometric analysis which requires more clinical study.

2.3.3 Infectious disease monitoring and diagnosis

LFHM techniques have a wide variety of configurations and coupled methodologies when applied to infectious disease monitoring and diagnosis. Typically, traditional infectious disease diagnosis involves microscopic visualization of individual infectious particles such as malaria or parasites, visualization of colony-forming units (CFUs) or plaque-forming units (PFUs) in bacterial or viral culture, measurement of viral or bacterial load like what is done in lateral flow assays (LFAs) or polymerase chain reaction (PCR) analysis, or a combination of these techniques depending on the specific disease. LFHM has been tested successfully for each of these detection methodologies.

Direct visualization of individual bacteria with LFHM imaging has been achieved in a variety of configurations and contexts. The simplest LFHM systems are capable of imaging disperse samples of microorganisms. However, because of their simplicity, these systems can

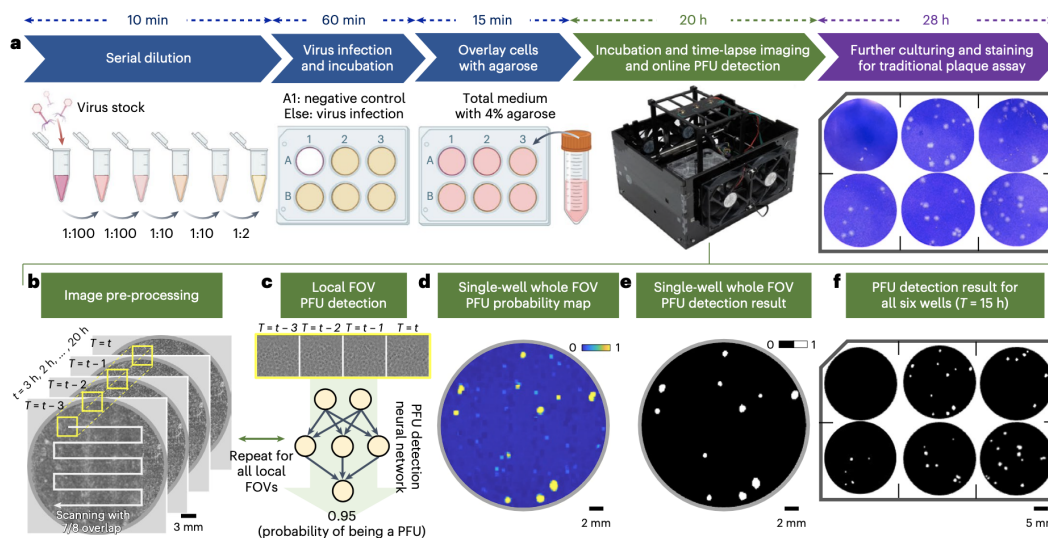


Figure 2.6: Workflow for a LFHM-based system to quantify viral plaques. a) Sample preparation for plaque assay, with a traditional plaque assay shown at the end. b-f) LFHM imaging and live viral plaque quantification workflow that is performed before the traditional quantification assay. b) Whole-well holograms are captured for different time points. c) A DenseNet-based [134] neural network is used to create (d) a probability map for plaque-forming units (PFUs) for each hologram by scanning across the hologram spatially and temporally. e) PFU detection performed through application of a threshold of 0.5 to the probability map. f) Result of processing of whole 6-well plate. This method yielded an assay with a 10-fold higher dynamic range with reduced incubation times than conventional approaches without the need for staining. Figure reproduced with permission from [135].

suffer from poor resolution limits, which makes visualizing organisms any smaller than large bacteria challenging [136]. Fundamentally, LFHM resolution, under optimal configurations based on the sensor, wavelength of light used, and source-sample-sensor distances, is limited by the sensor's pixel size [137]. Under optimal configurations, *Schistosoma haematobium* eggs, parasitic eggs present in stool and urine of infected individuals, and *t. vaginalis* parasites have been imaged [105]. 3D motility of *t. vaginalis* has been used as an endogenous biomarker for automated biosensing of this parasite in dense blood or cerebrospinal fluid with an LFHM system that scans across a capillary tube containing 3.2 mL of fluid [138]. A three-wavelength LFHM configuration has been shown to provide micrometer resolution to image *Giardia duodenalis* cysts in contaminated water [139].

Tightly tuned LFHM configurations enable detection of parasites or even large bacteria, but typically not smaller pathogens. Several techniques have attempted to split the reference and sample waves to achieve higher resolution, a technique which produces global interference fringes similar to Michelson interferometer-like digital holographic microscope configurations. One LFHM which used two small GRIN lenses to do this still had difficulty resolving bacteria like *Bacillus subtilis* [140]. This reference and sample wave splitting has also been achieved by collecting holograms from a reflected field created by a step-down chip design [141], and by passing the source wave through a prism with two diffraction gratings which direct a single diffraction order each towards the image sensor, with one beam passing through the sample and the other reference beam propagating unaffected [142].

PSR techniques, which computationally reduce pixel size, are therefore often necessary to achieve the resolution required to visualize pathogens directly. One configuration used an LED array to achieve PSR-based imaging of malaria (*Plasmodium falciparum*) parasites in an LFHM system [119]. A similar PSR technique coupled with on-chip immune-based immobilization of HSV-1 and HSV-2 viruses enabled the visualization and sizing of these small viral particles directly [143]. A simplification of typical LFHM systems through the substitution of a cone-shaped optical fiber tip instead of a pinhole filter in a single-source LFHM setup also enabled direct visualization of microorganisms in pond water [116].

Other, even more creative (although potentially difficult to implement translationally) methods have been explored to improve LFHM imaging for pathogens. The deposition of polyethylene glycol onto immobilized adenovirus and influenza A virus created small nanolenses which enabled visualization of the virus [144]. Ultrasonic wave propagation has been shown to similarly produce nanolenses around nanoparticles, rendering them detectable

in solution through LFHM, which could theoretically be possible with small pathogens [145].

When performing bacterial or viral culture for diagnosis of infectious disease, often time is the main cost. LFHM presents some compelling methods that reduce the time it takes to process these types of samples, and even reduces the sample processing complexity. Since effective imaging of bacterial and viral culture involves quantification of colonies or plaques rather than single microbes, high resolution techniques do not need to be used. This allows for the use of simple LFHM imaging configurations that permit use within incubators, or the incorporation of additional sample handling and environmental control components within the LFHM microscope itself. Recent examples of LFHM used for this application include bacterial culture imaging, where a moving stage and heating plate are introduced into the microscope to take scanning images of an entire bacterial culture plate [146]. Stitched images were paired with a deep learning algorithm so that bacterial growth was detectable in only 3 hours, and classification among 3 different disease-causing bacterial strains was reliable within 7–12 hours. Viral plaques have also been quantified using a very similar setup (Figure 2.6), which combines a simple LFHM imaging configuration with in-microscope temperature control and deep learning to quantify plaque-forming units (PFUs) for viral cultures of VSV, HSV-1, and EMCV more rapidly than conventional approaches and without the need for staining [135]. LFHM has also been used to visualize and quantify *Staphylococcus aureus* phage plaque growth in nearly half the time of conventional assays, which is important for the development of novel antibacterial targeted phage therapeutics [147].

LFHM has also been applied as a component of immunoassays for sensing of pathogens. These systems generally image infectious particles indirectly through a sandwich assay, where one antibody is used to fix the target to a surface, and a second antibody is conjugated to

some reporter molecule or microparticle. Immunoassays have been coupled with LFHM in several ways. One unique method immobilized *Staphylococcus aureus* bacteria onto a contact lens surface, using 5 μm polystyrene microspheres to visualize bound bacteria, and accounted for surface topology with computational techniques to achieve a detection limit of 16.3 colony-forming units (cfu) / μL [148]. Agglutination assays, discussed in more detail in Section 2.3.4, have also been shown to detect infectious diseases indirectly. Using a single illumination source, 2 μm polystyrene spheres can be resolved [149]. Tracking the agglutination of these particles in response to HSV-1 with LFHM enabled a limit of detection of 5 HSV-1 viral copies/ μL to be achieved. In this method, a deep learning algorithm was used to perform autofocusing and phase recovery of particle clusters. Deep learning and particle agglutination have been combined in a LFHM-based portable COVID-19 assay as well, enabling detection of SARS-CoV-2 virus at concentrations as low as $1.27 \cdot 10^3$ copies/mL while using deep learning to accommodate cellular debris in LFHM reconstructions [75]. This limit of detection is similar to that in polymerase chain reaction (PCR) tests, but is simpler and faster to perform than PCR.

Culture and PFU analysis is the most commonly used method to determine the appropriate antibiotic to use for treatment in an inpatient clinical scenario. Some diseases are diagnosed through a patient's history or physical exam findings, but sometimes empirical antibiotic treatment is started without fully knowing which bacteria is present due to the time it takes for a culture to grow. This delay can be a contributing factor for the development of antibiotic-resistant bacteria. A better approach could be provided through LFHM, since these methods can detect and quantify infectious diseases much faster than traditional methods, without the need for sample processing, and in POC settings. The FOV, high

resolution, and component simplicity of LFHM enables this method to be used effectively for clinical infectious disease diagnosis. Some of the typical limitations of LFHM continue to be disadvantageous in this application, including sensitivity to dust and debris, and computational load, but several of the above referenced studies have shown that computational techniques and deep learning methods are starting to resolve these limitations and make LFHM a compelling approach in this field.

2.3.4 Molecular diagnosis and biosensing

As modern medicine advances, biomarkers for disease are becoming important areas of research. Current widespread methods of performing molecular biosensing are the enzyme-linked immunosorbent assay (ELISA), LFAs, PCR, and others (see Chapter 1). Each of these approaches has their own advantages and drawbacks—for example, PCR and ELISA are both known to be sensitive tests with very low limits of detection, but they require technician training to perform and often are unavailable in POC settings due to system bulk and infrastructure requirements. LFAs are ubiquitous, as they can be utilized in virtually any environment and are inexpensive to manufacture, however they are not very sensitive, requiring a high target concentration to yield a positive test, and are not quantitative. LFHM-based techniques have recently attempted to combine a very low limit of detection with POC utilization in a number of ways to detect biomolecules.

As mentioned in Section 2.3.3, agglutination assays present a powerful sensing methodology when combined with LFHM. In an agglutination assay, microparticles or nanoparticles are functionalized with an antibody or capture molecule to detect a specific target biomolecule or cellular surface marker. In the presence of this target, the particles will

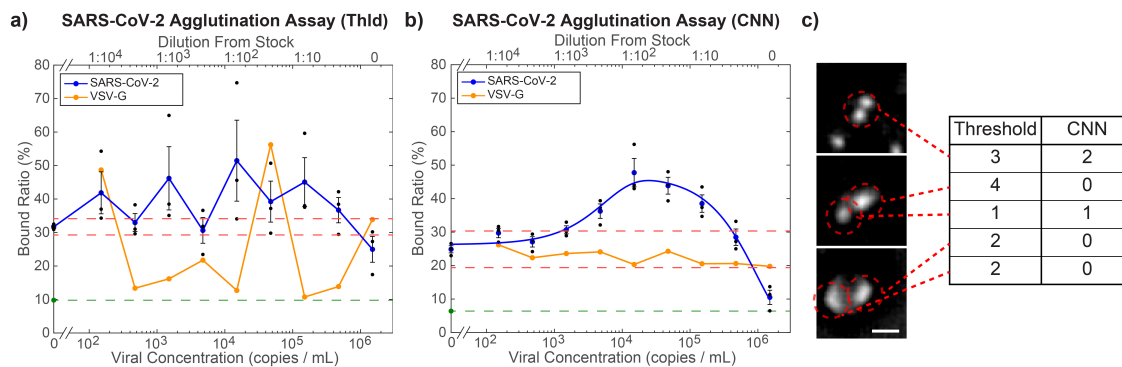


Figure 2.7: Quantification results from a LFHM biosensor used to image an agglutination assay for the detection of SARS-CoV-2 pseudovirus. a,b) Analysis of pixel super-resolved hologram reconstructions of agglutinated microparticles mixed with viral particles and cell debris using either (a) a thresholding-based image segmentation approach or (b) a residual CNN-based feature classification approach. Vesicular stomatitis virus G (VSV-G) served as a negative control and three times the standard deviation of variation of the zero-concentration point was used to calculate a limit-of-detection threshold (red dashed lines). c) The CNN performed better on feature classification than the thresholding approach as it was able to distinguish debris in the sample from agglutinated particles. This enabled the detection and quantification of viral particles at a concentration as low as $1.27 \cdot 10^3$ copies/mL. Figure reproduced with permission from [75] and more information is presented in Chapter 3.

sandwich the target, resulting in agglutination of particles. At high enough concentrations, particle aggregates can even become visible with the naked eye. So long as a system exists to quantify this agglutination, the particles can be functionalized to detect virtually any biomolecule. LFHM's large FOV and high resolution enables it to detect very subtle changes in particle agglutination as target concentration increases, enabling a much more sensitive readout of particle agglutination assays. Figure 2.7 shows results from an agglutination based biosensor for SARS-CoV-2 virus [75]. In this configuration, also discussed in Section 2.3.3, PSR was performed using a high-speed LED array to limit blur from Brownian motion, and deep learning was implemented to quantify agglutination while accounting for debris in the large FOV. This enabled a limit of detection on the same order as PCR. Additionally, this method was portable and achieved a readout of results in less than 3 hrs in POC settings, showing effective combination of the sensitivity of PCR and portability. This

same PSR LFHM system has also been used to detect biomolecules like interferon- γ , a pro-inflammatory molecule present in sepsis [11]. In non-PSR LFHM configurations, a detection method for HSV-1 has already been discussed in Section 2.3.3, but the deep learning-based autofocus and phase reconstruction can easily be translated to any biomolecule assay by changing particle functionalization [149]. Another LFHM agglutination assay was unable to resolve individual nanoparticles, but could detect the agglutination of large enough particle clusters which, when coupled with a deep learning quantification algorithm, enabled c-reactive protein (CRP) concentrations as low as 0.5 $\mu\text{g}/\text{mL}$ and as high as 500 $\mu\text{g}/\text{mL}$ to be detected, relevant for heart failure and inflammation [12]. DNA molecules have also been sensed with magnetic particles, albeit not through agglutination, but rather a sandwich assay where magnetic particles acted as reporters to visualize target DNA linkage using LFHM [150]. This resulted in the detection of DNA concentrations down to 10 pM.

LFHM biosensors are an emerging field that has the potential to have a high impact on the way clinical tests are performed. The portability and imaging characteristics of LFHM systems enable a single system to be effectively coupled with microparticles and nanoparticles to indirectly sense the presence of important biomolecules for many diseases. However, these LFHM systems still present a typical cost of around \$200, and users would need training and access to moderate computational resources. Fortunately, once LFHM platform access has been established, individual tests for these systems tend to be on the order of a few cents per test, and deep learning algorithms have been shown to lighten computational load, reducing the cost over time and making LFHM an active area of research for novel biosensor platforms. As biomarkers become more important in the diagnosis of neurodegenerative disorders, cancer, and in the development of personalized medicine, LFHM technologies can

help meet the clinical demand.

2.4 Use of lens-free holographic microscopy in biomedical research

LFHM-based methods have seen increased use in the last five years in the context of biomedical research, impacting clinical medicine and our understanding of disease, treatment, and fundamental biology and medicine. LFHM presents a unique and potentially transformative technique that in recent years has enabled researchers to make observations and to answer questions in novel workflows that would otherwise be impossible without LFHM. LFHM has also been shown to be an alternative to conventional imaging for several applications in biomedical research, and has been implemented into existing workflows seamlessly. In this section, LFHM within the context of biomedical research is discussed, focusing on basic science uses of LFHM and how LFHM can enable these types of research endeavors.

2.4.1 *Live-cell imaging and cell culture analysis*

Within the context of biomedical research, perhaps no application is more suited to LFHM than live-cell imaging. This type of imaging is widely used for research involving cell growth and cultures, including cancer research, developmental biology, and stem cell biology. The absence of objective lenses in LFHM systems means that these systems can operate in a variety of conditions, including high humidity and warm temperature environments like those inside incubators used to grow and maintain cell cultures. Figure 2.8 shows results from one particular system that captured multi-angle holograms to retrieve 3D information from cells as they grew in culture inside an incubator [151, 152]. The frequently captured

timecourse reconstructions enabled researchers to discover novel cell-to-matrix and cell-to-cell interaction and migration phenomena, without disturbing or removing cells from the incubator. Simple single-source LFHM configurations have tracked and quantified cell growth and cell motility as well, including analysis of neuroblastoma cells in culture [153]. A novel 4-hour ultradian rhythm was discovered through single-source LFHM imaging of the dry mass of thousands of cells in culture, which, when coupled with pharmacological interventions to probe different points of the cell cycle, revealed that the rhythm represents a massive degradation and re-synthesis of protein during the cell cycle [154]. Cell cycle tracking of individual cells has been achieved with single-source LFHM configurations, and the inhibitory effect of actinomycin D on the cell cycle has been observed [155].

To aid in and automate the reconstruction and quantification of LFHM holograms, parafocal autofocusing methods have been created, where wave propagation properties and image intensity distribution are used to establish a continuous autofocus condition, similar to a parafocal lens. This approach can continuously monitor growing cells and track the motility of neuroblastoma cells and bacteria [156]. Cell tracking has been automated computationally in another simple LFHM configuration, which enabled researchers to compare cell motility for NIH 3T3 cells on substrates of fibronectin and type IV collagen [157]. Deep learning methods have also been used to analyze LFHM images of live cell culture, where they perform everything from phase unwrapping for phase retrieval to estimation of cell metrics for analysis, processing over 25,000 cells per second [82].

Some samples of cell culture can be quite dense, creating problems for hologram reconstruction. To improve reconstruction under these conditions, several methods have been explored. One multiwavelength LFHM system used red, green, and blue LED illumination

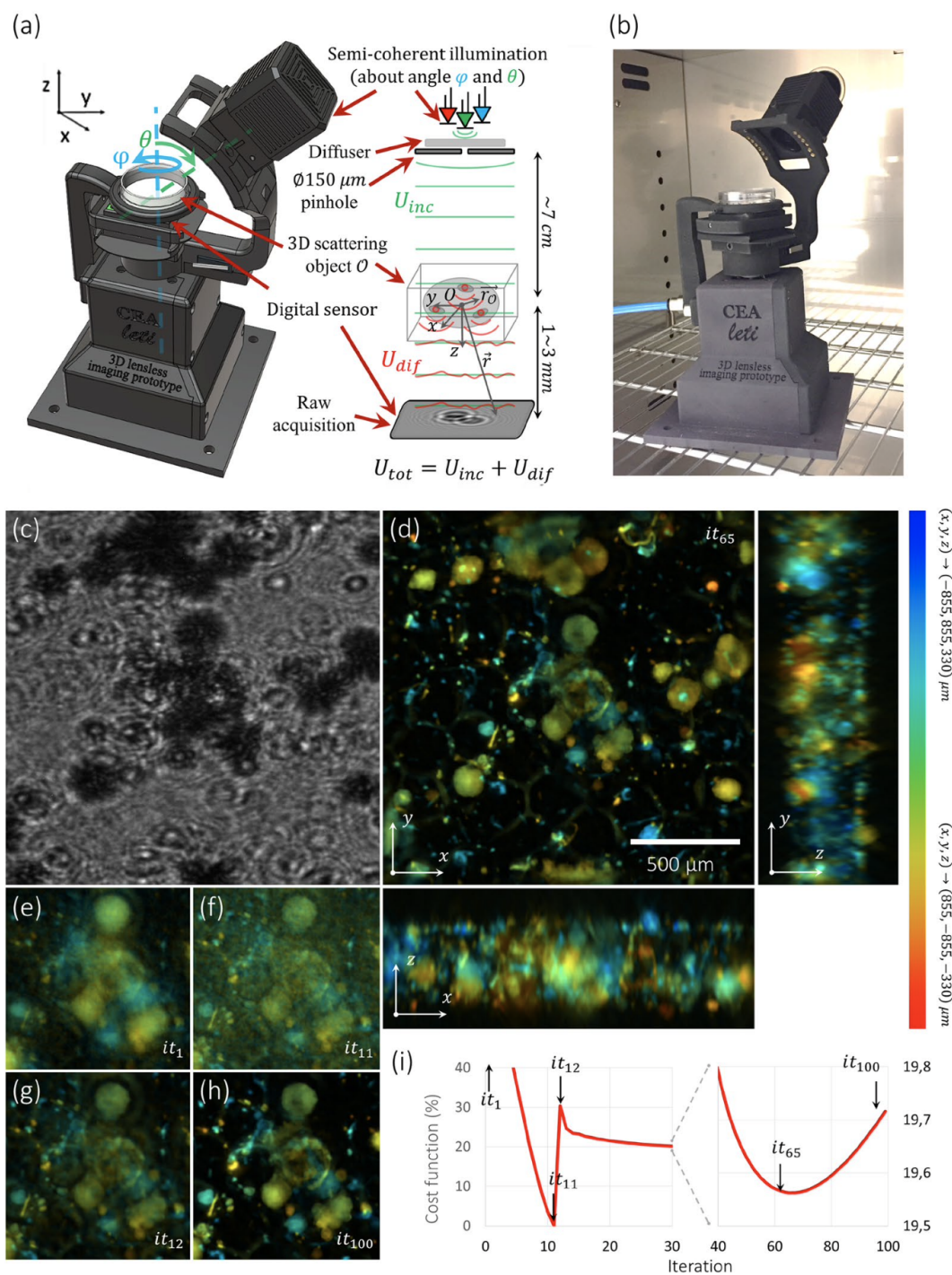


Figure 2.8: a,b) In-incubator compact LFHM device used to reconstruct 3D information from prostatic RWPE-1 cells in culture over time. c) 1 of 31 raw holograms captured with this device and used to perform the 3D reconstruction. d) 3D orthogonal average intensity projection for the reconstructed sample volume where color denotes object depth relative to the plane shown: blue being high, red being low. e-h) Average intensity projections at the data processing iteration shown in the bottom right of each image. Each iteration fills in additional information according to a cost function (i). This device was used to discover a new phenomenon regarding cell-to-matrix and cell-to-cell interactions and migrations of growing tumor cell cultures. Figure reproduced with permission from [151].

sources to collect holograms from dense cell cultures [158]. This enables phase retrieval and resolves the twin-image artifact without relying on a sparsity assumption, which allowed researchers to track cell confluence as growth and proliferation occurred. A similar configuration imaged and tracked individual cells as they progressed through the cell cycle and divided, yielding over 2×10^6 measurements [159]. Another compressive sensing approach showed promise as an alternate method to remove this twin-image artifact and was tested for images of cells in culture [53].

LFHM can also be used in situations where light must be kept to a minimum to prevent disturbing or harming cell growth. In one such low photon budget application, live glial progenitor cells were imaged successfully in-incubator using as little as $7 \mu\text{W}$ of illumination power in a simple single-source LFHM system [160]. This method was also effective for imaging stained sections of ex-vivo rodent neural tissue.

The main advantage of using LFHM to monitor and quantify growing cells in culture is its ability to do so in-incubator with minimal sample interference. The compactness, FOV, resolution, and absence of lenses in LFHM systems enables them to function well even within this challenging environment. Furthermore, imaging protocols can be automated to continuously monitor samples without sample alteration. The performance of LFHM under low photon budget constraints further reduces cell damage that can occur with extensive sample manipulation and conventional imaging. Drawbacks of using LFHM such as the density of samples affecting the image quality are being addressed. These factors, combined with the novel workflows developed and the discoveries that have been made using LFHM, make LFHM a compelling choice for future biomedical research involving live cell culture.

2.4.2 Pharmacological testing

Biomedical research on pharmaceutical development is important for drug discovery and the initial stages of drug testing before clinical trials. Pharmacological testing, particularly of chemotherapeutic drugs for cancer treatment, has recently begun to benefit from LFHM-based imaging and analysis methods. Utilizing the same in-incubator approaches that make LFHM ideal for live-cell imaging in culture, LFHM also presents an ideal platform for cell viability analysis. This has been accomplished with a single-source LFHM setup used to image cultured cells exposed to methyl mercury in a 96-well plate [161]. Other similar LFHM configurations have been used to perform cell viability testing for scraped and suspended cells in solution, enabling viability analysis to be performed on triple negative breast cancer cells exposed to apoptotic and necrotic drugs with the incorporation of a deep learning algorithm for live/dead cell classification [162]. This bypasses the need for flow cytometry in this type of research. Cell cycle arrest has also been observed through LFHM imaging of cells treated with doses of several inhibitory drugs [163]. Another method used fractal geometries of suspended cells with machine learning to classify live and dead MCF-7 cancer cells stained with tryptan blue [81].

Several on-chip methods have also been developed for LFHM-based viability analysis. One method simply characterized cells into live and dead populations based on their diameter and refractive index as cells flowed through a microfluidic chip without the need for staining or additional processing [164]. Another on-chip method first placed cells in a paramagnetic medium before applying a magnetic field across a microfluidic chip [165]. Under these conditions, cells will levitate towards the center of the chip, with live cells, being denser than

dead ones, moving towards the center more quickly. In-depth image processing was used to detect mouse bone marrow cells and breast cancer cells and determine whether populations of these cells were alive or dead via apoptosis. The previously described commercial LFHM cytometer (Section 2.3.2) is also capable of performing cell viability analysis [133].

Research into the use of LFHM for cell viability analysis has resulted in the development of multiple methodologies to assess the effects of novel therapeutics on cells. This has been shown in on-plate, on-chip, and in-suspension analysis methods, which have used stained, or labelled, and unlabelled samples. For this application, superresolution techniques are unnecessary since mammalian cell lines, which are most commonly used for viability analysis, are on the order of tens of microns, making them easily resolvable by most LFHM systems. Additionally, LFHM is well suited for this application because cells can be analyzed on-plate over time after drug exposure without disturbance.

2.4.3 Basic biological science

This final category of LFHM application is the furthest removed from the clinic, however it is nonetheless important to cover as the dissemination of basic biological discoveries often has transformative effects on translational research and patient treatment in the clinic. To this end, LFHM has been used to investigate various basic biological science questions. PSR techniques in LFHM have enabled the investigation of microorganisms like *Caenorhabditis elegans* with resolution comparable to a 40 \times microscope objective [64]. At this resolution, organelles and internal structures of *C. elegans* are visible. PSR in LFHM has also been shown to enable reconstruction of multilayer samples by leveraging the 3D information preserved in the holograms [166]. More advanced PSR algorithms have been demonstrated that

virtually rotate the pixel layout of a color image sensor to achieve amplitude and phase reconstructions with 350 nm lateral resolution and gigapixel images of *C. elegans* [167]. Additionally, tomographic or 3D reconstructions have been obtained using this LFHM setup by capturing angled holograms. Another approach to enhancing LFHM resolution for basic biological research involved laterally shifting a sample and capturing multiple holograms, which enhanced the FOV of the image and, through a unique PSR algorithm, resulted in higher resolution in the center of the image and lower resolution around the outer edges with reduced data volume [168]. This approach was used to image the leg of a fly. Other methods of LFHM image quality improvement have also been applied to biologically relevant samples. An algorithmic approach with a parameterized sharpening step was able to significantly improve the contrast of LFHM images of the head section of a *Drosophila melanogaster* fly [169].

To address drawbacks of conventional biological imaging, several LFHM techniques have been developed and tested. For samples where light could impact growing or sensitive samples, imaging must use a low-photon schema. One LFHM system managed to produce images of ex-vivo rat neural tissue and live glial progenitor cells with illumination intensity as low as 7 μW (also discussed in Section 2.4.1) [160]. Autofocusing methods, whereby an LFHM hologram reconstruction distance is selected by scanning through several reconstruction distances and a distance with a local minimum pixel value is selected, enabled effective resolution of paramecium floating in solution and of section of a *D. melanogaster* fly [170]. Finally, to address the computational load that phase retrieval can have on LFHM, a subsampled pixel approach has been developed, enabling a $5.5\times$ improvement in video framerate and order of magnitude fewer pixel measurements in the phase imaging of paranema microor-

ganisms [171].

LFHM configurations in basic biological applications tend to be fairly simple in their design, consisting of a single illumination source or otherwise employing an array of sources or a moving sample stage to acquire images for PSR. For these applications, high-resolution imaging tends to be the most desirable, and so algorithms that either improve resolution like PSR, aid in focusing like autofocusing algorithms, or improve image quality like contrast enhancement are indispensable. LFHM can easily be tuned to operate within the constraints imposed by biological samples, such as low-light conditions, or even (multi-layer) cell growth conditions. Additionally, fluorescent imaging, which is generally incompatible with LFHM due to its incoherent nature, has been demonstrated which could enable lensless imaging of fluorescently labelled samples [110]. LFHM can suffer from high computational cost in this application as well, however the introduction of subsampling and even deep learning can alleviate the computational load and enable LFHM to have a great impact in basic biological research in the future.

2.5 Conclusions and Outlook

In this Chapter, number of key innovations for LFHM that enabled its application to many high-impact regimes in clinical medicine and biomedical research have been discussed. In clinical pathology, LFHM benefits from being compact and POC, and can become transformative in this field through 3D imaging of bulk tissues. On-chip functionality is key for LFHM's success in cytometric applications. High-resolution LFHM configurations are very useful for infectious disease monitoring and for biosensors utilizing micro or nanoscale particles. In biomedical research, LFHM enables unique and compelling new workflows through

in-incubator continuous monitoring of cell culture and cell viability analyses. Finally in basic biological research, high-resolution LFHM and the customizability of LFHM systems is particularly beneficial. Overall, the breadth of computational and deep learning approaches for image processing and quantification have played a major role in LFHM's success in these fields.

Several key aspects of imminent LFHM research will likely lead to transformative clinical and biological impact. One clear example is to extend the work done with 3D sample imaging, especially for treatment and excision of cancers, which could significantly improve surgical outcomes in cancer patients. Another is the in-incubator approaches for LFHM cell culture monitoring. Refining and translating these systems could enable quite novel workflows in biomedical research to answer questions relating the stem cell research and regenerative medicine, as well as infectious disease and pharmacology. The translation of technology into this field is still nascent, with great future potential. The absence of many commercial LFHM-based systems in clinics and in laboratories indicates the need for more work in this area.

Other areas of future research will be directed at addressing the common drawbacks of LFHM in clinical and biomedical applications, such as LFHM's sensitivity to dust or debris in a given sample, the difficulty of reconstructing dense samples without artifacts, and the computational load of LFHM, which presents the main barrier for effective POC implementation. Deep learning in particular seems to be an ever-growing method in LFHM applications and can pose some significant advantages for data processing and visualization, as well as some risks. Traditional LFHM image reconstruction and quantification is based on physical properties of either light or of the sample. As such, traditional image reconstruction is a

physics-based method that can produce accurate images of unexpected outcomes, perhaps of tissue that was not stained correctly but tells us something new or unique cell growth characteristics never observed before. Deep learning, on the other hand, can be unreliable in processing data that is dissimilar from what it was trained on. This is because it optimizes its performance from a limited training set and is unconstrained by physics. The training dataset, therefore, should ideally encompass examples of all possible outcomes. This is nearly impossible to do, so each network will need to generalize to unfamiliar inputs occasionally, in which case it could “hallucinate” and generate reconstructions that are not truly present in the sample. This could be a massive problem in clinical application, so caution is essential.

Some interesting research has been performed on lens-based holographic systems (often referred to as digital holography) that could easily be converted into LFHM systems. These systems often place a lens between the sample and the sensor, using the lens to magnify a hologram before recording it. This improves the resolution of the system, but reduces the field of view. Placing the sensor at the focal plane of the objective, along with some PSR and other image improvement techniques would convert these systems to operate lens-free, reducing cost, improving portability, and enabling them to function in a wide range of environmental conditions. Systems like this have been applied to some of the same applications already discussed, such as on-chip leukemia detection [172], red blood cell imaging for anemia diagnosis [173], and malaria diagnosis [174]. Others have explored novel applications like observation of neuronal network activity [175], observation and characterization of protein and colloidal aggregates [176–180], investigation of *Streptococcus mutans* biofilm microrheology [181], investigation of cell adhesion gaps in various cancer cells [182], and sensing bone cell morphogenesis under shear stress [183]. Each of these applications presents a poten-

tial area of investigation for LFHM system development, and would expand the range of applications for LFHM.

LFHM presents a compelling technique for many clinical and biomedical applications. Its unique characteristics enable it to simultaneously replace conventional microscopic imaging techniques in many ways while also enabling novel imaging and treatment workflows. Future research in LFHM would be best directed towards improving its transformative aspects, such as on-chip functionality, in-incubator approaches, 3D reconstructions, novel deep learning approaches, and translational studies to drive LFHM adoption in the clinic and biomedical research.

CHAPTER 3

A Biosensor for SARS-CoV-2 Diagnosis¹

As a result of the COVID-19 pandemic and the initial limited availability of effective testing resources, a previously tested LFHM-based biosensor was modified, improved, and applied to sense severe acute respiratory syndrome coronavirus 2 (SARS-CoV-2) particles in a complex, biological debris-filled solution at POC settings. This technique uses a combination of a microparticle agglutination immunoassay and a classification convolutional neural network (CNN) in addition to LFHM to detect and diagnose SARS-CoV-2.

3.1 Introduction

As we have seen in Chapter 2, LFHM has been used in a variety of biosensing applications, often involving the use of microparticles as indicators for a target. The portability and sensitivity of LFHM as a biosensing platform enables it to function well in point-of-care (POC) applications, sensing biomolecules that are of clinical interest in those environments. In the last decade, perhaps no sensing application has been as pressing or as impactful as sensing for SARS-CoV-2 virus, the virus responsible for the COVID-19 pandemic. The disproportionate impact the pandemic had on low-resource and remote communities was

¹This chapter has been published previously as [75] and partially as [11], reprinted with permission from [75] and [11]. Copyright 2022 The Royal Society of Chemistry and 2021 American Chemical Society.

particularly striking.

As the pandemic persisted and new strains of the virus emerged that evaded the human immune response, there continued to be a need for powerful point-of-care (POC) tests to diagnose infection and limit the impact of new viral mutations [184]. Currently, the main biosensors used in clinical settings are LFAs, used in rapid antigen tests, and the gold standard technique of RT-qPCR, used to detect viral genetic material [185–189]. LFAs for SARS-CoV-2 can be implemented in point-of-care (POC) settings or as take-home tests and give a readout of results within minutes. However, their drawback is a relatively high limit of detection (LOD), as there needs to be a lot of viral antigen present to receive a positive test. Widely used LFAs for SARS-CoV-2 have a LOD of 3×10^6 copies per mL, which contributes to a large proportion of tests returning false negatives and can contribute to the spread of SARS-CoV-2 as infected individuals assume they are not contagious and fail to limit exposure to others accordingly [188–190]. RT-qPCR by contrast has a very low LOD, from 560 copies per mL to 1,065 copies per mL depending on the individual test [191]. This enables it to diagnose SARS-CoV-2 infection even before patients become symptomatic. However, this sensitivity comes at a cost of a slow turnaround time. RT-qPCR tests typically take days to come back with results, and it requires specialized equipment, training, and personnel to perform, as discussed in Chapter 1 [23, 24]. A turnaround time of days can result in patients spreading the virus before receiving results [13, 192].

To address these issues, several groups have been experimenting with alternative POC biosensors. One promising approach is an agglutination assay [193–198]. As described in Chapter 1, it is performed by coating latex or polystyrene microspheres with a functional capture molecule, typically an antibody, and mixing these microbeads with the test sample.

In the presence of the target biomolecule or pathogen, beads will bind together, aggregating and resulting in bead precipitation from suspension. In conventional agglutination assays, agglutination is seen qualitatively, not quantitatively, and typically requires the target to be cultured or amplified in some way to get enough agglutination to be visible. Agglutination assays are commonly used in food safety applications, as well as in the diagnosis of infectious diseases, and, barring the need for complex analyte amplification techniques, can be used in POC settings [199, 200].

As a brief reminder, recently, LFHM has been combined with agglutination assays that make these tests more sensitive, quantitative, and easier to perform in POC settings than conventional qualitative agglutination assays[12, 149]. In these in-line LFHM systems, a coherent light source is used to generate an interference pattern from a sample placed between the source and the sensor and an image of the sample is computationally reconstructed based on the interference pattern [47, 201]. This enables LFHM to maintain a wide FOV, essentially the size of the image sensor itself, while achieving a high resolution [67, 202]. To achieve the sub-micron resolution necessary to resolve microbeads for agglutination assays, pixel superresolution LFHM designs and corresponding algorithms have been utilized [57, 64, 119]. This resolution is necessary to detect subtle changes in agglutination of microbeads.

To address the unmet need exposed by the pandemic and take steps to bring a POC, rapid, low-cost biosensor to low-resource communities, a portable LFHM-agglutination assay sensor was developed. This sensor has been optimized for SARS-CoV-2 pseudovirus sensing and is coupled with a deep-learning (DL) algorithm that can distinguish beads in the sample from cell debris and viral particle aggregates in order to aid in the computational speed and accuracy of agglutination quantification. This sensor can resolve and track $2\ \mu\text{m}$ - diameter

latex microspheres undergoing Brownian motion in solution to detect subtle agglutination changes in a sample of over 10,000 beads. Compared to similar biosensors [12], the one that has been developed here utilizes a unique quantification method for individually resolved beads in clusters, is robust in handling samples polluted with unpredictable debris, exhibits a large dynamic range, and is accurate in quantifying analyte concentration. The biosensor is able to provide a POC readout of SARS-CoV-2 pseudovirus concentration within 3 h of sample collection and has a LOD within an order of magnitude of RT-qPCR tests.

3.2 Experimental Methods

3.2.1 *Quantitative large-area binding sensor*

The light source of the system consists of a 15 green light-emitting diode (LED) array positioned 15 cm above the sample. LEDs illuminate one at a time for 120 ms each, with a delay of 15 ms between each LED, resulting in 15 sub-pixel shifted images captured over 2.025 seconds that are used for pixel super-resolution (PSR) (Fig. 3.1a). Spatial coherence is provided by 180 μm - diameter hole punches placed just below each LED, and temporal coherence is provided by a bandpass filter with central wavelength 532 nm and bandwidth 3 nm, which results in the generation of holograms on imaging. At the base of the biosensor is a CMOS monochromatic image sensor (ON Semiconductor AR1335) with a pixel width of 1.1 μm .

The rapid image capture sequence performed is designed to maximize the signal-to-noise ratio of the reconstructed image after PSR. Shorter on-times (t_{on}) result in less blur as a result of particles undergoing brownian motion, while longer on-times result in higher signal

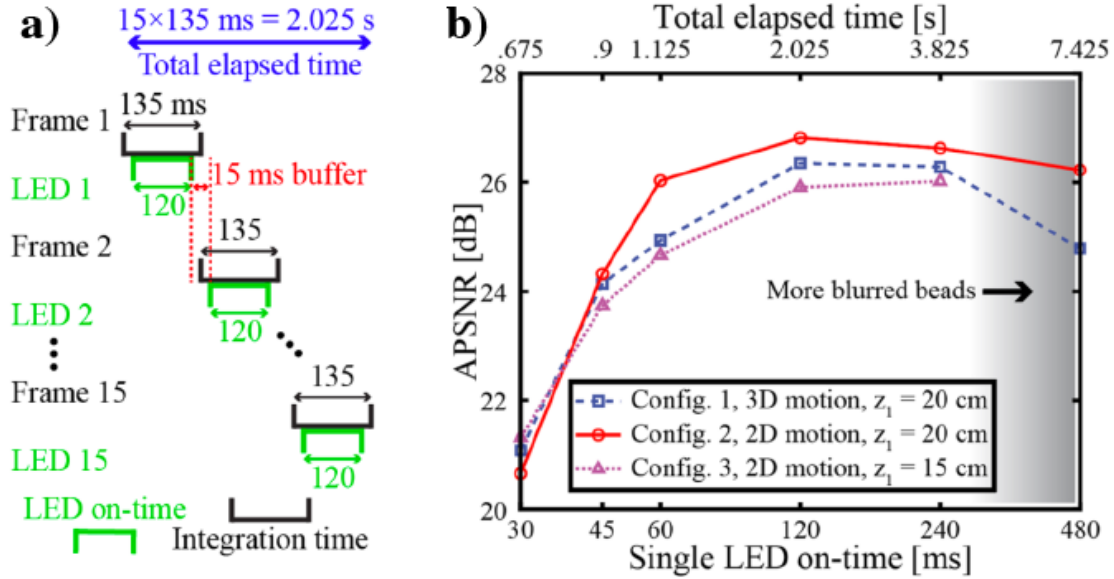


Figure 3.1: QLAB sensor configuration. a) Illustration of the exposure sequence for an LED on-time of $t_{on} = 120$ ms. The sensor integration time for each frame is $t_{on} \pm 15$ ms of buffer, providing 7.407 sensor frames per second in this example. b) Imaging performance for beads undergoing Brownian motion. Performance for the three system configurations plotted on a log-log scale. Average pixel signal-to-noise ratio, which peaks for $t_{on} = 2.025$ s, is limited by brightness for small t_{on} and by motion blur for large t_{on} . Each point represents one reconstructed image.

collection by the sensor are lower SNR (Fig. 3.1b). The on-time used in these experiments optimizes these two opposing factors.

3.2.2 Novel modifications to the QLAB sensor

The main alteration to the LFHM system described above that is different than previous publications is that it is fully contained in a light-weight portable housing weighing less than 800 g. This custom housing was designed and then printed in a FlashForge Creator 3 3D printer with black polylactic acid (PLA) (Fig. 3.2a). The housing was designed to optimize deployment in a portable setting by blocking all ambient light from the image sensor for maximum optical signal-to-noise ratio. The entire top portion of the housing is hinged, allowing the device to be opened for easy placement of the microfluidic chip over the image

sensor, and then closed again for imaging. The footprint of the device is only 15×15 cm, and images were captured using this setup paired with a laptop computer outside of the environment in which the LFHM was initially tested and constructed, i.e. at a POC site. Figure 3.3 shows images of the fully assembled LFHM components inside the housing. The total cost of this prototype device is \$1,382, with the majority of the cost allocated to a development board attached to the image sensor. Future iterations of this device would not include this board, reducing the cost to \$517. The cost could further be reduced to \$267 by using a different image sensor, such as a Sony IMX519.

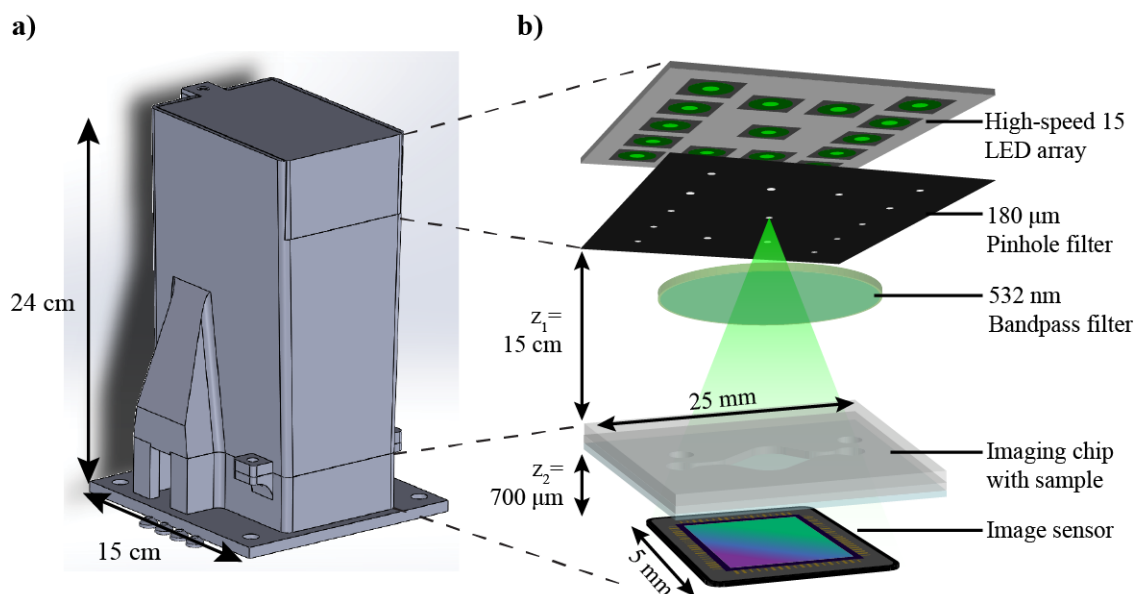


Figure 3.2: Portable QLAB sensor. a) CAD design of all components of the portable sensor housing. The housing was 3D printed from black PLA. b) Functional components of the LFHM inside the sensor.

The liquid sample is loaded into a large-area (65 mm^2) microfluidic chamber, or imaging chip, constructed out of 2 layers of clear, laser-cut polycarbonate and a single No.1 glass coverslip constructed in advance of performing the assay (Fig. 3.4). The center layer forms the boundary and thickness of the open chamber and is cut from a $125 \mu\text{m}$ polycarbonate

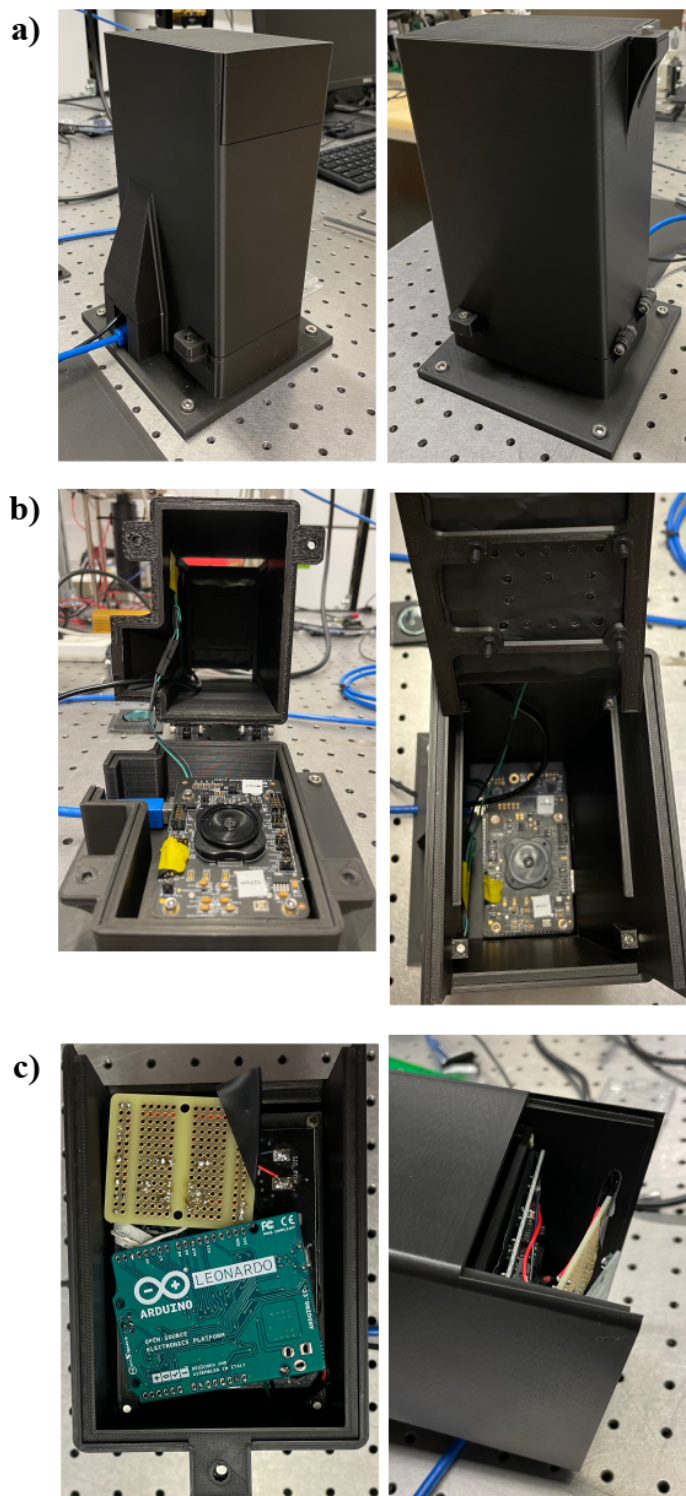


Figure 3.3: Fully assembled portable QLAB sensor. a) External view of portable LFHM housing. Top portion is hinged to facilitate loading of imaging chamber into the biosensor. b) Placement of image sensor within the base of the housing. c) Custom LED array and Arduino Leonardo microcontroller in top compartment of the housing. The underlying optical table has holes on a one-inch grid.

sheet. Inlet and outlet ports are cut from a 250 μm thick upper polycarbonate sheet. The coverslip serves as the bottom of the chip and is placed closest to the image sensor. The imaging chips can be fabricated for as little as \$0.11 each. To ensure optical clarity of the coverslip and to remove dust and other particles, coverslips were treated using a piranha solution. For this procedure, 30% H_2O_2 was mixed with sulfuric acid (H_2SO_4) in a 1:3 ratio, then coverslips were placed into this piranha solution for 1 h. Treated coverslips were washed with Milli-Q ultrapure water before being dried and assembled into the finished imaging chip. All layers were adhered to each other using UV-curable adhesive (Norland Products 7230B).

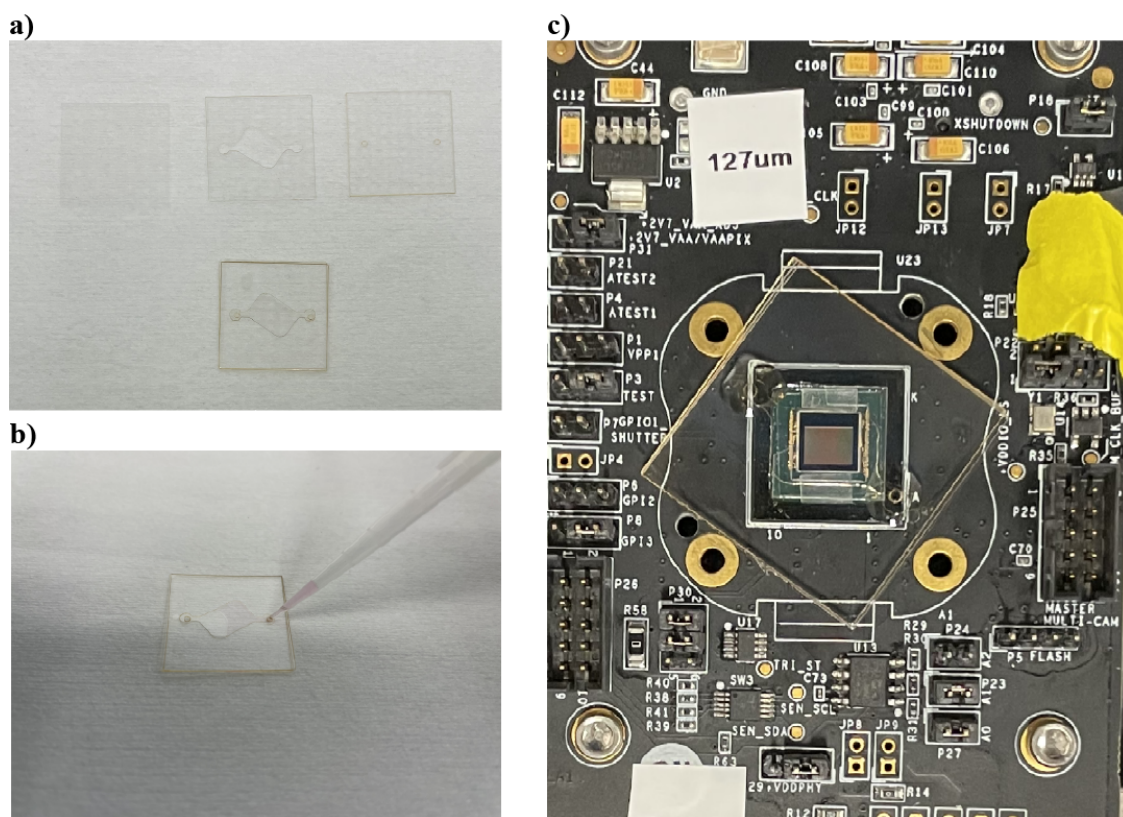


Figure 3.4: Imaging chip assembly. a) Imaging chamber components, from left to right on top: glass coverslip, 125 μm thick polycarbonate (PC) chamber spacer, 250 μm thick PC cover. b) Imaging chamber filling with 1:1 DMEM + pseudovirus and PBS + latex bead suspension. c) Imaging chip placed on top of image sensor inside the portable LFHM. Scale bars = 25 mm.

3.2.3 SARS-CoV-2 pseudovirus

The pseudovirus used for these experiments is a pseudotype HIV-1-derived lentiviral particle bearing SARS-CoV-2 spike protein. The particle has a lentiviral backbone and expresses luciferase as a reporter. Viral particles were produced in HEK293T cells engineered to express ACE2, the SARS-CoV-2 receptor, as previously described [203–205]. Cells were lysed using the Bright-Glo Luciferase Assay System (Cat: E2610, Promega, Madison, WI, USA). Lysate was transferred to 96-well Costar flat-bottom luminometer plates where relative luciferase units (RLUs) were detected using Cytation 5 Cell Imaging Multi- Mode Reader (BioTek, Winooski, VT, USA). Luciferase luminescence scales linearly with the concentration of pseudovirus copies in a given sample, and enabled calculation of pseudoviral copies per mL [204]. For these experiments, the initial pseudoviral concentration was determined to be 3×10^6 copies per mL.

Vesicular stomatitis virus G (VSV-G), a lentivirus similar to the SARS-CoV-2 pseudovirus, but which does not bear the acetyl cholinesterase 2 (ACE2) binding spike, was used as a control to confirm assay specificity. VSV-G concentrations were not separately quantified using luminescence, but the virus was produced similarly to the SARS-CoV-2 pseudovirus, and a wide range of dilution concentrations were tested to confirm an absence of agglutination signal.

3.2.4 Particle preparation and SARS-CoV-2 agglutination assay

The protocol for performing the agglutination assay is depicted in Figure 3.5. Polystyrene microspheres $2 \mu\text{m}$ in diameter and conjugated with streptavidin (Nanocs PS2u-SV-1) were

diluted to a concentration of 0.005% and mixed with 0.01 mg of ACE2 per mL of bead suspension. This concentration corresponds to approximately 50,000 molecules of ACE2 per microsphere. Microspheres and biotinylated ACE2 were incubated for 2 h at 25 °C on a shaker at 1,200 rpm. Functionalized beads were stored at 4 °C before use.

Extracted pseudovirus or VSV-G was filtered using a syringe filter with a 0.22 μm pore size to remove larger cell debris from the sample. The filtered virus was diluted in Dulbecco's modified Eagle medium (DMEM) in half-log dilutions ranging from 3×10^6 copies per mL to 3×10^2 copies per mL, with a negative control of pure DMEM. Functionalized microbeads were mixed 1 : 1 with each pseudovirus dilution for triplicate samples per dilution, creating 30 samples with a microbead concentration of 0.0025% or 0.005% and pseudovirus concentration ranging from 1.5×10^6 copies per mL to 1.5×10^2 copies per mL, including the 3 negative controls. In this procedure, only 40 μL of viral sample is required per test. A single microbead sample was reserved in pure PBS for comparison. Samples were incubated for 2 h at 25 °C on a shaker at 1,200 rpm and then 25 μL were micropipetted into the imaging chip. The chamber was sealed using UV-curable adhesive, allowed to sediment for 15 minutes to ensure particles were at the bottom plane of the chip, and placed inside the portable LFHM for on-chip imaging of the completed agglutination reaction. Sealing the chip is only necessary for preventing evaporation when storing the chip to make repeated measurements at later times.

3.2.5 Image processing and analysis

To process the low-resolution (LR), sub-pixel shifted holograms captured of the SARS-CoV-2 agglutination assay, the following workflow was employed. LR holograms are first

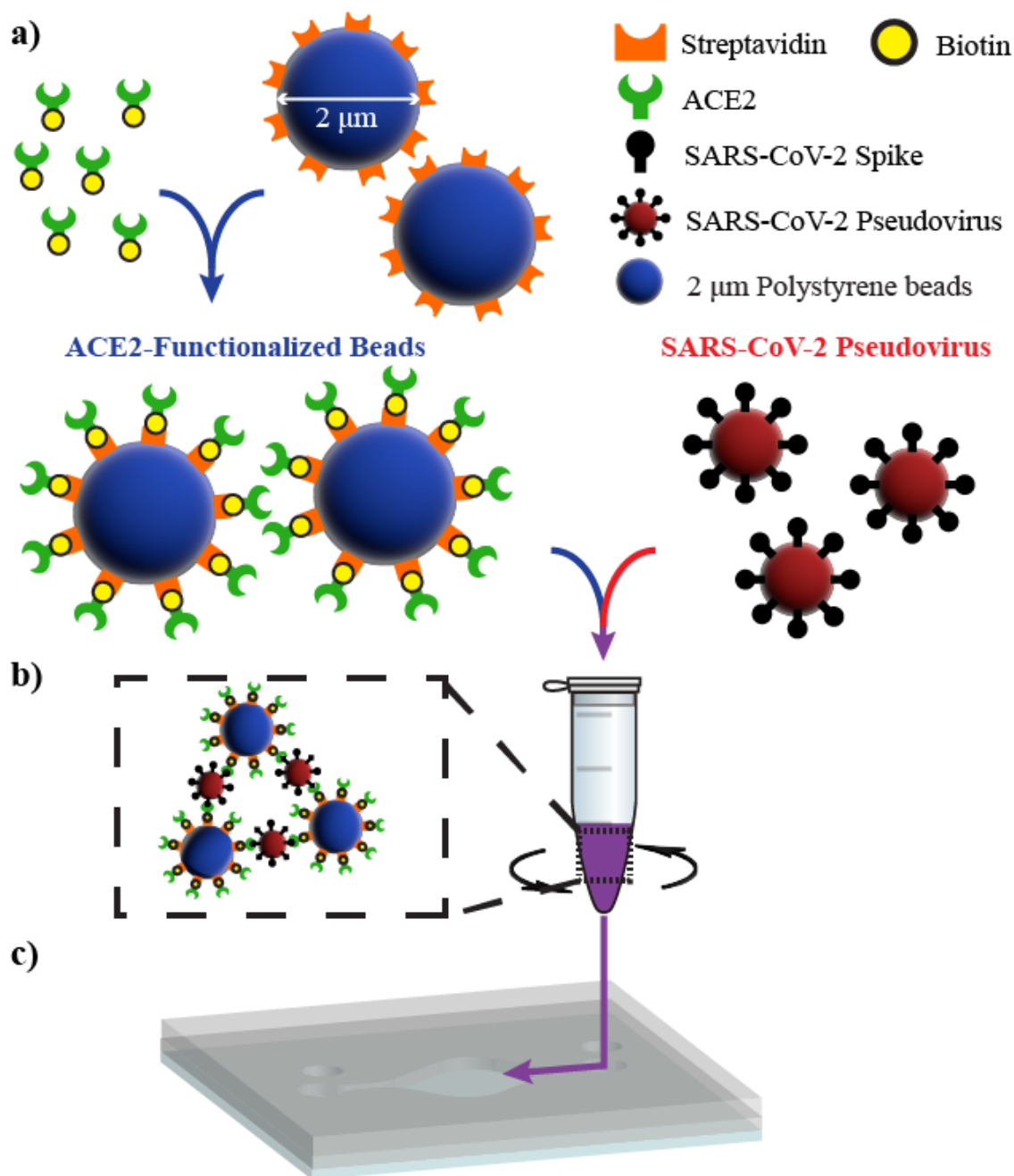


Figure 3.5: SARS-CoV-2 agglutination assay procedure. a) 2 μm polystyrene beads conjugated with streptavidin are incubated with biotinylated ACE2, yielding ACE2-functionalized microbeads. b) Functionalized beads are incubated with SARS-CoV-2 pseudovirus within a 1.5 mL test tube on a shaker at 1200 rpm, resulting in microbead agglutination. c) The completed assay is loaded into the imaging chip via micropipette direct injection.

divided into 5×7 partially overlapping patches. A PSR technique that has been optimized for small targets was used to synthesize a high-resolution (HR) hologram from the LR holo-

grams for each patch in parallel [57]. HR hologram patches are then back-propagated to the sample plane. Cardinal-neighbor regularization (weight = 200) and twin-image noise suppression were used to improve the signal-to-noise ratio of the back-propagated HR reconstructions. Then, the reconstructed HR patches are stitched back together to create a single image of the full FOV that is used for assay analysis. This image processing is performed using the University of Arizona's high-performance computing clusters, which are accessed remotely on a portable laptop computer, and takes on average 20 minutes per image to process. Performing the data processing on the laptop alone without access to a cluster takes approximately 42 minutes. Similar holographic reconstruction tasks using parallel processing on a graphical processing unit (GPU) have demonstrated approximately an order of magnitude improvement in processing time, and so processing time could potentially be reduced to just a few minutes [167, 206, 207]. Figure 3.6 depicts LR holograms and their fully processed HR reconstructions.

Two methods of feature analysis were used to quantify the agglutination assay from these HR reconstructions. In one method, image features (monomers and clusters) were isolated by applying a binary threshold to the reconstructed HR image, and then finding connected features. Feature area and eccentricity were calculated and a boundary in this parameter space was automatically determined to separate monomer features from clusters. Cluster size was then extrapolated based on the given feature's area. Intensity (brightness) and size (area) thresholds were selected to include as many true beads as possible, while excluding non-bead features. All features are plotted based on these two parameters, as shown in Figure 3.7. A built-in Matlab classifier function (`fitcsvm`) was used to draw a monomer-cluster boundary line (red line) for 18,747 beads which enables the quantification

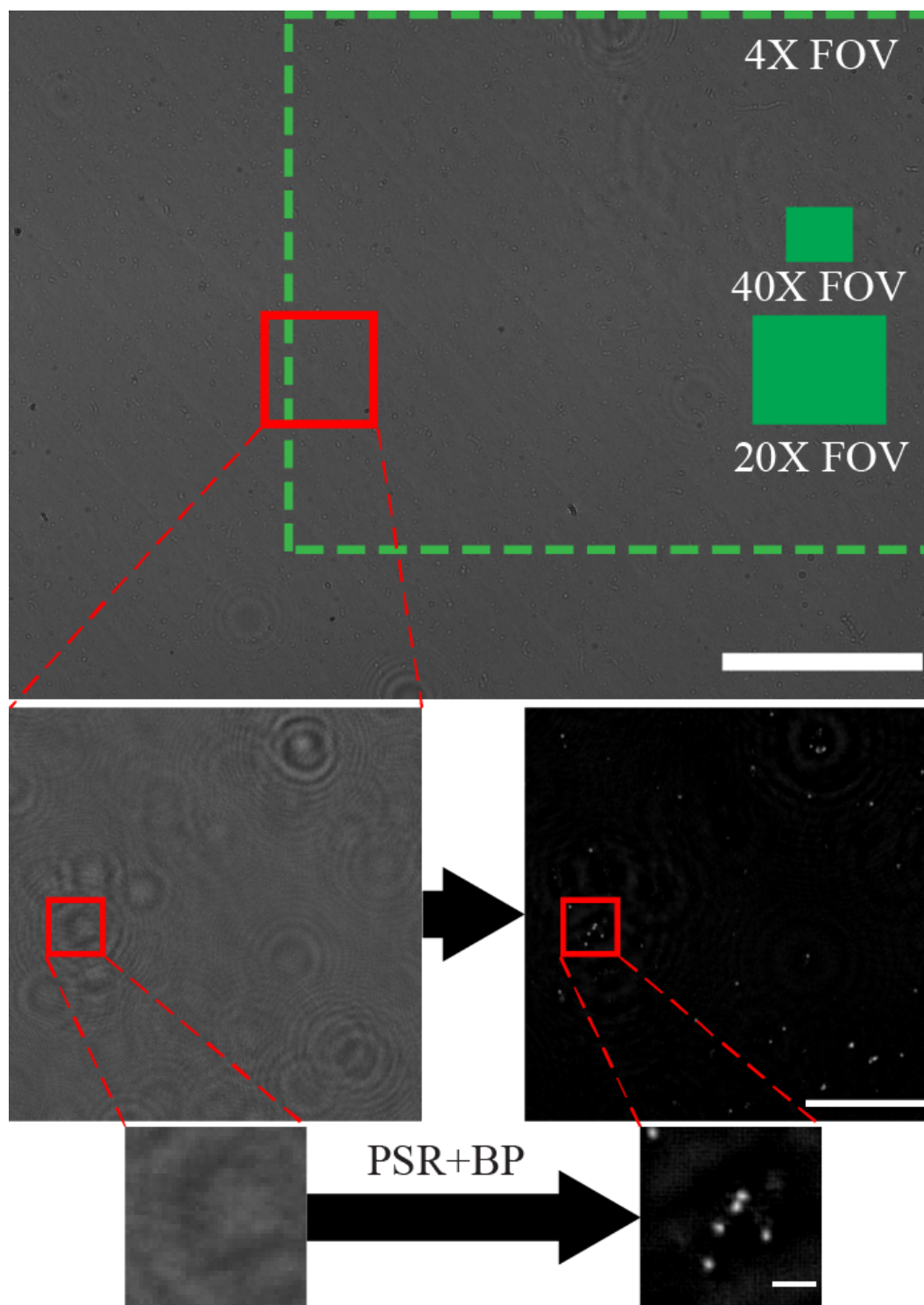


Figure 3.6: Hologram reconstruction and PSR. The top image is a single LR hologram captured with the portable LFHM. Green boxes represent the FOV of a conventional microscope using different objective lenses. Scale bar = 1 mm. The second row is a small region of interest showing a comparison of a LR hologram (left) to the reconstructed HR image after PSR and back propagation (right). Scale bar = 100 μm . The bottom row is a further zoomed-in region of this image, depicting the LR hologram (left) and HR reconstruction of fully resolved beads (right). Scale bar = 10 μm .

of binding during agglutination.

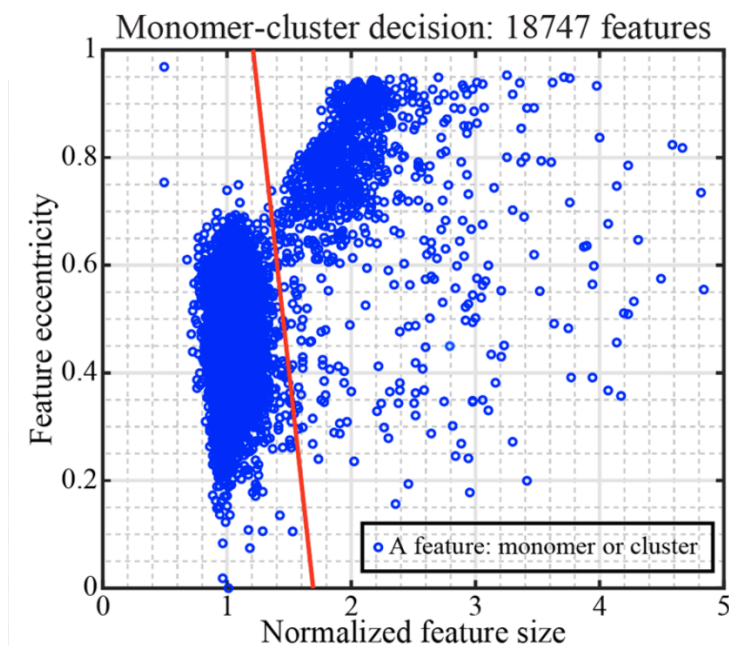


Figure 3.7: Threshold-based binding quantification algorithm. Scatter plot of a single sample with 18,747 features, exhibiting a clear monomer-cluster boundary (red line) drawn automatically with the Matlab classifier function.

To further optimize thresholding, a range of intensity and size thresholds were scanned through and the combination of values that resulted in calculated monomer and dimer areas most similar to expected areas were selected. This slightly improved the performance of this technique when used with images containing features other than microspheres. Bound ratio (BR) was calculated with the following equation based on the results of the thresholding analysis.

$$\text{BR} = \frac{\text{Number of Beads in Clusters}}{\text{Number of Beads in FOV}} \quad (3.1)$$

The LOD for the overall assay was determined by calculating the mean and standard deviation of the BR for the negative control sample and using Eqn. 3.2, which combines the mean and standard of deviation of the negative control data points, to determine the BR_{LOD}

cutoff. The range of SARS-CoV-2 concentrations with a BR above this cutoff determine the dynamic range of this assay, while the LOD is given by the lowest concentration where $BR \geq BR_{LOD}$. Similarly, any BR that falls below the lower limit of detection cutoff, BR_{LLOD} (Eqn. 3.3), is also within the dynamic range of this assay.

$$BR_{LOD} = \mu_{Control} + 3\sigma_{Control} \quad (3.2)$$

$$BR_{LLOD} = \mu_{Control} - 3\sigma_{Control} \quad (3.3)$$

3.2.6 Residual convolutional neural network

The second method of image analysis was implementation of a deep convolutional neural network (CNN) with residual connections to classify image features (Fig. 3.8). This network was designed to account for the complex imaging conditions present in the SARS-CoV-2 agglutination assay that contains cell debris, viral particles, and other contaminants. To accomplish this, a 4-block deep CNN with residual connections was designed with the MATLAB deep learning toolbox. This network updates convolutional filters, weights, and biases according to the built-in stochastic gradient descent with momentum optimizer, and employs L2 regularization to prevent overfitting. Classification loss is calculated using the following equation and used to update values in the network:

$$Loss = -\frac{1}{N} \sum_{n=1}^N \sum_{i=1}^K w_i t_{ni} \ln(y_{ni}), \quad (3.4)$$

where N is the number of samples, K is the number of classes, w_i is the weight for class i , t_{ni} is the indicator that the n th sample belongs to the i th class, and y_{ni} is probability that the network associates the n th input with class i .

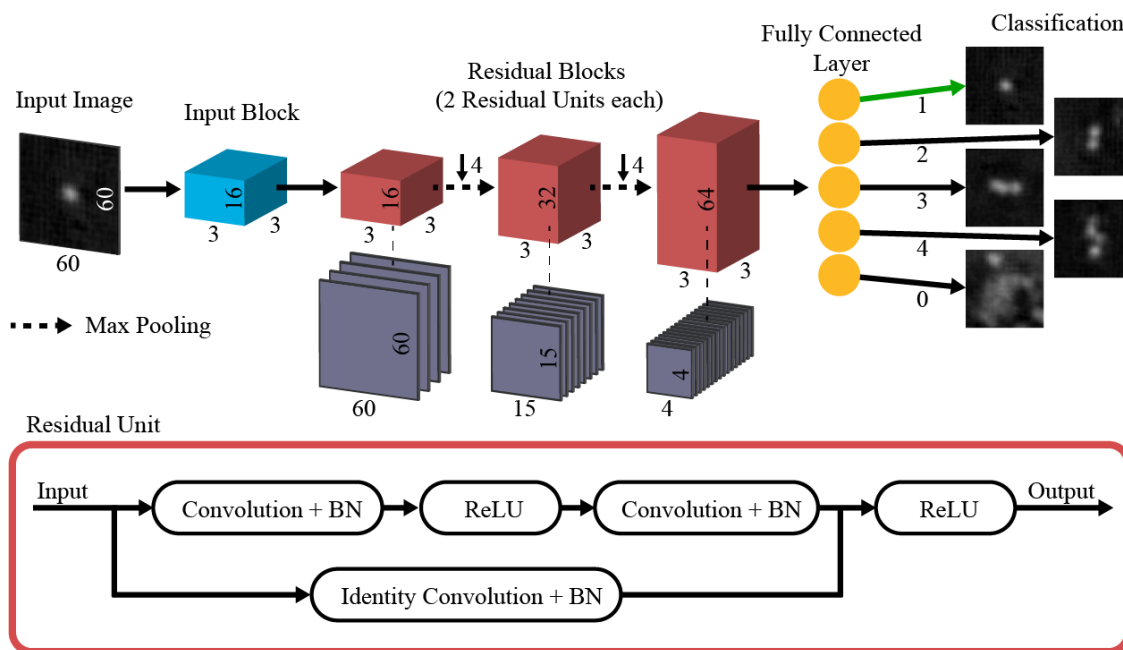


Figure 3.8: Residual CNN architecture. Input images of size 60×60 pixels are fed individually into the network. Each image passes through the input block, consisting of a convolutional layer with 16 3×3 filters, a batch normalization (BN) layer, and ReLU activation layer. Then the data, now 16 channels wide, is passed to the first of 3 residual blocks. Each residual block consists of 2 residual units, and connections between the blocks contain pooling layers that reduce the data size by a factor of 4^2 . Each residual block increases the width of the network by a factor of 2. Finally, data is passed into a fully connected layer which outputs a classification for the input image. Examples of the classification result for 5 input images are shown in the last column of the diagram.

Training of this network was accomplished by using a single intensity threshold to identify features of interest in several agglutination assay images and cropping a subset ($\approx 1\%$ of the total features in any given image) of these features into small images 60×60 pixels in size. These 1,410 unique images were hand-classified into 5 categories: features consisting of 1, 2, 3, or 4 microspheres, as well as a fifth category for cell debris or unknown features that should not contribute to the calculation of BR. Cluster sizes greater than 4 are disregarded

because their size cannot be measured as accurately and this sensor is optimized for very low concentrations of SARS-CoV-2, where very large cluster sizes are rare. To augment the training dataset, the cropped and hand-classified feature images were rotated and mirrored, to yield a total of 11,280 images. Of these images, 75% were used for training and 25% were reserved for validation. Training data was fed into the network in a random order each epoch to ensure generalizability of the training. Validation was performed every 2 epochs. A 2-core Intel® Xeon® Gold 5218 2.29 GHz processor was used to train the network. To prevent overtraining, training was halted after the classification accuracy of the validation image set stopped improving.

3.3 Experimental Results and Discussion

CNN training took 1,980 iterations or 30 epochs (Fig. 3.9a and b). Each iteration consisted of a batch of 128 training images. After 30 epochs, validation accuracy ceased improving so the training was halted to prevent overtraining (training accuracy and loss diverging from validation accuracy and loss). The final validation accuracy of the trained CNN was 82.06%. Due to the complexity of appearance of the debris in the training images, varied bead configurations for any given cluster size (e.g. linearly arranged, beads touching all other beads in the cluster, etc.), and slight variations in focus of the individual features, the image data was highly heterogeneous. Because of this heterogeneity, CNN validation accuracy could not be further improved without sacrificing generalizability to the broader intended dataset. To account for this, the CNN was designed to place features with low maximum softmax probabilities or activations, or ones that could be classified incorrectly, into smaller feature size categories, rather than larger ones (Fig. 3.9c). The net effect of

this “rounding down” network behavior is the undervaluation of BR, as cluster size tends to be undercounted rather than overcounted. Thus, even though validation accuracy never reached 100%, the network is not artificially inflating the BR for any samples and that the calculation of LOD for the assay is therefore conservative. Furthermore, since this behavior is consistent among all samples tested, it is unlikely that the validation error had a significant impact on the assay. Precision and recall measurements for each classification category are shown in Figure 3.9c, with averages across all categories of 83.21% and 82.04% respectively.

To ensure the network was not overfit to augmented data, a test data set of 1,200 images without augmentation was analyzed using the CNN (Table 3.1). Unlike the training and validation sets, the test data set did not have an equal number of images in each category, and instead the category distribution was representative of the distribution seen in real images. The accuracy for this real-world application of the network was 88.58%. Since the images of this test set consist predominately of single beads (874 out of the 1,200), this high accuracy is consistent with the accuracy values shown in Figure 3.9c. To better compare this result to the training and validation accuracy, images in test data set were removed and features of size 3 and 4 taken from other sample images were added such that the categories were balanced and large enough to provide an adequate comparison (150 images total). The resulting accuracy of 81.33% is within a percent of the validation accuracy and definitively confirms that this network is not overfit and performs well for real images.

The network also exhibited higher maximum softmax probability values for correctly identified features than for incorrectly identified features (Table 3.2). In this case, maximum softmax probability values represent the relative activation of the network output layer neurons and give an indication of the “certainty” the network has for a given prediction, with

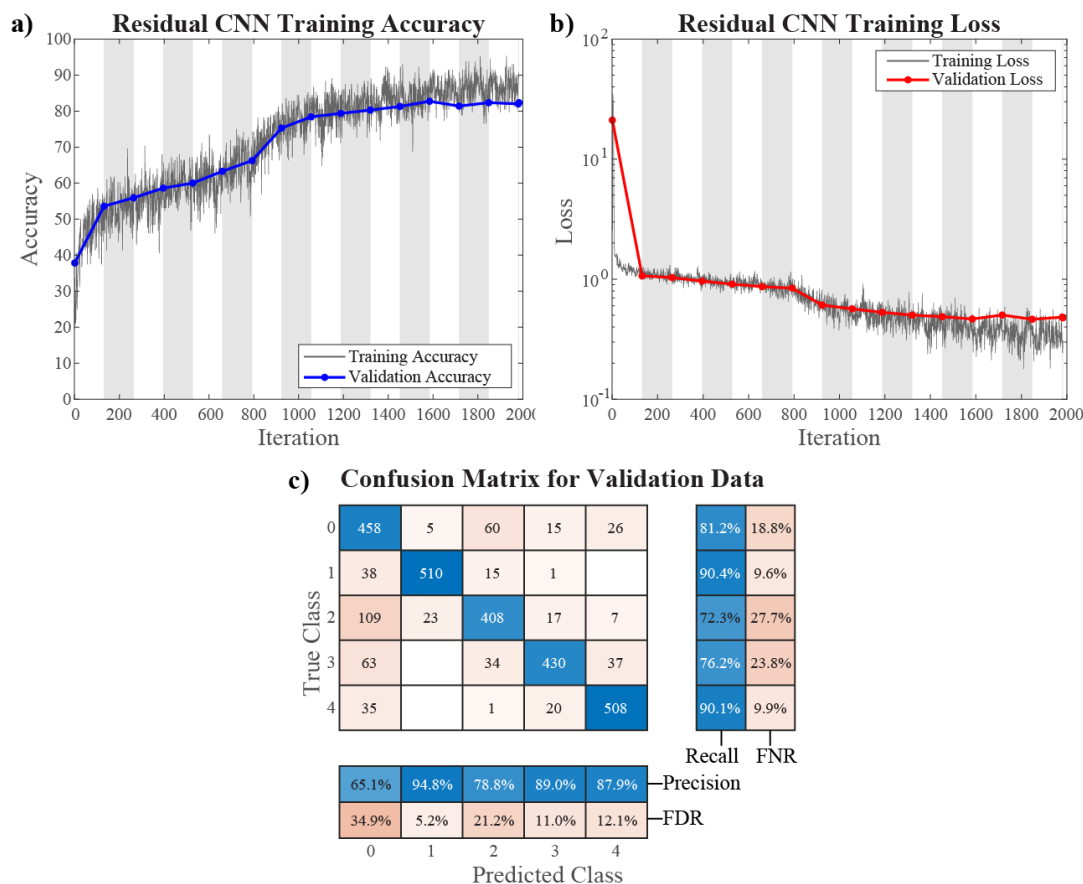


Figure 3.9: Results of CNN training. a) Accuracy of the training and validation data over the course of training. Validation accuracy does not diverge from the training accuracy over the course of training, indicating the network is not overtraining. b) Loss calculation for the training and validation data over the same training timespan. Again, validation loss does not diverge from training loss, indicating the network has not been overtrained. The training duration of 1,980 iterations corresponds to 30 epochs. White and grey chart backgrounds denote 2 epochs in width each. c) Confusion matrix for validation data classification. The blocks at the right and bottom show the total correct and incorrect classifications in each row and column of the confusion matrix. 63.83% of all incorrectly classified features are classified as smaller than they actually are, resulting in a slight undervaluation of bound ratio.

high values indicative of a high degree of certainty that the classification is indeed accurate [208]. This network behavior was unexpected, but unsurprising as the network training is designed to minimize training loss (a more complex measure of network error that includes all softmax probabilities), rather than maximizing accuracy (see Eqn. 3.4). Low maximum softmax probability for incorrectly classified images represents lower loss than high maxi-

Table 3.1: Network output results for test data sets. Training and validation images are drawn from an augmented data set. Test data are unaugmented. Balanced test data include equal numbers of images with 0, 1, 2, 3, and 4 beads, while representative test data include a distribution of bead cluster sizes that is representative of real samples.

Image Data Set	Network Output Accuracy
Training	89.28%
Validation	82.06%
Test (Balanced)	81.33%
Test (Representative)	88.58%

softmax probability for incorrect classifications. While softmax probabilities provide some indication of certainty, and can be used to derive useful statistics, they should not be used as direct measures of statistical confidence [208].

Table 3.2: Network confidence values for image classification of training and validation data.

	Mean Confidence (correctly classified)	Mean Confidence (incorrectly classified)
Training	90.31%	63.11%
Validation	90.27%	68.02%

The training time for this network was 175 s. Feature classification using the trained CNN takes 14.11 s for an average full field of view sample, which is 2.74x faster than the previous thresholding-based classification, which takes 38.65 s for an average full image.

3.3.1 SARS-CoV-2 biosensing assay

The SARS-CoV-2 agglutination assay dilutions were imaged and analyzed following the procedures described in Section 3.2. The optimized thresholding analysis and CNN-based results are shown in Figure 3.10a and b, respectively. The BR_{LOD} cutoff for thresholding analysis was calculated to be 34.13%. According to this calculation, the lowest sample concentration in Figure 3.10a whose mean minus one standard error of the mean (SEM) falls

above the LOD cutoff corresponds to 1.5×10^2 copies per mL. However, for an imaging chamber with $25 \mu\text{L}$ of sample, one would expect < 4 viral particles in the chamber. Therefore, this point is very unlikely to be a true LOD and only falls above the LOD cutoff due to the high variability (average standard of deviation of 10.66% over all non-control points) in the thresholding analysis process. Additionally, the VSV-G specificity control shows this same high variability as its concentration changes, even though the BR for this control should remain constant at or near the BR of the negative SARS-CoV-2 pseudovirus control at 31.70%. Overall, thresholding analysis had a very high average standard of deviation for all non-control points of 10.66%. This makes determination of a true LOD from these data impossible, as there appears to be no clear trend as either virus concentration increases. For this dataset, thresholding analysis fails as it is not robust enough to account for the heterogeneous nature of a sample with cell debris and higher levels of non-specific binding.

For CNN-based analysis (Fig. 3.10b), the BR_{LOD} cutoff was calculated to be 30.33%. The mean BR corresponding to 1.5×10^3 copies per mL is the first to fall above the LOD cutoff. VSV-G control points all remain within the negative control zone, indicating assay specificity for SARS-CoV-2. Additionally, measurements for each dilution using the CNN show a much lower variability (average standard of deviation for the BR of all non-control virus concentrations is 3.89%). An empirical curve of best fit, plotted in Figure 3.10b, was determined according to the following equation:

$$\text{BR}(x) = Ae^{-x/10^b} - Ce^{-x/10^d} \quad (3.5)$$

The functional form of this empirical curve is useful for inferring the analyte concentration

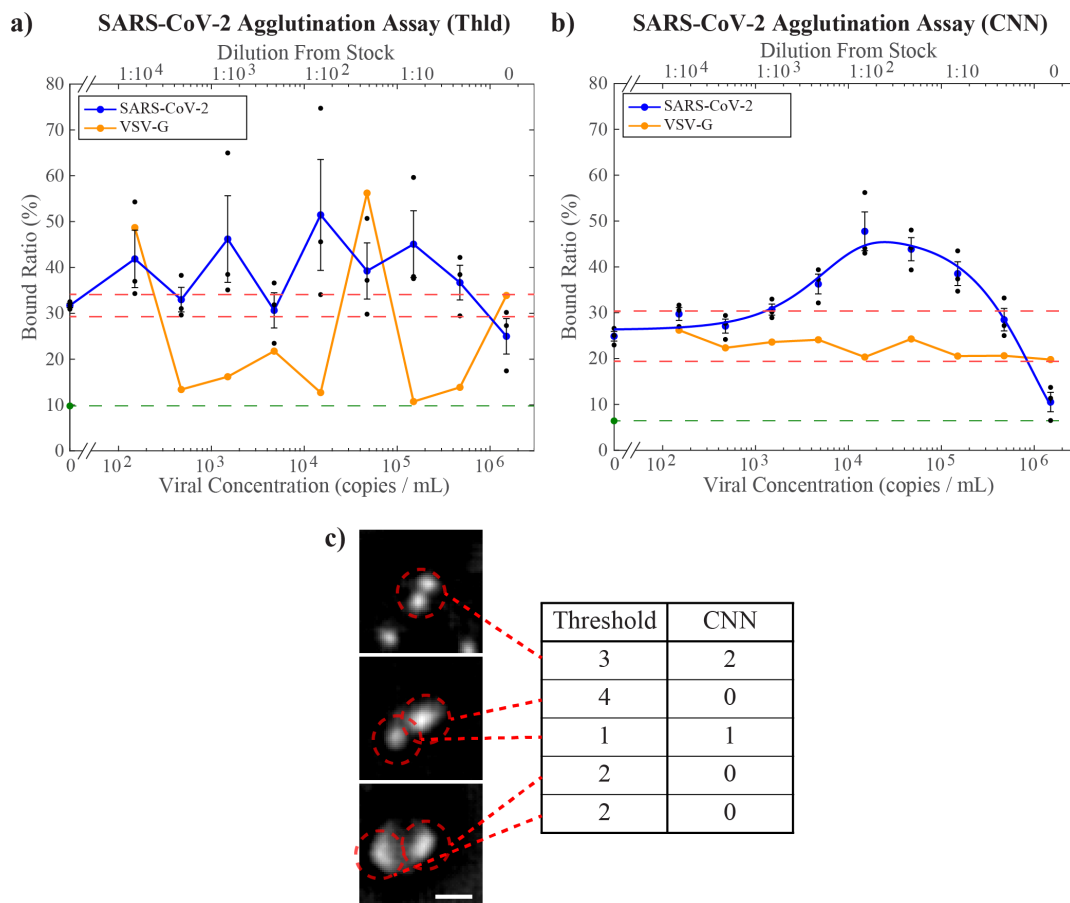


Figure 3.10: Results of SARS-CoV-2 agglutination assay. a) Optimized threshold-based quantification of the agglutination assay, which fails to find a clear trend in BR as a function of concentration. b) CNN-based agglutination quantification. The blue curve is a best fit to Eq. 3.5 ($R^2 = 0.974$). The LOD based on this curve is 1,270 viral copies per mL. For both graphs, orange points indicate measurement results for the negative control VSV-G. As the viral concentration of the VSV-G was not independently measured, the dilutions of the sample relative to the stock solution (top axis) were matched to the same dilutions of the SARS-CoV-2 pseudovirus, whose stock concentration was independently measured, yielding the bottom axis values. The red dashed lines are the upper and lower LOD cutoffs, while the green point and dashed lines indicate the BR in pure PBS. Black points indicate triplicate samples for each concentration and error bars are standard error of the mean. c) Example images classified by thresholding vs CNN. Scale bar = 5 μm .

of an unknown sample from its BR, as described below, but is not intended as a physical model of the binding process, which is a more complex relationship [11]. The coefficients and 95% confidence intervals are: $A = 46.86 \pm 4.11$, $b = 5.982 \pm 0.125$, $C = 20.60 \pm 4.86$, $d = 3.753 \pm 0.328$ ($R^2 = 0.974$). Since measurements of BR are compared to this curve,

the LOD can be determined by where the curve first exceeds the BR_{LOD} , which occurs at a concentration of 1.27×10^3 copies per mL.

Unlike the thresholding analysis (Fig. 3.10a), the CNN-based analysis (Fig. 3.10b) exhibits a clear peak in BR, where higher viral concentration ultimately leads to bead saturation and therefore reduced binding, which was observed previously in agglutination assays for other proteins [11]. As a result, it is not possible to determine the exact concentration of virus in a sample from a single BR measurement when the $BR > 19.40\%$. Nonetheless, a $BR > BR_{LOD} = 30.33\%$ would be an unambiguous positive result, which is most relevant for rapid COVID-19 diagnosis. The CNN resolves the variability seen in the VSV-G specificity control and those points are seen to lie within the LOD cutoffs, correctly interpreted as a negative result.

Interestingly, the BR for the highest concentrations of SARS-CoV-2 fell well below the BR for the negative control samples that still contained DMEM (black points at zero concentration in Fig. 3.10b). This can be explained by DMEM causing non-specific binding [193]. For comparison, negative control samples of PBS without DMEM (green point at zero concentration in Fig. 3.10b), exhibit a significantly lower BR than the negative control samples with DMEM. At very high viral concentrations, the beads in the sample become saturated with viral particles before the beads can collide with one another. In this way, the viral particles effectively act as blockers for both specific and non-specific bead-to-bead binding. Hence, for high viral concentrations, the BR trends toward the BR found in PBS in the absence of DMEM. This behavior indicates that the use of fully saturated beads as a control for nonspecific binding [12] would be inappropriate for this type of agglutination assay because it fails to account for non-specific binding that occurs as a result of bead-to-bead

interactions in different media. Additionally, this result means that this assay can distinguish between low levels and very high levels of virus by defining a lower LOD cutoff as specified in Eqn. 3.3. For the CNN-based assay with 0.0025% bead concentration, $BR_{LLOD} = 19.40\%$, which corresponds to viral concentrations of 8.45×10^5 copies per mL and greater on the best-fit curve.

Overall, compared to traditional image processing based on thresholding, CNN-based analysis enables successful and robust quantification of BR from complex pseudovirus samples, and extends the assay's dynamic range by enabling sensing of higher pseudovirus concentrations whose BR falls below BR_{LLOD} . Figure 3.10c shows a selection of features that were incorrectly classified by thresholding, but correctly classified by the CNN.

3.3.2 Quantitative and unambiguous assay readout

Unfortunately, there is still a blind spot between 1.5×10^5 copies per mL and 1.5×10^5 copies per mL, where a false negative result would occur since $BR_{LLOD} < BR < BR_{LOD}$ for these concentrations. One method to reduce this blind spot and infer specific viral concentrations from BR measurements throughout the dynamic range is to perform a second BR measurement on the same original sample, but with a higher bead concentration. Previous work with agglutination assay-based sensing has shown that increasing bead concentration shifts the binding curve from left to right [11]. Here, a second measurement on an unfiltered pseudovirus sample with a 0.005% bead concentration was instead of 0.0025% was performed (Fig. 3.11a). The higher negative control BR can be explained by a higher number of bead-bead interactions in the higher bead concentration, resulting in more non-specific binding. Since the CNN analyzes small images of individual features, the network performance was

not impacted by a higher bead concentration or a lack of pseudovirus filtration because those factors only increased the number of features classified without changing their appearance. The only effect an unfiltered sample had was a slight increase in average standard deviation of non-control BR measurements: 4.45% compared to 3.89% for filtered sample at a lower bead concentration (representative images shown in Fig. 3.12). A curve was fitted using Eqn. 3.5 with the following best-fit coefficients: $A = 59.79 \pm 4.00$, $b = 6.429 \pm 0.132$, $C = 20.88 \pm 4.60$, $d = 4.077 \pm 0.301$ ($R^2 = 0.962$). This leads to a LOD of 4.81×10^3 copies per mL, were this measurement to be used in isolation.

By combining the binding results from the two bead concentrations, the exact viral concentration of almost any given sample (above the LOD) can be inferred due to the relative shift in binding curves for the two concentrations (Fig. 3.11b). To incorporate this into the assay workflow, the procedure depicted in Figure 3.11c was performed. For example, a BR of 35% using a single 0.0025% bead concentration assay would yield 2 possible viral concentrations of 3.20×10^3 copies per mL or 2.80×10^5 copies per mL. However, when combined with a BR of 54% from the 0.005% bead concentration assay, the true viral concentration of 2.80×10^5 copies per mL would be selected. The outcome of this process for all mean points is illustrated in Figure 3.11d ($R^2 = 0.993$ for values within the assay's dynamic range). The effect of this extra step on assay time would only be an additional 20 min for image processing, as the incubation and imaging could be done for both samples concurrently while the additional final calculation step occurs in a matter of 1–2 seconds, resulting in a total assay time of less than 3 h. Although this procedure is successful in inferring concentration for most of the experiments, a small blind spot remains, corresponding to where both best-fit curves fall between the BR_{LOD} and BR_{LLOD} cutoffs at

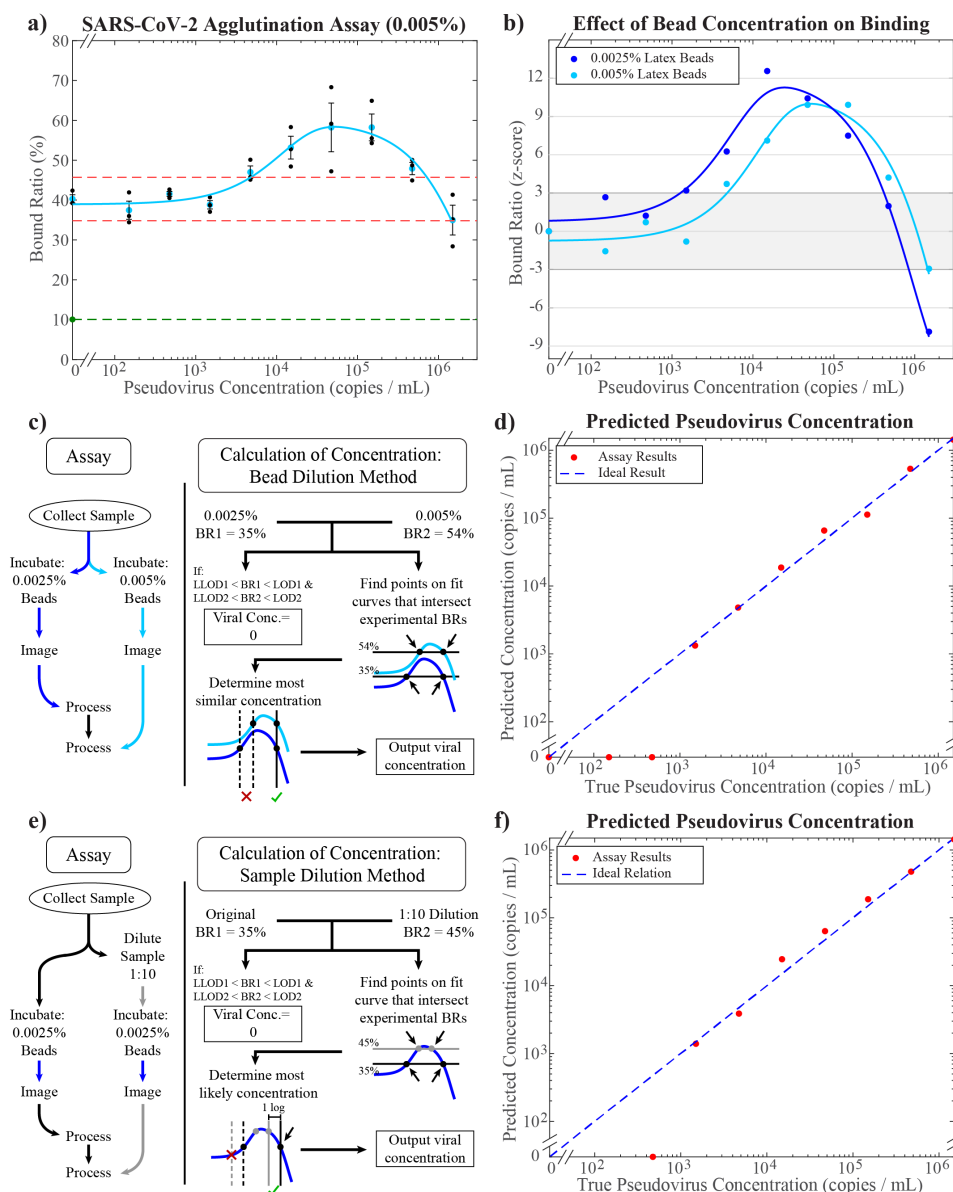


Figure 3.11: Two-measurement assay. a) CNN-based agglutination quantification on unfiltered pseudovirus lysates with 0.005% bead concentration. The LOD cutoffs (red dashed lines) are calculated as 45.72% and 34.86%. The light blue curve is fitted using Eq. 3.5 ($R^2 = 0.962$). The green point and dashed line indicate the BR in pure PBS. b) Comparison of binding curves for 0.0025% (blue) and 0.005% (light blue) bead assays normalized by their z-score: how many standard deviations a measurement is away from the negative control value. A z-score of ± 3 corresponds to the BR_{LOD} and BR_{LLOD} for each assay. c) Flowchart of combined assay to achieve accurate quantification of viral concentration using the bead dilution method. d) Results of quantification based on the method in (c) performed on the two mean BR values for each viral concentration. The R^2 is 0.993, calculated based on the log of the y -values above the LOD compared to ideal result. e) Flowchart of assay using the sample dilution method. f) Results of quantification based on the method in (e) performed on the mean BR values from the 0.0025% bead curve for each viral concentration. The R^2 is 0.989, calculated based on the log of the y -values above the LOD compared to ideal result.

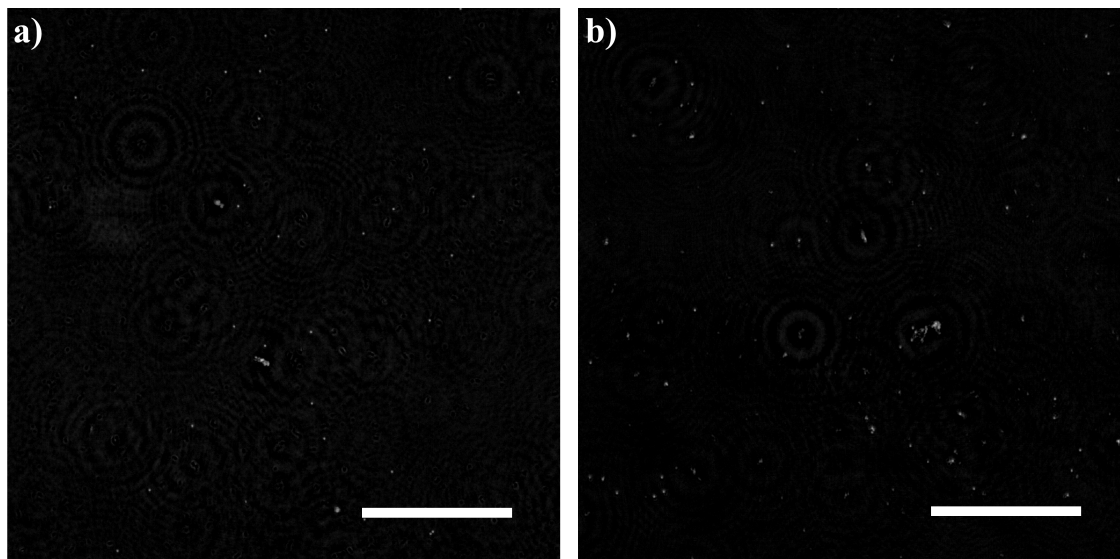


Figure 3.12: Comparison of filtered and unfiltered samples. a) Representative image of sample of filtered SARS-CoV-2 pseudovirus with 0.0025% latex beads. Despite filtering, there is still debris present. b) Representative image of sample of unfiltered SARS-CoV-2 pseudovirus with 0.005% latex beads. Lack of filtering adds more debris and particle irregularity. Scale bars = 150 μm .

concentrations greater than the LOD: 7.26×10^5 copies per mL to 8.45×10^5 copies per mL. This approach likely could completely remove the blind spot if an even higher bead concentration were used for the second measurement.

A second alternate method of performing this assay, which completely resolves any blind spot using only one binding curve, is described in Figure 3.11e and f. By diluting the original sample by 1 : 10 and performing the agglutination assay on this dilution as well as the initial sample, both using the same bead concentration, 2 points along the binding curve are retrieved that can be used to determine which side of the peak the points correspond to. While this gives a slightly less accurate measurement of the true concentration ($R^2 = 0.989$ for values within the assay's dynamic range) and adds an extra dilution step over the two-bead concentration method, it nevertheless shows that the blind spot observed in this assay can be fully resolved through at most one additional measurement.

3.4 Summary

In this chapter, a portable LFHM biosensor capable of detecting SARS-CoV-2 pseudovirus concentrations at least as low as 1,270 copies per mL within 3 hours, using only 40 μL of viral sample per test was developed and tested successfully. This LOD is within an order of magnitude of widely used RT-qPCR tests for SARS-CoV-2 and greatly improves upon the LOD of 3×10^6 copies per mL for SARS-CoV-2 LFAs. Additionally, a deep-learning based categorization method that can accommodate heterogeneous solutions by distinguishing cell debris and other non-bead particles from microbead clusters was developed, improving on traditional algorithms in speed, accuracy, and versatility. The results produced during testing indicate that the choice of negative control beads (fully saturated vs. unsaturated) for high-sensitivity agglutination assays is important by showing that fully saturated beads fail to take into account non-specific binding that occurs as a result of exposure to different liquid media, potentially leading to a miscalculation of LOD. Finally, two methods were shown by which two measurements of BR can be used to compensate for the blind spots of a single individual assay and accurately determine the exact viral load of the sample across a dynamic range of at least 3 orders of magnitude in concentration.

CHAPTER 4

Deep Learning Algorithms for LFHM Image Classification¹

The positive impact that utilization of deep learning approaches had on this LFHM-based biosensor prompted further characterization of the effects different convolutional neural network (CNN) parameters had on network training outcomes. Given that few existing publications discuss the impact of CNN hyperparameters on CNN performance for datasets limited by real-world constraints on data collection, various hyperparameter settings were thoroughly tested and network performance and training was quantified to provide a comprehensive source for implementation of simple deep learning algorithms to LFHM and biological image classification.

4.1 Introduction

As shown in Chapter 3, the performance of any real-world point-of-care (POC) biosensor that utilizes LFHM poses imaging limitations in terms of the quality of samples that can be produced, where low-quality or low-purity samples tend to result in worse image quantification. Ideally, the sample would have solely sub-nanoscale proteins for detection, resulting in a clean, transparent medium through which to image microparticle agglutination. In

¹This chapter is currently submitted to Optics Express

practice, however, this is rarely the case, as cells and other large particles are often present. Deep learning was used to resolve these issues, but the impact network structure and hyperparameters had on training and performance outcomes remain unclear. To address this and better understand the impact of various hyperparameters on network performance, a characterization study was performed in which layers and parameters of a CNN were adjusted and the resulting training outcome was measured.

In lensfree holographic microscopy (LFHM, Fig. 4.1(a)), images are reconstructed from diffraction patterns captured by an image sensor. In many cases, these diffraction patterns can be treated as in-line, or Gabor, holograms [54]. The LFHM hardware configuration is simple and cost-effective when compared to conventional microscopy, making LFHM well-suited for portable imaging and sensing devices deployed in low-resource settings. Furthermore, LFHM offers an ultra large space-bandwidth product: the combination of an ultra-large field of view (FOV) together with high resolution [47]. Often, FOVs exceed 15 mm^2 and the smallest resolvable features are smaller than $1 \text{ }\mu\text{m}$. LFHM has been applied to a range of imaging applications, including pathological imaging [98], cell cytometry [112], infectious disease monitoring and diagnosis [105], and in-incubator cell culture monitoring [153].

Recently, LFHM has been applied to sensing applications by using automated image processing routines to count and classify small objects distributed across the FOV. Fine (diameter $< 2.5 \text{ }\mu\text{m}$) and ultrafine (diameter $> 100 \text{ nm}$) aerosols have been individually sized and quantified [110, 209–211]. LFHM has also been combined with agglutination assays to quantify specific protein concentrations, including herpes simplex virus [149], C-reactive protein [12], interferon gamma [11], and SARS-CoV-2 [75]. Nanoparticles have been used as labels for LFHM sensing of interferon gamma [212] and CD4+ and CD8+

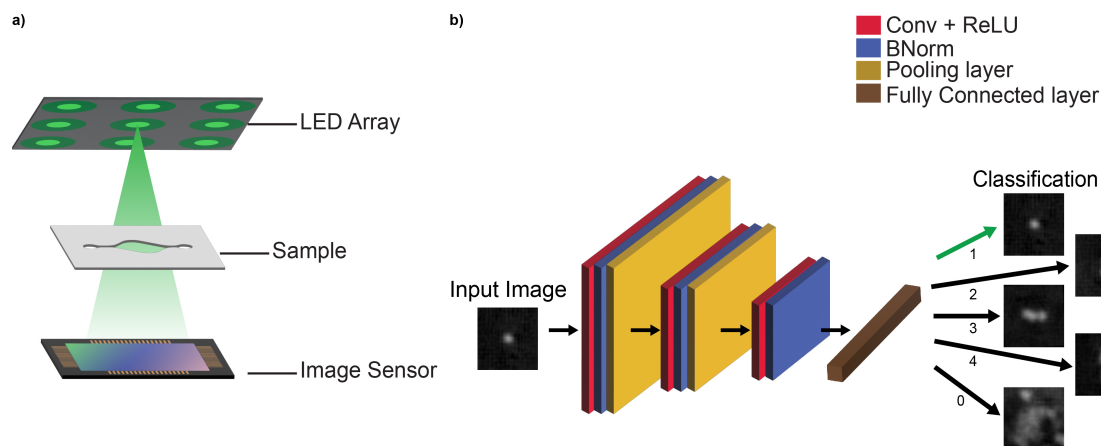


Figure 4.1: (a) Schematic of a single LED illumination condition of the lensfree holographic microscope used in this study. (b) Architecture of the baseline CNN model used for training. This shallow CNN is comprised of three convolutional (conv) layers, serving as the foundational elements of the network. Subsequent to each convolutional layer is an activation layer, such as a rectified linear unit (ReLU), which introduces non-linearity to the learning process, and a batch normalization (BNorm) layer to stabilize the process. These layers collectively form the initial stages of the network. The first two layers among these initial stages also incorporate pooling layers to downsample the input image. The architecture is concluded with a fully connected layer that utilizes the outputs from these preceding layers that predicts the class of the input image.

proteins on lymphocyte membranes [58]. These applications used a variety of computational methods to classify, count, and size small targets, including iterative thresholding-based image segmentation [201], support vector machines [11], sparsity promoting reconstructions [57], and convolutional neural networks.

Convolutional neural networks (CNNs) [213, 214], a form of deep learning and artificial intelligence, offer superior classification than the other methods above, especially for biomedical imaging and microscopy [215, 216]. Although training is often more time consuming, once trained, CNNs provide computationally speedy classification and are more robust to real, “messy” data [75, 76, 82, 98, 217]. Deep learning neural networks can be used to solve complex classification tasks that have seen successful implementation across a wide range of applications, demonstrating their potential to solve difficult problems that other processing algorithms cannot [218]. The identification of individual cells, cancerous tissue, and infec-

tious pathogens is central to biomedical microscopy, and CNNs can rapidly classify these objects [219].

CNNs have previously been used to process LFHM images for image classification, regression model fitting, pixel super-resolution, and image reconstruction tasks [12, 74, 75, 78, 79, 81, 96, 104, 128, 130, 131, 146, 220, 221]. However, for small-object classification tasks, such as those introduced above, it has been unclear how to best design the architecture and tune the hyper-parameters of a CNN. In most of the previous applications of CNNs to LFHM, CNNs were just presented as satisfactory solutions to a problem, without discussion of how they were selected and tuned, or whether they are optimal.

A researcher wishing to utilize a CNN can either adapt an existing network design using what is known as *transfer learning*, or they can design their own network. Existing CNNs for broad image classification tasks, such as VGG16, VGG19, or AlexNet, have deep and complex architectures [216, 222, 223]. To adapt these networks to a particular application, the user replaces the final layer of the network and performs training on this layer only, as the networks are already trained to pick out specific image features, and it is only the final layer that needs to be retrained to associate these features with new image classes. Drawbacks of transfer learning include the need to resize images to conform to the network's input requirements, and the length of time required for training [224, 225].

An effective alternative to transfer learning is to construct a custom, shallow CNN and fully train it using a dataset of images similar to those for the specific task at hand [226]. However, the number of possible configurations can be quite daunting for even a shallow CNN, which is generally defined as a CNN with fewer than 5 layers. Design decisions span the selection of the overall CNN structure and order of the hidden layers to the types of layers

and hyperparameters that define them. Furthermore, it can be unclear what effect, if any, changes to these variables have on the overall performance of the CNN—such is the nature of a self-optimizing algorithm. In this article, we discuss nearly every commonly understood layer and hyperparameter that can be readily incorporated in a shallow, linear CNN. We then discuss the training accuracy and time required for each CNN variation to process a dataset of LFHM images. Our results provide a comprehensive guide to the construction and customization of a shallow, linear CNN for future biomedically relevant image classification tasks.

4.2 Materials and methods

4.2.1 *Portable lens free holographic imaging*

Our LFHM system is based on Gabor’s in-line imaging method [54]. Fifteen green LEDs illuminate the sample in series. Spatial and temporal coherence is provided through the use of pinhole and bandpass filters positioned between the LED source and the sample, as described previously (Fig. 4.1a) [11, 75]. Fifteen sub-pixel shifted low-resolution holograms were collected by a monochrome CMOS image sensor (pixel size 1.1 μm) over 2.025 seconds and a pixel super-resolution algorithm was employed to obtain a high-resolution hologram [57]. This high-resolution hologram then underwent angular spectrum method back-propagation to computationally reconstruct an image of the sample. Sub-micron resolution was achieved over an ultra large field-of-view (around 17.5 mm^2).

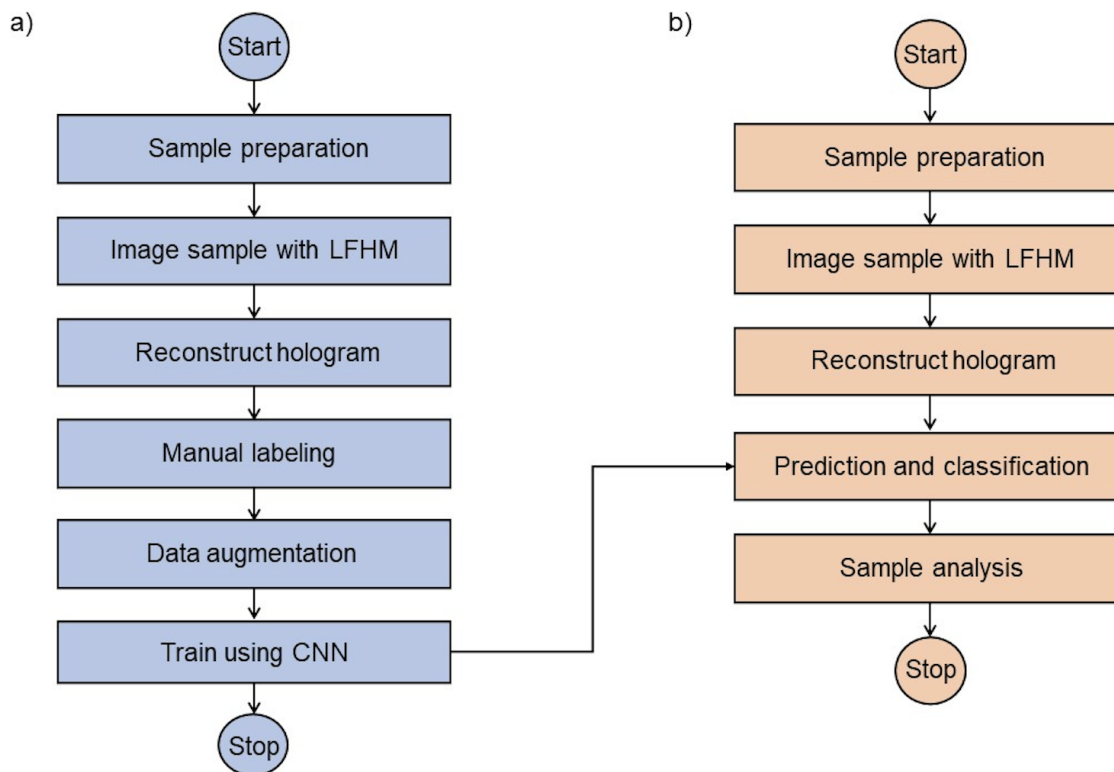


Figure 4.2: (a) Dataset image preparation and CNN training workflow. (b) Implementation of the trained CNN in an experimental context.

4.2.2 Training dataset generation

The samples that were imaged to form the CNN training dataset were prepared according to the protocol previously described [75]. Briefly, SARS-CoV-2 pseudovirus was incubated and suspended in Dulbecco’s modified Eagle medium (DMEM). Half-log dilutions of pseudovirus were prepared such that viral concentrations in samples ranged from $3 \cdot 10^6$ copies \cdot mL $^{-1}$ to $3 \cdot 10^2$ copies \cdot mL $^{-1}$. These dilutions were mixed 1:1 with a suspension of colloidal 2- μ m diameter polystyrene microspheres, which had been functionalized with ACE2 protein. After incubation for 2 hours at 25°C, particle agglutination occurred as a result of multiple pseudovirus-ACE2 interactions. Samples were then loaded into a thin imaging chip and imaged with the LFHM system so that agglutination could be quantified.

Table 4.1: Baseline CNN architecture. Conv: convolutional. BNorm: batch normalization. ReLU: rectified linear unit. MaxPool: maximum pooling. FConn: fully connected.

Layer	Type	Filter dimension	Stride	Padding	Data dimension
0	Input	-	-	-	$60 \times 60 \times 1$
1	Conv	$3 \times 3 \times 8$	1	same	$60 \times 60 \times 8$
2	BNorm	-	-	-	$60 \times 60 \times 8$
3	ReLU	-	-	-	$60 \times 60 \times 8$
4	MaxPool	2×2	2	0	$30 \times 30 \times 8$
5	Conv	$3 \times 3 \times 16$	1	same	$30 \times 30 \times 16$
6	BNorm	-	-	-	$30 \times 30 \times 16$
7	ReLU	-	-	-	$30 \times 30 \times 16$
8	MaxPool	2×2	2	0	$15 \times 15 \times 16$
9	Conv	$3 \times 3 \times 32$	1	same	$15 \times 15 \times 32$
10	BNorm	-	-	-	$15 \times 15 \times 32$
11	ReLU	-	-	-	$15 \times 15 \times 32$
12	FConn	5	-	-	$1 \times 1 \times 5$
13	Softmax	-	-	-	$1 \times 1 \times 5$
14	Classification	-	-	-	$1 \times 1 \times 5$

The images used to train and validate the CNNs tested here were reconstructions from high-resolution holograms of pseudovirus-microparticle agglutination. Features of interest such as pseudovirus aggregates, cell debris from viral incubation, and agglutinated microspheres were identified through simple pixel intensity thresholding and object grouping implemented in MATLAB, and small $60 \text{ pixel} \times 60 \text{ pixel}$ regions of interest (ROIs) surrounding each feature were cropped from the whole FOV. The complexity of these images, the number of conformational positions the microparticles could be in, and the ambiguity (from a traditional image segmentation approach) of feature characteristics made this image set ideal for a CNN application. In total, 1,410 images of features were extracted and manually assigned to 1 of 5 possible categories: features consisting of exactly 1, 2, 3, or 4 microspheres, and a fifth category for debris or unknown features. This dataset was further augmented by rotating and mirroring each image to yield a total of 11,280 images evenly distributed across the 5 training classes or groups. This overall workflow and the application of the CNN

post-training is detailed in Fig. 4.2.

4.2.3 Convolutional Neural Network Architectures

The baseline neural network architecture used in this study is a shallow, three-layer CNN with standard rectified linear unit (ReLU) activation and batch normalization layers. This network is illustrated in Fig. 4.1b, and the dimensionality, full CNN architecture, and associated hyperparameter values for this baseline network are shown in Table 4.1.

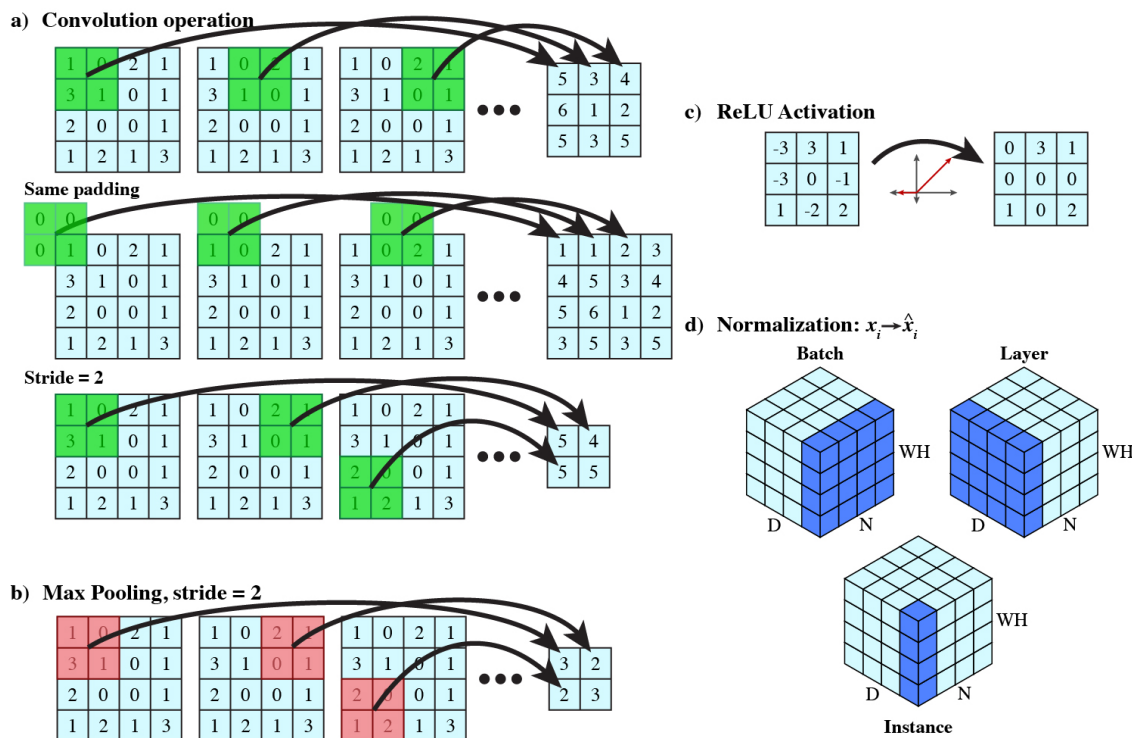


Figure 4.3: Examples of several key layers. (a) Convolutional layers perform convolution operations as they slide across the image or data. The hyperparameters of padding and stride influence this sliding and determine the output dimension. Here, the convolution kernel is a 2 by 2 kernel with all values set to 1. (b) Max pooling layers slide across the data and are influenced by stride just like convolutional layers, but return only the highest value in each filter. (c) A ReLU activation sets all negative values in the data to 0. Other activation layers alter the data differently, but each act as a function with a single value as the input variable, returning the output value. (d) Values included for batch, layer, and instance normalization. W and H represent the 2 data dimensions corresponding to rows and columns in the raw images, or the output of each convolutional layer operating on a single image (first two data dimensions in Table 4.1). N is the number of images in a mini-batch, and D is the depth of the data at that point in the network, or the third data dimension in Table 4.1.

Each layer type from Table 4.1 serves a role in the task of image classification, and some have adjustable hyperparameters. Some key CNN layers, hyperparameters, and the operations they perform are depicted in Fig. 4.3. The convolutional layer (layers 1, 5, and 9 of the baseline network) serves as a foundational building block in CNNs. Its convolution operation involves sliding a filter (also known as a kernel) over the input data, multiplying the kernel by the overlapping input data, and summing the result (Fig. 4.3a)[214]. Depending on the filter, some regions of input data will produce high values (where data is similar to the filter), and some will produce low values (where data is dissimilar to the filter), enabling the particular kernel to detect various patterns and features, which helps the network identify distinctive characteristics in the data. The filter is initialized with random values at the start of training, and each iteration through a mini-batch, the CNN updates the filters (or weights) for each filter in each convolutional layer to improve the accuracy of the network according to Equations 4.3 and 4.4. The efficacy of this layer in facilitating optimal feature extraction relies on layer hyperparameters such as the filter size (e.g., 2×2 pixels), the number of filters (which affects the data depth, shown as the last dimension in the last column of Table 4.1), the filter stride, and the padding (see Fig. 4.3a). Filter stride indicates the number of pixels the filter is shifted over between each multiplication operation during convolution, while padding involves the addition of extra empty pixels to the input image, often used to preserve the spatial dimensions of the input. Without padding, the dimensions will shrink, limiting the number of usable convolutional layers and impacting overall performance. Additionally, without padding, pixels at the corners and edges undergo fewer operations during convolution or pooling compared to central pixels.

Normalization layers, such as batch normalization, are integral to CNNs due to their

crucial role in stabilizing and accelerating the training process, noted in layers 2, 6, and 10 of the baseline network (Table 4.1). One of the primary challenges they address is the internal covariate shift, a phenomenon where the distribution of the network’s activations or data values in a given layer changes as data progresses through the layers during training [227]. This shift hinders the model’s ability to learn effectively. Batch normalization counteracts this internal covariate shift by normalizing the activations within each mini-batch to a normal distribution, with the addition of a learnable scale and shift, during training, thereby ensuring a more consistent and stable learning environment. Normalization employs the following equation to achieve this:

$$\hat{x}_i = \eta \frac{x_i - \mu_B}{\sqrt{\sigma_B^2 + \epsilon}} + \beta, \quad (4.1)$$

where the initial value, x_i , is normalized by the mini-batch data’s mean μ_B and variance σ_B^2 , with the addition of a constant, ϵ , that improves numerical stability when variance is very small, to produce the new data value, \hat{x}_i . To account for the possibility that optimum input data populations do not have a mean of zero and unit variance, two additional learnable parameters are added, η and β , which scale and offset the data respectively and are updated during training.

Normalization layers not only facilitate faster convergence, but also enhance the network’s ability to generalize from the data. In the context of neural networks, convergence refers to the point at which the model’s parameters stabilize, and the loss function reaches a minimum. It signifies that the network has learned the underlying patterns in the data and can make predictions with a high degree of accuracy. Generalization, in this context, means that the trained model can make accurate predictions on unseen data that was not

part of the training set. This is crucial for the practical application of CNNs in real-world scenarios, where the model needs to perform well on diverse and previously unseen inputs.

In this article, various normalization layers are investigated, including batch, where normalization is performed for each filter using all data in the mini-batch; instance, where normalization is performed for each filter independently using only one set of data values that corresponds to a single input image; and layer normalization, where normalization is performed for only one set of data values corresponding to a single input image, but over all filters together. Fig. 4.3 depicts these differences. Layer normalization is typically utilized after all the learnable layers, specifically following layer 12 in Table 4.1. In this study, we explore the effects of employing various normalization layers, including the combination of layer normalization with batch and instance normalization.

Activation layers, like ReLU in layers 3, 7, and 11 (Table 4.1), bring a crucial aspect to the network by introducing nonlinearity, which allows it to handle more intricate relationships within the data [228]. In a linear system, the model can only grasp straightforward connections, limiting its ability to understand complex patterns. Some activation functions, such as ReLU, replace negative values with zero. This prevents the neurons from saturating, where the gradient, ∇L from Equation 4.4, gets small as training progresses and training slows. While ReLU stands as the predominant activation layer choice, noteworthy improvements in CNN validation accuracy have been observed in certain cases by introducing a nonzero value for the negative inputs [229–231]. Here we investigate several ReLU variants, such as leaky ReLU, which has a small, near-zero, positive slope for negative inputs; clipped ReLU, where values greater than a ceiling are clipped to the ceiling; and Elu, which is the same as ReLU for positive inputs but applies an exponential function to negative inputs.

Clipped ReLU was tested with lower, mid-level, and higher ceiling values. In addition, we compare the network performance among other types of activation layers, including tanh, softplus, and swish. The swish operation is given by the equation:

$$f(x) = \frac{x}{1 + e^{-x}}, \quad (4.2)$$

Pooling layers, such as max pooling in layers 4 and 8 in Table 4.1, downsample the data. This is apparent from Table 4.1, where the total data dimensionality, equal to the product of the first two dimensions in the last column, only drops during pooling by a factor corresponding to the pooling layer filter dimension. By down-sampling the input image, pooling layers can prune insignificant data, while retaining significant values, no matter what location they correspond to in the original image. This feature is called transverse invariance. There are two types of pooling layers tested here: maximum (max) and average pooling, which capture either the max or average value over the region of overlap between the data and the filter. As with convolutional layers, both types of pooling layers can be tuned by stride and padding (see Fig. 4.3).

Although dropout layers are not present in our baseline architecture, they can significantly mitigate overfitting, a common challenge in deep learning models [232]. Dropout layers randomly deactivate a subset of neurons in a fully connected layer, which appears as layer 12 in Table 4.1, during each training iteration, preventing the network from relying too heavily on specific features or patterns and, thereby, improving its ability to generalize. During some of our tests, we introduced a dropout layer immediately following layer 11 in Table 4.1. The dropout layer hyperparameter ranges from 0 to 1, where 1 deactivates 100%

of the neurons, while 0, as the default, keeps all the neurons activated. The effect of this layer and its hyperparameter value on the CNN was investigated.

4.2.4 CNN training and validation

The network was trained using MATLAB on a 2-core Intel® Xeon® Gold 5218 2.29 GHz processor. The augmented dataset comprised 11,280 images, of which 75% ($N = 8,460$) were allocated for training, and the remaining 25% were designated for validation. Each network underwent training and validation three times. Each time, data was randomly re-assigned into training and validation groups and filter weights and biases were randomly re-generated, ensuring that the training behavior observed was not due to the specific assignment of data to either training or validation.

Learning is achieved through updating weights and biases of the CNN to minimize cross-entropy loss:

$$L = -\frac{1}{N} \sum_{n=1}^N \sum_{i=1}^K c_i t_{ni} \ln(y_{ni}), \quad (4.3)$$

where L is the loss, $K = 5$ denotes the number of distinct classifications, c_i stands for the weight assigned to class i , t_{ni} is an indicator (either 0 or 1) that a given input, n , is associated with class i , and y_{ni} represents the network's calculated probability of associating the n^{th} input with class i . These components enable the network to assign a loss value for its performance, which it then tries to minimize by adjusting the learnable parameters in the network (commonly referred to as weights and biases), such as the convolutional filters in a CNN, to increase the probability, y_{ni} of an input being associated with the correct class. To adjust the learnable parameters in the network contained in the vector θ , a stochastic

gradient descent with momentum solver is used, where the parameters in the $(l+1)^{\text{th}}$ iteration are set as:

$$\theta_{l+1} = \theta_l - \alpha \nabla L(\theta_l) + \gamma(\theta_l - \theta_{l-1}), \quad (4.4)$$

where α is the training rate and γ is a momentum constant that influences the impact that the change in parameter values from the previous iteration has on training. Here, γ is always set to 0.9. A fixed learning rate of $\alpha = 0.0001$ (Eqn. 4.4) was employed throughout the training of all networks.

This solver is applied after each iteration, which corresponds to a pass through a “mini-batch” of input images, rather than the whole training dataset. The duration of each iteration spanned from 1.2 seconds to 27 seconds, contingent upon factors such as the network’s complexity, the order in which training data was presented, and the convergence rate. By updating the parameter set after each mini-batch, the CNN can be more rapidly trained. In our case, each mini-batch is 64 images that are randomly selected from the unused training dataset images remaining in the current epoch. The random order in which images are incorporated into mini-batches during each epoch adds variability that enhances the model’s adaptability and robustness. Validation is performed after every 100 iterations. Once all training dataset images have been used, a new epoch begins, and the process repeats until there has been no improvement over three consecutive validation cycles. Ceasing training at this point prevents overfitting (overtraining), which is defined as when a network exhibits close to 100% training accuracy but significantly lower validation accuracy, indicating reliance on the training data and poor generalization to unseen data.

Another way in which we mitigate overfitting and enhance generalization is by employing

L2 regularization during training. A penalty term proportional to the squared magnitude of the network’s weights is added to the loss function:

$$L_R(\theta) = L(\theta) + \lambda \left(\frac{1}{2} w^T w \right), \quad (4.5)$$

where λ is the regularization factor, which we range from 0 to 1, and w represents a vector of each of the weights, with w^T being the transpose of that vector. The inclusion of the L2 regularization term discourages the model from assigning excessively large weights to individual parameters, effectively preventing the network from becoming overly reliant on any given feature in the training data, and it improves the network’s ability to generalize to unseen data. Here, we investigate the effect that different levels of L2 regularization has on performance.

4.3 Results and discussion

The modifications to the baseline network were performed in the order below. At each stage, a range of different network parameters was considered, and then the optimal parameter choice was retained for the next stage of network modification, rather than returning to the baseline network. Network optimality was quantified by the highest end validation accuracy. This approach ensured that the best-performing layer or parameter used to effectively define a new “baseline” before introducing subsequent modifications.

Each test involving a modified layer or parameter was conducted three times to account for variability from randomized weight and bias starting conditions and dataset distribution, with the average end validation accuracy represented by the blue dots in the figures below.

Error bars, indicative of the standard error of the mean, were calculated based on the results of these three independent training trials.

4.3.1 Dropout layer

Initially, the dropout layer was introduced following layer 11 in Table 4.1, aimed at mitigating overfitting and enhancing the CNN's performance. In Fig. 4.4a, it is apparent that deactivating 80% of neurons yielded the highest end validation accuracy; with all neurons activated and no dropout layer, the network exhibited greater variability and instability. The number of training iterations required to achieve convergence correlates with the exposure of the network to the data. Without dropout, all neurons are always active and undergo optimization, thus fewer iterations occur before training converges to its final minimum loss. With dropout, the training in general demands more iterations for the network to achieve a higher validation accuracy. In summary, while training with an 80% dropout incurs more iterations, the superior performance of this network outweighs the slightly extended training time.

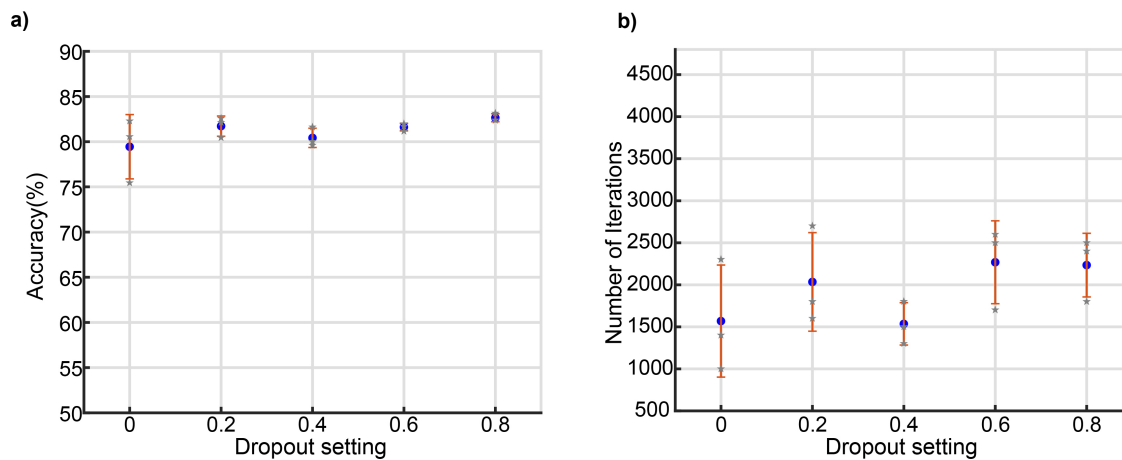


Figure 4.4: (a) The end validation accuracy of the CNN is plotted as a function of the fraction of neurons deactivated in the dropout layer. (b) The required number of iterations before the network ceased to improve after three consecutive validation cycles.

4.3.2 Convolutional layers

For the convolutional layers, two critical parameters were considered: the number of filters and the size of the filters, as outlined in Table 4.1 for the baseline architecture. In the baseline network, the first, second, and third convolution layers had 8, 16, and 32 filters, respectively, with dimensions of 3×3 for each filter. From Fig. 4.5a, the network with the highest end validation accuracy had 16, 16, and 32 filters in the three respective layers and achieved an average end validation accuracy of 82.51%. Although the networks with (20, 20, 36) and (8, 8, 24) filters each showed comparable results to the network with (16, 16, 32) filters, the former, having more learnable layers, required an extended training time (Fig. 4.5b), while the latter exhibited greater training instability evidenced through higher variability. For these reasons, we selected (16, 16, 32) as the optimal numbers of filters in each layer.

When testing filter dimensions, the number of filters in each convolutional layer was kept constant (16, 16, 32). In Fig. 4.5c and d, the lower axes labels indicate the filter dimensions. Note that all filters are square with an equal number of rows and columns. The (15, 15, 10) network with filter dimensions 15×15 for the first two convolutional layers and 10×10 for the last layer attained the highest end validation accuracy at 81.31%. A comparison with networks having filter dimensions (10, 10, 6) and (20, 20, 15) showed that training for the former, while more stable, had significantly lower end validation accuracy, and that the latter, though unstable, required more iterations for a slightly higher average accuracy (Fig. 4.5d).

In summary, the combination of using (16, 16, 32) for the number of filters and (15, 15,

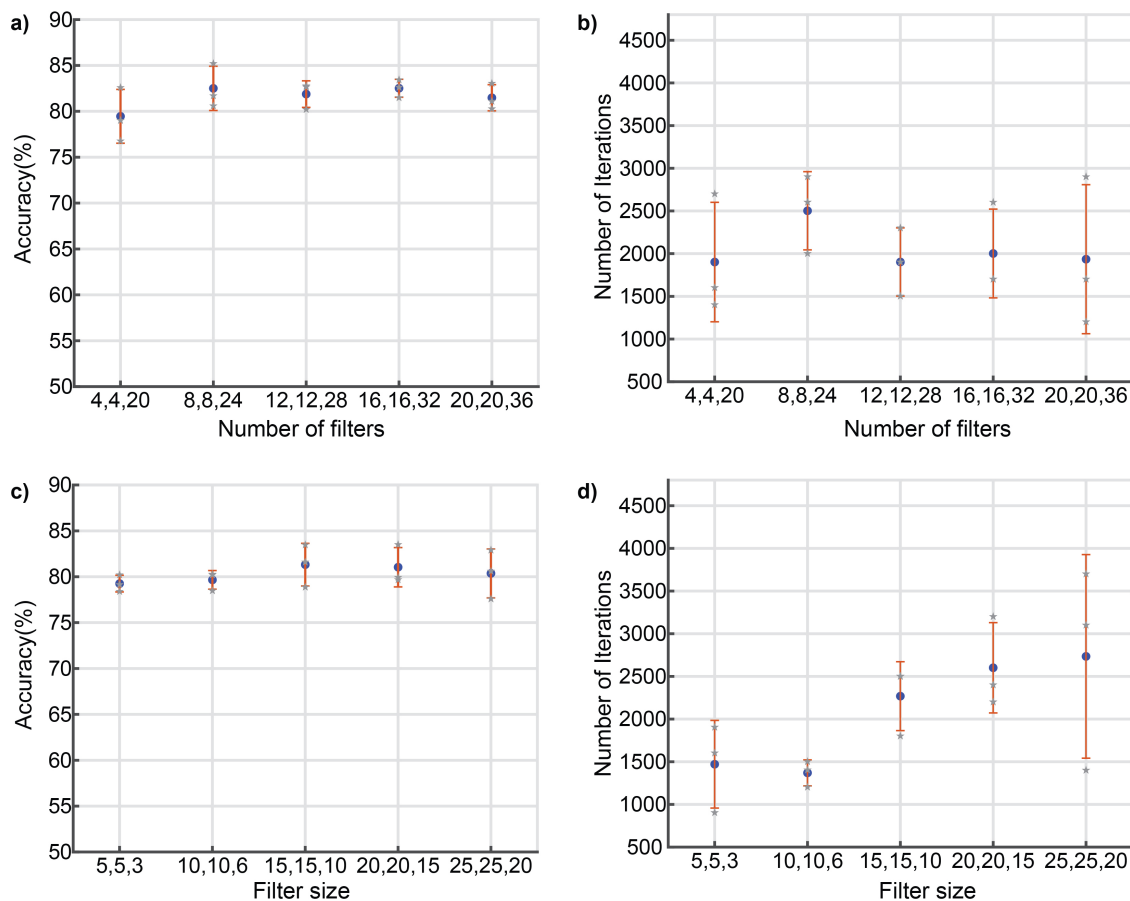


Figure 4.5: (a) The end validation accuracy and (b) number of required iterations of the CNN is plotted as a function of number of filters in each of the three convolutional layers (D_1 , D_2 , D_3). (c) The end validation accuracy and (d) number of required iterations of the CNN is plotted as a function of dimension of filters (m_1 , m_2 , m_3).

10) for filter dimensions in the three convolutional layers yielded the best results. Exploring more filters in each layer and larger filter dimensions did not exhibit significant improvements and prolonged network training.

4.3.3 Normalization layers

In the initial architecture (Table 4.1), normalization was performed in layers 2, 6, and 10. We investigated the effect of using batch normalization versus instance normalization in these layers (see Fig. 4d for an explanation of these types of normalization), as well as

removing the normalization layers entirely. We also investigated adding layer normalization near the end of the network, after layer 11 in Table 4.1) The results are shown in Figure 4.6. The configurations with no normalization and with solely layer normalization proved impractical, exhibiting poor end validation accuracy and high instability. The most effective option emerged as batch + layer normalization, achieving an average end validation accuracy of 83.53%, which is higher than that of batch normalization alone, and this combination is also more stable, but it requires slightly more training time.

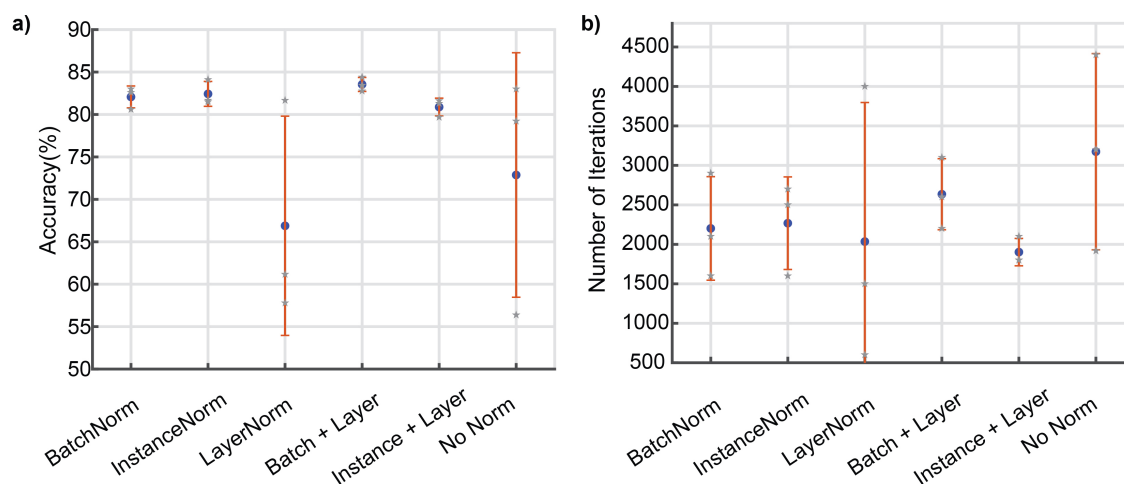


Figure 4.6: (a) The end validation accuracy of the CNN is plotted for different normalization layers. (b) The number of required iterations for training for each normalization layer.

4.3.4 Pooling layers

Pooling occurred in layers 4 and 8 of the baseline network (Table 4.1). We explored two distinct pooling layer types (max and average pooling) and two adjustable parameters (filter size and stride). We tested big (B) filter sizes of 4×4 for the first pooling layer (layer 4 from Table 4.1) and 3×3 for second pooling layer (layer 8 from Table 4.1) versus small (S) filter sizes of 2×2 for layer 4 and 1×1 for layer 8. A big (B) stride value was defined as 4 and 3 respectively for the two layers, whereas a small stride was defined as 1 for both

layers. A particular combination of filter and stride size is denoted, for example, as (S,B), which corresponds to small filter sizes and big strides. The effects of filter and stride size were quantified for both max and average pooling.

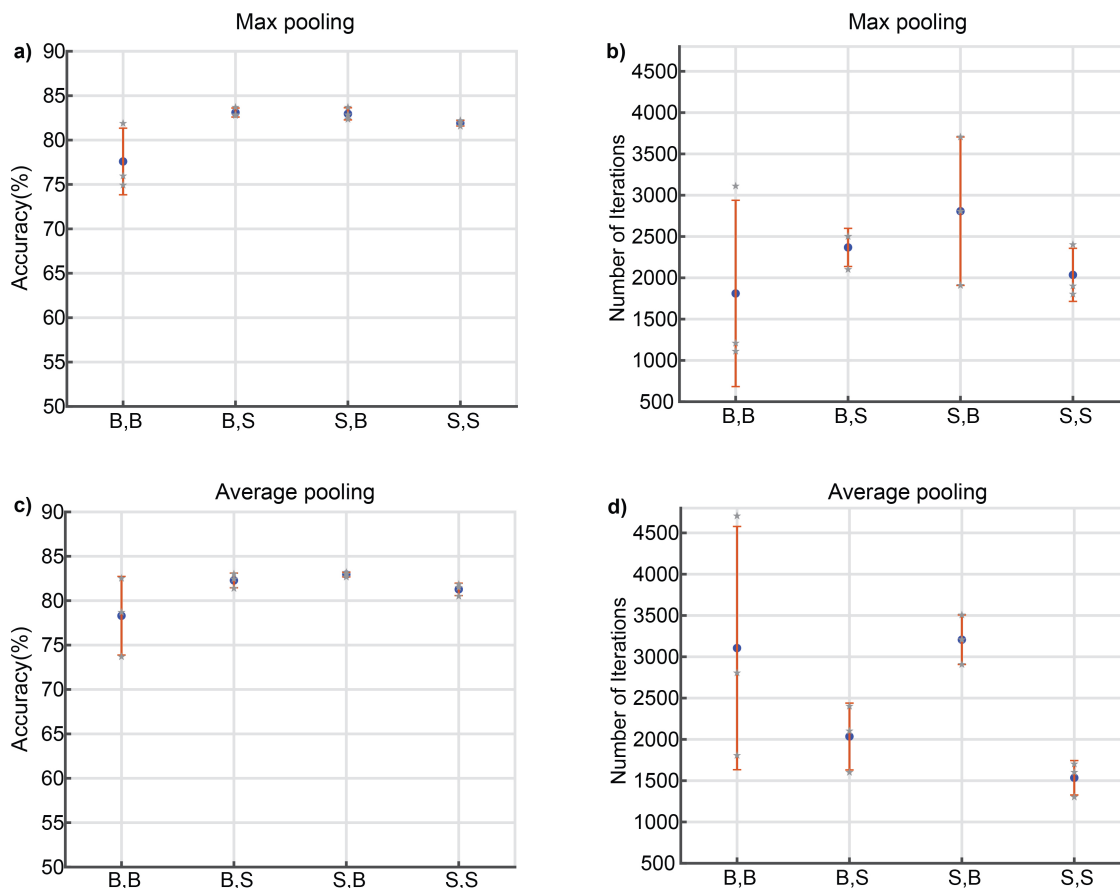


Figure 4.7: (a) The end validation accuracy and (b) number of training iterations of the CNN is plotted as a function of filter size and stride for max pooling. The lower axes labels correspond to (filter size, stride size), where B stands for “big” and S stands for “small.” See the main text for the precise definitions. (c) The end validation accuracy and (d) number of iterations of training is plotted as a function of filter size and stride for average pooling.

Fig. 4.7a and b show the results for Max Pooling. Overall, the big filter and small stride (B,S) achieved the highest end validation accuracy of 83.1%. With this configuration, more information is combined in each new data point, with potentially large regions in a data block set to the same value, but a higher dimensionality is retained due to small stride. With a negligible difference in the number of iterations required for convergence (Fig. 4.7b),

the substantial accuracy improvement makes (B,S) the optimal choice.

For average pooling, results in Fig. 4.7 show that a small filter but big stride (S,B) yields the highest average end validation accuracy at 82.94%. Compared to the other conditions, this configuration exhibits greater stability, albeit requiring more iterations to train. When comparing this result to the max pooling optimal configuration of a big filter and small stride, we find that max pooling not only achieves higher validation accuracy but also requires fewer iterations to achieve convergence. In summary, utilizing max pooling with a big filter and small stride emerges as the superior option.

4.3.5 Padding for Convolutional and Pooling layers

In the previous section, the application of a max pooling layer with a large filter and a small stride proved to be superior. Additionally, a combination of employing (16, 16, 32) filters in each convolutional layer with (15, 15, 10) filter dimensions in each layer yielded optimal results. In the following tests, these parameters were all held fixed.

Both convolutional and pooling layers enable the user to add padding to the filter as it steps across the data. As illustrated in Fig. 4.8a, the use of “same” padding in the convolutional layer, which preserves the data size as it passes through the layer, led to higher validation accuracy, averaging 82.51%. The absence of any padding resulted in a significant drop in accuracy, while “same” padding necessitated more iterations before convergence. A similar analysis was conducted for pooling layers, shown in Fig. 4.8c. No padding yielded a higher average end validation accuracy of 82.1%. Typically, padding in pooling prevents neglecting corner and edge pixels during down-sampling. However, given that the dataset lacks crucial features in these regions, the absence of padding for pooling

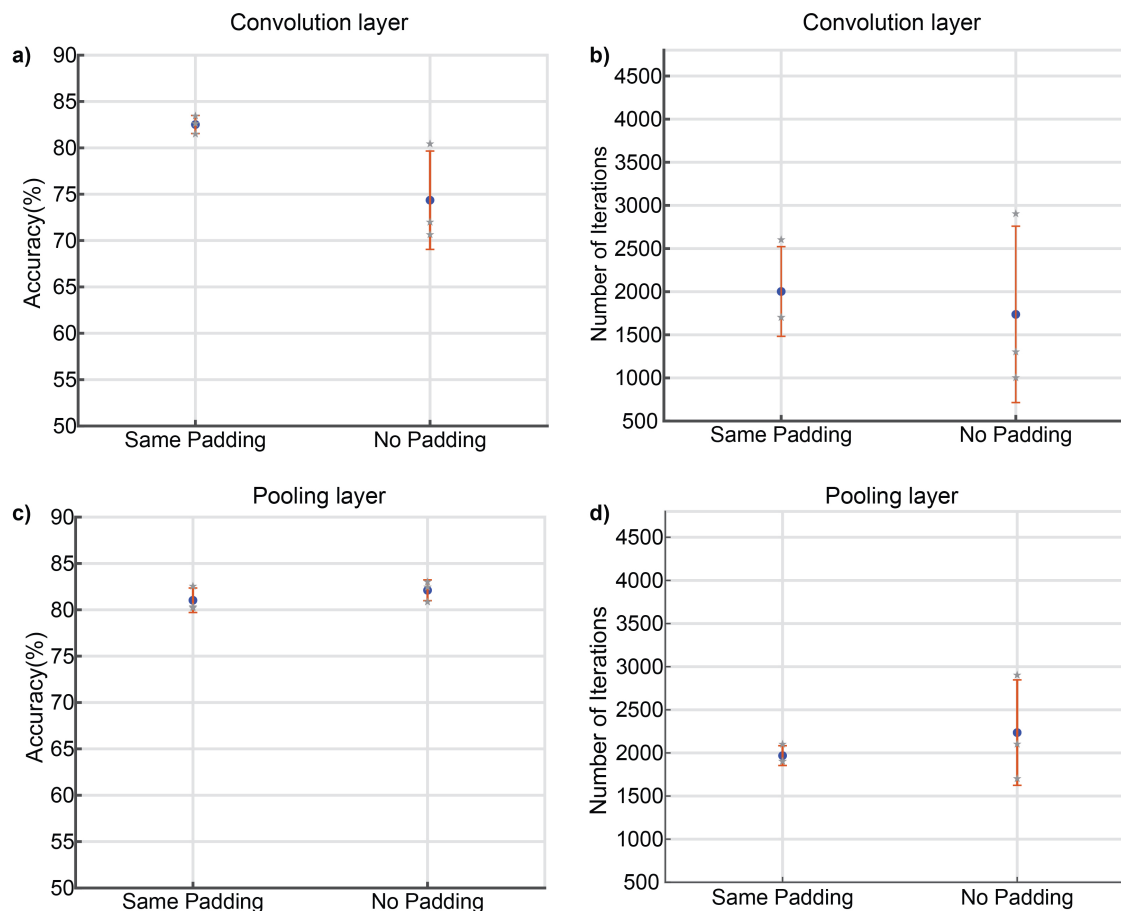


Figure 4.8: (a) The end validation accuracy and (b) number of iterations trained of the CNN is plotted for convolutional layer padding hyperparameters. (c) The end validation accuracy and (d) number of iterations trained of the CNN is plotted for Pooling layer padding hyperparameters.

emerged as the optimal choice. In summary, for this particular dataset, the use of padding for the convolutional layers proved beneficial, while no padding in pooling layers yielded superior results.

4.3.6 *L2 regularization*

Accuracy varies with the L2 parameter, with lower parameter values tending to yield better results (Fig. 4.9). Optimal performance was achieved without utilizing L2 regularization with an average end validation accuracy of 82.91%. It is typically not recommended to construct a network without regularization due to the risk of data overfitting. In our

application, the network incorporates an auto-stop function, terminating training if no improvement is observed after three validation cycles. This could explain why the network achieved a high accuracy for validation data after training with no regularization. Due to the potential negative effect this can have to a CNN's generalization performance on expanded or dissimilar data, more testing would be needed to ensure network performance is unaffected in the end application.

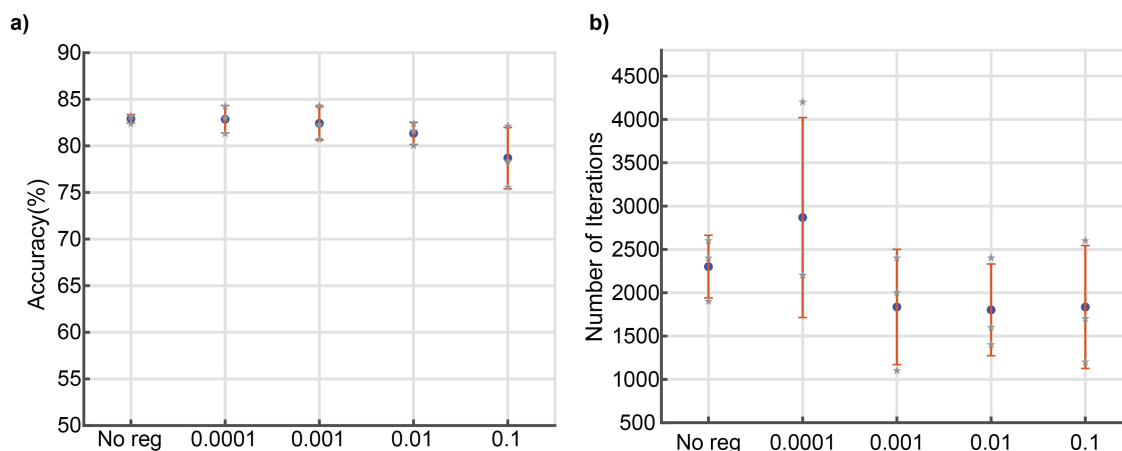


Figure 4.9: (a) The end validation accuracy of the CNN and (b) The number of iterations trained is plotted as a function of different L2 parameters.

Fig. 4.9b provides additional insights, suggesting that the network with a 0.1 L2 regularization coefficient trains in fewer iterations, converging earlier. This implies a potential improvement in mitigating overfitting, although the presence of the auto-stop function makes it challenging to unequivocally attribute these improvements to L2 regularization alone.

4.3.7 Activation layer

The activation layer introduces non-linearity to a neural network, with ReLU commonly being the preferred choice. In the baseline network, ReLU was employed in layers 3, 7, and 11, as outlined in Table 4.1. To explore alternatives that might outperform ReLU, these

layers were replaced with different activation layers.

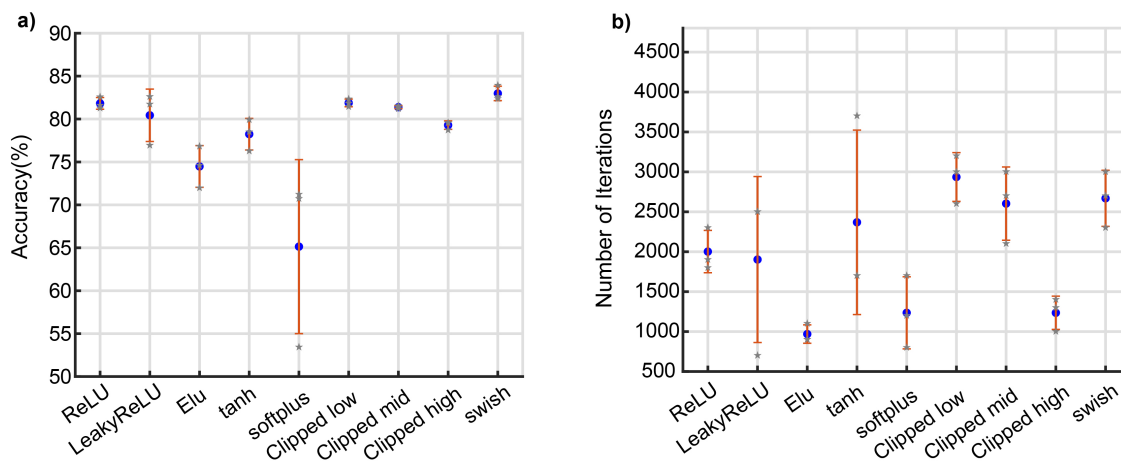


Figure 4.10: (a) The end validation accuracy of the CNN and (b) the number of iterations trained is plotted for a variety of activation layers.

As depicted in Fig. 4.10a, the swish layer exhibited the best overall performance, achieving an average end validation accuracy of 82.98% and lowest variability between training sessions. Clipped-low demonstrated comparable accuracy to ReLU, while Clipped-mid and -high showed worse end validation accuracy. ReLU proved the second best after swish in our testing, however it is worth noting that in some cases, it might not be the most suitable choice. For example, tanh, characterized by an S-shaped function, is commonly utilized in applications with only two classes [233]. ReLU’s characteristic of discarding negative values and converting them to zero can lead to issues such as vanishing gradient problems [234]. The choice of activation layer depends on the specific characteristics and requirements of the given task.

4.3.8 Final Optimized Network

After thorough exploration and experimentation with various layers and hyperparameters we have identified the layers and hyperparameters that worked best. The layers and

their corresponding hyperparameters are presented in table 4.2.

Table 4.2: Updated CNN after optimization of layers and hyperparameters. Conv: convolutional. BNorm: batch normalization. LayerNorm: layer normalization. MaxPool: maximum pooling. FConn: fully connected.

Layer	Type	Filter dimension	Stride	Padding	Data dimension
0	Input	-	-	-	$60 \times 60 \times 1$
1	Conv	$15 \times 15 \times 16$	1	same	$60 \times 60 \times 16$
2	BNorm	-	-	-	$60 \times 60 \times 8$
3	Swish	-	-	-	$60 \times 60 \times 8$
4	MaxPool	4×4	1	0	$57 \times 57 \times 8$
5	Conv	$15 \times 15 \times 16$	1	same	$57 \times 57 \times 16$
6	BNorm	-	-	-	$57 \times 57 \times 16$
7	Swish	-	-	-	$57 \times 57 \times 16$
8	MaxPool	3×3	1	0	$55 \times 55 \times 16$
9	Conv	$10 \times 10 \times 32$	1	same	$55 \times 55 \times 32$
10	BNorm	-	-	-	$55 \times 55 \times 32$
11	Swish	-	-	-	$55 \times 55 \times 32$
12	LayerNorm	-	-	-	$55 \times 55 \times 32$
13	FConn	5	-	-	$1 \times 1 \times 5$
14	Softmax	-	-	-	$1 \times 1 \times 5$
15	Classification	-	-	-	$1 \times 1 \times 5$

4.4 Conclusions

In this Chapter, the effect that a wide range of layer types, including dropout layers, normalization layers, pooling layers, and activation layers, and the effect that a wide range of their hyperparameters, including filter size, stride, padding, and regularization, on the training outcomes of a shallow CNN has been demonstrated. The highest average end validation accuracy achieved by using each of the optimal settings was an average validation accuracy of 81.75%. This seems to indicate that the stochastic nature of the solving process, data segmentation, and initial network conditions plays a large role in these shallow networks. The best solution continues to be expansion of the utilized dataset to improve validation

performance. While it is not possible to say what will be the best combination of settings and layers for any given image classification application, it is still useful to look at how the changes to each layer and hyperparameter affected accuracy and training variability. For instance, the greatest change in end validation accuracy from worst to best performing CNN was achieved by changing the activation layer, so starting here when developing a custom CNN for a new task would be a good place to begin. Additionally, if it is observed that a network is training inconsistently, sometimes getting low end validation accuracy and sometimes high as a result of random training/validation data splits, adjustment of normalization layer or L2 regularization tended to have the greatest effect in stabilizing this end validation accuracy. While this is by no means a fully comprehensive analysis of these layers and hyperparameters, since it is not feasible to test every single combination, it nevertheless serves as a thorough analysis of these layers and the effects they have on CNN training. The data presented here should serve as an excellent reference for researchers developing and fine-tuning CNNs for use in image classification applications.

CHAPTER 5

A Novel Polarization- and LSPR-Based Lens-Free Microscope and Biosensor

In Chapter 3, a novel point-of-care (POC) biosensor for SARS-CoV-2 was developed. It combined sensitivity close to that of the gold standard RT-qPCR with some of the portability of an LFA, resulting in a compelling biosensing platform and assay. To improve upon this sensor's LFHM platform, a novel, polarization-based LFHM was developed for detection of gold nanorod agglutination.

5.1 Introduction

As discussed in Chapter 1, ELISA and LFAs provide compelling reasons for use as a biosensing assay for a variety of proteins, with ELISA attaining a high sensitivity at the cost of portability, and LFAs achieving portability at the cost of high sensitivity. Plasmonic ELISA, also discussed in Chapter 1, is a method for improving the sensitivity and POC readout of ELISA [28, 29]. This technique relies on the plasmonic properties of gold nanoparticles to create a hue change rather than saturation change for enhanced eye visualization without expensive and bulky spectrophotometer. This work shows the usefulness of plasmonic gold nanoparticles for greatly enhancing the sensitivity traditional assays, but its need for specialized equipment for quantitative readout of protein concentration hampers its widespread

use.

Biosensors that rely on surface plasmon resonance (SPR) are also quite compelling. As discussed in Chapter 1, these sensors have a variety of forms and mechanisms, but in general rely on detecting subtle changes in the wavelength of evanescent fields launched along the surface of a probe material, such as gold, termed SPR. Single-molecule detection using this technique has been achieved using a single immobilized gold nanorod (AuNR) as a particle to enhance SPR resonance shifts that occur as proteins bind to the AuNR [38]. This represents one of the highest sensitivities of any biosensing technology. Other SPR sensors use a thin layer of gold on a prism or a gold nanohole array to achieve biosensing of proteins [34–36]. These sensors have very high sensitivities, but can suffer from a lack of portability, high equipment and training cost, and are sensitive to experimental conditions [9].

To address some of these drawbacks of SPR biosensors while improving upon the previous LFHM biosensor that was designed [75], a new LFHM biosensor was designed and tested. The LFHM portion of this new biosensor is based on an 850 nm wavelength laser diode array rather than an LED array. This enables a high degree of temporal coherence without the use of an expensive bandpass filter, and adequate spatial coherence without a pinhole filter, thus simplifying the LFHM design. Additionally, a linear polarizer is inserted into the light path between source and sample. AuNRs sized 93 nm on the long axis and 25 nm in diameter are used as a particle rather than latex microspheres because AuNRs exhibit localized SPR (LSPR) resonance that depends mainly on their aspect ratio. Light at the resonant wavelength of the rods and polarized along the long axis will cause the rod to scatter more than light polarized along the short axis of the rod. Using these properties, this LFHM biosensor is designed to detect AuNRs by visualizing high and low intensity

diffraction-limited objects in the FOV under perpendicular polarizations and quantifying the dichroism observed under these two conditions.

These modifications to the LFHM device, particles used, and quantification methodology enable a faster assay time, as smaller particles undergo diffusion more rapidly than larger ones, resulting in a more rapid readout in POC settings. This also presents a novel LFHM methodology that improves on existing LFHM techniques in terms of the size of particles quantified and potentially the sensitivity of LFHM biosensors.

5.2 Methods

5.2.1 *AuNR scattering*

In all imaging systems, there exist limitations that prevent the system from resolving very small objects and features. If a system is properly optimized, the fundamental resolution limit is the diffraction limit, which is determined by the numerical aperture of the system as well as the working wavelength of light used by the system. In coherent systems like LFHM, objects smaller than the diffraction limit of the system are imaged as diffraction-limited spots, where the object appears as a point source imaged through the system, and thus is dependent on both the coherent transfer function of the system, and the fundamental diffraction limit of $\lambda/2$. For LFHM systems, temporal coherence tends to be the limiting factor, as seen when investigating the temporal coherence transfer function (TCTF):

$$TCTF(\mathbf{u}) = \text{sinc} \left(z_2 \frac{\Delta\lambda}{2} |\mathbf{u}|^2 \right), \quad (5.1)$$

where \mathbf{u} is the coordinates in frequency space, z_2 is the sample-to-sensor distance, and $\Delta\lambda$ is the FWHM of the source [235]. A reduction in z_2 or in $\Delta\lambda$ widens the TCTF, enabling the collection of higher frequency components before the sinc function drops to zero. This leads to the first cut-off frequency of:

$$|\mathbf{u}| = \sqrt{\frac{2}{z_2\Delta\lambda}}, \quad (5.2)$$

and a half-pitch resolution of the reconstructed image of:

$$q = \frac{1}{2|\mathbf{u}|} = \sqrt{\frac{z_2\Delta\lambda}{8}}. \quad (5.3)$$

To ensure the fundamental diffraction limit ($q < \lambda/2$) can be achieved, it is important that z_2 be smaller than $2\lambda^2/\Delta\lambda$. For the LFHM system described here, this condition is satisfied by the system constraints of $z_2 = 450 \mu\text{m}$, $\Delta\lambda = 1 \text{ nm}$, and $\lambda = 850 \text{ nm}$. This results in a value of $q = 0.237 \mu\text{m}$. Even if the FWHM of the diode was 3.2 nm , this condition would still be satisfied. Based on Eqn. 2.1, the theoretical resolution of this system is $0.5242 \mu\text{m}$ based on a calculated NA of 0.8108.

The AuNRs used in this study (Nanopartz C12 25 nm diameter, SPR = 850 nm, Neutra-vidin, 50 OD, Lot # 2442) are much smaller than the fundamental diffraction limit ($\sim \lambda/9$ on the long, 93 nm axis) and thus are expected to be diffraction-limited in this system, even though the system constraints satisfy the above condition for temporal coherence. The difficulty with using AuNRs as an agglutination particle, therefore, is any LFHM system's inability to distinguish single particles from particles in small clusters of 2 or 3. To address

this problem, the LSPR scattering properties of AuNRs will be used.

The AuNR scattered electric field is dependent on their polarizability, α , which is heavily influenced by the aspect ratio of the rods themselves:

$$\overleftrightarrow{\alpha} = \begin{pmatrix} \alpha_{\parallel} & 0 & 0 \\ 0 & \alpha_{\perp} & 0 \\ 0 & 0 & \alpha_{\perp} \end{pmatrix}, \quad (5.4)$$

$$\alpha_{\parallel,\perp} = V\epsilon_0 \frac{\epsilon - \epsilon_b}{L_{\parallel,\perp}\epsilon + (1 - L_{\parallel,\perp})\epsilon_b}, \quad (5.5)$$

where the AuNR is modelled as a prolate spheroid with α_{\parallel} oriented parallel to the long axis of the rod and:

$$V = \frac{4}{3}\pi \left(\frac{d}{2}\right)^2 \left(\frac{l}{2}\right), \quad (5.6)$$

$$L_{\parallel} = \frac{1 - e^2}{e^2} \left(-1 + \frac{1}{2e} \ln \left(\frac{1+e}{1-e}\right)\right), \quad (5.7)$$

$$L_{\perp} = \frac{1 - L_{\parallel}}{2} \quad (5.8)$$

$$e = \text{eccentricity} = \sqrt{1 - \left(\frac{d}{l}\right)^2} \quad (5.9)$$

ϵ is the electric permittivity of the rod material, in this case gold, and ϵ_b is the permittivity

of the background media [33]. The AuNRs used in this study are on-resonance with the 850 nm wavelength diodes used in the LFHM, which maximizes the scattering of the rods. Figure 5.1 shows the absorption spectrum and a transmission electron micrograph (TEM) image of these AuNRs pulled from the certificate of analysis. Based on Equation 5.5, and using the appropriate wavelength, material properties of gold, and aspect ratio of these rods, the polarizability of the long axis (α_{\parallel}) is over 16 times higher than that of the short axis (α_{\perp}). A simulation of scattering intensity from a single cylindrical-shaped rod with spherical end-caps in a linearly-polarized plane-wave source field in Figure 5.2 shows this dichroic scattering response, indicating that the scattered intensity when light is polarized aligned with the short axis is only around 0.4% that of the long axis.

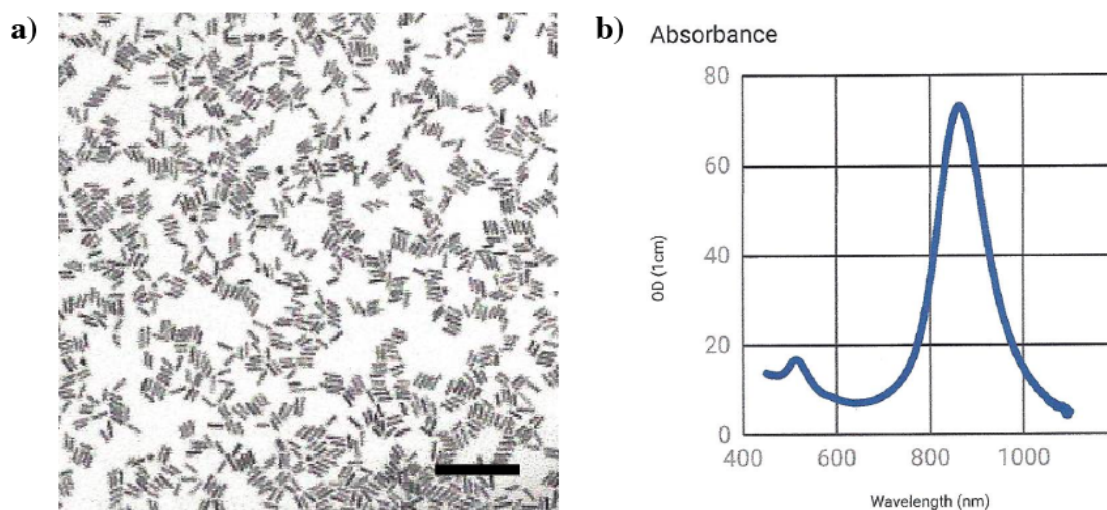


Figure 5.1: Gold nanorod characteristics. a) TEM image of stock AuNRs. Scale bar is 500 nm. b) Absorbance spectrum of AuNRs in the visible and IR spectrum. LSPR absorption peak occurs at 850 nm. Reproduced from Nanopartz Certificate of Analysis for gold nanorod product C12-25-850-TN-DIH-50, Lot # N2442

Combining images of single AuNRs reconstructed using two perpendicular polarizations will result in a dim or undetectable diffraction-limited spot in one polarization, and a bright and detectable spot in the other. Larger clusters, where the AuNRs will be randomly ori-

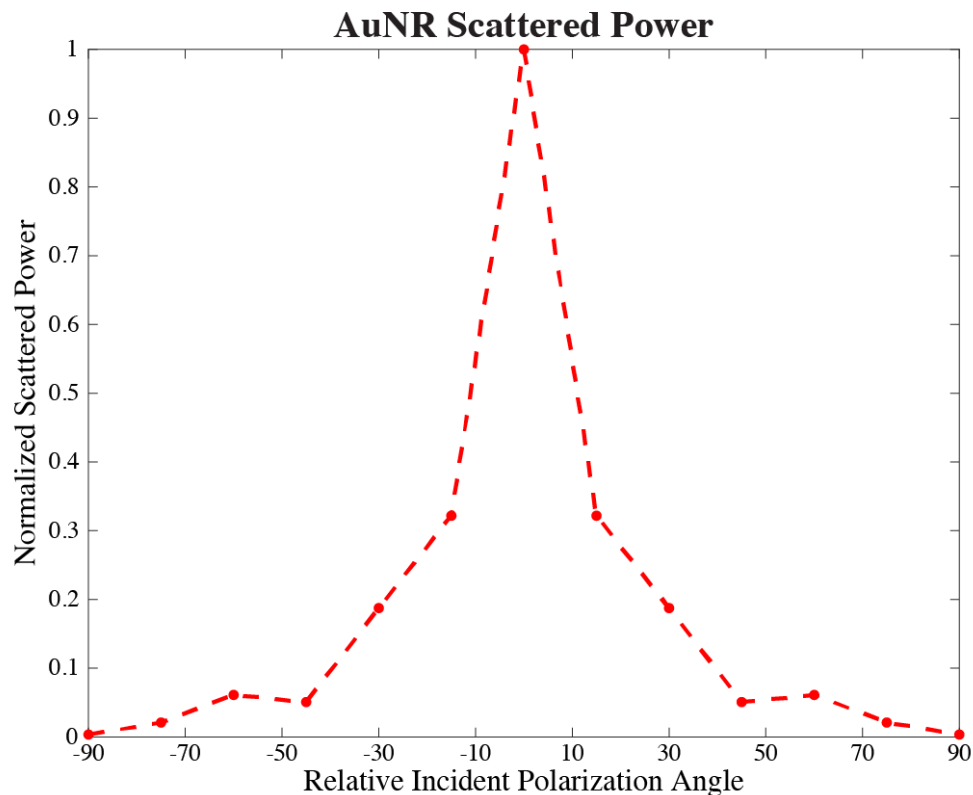


Figure 5.2: Gold nanorod simulated scattering response under linearly polarized 850 nm light. The x-axis denotes the angle of the linear polarization relative to the long, resonant axis of the AuNR, with 0 degrees indicating the rod is perfectly aligned with the polarization vector. Response is normalized to the maximum scattering response. Simulation shows a high degree of polarization dichroism, with the majority of the scattered power produced between ± 20 degrees from 0 while outside of 40 degrees is less than 10% of the maximum response.

ented and bound together, will exhibit more scattering, but a lesser degree of dichroism, enabling the LFHM system to distinguish between single AuNRs oriented in one of the two polarization directions and clusters of bound AuNRs that have agglutinated in the presence of a target biomolecule for biosensing.

5.2.2 Polarization-based LFHM design

The new LFHM design is similar to the system described in Chapter 3, but with several changes that enable it to image AuNRs effectively (Fig. 5.3). The primary alteration is

that laser diodes centered at 850 nm (ThorLabs L850P010), rather than high-power LEDs centered at 532 nm are used. These diodes not only align with the LSPR peak of the AuNRs, they are also smaller, consume less power, are highly temporally coherent with a full-width half-max (FWHM) of < 1 nm compared to a bandpass filter with a FWHM of 5 nm, and are more spatially coherent than LEDs. These characteristics allow the pinhole filter and bandpass filter to be removed from the system, improving system robustness, reducing cost, and reducing the size of the system. It also enables polarization filters to easily be inserted into the system for AuNR imaging. Figure 5.4 shows the completed laser diode-based LFHM system, termed the P-LFHM, while Figure 5.5 shows a side-by-side comparison to the previously reported LFHM system. The system featured in Chapter 3 weighs 835 g while the P-LFHM system weighs just 540 g.

The laser diodes of the P-LFHM are positioned directly above the image sensor on a custom-built laser diode array (Appendix C). A 5V source powers the array through a constant current source using a single NPN transistor (2N3904TA). A trimmer resistor (3296W-1-101LF) is incorporated into the constant current source which enables fine-tuning of current delivery to the diodes and therefore diode intensity, while also preventing damage to the diodes. The tunable diode output power is useful when balancing laser intensity with sensor exposure settings to achieve optimal imaging results. The diodes are switched on and off one at a time by 16 MOSFET transistors (STP160N3LL).

The image sensor is the Pi-Hawk 64MP CMOS image sensor from Arducam. This sensor has a working area of 41.07 mm^2 and a pixel size of $0.8 \text{ }\mu\text{m}$. This large working area enables simultaneous imaging of tens of thousands and potentially hundreds of thousands of AuNR's simultaneously, while the sub-micron pixel size should improve imaging resolution.

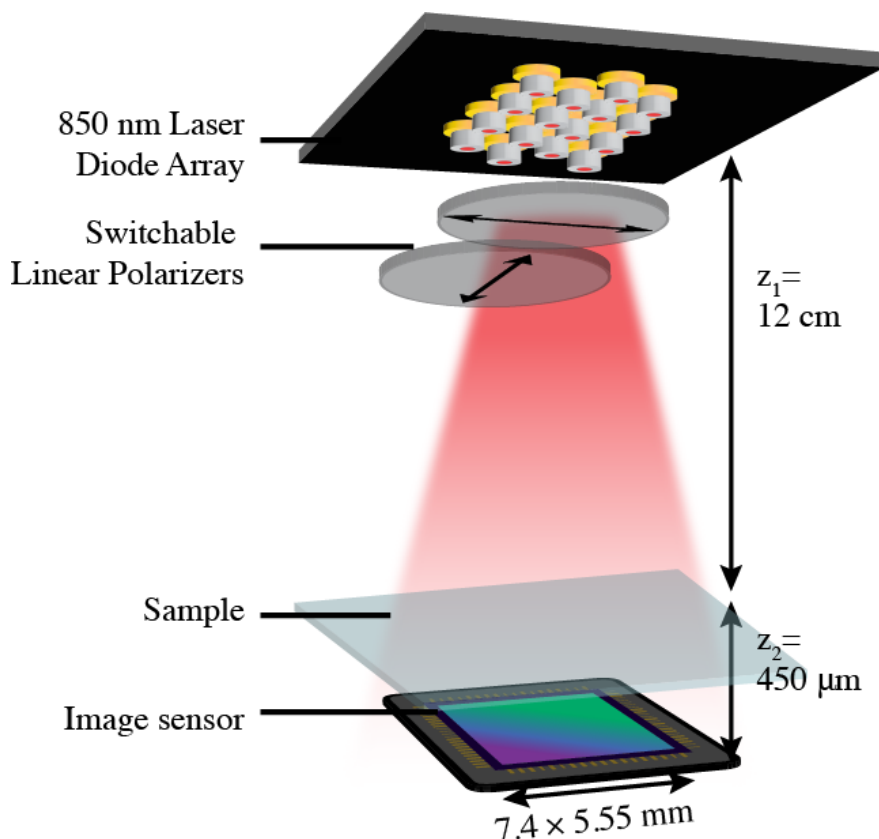


Figure 5.3: Polarization-LFHM schematic. An array of 16 850 nm laser diodes is positioned directly above the image sensor. Two linear polarization filters that can be shifted back and forth to achieve two different source polarizations are positioned between the diodes and sensor, and the sample is placed atop the sensor beneath the filters.

The sensor itself has a Bayer color filter on it, which would present a significant problem in the visible color spectrum. To test the sensor performance in the near infrared spectrum, the IR filter of the sensor was removed and a supercontinuum laser was used to scan across the visible and near IR spectrum. The response for each of the red, green, and blue channels was collected and normalized by the power of the supercontinuum laser.

Both the image sensor and the laser diode array are controlled by a Raspberry Pi 4B with 8 GB of RAM. The image sensor itself is simply connected to the CSI-2 port on the board and is controlled with the Python package, Picamera2. Raw digital negative (.dng) format

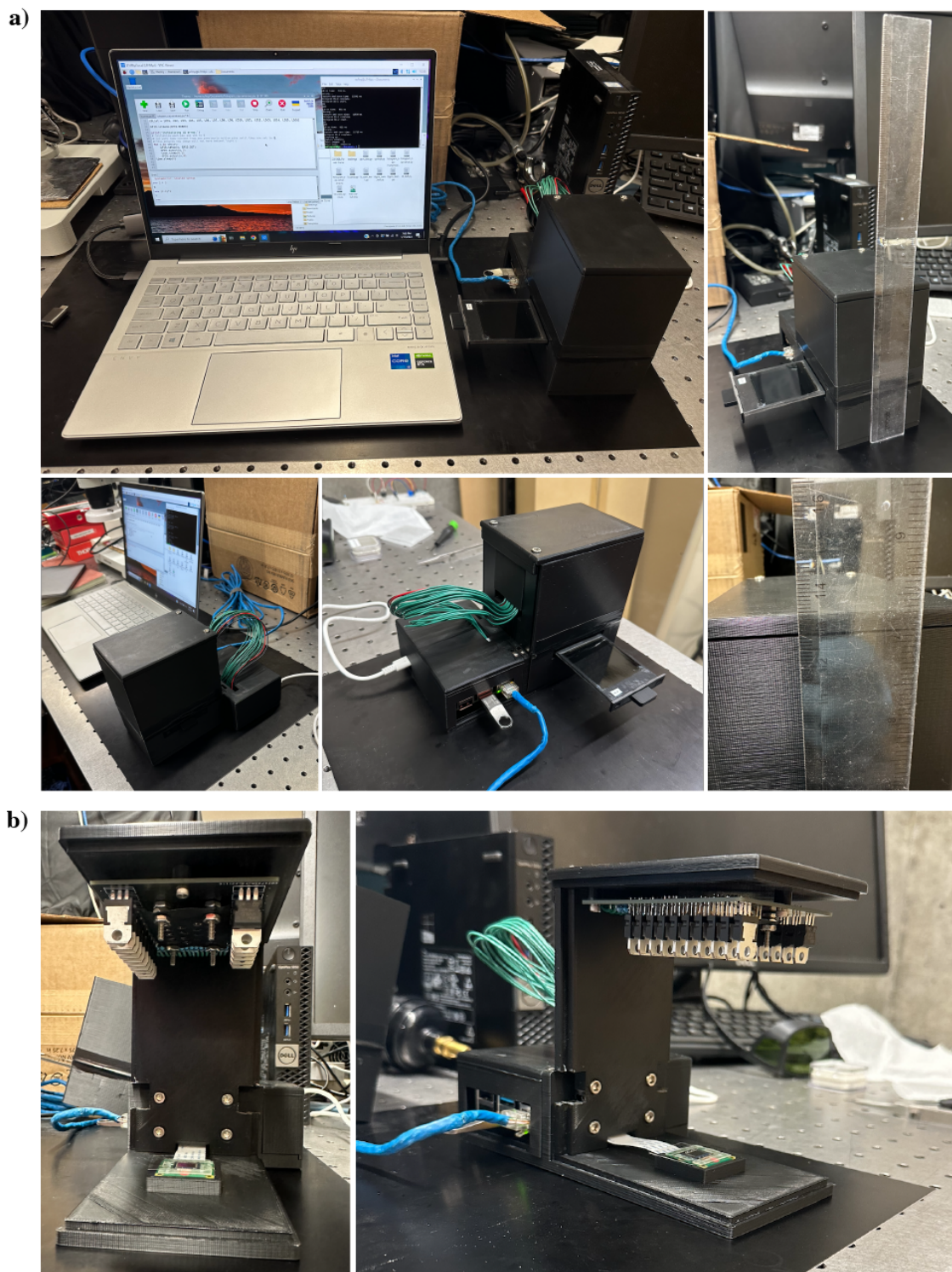


Figure 5.4: Fully assembled P-LFHM device. a) External views of the operating P-LFHM device with paired laptop computer connected via SSH. b) View of imaging area with laser diode array and image sensor visible. Polarization filters are embedded in the sliding component visible in the walls of the main imaging chamber, which are removed and replaced when loading and unloading samples into the microscope.



Figure 5.5: Comparison of two LFHM devices. Both LFHM devices used in this dissertation are shown side-by-side. On the left side of the images is the QLAB sensor used in SARS-CoV-2 quantification in Chapter 3, and on the right is the new P-LFHM sensor, which stands half as tall with a similar footprint as the QLAB sensor.

images are captured using the code shown in Appendix B. The diode array is connected to 18 total GPIO pins on the Raspberry Pi board: one pin to ground, one 5V power pin that supplies the constant current source on the array board, and 16 output pins that switch the MOSFET transistors on the laser diode array board. Images are saved directly on the Pi and can be exported to a portable laptop computer for processing via a flashdrive or directly over an ethernet connection.

The Pi is setup in a headless configuration. In this configuration, a laptop computer can connect to it directly via an ethernet cable and SSH, eliminating the need for a separate monitor for the Pi. Internet access can be shared from the laptop to the Pi if needed over this connection, however no internet connection is needed to operate the P-LFHM and process the holograms. The laptop can operate on battery for several hours at a time, and the Pi only needs a single outlet to run all of the components, making the only requirement necessary for imaging access to power. Imaging with this system currently takes 10 s per frame or 2.5 minutes for a single set of holograms to be captured from one polarization. This can be sped up significantly to only 6 s by using Python multiprocessing to capture a video feed from the image sensor at 2.7 frames per second (the maximum frame rate of a full resolution image) and sync laser diode flashing using code provided in Appendix B.

5.2.3 AuNR agglutination assay

AuNR agglutination is performed to detect the presence of a small molecule, biotin. AuNRs are functionalized with Neutravidin by the manufacturer, enabling the use of a 4-arm PEG biotin molecule (Creative PEGWorks PSB-4202) as a sensing target. Figure 5.6 shows the agglutination assay procedure which relies on Neutravidin-biotin binding to agglutinate AuNRs. AuNRs diluted 1:100,000 from a stock of 0.36% w/v are mixed with 4-arm biotin at a final concentration of 100 μg per mL for 40 minutes on a shaker at 1400 rpm at room temperature.

Due to the current long capture time of the P-LFHM, the agglutinated AuNRs have to be immobilized before imaging. Without this step, motion blur from the AuNRs undergoing Brownian motion would prevent any imaging of single AuNRs in the sample and

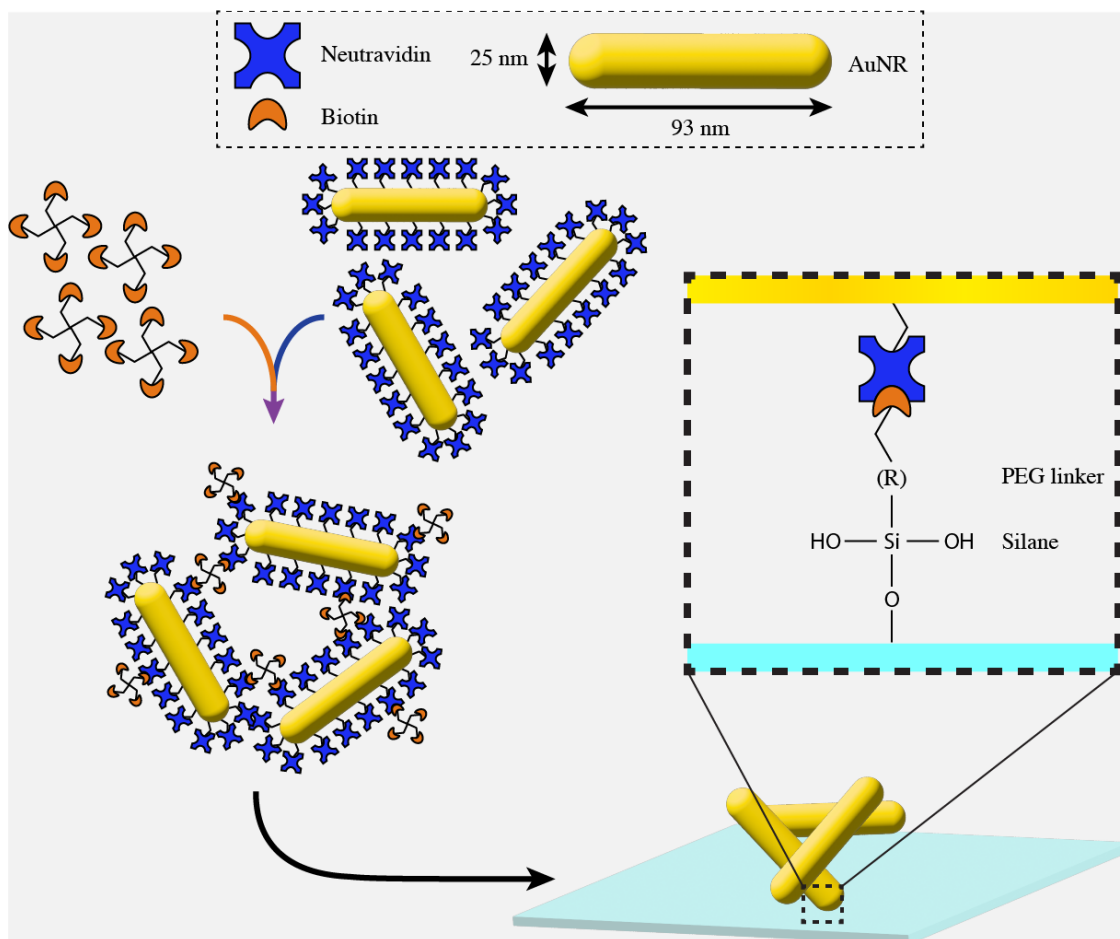


Figure 5.6: Agglutination assay of AuNRs. AuNRs are diluted 1:100,000 and incubated with 100 μg per mL of 4-arm PEG biotin (MW 5,000) for 40 minutes at room temperature on a shaker at 1400 rpm. The agglutinated particles are dropped onto a silane-functionalized glass coverslip, dried, and imaged.

effectively prevent quantification of agglutination [236, 237]. Immobilization is achieved through silanization of a glass coverslip. 3400 MW Silane-PEG-Biotin is dissolved in DMSO at a concentration of 20 mg per mL and deposited onto a plasma-treated coverslip. After 20 minutes, the silane solution is washed off first with fresh DMSO, then with ultrapure water and lightly blown dry with compressed air. Agglutinated AuNRs are dropped onto the silanized glass coverslip and allowed to sit for 5 min before washing with ultrapure water and lightly blowing dry with compressed air before being ready for imaging in the P-LFHM.

5.3 Results

5.3.1 *P-LFHM sensor response*

The PiHawk image sensor showed little to no channel difference at a wavelength of 850 nm. Figure 5.7a depicts the normalized red, green, and blue channel response to the supercontinuum laser at different wavelengths, which reveals that the channel response converges at 850 nm and then follows the expected response decay that is indicative of silicon-based CMOS sensors. Closer inspection of the response curves shows that they remain consistently within 3% of each other, indicating that the Bayer pattern has little impact on images produced at 850 nm.

This indicates that the PiHawk sensor is a good choice for operating at this wavelength. Its uniform response across all 3 channels enables the use of every single pixel on the sensor instead of just the red channel, making the effective pixel size of a raw hologram the sensor pixel size of 0.8 μm .

5.3.2 *Image benchmarking analysis*

To assess the imaging performance of the P-LFHM system, a USAF 1951 test target was imaged, as shown in Figure 5.8. Reconstructions of single holograms captured with the P-LFHM are achieved here, with a reconstruction of the USAF test target shown on the left side of the figure. Quantification of the pixel variation along each line (shown on the right of the figure) reveals that the resolution of vertical lines is 1.74 μm while for horizontal lines it is 1.38 μm . This discrepancy can be explained by the presence of large, vertical lines from group 6 immediately to the left of group 8. Sharp lines like this generate many high

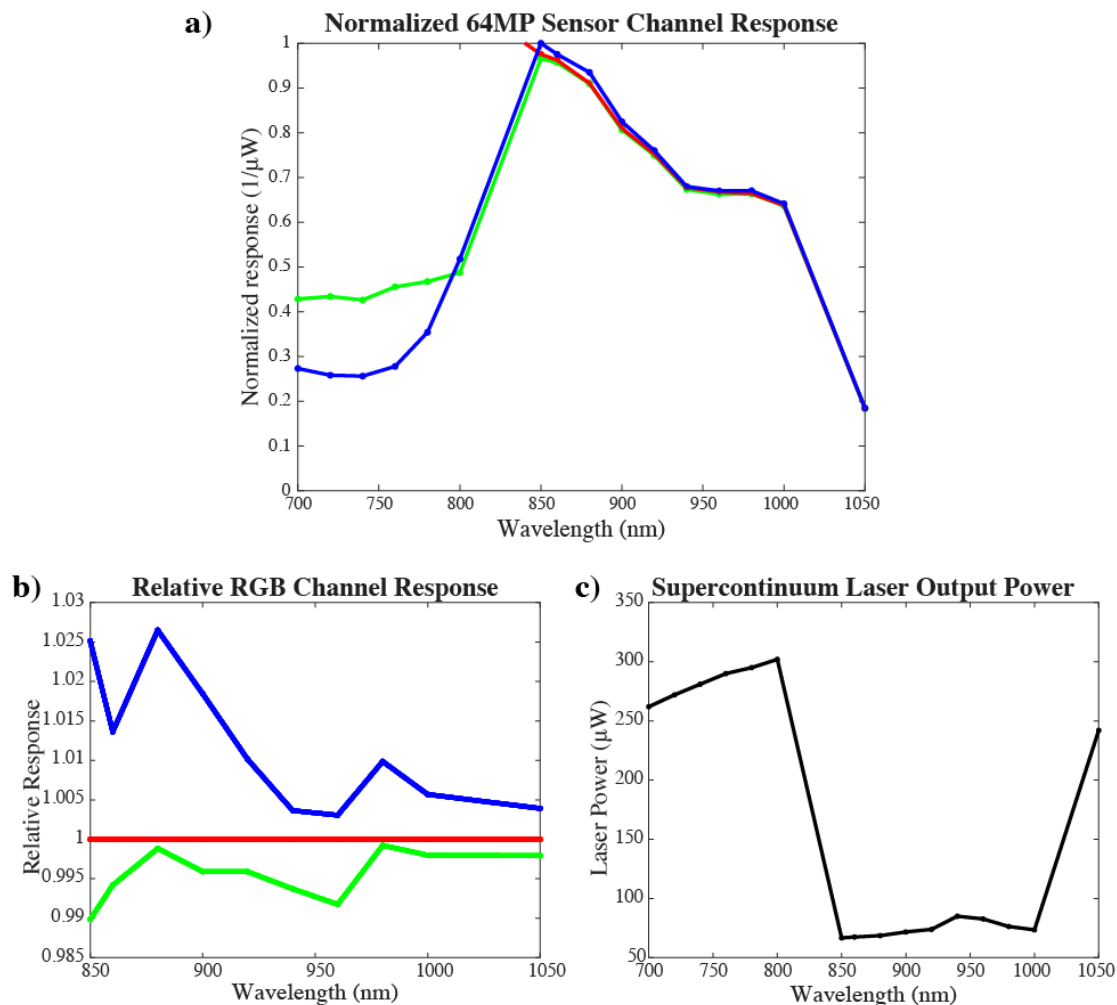


Figure 5.7: PiHawk sensor channel response at 850 nm. a) All three channels exhibit a similar response to 850 nm wavelength light, retaining a 3% range between the individual channels, shown in (b). c) Shows the laser power of the illuminating laser that was used to normalize the graph in (a). For all, red, green, and blue lines indicate the response of the red, green, and blue channels respectively.

frequency fringes, exacerbating common holographic reconstruction problems like the twin image artifact, and likely contribute to a lower resolution of these vertical bars.

5.4 Summary

As a result of the research presented in this Chapter, several things have been accomplished. First, a novel LFHM design has been developed. No LFHM sensor has yet been

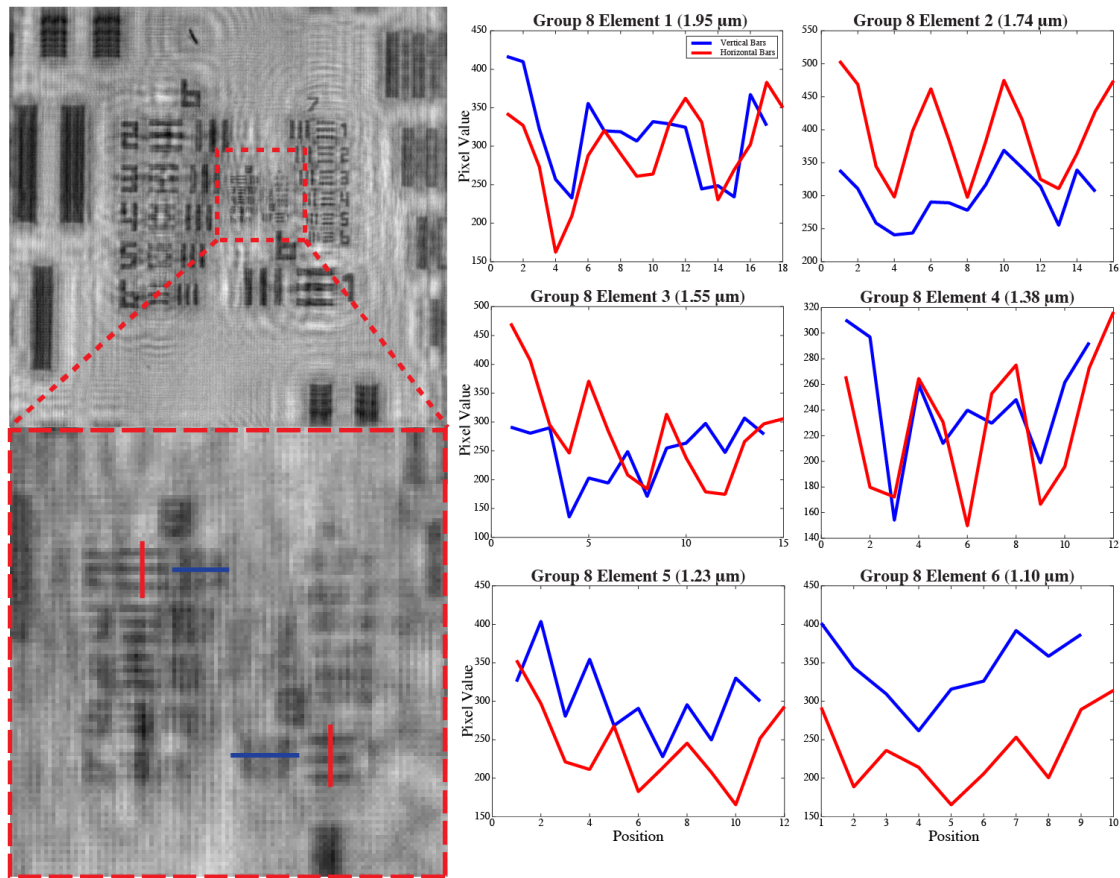


Figure 5.8: Single low-resolution hologram USAF reconstruction. Left is a small FOV of the USAF 1951 test target, depicting groups 6 and smaller, and a zoomed in FOV of this image around group 8 with red and blue lines indicating the pixels measured in the graphs on the right. The graphs to the right show the pixel value of the image along the lines shown in the left for each of the elements in group 8 with their corresponding bar widths. For horizontal groups (red), group 8 element 4 ($1.38 \mu\text{m}$ resolution) is clearly resolved, with even up to element 6 ($1.1 \mu\text{m}$) exhibiting intensity dips corresponding with the dark bars. Vertical bars are resolved clearly until group 8 element 2 ($1.74 \mu\text{m}$) with some intensity drops present up until group 8 element 4.

reported that utilizes a sensor with a pixel size of under a micron. The benefit of this can be seen in the single hologram reconstruction, which produces a higher resolution image than a single hologram from the previously reported QLAB system [11, 57, 75]. Additionally, this system satisfies constraints imposed by the LFHM temporal coherence transfer function which indicate that the system is only limited by the physical diffraction limit imposed by using 850 nm light, something which is difficult to achieve.

In addition to the theoretical implications this system exhibits, a significant amount of benchmarking has been performed that indicate its usefulness as a novel LFHM imaging platform. The sensor response data indicate that the P-LFHM will be able to image colloidal particles, effectively utilizing all channels of the sensor for the highest possible resolution. Furthermore, simulation results of AuNR scattering supports the use of polarized light when imaging agglutinated AuNRs. The combination of these factors support the P-LFHM's use as a biosensor using agglutinated AuNRs as described above.

CHAPTER 6

Conclusions and Future Directions

The work in this dissertation represents a substantial advancement in LFHM biosensor technology. First, a LFHM biosensor was applied to biosensing of SARS-CoV-2 virus, successfully addressing a pressing need during the COVID-19 pandemic. This biosensing platform excelled in combining portable, point-of-care readout with an assay sensitivity approaching that of the gold standard of PCR. This sensor achieved a limit of detection of 1,270 copies of virus per mL within 3 hrs of sample collection. Furthermore, it incorporated a deep learning algorithm to improve the robustness of data quantification, enabling samples filled with debris to be used for quantification. This advancement addresses a key drawback of LFHM technologies in that they are sensitive to this type of debris in imaging. As a final step in this research, the agglutination assay was made quantitative and unambiguous. By using 2 samples, either at a higher microbead concentration or at a diluted sample concentration, the true concentration of virus could be obtained using this assay, only increasing assay time by a few minutes in the process. These advancements represent a novel and compelling contribution to LFHM biosensing technologies and provide a basis for LFHM biosensors moving forwards.

In the process of developing a deep learning algorithm to quantify the COVID-19

biosensor samples, a characterization study was performed on shallow convolutional neural networks. Commonly used and adjusted layers and hyperparameters were systematically changed, with the resulting effect on network behavior quantified and reported. This yielded critical information that makes it possible to efficiently approach construction and refinement for these types of networks. For example, if specific undesirable behaviors in future neural networks are observed such as overtraining, variability between training iterations, and low validation accuracy, the knowledge cataloged here can provide a guide for which factors to adjust and in which order. The usefulness of this research can also extend to other datasets of biomedically relevant images as well, not just LFHM imaging.

Finally, a new LFHM microscope was developed for use in a novel biosensing platform. Its novelty lies in the specific combination of components that combine portability with ultra-small pixel size and custom laser diode array, and in its use of gold nanorods as a particle for an agglutination assay. The use of LSPR-dependent scattering under linearly polarized light is particularly unique and will set future research with this device apart from other research in the field. The thorough examination of this P-LFHM device as a microscope, and the performance of the necessary calculations, simulations, and testing lay the ground work to proceed to the next research step of performing a biosensing assay for a relevant target biomarker of disease.

Future directions for this work primarily include the development and testing of this biosensing platform. Figure 6.1 depicts a vision of what this biosensor could eventually look like and how sensing for carcinoembryonic antigen (CEA) as a biomarker for cancer could be performed using this device. The advantage of the P-LFHM system lies in its ability to target multiple biomarkers for disease without changing the underlying LFHM device. Nanorods

functionalized with Neutravidin can easily be conjugated to biotinylated antibodies for any desired protein and even biotinylated DNA for nucleic acid detection. Furthermore, other capture molecules with known interactions can be used, expanding the sensing of this device to small molecules and unconventional proteins with ease. Going even further, multiple targets could be sensed in a single assay by using multiple source wavelengths and multiple nanorods with different resonance wavelengths. The research in this dissertation lays the foundation for all of these advances and more.

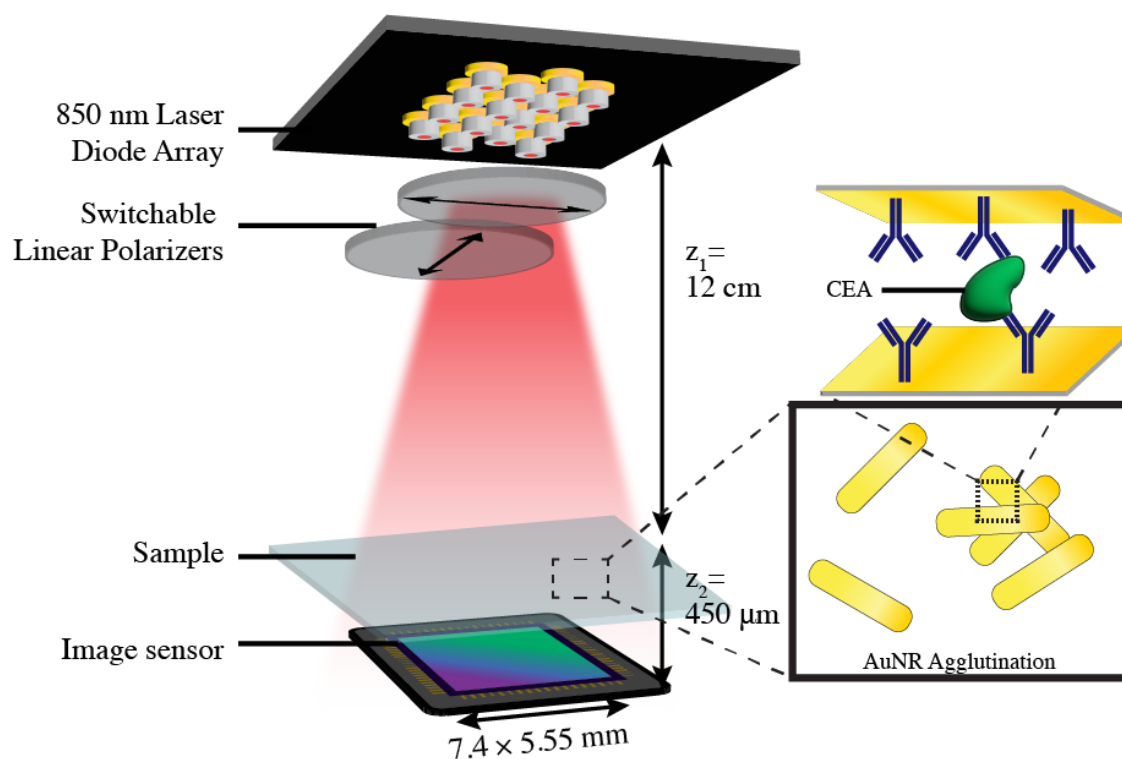


Figure 6.1: Next steps for the P-LFHM system. Depicted here is the P-LFHM system imaging agglutinated AuNRs functionalized with antibodies to detect CEA protein in a biosensing assay for cancer diagnosis.

APPENDIX A

Appendix A: 3D CAD models of LFHM housing

A.1 Portable QLAB designs

Below are images from the SolidWorks CAD environment where the housing for the portable housing for the QLAB sensor was designed for 3D printing. The design is hinged at the back to allow a sample to be loaded and unloaded easily. Bolts and nuts affix the more permanent components together (the lid at the top designed to access the LED array for maintenance and the side walls are bolted together during use. All seams in the device feature an interlocking step design to prevent ambient room light from affecting the holograms.

A.2 P-LFHM designs

Below is featured representative images of the 5 components comprising the P-LFHM housing in the CAD environment, Autodesk Fusion 360. These components were designed and assembled using Fusion 360 before 3D printing with black PLA. For assembly, M2 threaded screws were screwed directly into holes in the models, self-tapping threads and enabling a stable, semi-permanent connection for parts that were designed to be fixed together without moving (i.e. components that position the Raspberry Pi, image sensor, and array relative to each other, shown in the upper right photo). Other, movable components

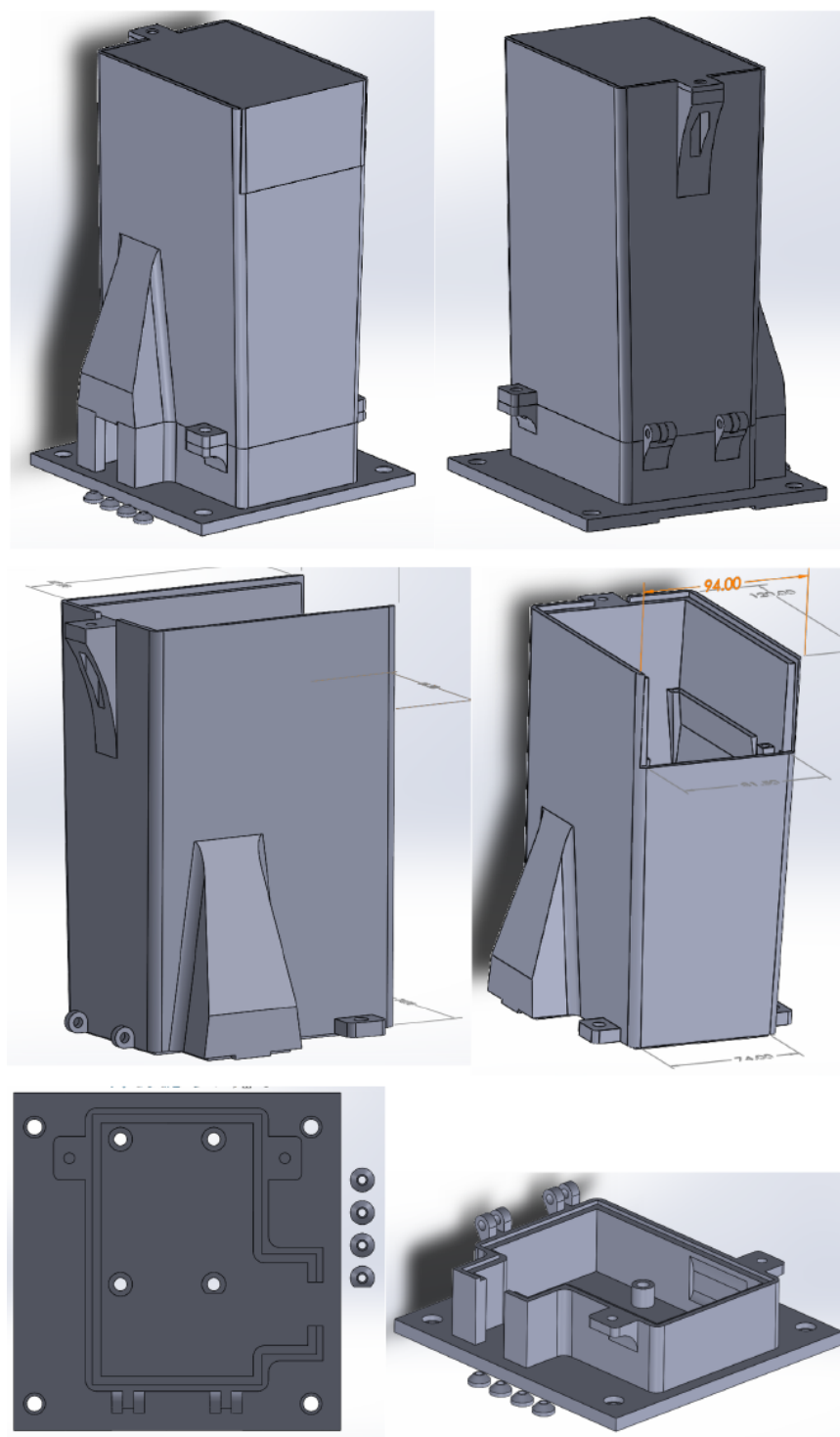


Figure A.1: Portable QLAB CAD designs. Each of the 3 main components are shown here, along with the assembly.

were attached together using magnets and friction for a firm, but easily removable contact, important for sample loading and unloading and Raspberry Pi maintenance. All seams into the imaging compartment are interlocking steps so that ambient room light cannot enter and wash out the hologram.

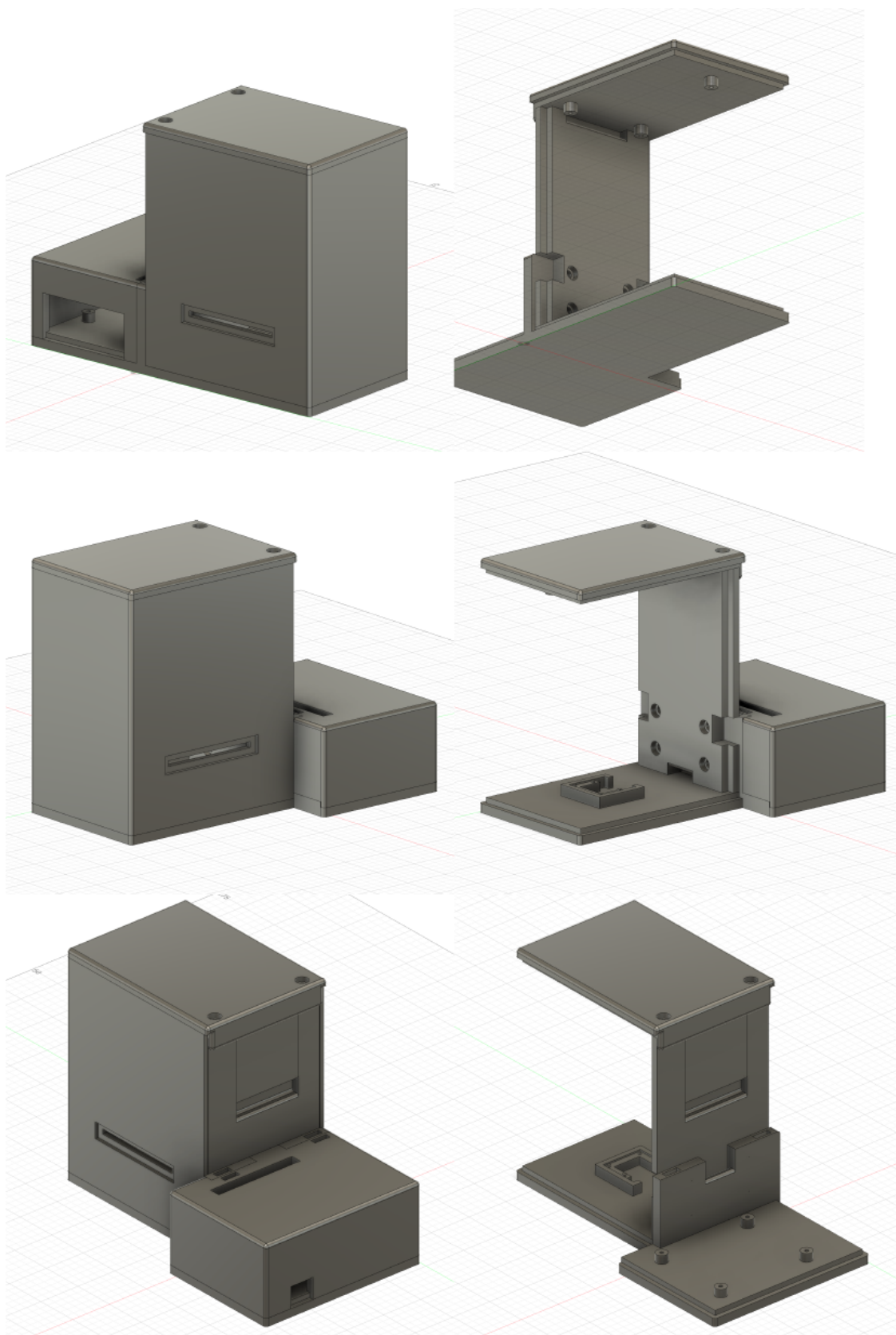


Figure A.2: P-LFHM CAD designs. Various rotations and states of disassembly are shown to demonstrate how the P-LFHM device was assembled.

APPENDIX B

Appendix B: Operating Python code for P-LFHM

B.1 Serial illumination and capture

Code for capturing a hologram illuminated throughout the image capture process. This code can also capture multiple images from a single diode for averaging.

```
import RPi.GPIO as GPIO
import time
import datetime
import multiprocessing

from picamera2 import Picamera2, Preview
from picamera2.controls import Controls
import time
import numpy as np
import pandas as pd

start = datetime.datetime.now()
print('Initializing GPIO.')
# List LD no. and GPIO pin pairs
LD1 = 11
LD2 = 12
LD3 = 13
LD4 = 15
LD5 = 16
LD6 = 18
LD7 = 22
LD8 = 29
LD9 = 31
LD10 = 32
LD11 = 33
LD12 = 35
LD13 = 36
```

```

LD14 = 37
LD15 = 38
LD16 = 40
LDList = [LD1, LD2, LD3, LD4, LD5, LD6, LD7, LD8, LD9, LD10, LD11, LD12,
    ↪ LD13, LD14, LD15, LD16]

GPIO.setmode(GPIO.BOARD)

print('Initializing LD array.')
# Initialize each pin and set to 0
# (pi will leak current from any previously active pins,
# this ensures new image will not have ambient light.)
for x in LDList:
    GPIO.setup(x, GPIO.OUT)
    GPIO.output(x,1)
    time.sleep(0.1)
    GPIO.output(x,0)
time.sleep(2)

print('Initializing camera.')
picam2 = Picamera2()
#format must be yuv for main stream - rgb is default and uses double the CMA
    ↪ memory as yuv so buffer frame won't allocate
capture_config = picam2.create_still_configuration(raw={"size": (9152, 6944)
    ↪ }, main={"format": "YUV420"})
picam2.options["compress_level"] = 0 #no .png compression performed
picam2.options["quality"] = 95 #highest quality .jpg
picam2.configure(capture_config)

picam2.start()
time.sleep(2)

with picam2.controls as ctrl:
    ctrl.AwbEnable = False
    ctrl.AnalogueGain = 1.0
    ctrl.ExposureTime = 371 #rounded from 2.7 fps
    ctrl.NoiseReductionMode = False
    ctrl.Sharpness = 0 #may want to change to 1 (default)
time.sleep(2)

print('Begin capture.')
request = picam2.capture_request() #initializes camera frame without saving

```

```

    ↪ it
request.release()
avgtot = 2
holonum = 1
for x in LDList:
    avgnum = 1
    for y in range(0,avgtot):
        print('Hologram ' + str(holonum) + '-' + str(avgnum) + ' start.')
        GPIO.output(x,1) #flash diode
        startld = datetime.datetime.now()
        print('ON')

        startcap = datetime.datetime.now()
        request = picam2.capture_request() #Capture all streams and metadata
            ↪ using request

        GPIO.output(x,0) #diode off
        stopld = datetime.datetime.now()
        print('OFF')

        deltald = stopld - startld
        print('LD on time: ', int(deltald.total_seconds() * 1000), 'ms')

        print('Saving...')
        request.save_dng('GNR-100ug_LRH_wpol' + str(holonum) + '-' + str(
            ↪ avgnum) + '.dng') #save raw stream
        request.release()
        stopcap = datetime.datetime.now()
        deltacap = stopcap - startcap
        print('Capture and save time: ', int(deltacap.total_seconds() *
            ↪ 1000), 'ms')
        print('Hologram ' + str(holonum) + '-' + str(avgnum) + ' complete.')
        avgnum = avgnum+1

    holonum = holonum+1

print('Cleaning up...')
picam2.stop()
GPIO.cleanup()
time.sleep(1)
print('Capture complete')
stop = datetime.datetime.now()
total = stop-start
imgtot = (holonum-1) * avgtot
print('Total images: ', str(imgtot))

```

```
print('Total time: ', int(total.total_seconds() * 1000), 'ms')
```

B.2 Multiprocessing parallel illumination and capture

Additional code using multiprocessing to illuminate diode independently of capture process. This framework will enable hologram capture during video recording.

```
import RPi.GPIO as GPIO
import time
import datetime
import multiprocessing

from picamera2 import Picamera2, Preview
from picamera2.controls import Controls
import time
import numpy as np
import pandas as pd

print('Initializing GPIO.')
```

List LD no. and GPIO pin pairs

```
LD1 = 11
LD2 = 12
LD3 = 13
LD4 = 15
LD5 = 16
LD6 = 18
LD7 = 22
LD8 = 29
LD9 = 31
LD10 = 32
LD11 = 33
LD12 = 35
LD13 = 36
LD14 = 37
LD15 = 38
LD16 = 40
LDList = [LD1, LD2, LD3, LD4, LD5, LD6, LD7, LD8, LD9, LD10, LD11, LD12,
↪ LD13, LD14, LD15, LD16]
```

```
GPIO.setmode(GPIO.BOARD)

print('Initializing LD array.')
```

Initialize each pin and set to 0
(pi will leak current from any previously active pins,
this ensures new image will not have ambient light.)

```

for x in LDList:
    GPIO.setup(x, GPIO.OUT)
    GPIO.output(x,1)
    time.sleep(0.1)
    GPIO.output(x,0)
time.sleep(2)

e = multiprocessing.Event()
t = multiprocessing.Event()
f = multiprocessing.Event()

# Process 1: Flash diode for specified seconds
def DiodeFlash():
    while True:
        if e.is_set():
            f.set()
            GPIO.output(x,1) #flash diode
            startld = datetime.datetime.now()
            print('ON')
            time.sleep(1)
            GPIO.output(x,0) #diode off
            stopld = datetime.datetime.now()
            print('OFF')
            deltald = stopld - startld
            print('LD on time: ', int(deltald.total_seconds() * 1000), 'ms')
            e.clear()
        if t.is_set():
            break

# Process 2: Start camera capture
def CameraCap():
    print('Initializing camera.')
    picam2 = Picamera2()
    capture_config = picam2.create_still_configuration(raw={"size": (9152,
        ↪ 6944)}, main={"format":"YUV420"})
    picam2.options["compress_level"] = 0 #no .png compression performed
    picam2.options["quality"] = 95 #highest quality .jpg
    picam2.configure(capture_config)

    picam2.start()
    time.sleep(2)

    with picam2.controls as ctrl:
        ctrl.AwbEnable = False
        ctrl.AnalogueGain = 1.0

```

```

    ctrl.ExposureTime = 371 #rounded from 2.7 fps
    ctrl.NoiseReductionMode = False
    ctrl.Sharpness = 0 #may want to change to 1 (default)
time.sleep(2)

print('Begin capture.')
request = picam2.capture_request() #initializes camera frame without
    ↪ saving it
request.release()
holonum = 1
for x in LDList:
    print('Hologram ' + str(holonum) + ' start.')
    startcap = datetime.datetime.now()
    e.set()
    request = picam2.capture_request() #Capture all streams and metadata
        ↪ using request
    stopcap = datetime.datetime.now()
    deltacap = stopcap - startcap
    print('Capture time: ', int(deltacap.total_seconds() * 1000), 'ms')
    print('Saving...')
    request.save_dng('PolLRH' + str(holonum) + '.dng') #save raw stream
    request.release()
    print('Hologram ' + str(holonum) + ' complete.')

    holonum = holonum +1

print('Cleaning up...')
picam2.stop()
t.set()

def Terminate():
    while True:
        if t.is_set():
            p.terminate()
            q.terminate()
            GPIO.cleanup()
            time.sleep(1)
            print('Capture complete')
            break

p = multiprocessing.Process(name='DiodeFlash', target = DiodeFlash, args =
    ↪ () )
q = multiprocessing.Process(name='CameraCap', target = CameraCap, args = ()
    ↪ )

```

```
r = multiprocessing.Process(name='Terminate', target = Terminate, args = ()  
    ↪ )  
  
q.start()  
p.start()  
r.start()
```

APPENDIX C

Appendix C: Laser diode array circuit schematics

C.1 Circuit design

The circuit for the custom laser diode array was designed using Autodesk Eagle.

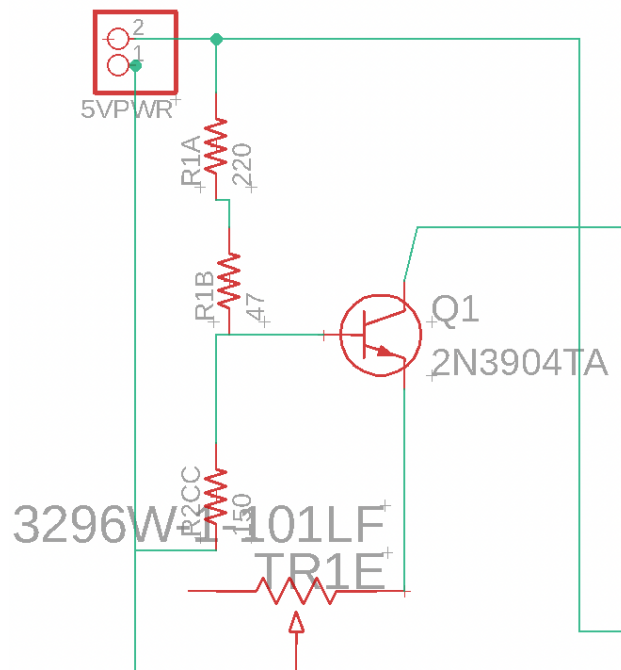


Figure C.1: Constant current source that powers the laser diode array. 5V power connects to the Raspberry Pi GPIO pin 2 and GND connects to the Raspberry Pi GPIO pin 6.

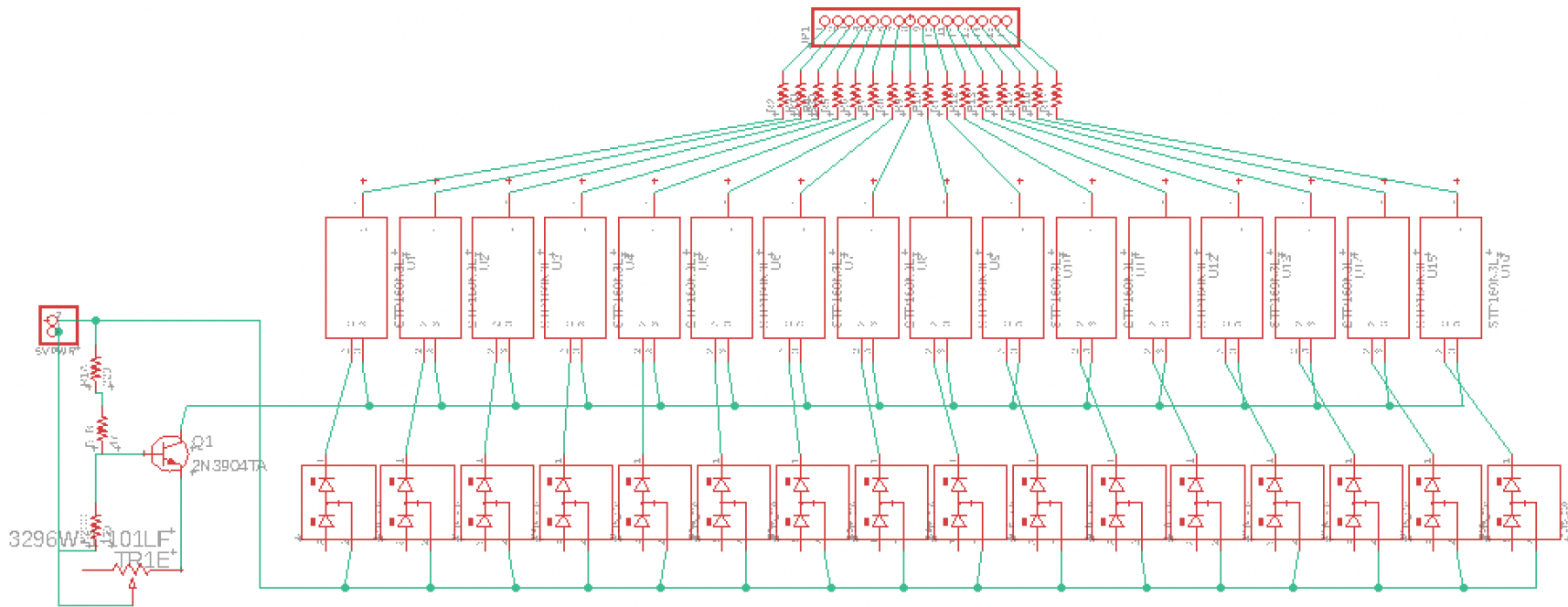


Figure C.2: Full circuit wire diagram of the laser diode array. Each of the 16 connections connects to one output pin on the GPIO. Resistors are placed between the MOSFET transistors and pin connections to prevent a runaway current as the transistor heats which could draw excess current from the Raspberry Pi and damage it.

C.2 PCB layout

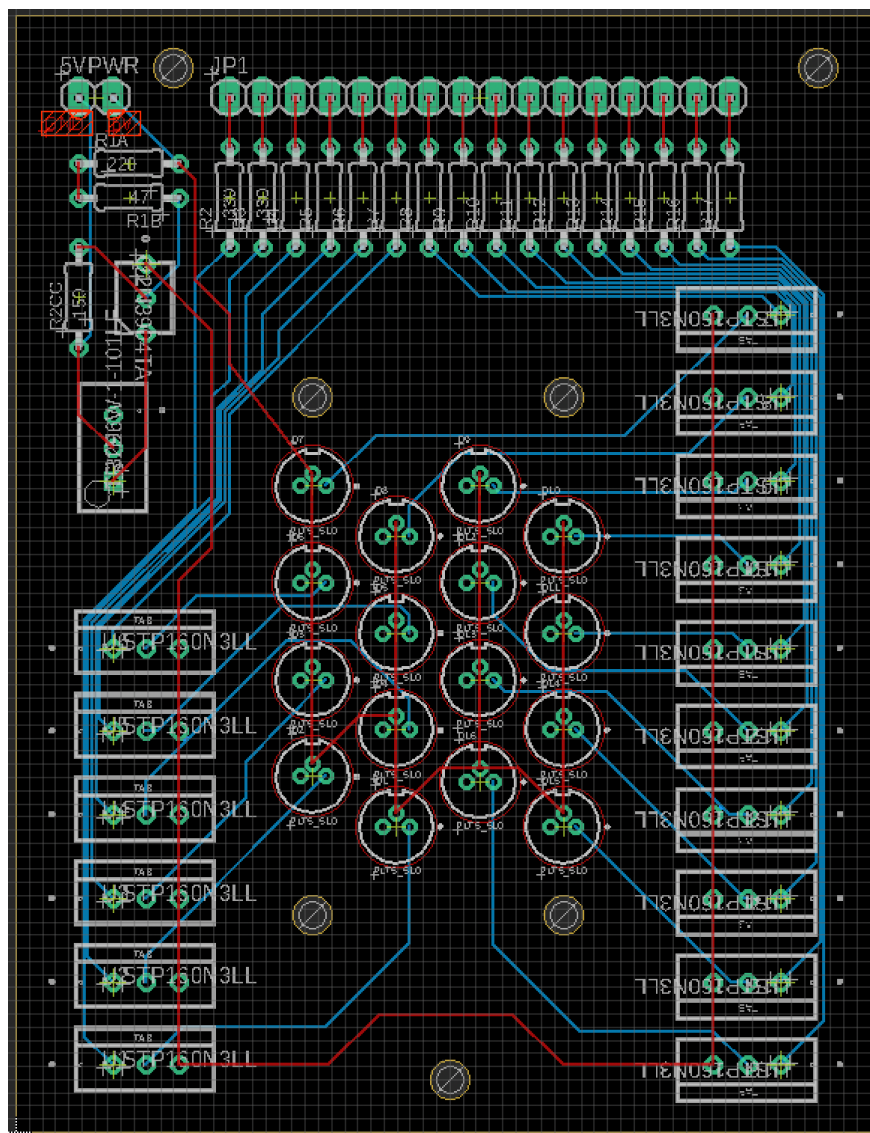


Figure C.3: Laser diode board schematics. The laser diode array was printed on an FR-4 base material with a top and bottom layer, and thickness of 1.6. The printed circuit board color was black. Total price for a single board was \sim \$2. Total price for the fully assembled array was \sim \$440, with the laser diodes comprising the majority of the cost (\sim \$415).

REFERENCES

- [1] Kevin Chu. An introduction to sensitivity, specificity, predictive values and likelihood ratios. *Emergency Medicine*, 11(3):175–181, September 1999. ISSN 1035-6851, 1442-2026. doi: 10.1046/j.1442-2026.1999.00041.x.
- [2] M. Burns and H. Valdivia. Modelling the limit of detection in real-time quantitative PCR. *European Food Research and Technology*, 226(6):1513–1524, April 2008. ISSN 1438-2377, 1438-2385. doi: 10.1007/s00217-007-0683-z.
- [3] Naveen Minhas, Yogesh K. Gurav, Susmit Sambhare, Varsha Potdar, Manohar Lal Choudhary, Sumit Dutt Bhardwaj, and Priya Abraham. Cost-analysis of real time RT-PCR test performed for COVID-19 diagnosis at India’s national reference laboratory during the early stages of pandemic mitigation. *PLOS ONE*, 18(1):e0277867, January 2023. ISSN 1932-6203. doi: 10.1371/journal.pone.0277867.
- [4] Anne Marie Kinn Rød, Nina Harkestad, Finn Konow Jellestad, and Robert Muriison. Comparison of commercial ELISA assays for quantification of corticosterone in serum. *Scientific Reports*, 7(1):6748, December 2017. ISSN 2045-2322. doi: 10.1038/s41598-017-06006-4.
- [5] Gary P. Wormser, Andrew Levin, Sandeep Soman, Omosalewa Adenikinju, Michael V. Longo, and John A. Branda. Comparative Cost-Effectiveness of Two-Tiered Testing Strategies for Serodiagnosis of Lyme Disease with Noncutaneous Manifestations. *Journal of Clinical Microbiology*, 51(12):4045–4049, December 2013. ISSN 0095-1137, 1098-660X. doi: 10.1128/JCM.01853-13.
- [6] David M Rissin, Cheuk W Kan, Todd G Campbell, Stuart C Howes, David R Fournier, Linan Song, Tomasz Piech, Purvish P Patel, Lei Chang, Andrew J Rivnak, Evan P Ferrell, Jeffrey D Randall, Gail K Provuncher, David R Walt, and David C Duffy. Single-molecule enzyme-linked immunosorbent assay detects serum proteins at sub-femtomolar concentrations. *Nature Biotechnology*, 28(6):595–599, June 2010. ISSN 1087-0156, 1546-1696. doi: 10.1038/nbt.1641.
- [7] Joshua D. Bishop, Helen V. Hsieh, David J. Gasperino, and Bernhard H. Weigl. Sensitivity enhancement in lateral flow assays: a systems perspective. *Lab on a Chip*, 19(15):2486–2499, 2019. ISSN 1473-0197, 1473-0189. doi: 10.1039/C9LC00104B.
- [8] Katarzyna M. Koczula and Andrea Gallotta. Lateral flow assays. *Essays in Biochemistry*, 60(1):111–120, June 2016. ISSN 0071-1365, 1744-1358. doi: 10.1042/EBC20150012.

- [9] Maria Soler, Cesar S. Huertas, and Laura M. Lechuga. Label-free plasmonic biosensors for point-of-care diagnostics: a review. *Expert Review of Molecular Diagnostics*, 19(1): 71–81, January 2019. ISSN 1744-8352. doi: 10.1080/14737159.2019.1554435.
- [10] Axel Warsinke. Point-of-care testing of proteins. *Analytical and Bioanalytical Chemistry*, 393(5):1393–1405, March 2009. ISSN 1618-2642, 1618-2650. doi: 10.1007/s00216-008-2572-0.
- [11] Zhen Xiong, Colin J. Potter, and Euan McLeod. High-Speed Lens-Free Holographic Sensing of Protein Molecules Using Quantitative Agglutination Assays. *ACS Sensors*, 6(3):1208–1217, March 2021. ISSN 2379-3694, 2379-3694. doi: 10.1021/acssensors.0c02481PMC8259606.
- [12] Yi Luo, Hyou-Arm Joung, Sarah Esparza, Jingyou Rao, Omai Garner, and Aydogan Ozcan. Quantitative particle agglutination assay for point-of-care testing using mobile holographic imaging and deep learning. *Lab on a Chip*, 21(18):3550–3558, 2021. ISSN 1473-0197, 1473-0189. doi: 10.1039/D1LC00467K.
- [13] Marek Kočańczyk, Frederic Grabowski, and Tomasz Lipniacki. Dynamics of COVID-19 pandemic at constant and time-dependent contact rates. *Mathematical Modelling of Natural Phenomena*, 15:28, 2020. ISSN 0973-5348, 1760-6101. doi: 10.1051/mmnp/2020011.
- [14] Minhaz Uddin Ahmed, Ishtiaq Saaem, Pae C. Wu, and April S. Brown. Personalized diagnostics and biosensors: a review of the biology and technology needed for personalized medicine. *Critical Reviews in Biotechnology*, 34(2):180–196, June 2014. ISSN 0738-8551, 1549-7801. doi: 10.3109/07388551.2013.778228.
- [15] Sven H Loosen, Ulf P Neumann, Christian Trautwein, Christoph Roderburg, and Tom Luedde. Current and future biomarkers for pancreatic adenocarcinoma. *Tumor Biology*, 39(6):101042831769223, June 2017. ISSN 1010-4283, 1423-0380. doi: 10.1177/1010428317692231.
- [16] Zaynab A. R. Jawad, Ioannis G. Theodorou, Long R. Jiao, and Fang Xie. Highly Sensitive Plasmonic Detection of the Pancreatic Cancer Biomarker CA 19-9. *Scientific Reports*, 7(1):14309, December 2017. ISSN 2045-2322. doi: 10.1038/s41598-017-14688-z.
- [17] Lisheng Qian, Qiaobin Li, Kwaku Baryeh, Wanwei Qiu, Kun Li, Jing Zhang, Qingcai Yu, Dongqin Xu, Wenju Liu, Randall E. Brand, Xueji Zhang, Wei Chen, and Guodong Liu. Biosensors for early diagnosis of pancreatic cancer: a review. *Translational Research*, 213:67–89, November 2019. ISSN 19315244. doi: 10.1016/j.trsl.2019.08.002.
- [18] Maria Moccia, Veronica Caratelli, Stefano Cinti, Biagio Pede, Concetta Avitabile, Michele Saviano, Anna Lisa Imbriani, Danila Moscone, and Fabiana Arduini. Paper-based electrochemical peptide nucleic acid (PNA) biosensor for detection of miRNA-492: a pancreatic ductal adenocarcinoma biomarker. *Biosensors and Bioelectronics*, 165:112371, October 2020. ISSN 09565663. doi: 10.1016/j.bios.2020.112371.

- [19] Tasuku Matsuoka and Masakazu Yashiro. Biomarkers of gastric cancer: Current topics and future perspective. *World Journal of Gastroenterology*, 24(26):2818–2832, July 2018. ISSN 1007-9327. doi: 10.3748/wjg.v24.i26.2818.
- [20] Chao-Zhu He, Kun-He Zhang, Qing Li, Xiao-Hua Liu, Yan Hong, and Nong-Hua Lv. Combined use of AFP, CEA, CA125 and CA19-9 improves the sensitivity for the diagnosis of gastric cancer. *BMC Gastroenterology*, 13(1):87, December 2013. ISSN 1471-230X. doi: 10.1186/1471-230X-13-87.
- [21] Leonidas Chouliaras, Alan Thomas, Maura Malpetti, Paul Donaghy, Joseph Kane, Elijah Mak, George Savulich, Maria A Prats-Sedano, Amanda J Heslegrave, Henrik Zetterberg, Li Su, James Benedict Rowe, and John Tiernan O’Brien. Differential levels of plasma biomarkers of neurodegeneration in Lewy body dementia, Alzheimer’s disease, frontotemporal dementia and progressive supranuclear palsy. *Journal of Neurology, Neurosurgery & Psychiatry*, 93(6):651–658, June 2022. ISSN 0022-3050, 1468-330X. doi: 10.1136/jnnp-2021-327788.
- [22] Lucilla Parnetti, Silvia Paciotti, Lucia Farotti, Giovanni Bellomo, Federica Nicoletta Sepe, and Paolo Eusebi. Parkinson’s and Lewy body dementia CSF biomarkers. *Clinica Chimica Acta*, 495:318–325, August 2019. ISSN 00098981. doi: 10.1016/j.cca.2019.04.078.
- [23] C. A. Heid, J. Stevens, K. J. Livak, and P. M. Williams. Real time quantitative PCR. *Genome research*, 6(10):986–994, October 1996. ISSN 1088-9051. doi: 10.1101/gr.6.10.986. Place: United States.
- [24] Aziz Eftekhari, Mahdieh Alipour, Leila Chodari, Solmaz Maleki Dizaj, Mohammadreza Ardalan, Mohammad Samiei, Simin Sharifi, Sepideh Zununi Vahed, Irada Huseynova, Rovshan Khalilov, Elham Ahmadian, and Magali Cucchiarini. A Comprehensive Review of Detection Methods for SARS-CoV-2. *Microorganisms*, 9(2):232, January 2021. ISSN 2076-2607. doi: 10.3390/microorganisms9020232.
- [25] Yun-Long Tsai, Han-Ching Wang, Chu-Fang Lo, Kathy Tang-Nelson, Donald Lightner, Bor-Rung Ou, Ai-Ling Hour, Chuan-Fu Tsai, Cheng-Chi Yen, Hsiao-Fen Grace Chang, Ping-Hua Teng, and Pei-Yu Lee. Validation of a Commercial Insulated Isothermal PCR-based POKKIT Test for Rapid and Easy Detection of White Spot Syndrome Virus Infection in *Litopenaeus vannamei*. *PLoS ONE*, 9(3):e90545, March 2014. ISSN 1932-6203. doi: 10.1371/journal.pone.0090545.
- [26] Jianqiang Zhang, Yun-Long Tsai, Pei-Yu Alison Lee, Qi Chen, Yan Zhang, Cheng-Jen Chiang, Yu-Han Shen, Fu-Chun Li, Hsiao-Fen Grace Chang, Phillip C. Gauger, Karen M. Harmon, and Hwa-Tang Thomas Wang. Evaluation of two singleplex reverse transcription-Insulated isothermal PCR tests and a duplex real-time RT-PCR test for the detection of porcine epidemic diarrhea virus and porcine deltacoronavirus. *Journal of Virological Methods*, 234:34–42, August 2016. ISSN 01660934. doi: 10.1016/j.jviromet.2016.03.016.

- [27] Samira Hosseini, Patricia Vázquez-Villegas, Marco Rito-Palomares, and Sergio O. Martínez-Chapa. *Enzyme-linked Immunosorbent Assay (ELISA)*. SpringerBriefs in Applied Sciences and Technology. Springer Singapore, Singapore, 2018. ISBN 978-981-10-6765-5 978-981-10-6766-2. doi: 10.1007/978-981-10-6766-2.
- [28] Roberto de la Rica and Molly M. Stevens. Plasmonic ELISA for the ultrasensitive detection of disease biomarkers with the naked eye. *Nature Nanotechnology*, 7(12): 821–824, December 2012. ISSN 1748-3387, 1748-3395. doi: 10.1038/nnano.2012.186.
- [29] Jitendra Satija, Nirmal Punjabi, Debasish Mishra, and Soumyo Mukherji. Plasmonic-ELISA: expanding horizons. *RSC Advances*, 6(88):85440–85456, 2016. ISSN 2046-2069. doi: 10.1039/C6RA16750K.
- [30] Ji Min Kim, Jung Soo Park, Tae Hwi Yoon, Junghun Park, and Ki Soo Park. Nucleic acid lateral flow assay for simultaneous detection of hygiene indicator bacteria. *Analytical and Bioanalytical Chemistry*, 413(20):5003–5011, August 2021. ISSN 1618-2642, 1618-2650. doi: 10.1007/s00216-021-03462-w.
- [31] Ioannis N. Katis, Peijun J.W. He, Robert W. Eason, and Collin L. Sones. Improved sensitivity and limit-of-detection of lateral flow devices using spatial constrictions of the flow-path. *Biosensors and Bioelectronics*, 113:95–100, August 2018. ISSN 09565663. doi: 10.1016/j.bios.2018.05.001.
- [32] Dohwan Lee, Yong Shin, Seok Chung, Kyo Seon Hwang, Dae Sung Yoon, and Jeong Hoon Lee. Simple and Highly Sensitive Molecular Diagnosis of Zika Virus by Lateral Flow Assays. *Analytical Chemistry*, 88(24):12272–12278, December 2016. ISSN 0003-2700, 1520-6882. doi: 10.1021/acs.analchem.6b03460.
- [33] Lukas Novotny and Bert Hecht. *Principles of Nano-Optics*. Cambridge University Press, second edition edition, 2012.
- [34] Bo Liedberg, Claes Nylander, and Ingemar Lunström. Surface plasmon resonance for gas detection and biosensing. *Sensors and Actuators*, 4:299–304, January 1983. ISSN 02506874. doi: 10.1016/0250-6874(83)85036-7.
- [35] Arif E. Cetin, Dordaneh Etezadi, Betty C. Galarreta, Mickael P. Busson, Yasa Eksioglu, and Hatice Altug. Plasmonic Nanohole Arrays on a Robust Hybrid Substrate for Highly Sensitive Label-Free Biosensing. *ACS Photonics*, 2(8):1167–1174, August 2015. ISSN 2330-4022, 2330-4022. doi: 10.1021/acsphotonics.5b00242.
- [36] Andreas Tittl, Aleksandrs Leitis, Mingkai Liu, Filiz Yesilkoy, Duk-Yong Choi, Dragomir N. Neshev, Yuri S. Kivshar, and Hatice Altug. Imaging-based molecular barcoding with pixelated dielectric metasurfaces. *Science*, 360(6393):1105–1109, June 2018. ISSN 0036-8075, 1095-9203. doi: 10.1126/science.aas9768.
- [37] Kathryn M. Mayer, Seunghyun Lee, Hongwei Liao, Betty C. Rostro, Amaris Fuentes, Peter T. Scully, Colleen L. Nehl, and Jason H. Hafner. A Label-Free Immunoassay Based Upon Localized Surface Plasmon Resonance of Gold Nanorods. *ACS Nano*, 2(4):687–692, April 2008. ISSN 1936-0851, 1936-086X. doi: 10.1021/nn7003734.

- [38] Irene Ament, Janak Prasad, Andreas Henkel, Sebastian Schmachtel, and Carsten Sönnichsen. Single Unlabeled Protein Detection on Individual Plasmonic Nanoparticles. *Nano Letters*, 12(2):1092–1095, February 2012. ISSN 1530-6984, 1530-6992. doi: 10.1021/nl204496g.
- [39] Jeff W Lichtman and José-Angel Conchello. Fluorescence microscopy. *Nature Methods*, 2(12):910–919, December 2005. ISSN 1548-7091, 1548-7105. doi: 10.1038/nmeth817.
- [40] M Wolman. Polarized light microscopy as a tool of diagnostic pathology. *Journal of Histochemistry & Cytochemistry*, 23(1):21–50, January 1975. ISSN 0022-1554, 1551-5044. doi: 10.1177/23.1.1090645.
- [41] Vladimir P Tychinskii. Coherent phase microscopy of intracellular processes. *Physics-Uspekhi*, 44(6):617–629, June 2001. ISSN 1063-7869, 1468-4780. doi: 10.1070/PU2001v044n06ABEH000841.
- [42] Chansuda Wongsrichanalai, Mazie J. Barcus, Sinuon Muth, Awalludin Sutamihardja, and Walther H. Wernsdorfer. A Review of Malaria Diagnostic Tools: Microscopy and Rapid Diagnostic Test (RDT). *The American Journal of Tropical Medicine and Hygiene*, 77(6_Suppl):119–127, December 2007. ISSN 0002-9637, 1476-1645. doi: 10.4269/ajtmh.2007.77.119.
- [43] R. Huisjes, W. W. Van Solinge, M. D. Levin, R. Van Wijk, and J. A. Riedl. Digital microscopy as a screening tool for the diagnosis of hereditary hemolytic anemia. *International Journal of Laboratory Hematology*, 40(2):159–168, April 2018. ISSN 1751-5521, 1751-553X. doi: 10.1111/ijlh.12758.
- [44] Senem Kamiloglu, Gulce Sari, Tugba Ozdal, and Esra Capanoglu. Guidelines for cell viability assays. *Food Frontiers*, 1(3):332–349, September 2020. ISSN 2643-8429, 2643-8429. doi: 10.1002/fft2.44.
- [45] Stefania Guida, Sabrina Longhitano, Marco Ardigò, Riccardo Pampena, Silvana Ciardo, Laura Bigi, Victor Desmond Mandel, Cristina Vaschieri, Marco Manfredini, Claudia Pezzini, Federica Arginelli, Francesca Farnetani, Nicola Zerbinati, Caterina Longo, and Giovanni Pellacani. Dermoscopy, confocal microscopy and optical coherence tomography features of main inflammatory and autoimmune skin diseases: A systematic review. *Australasian Journal of Dermatology*, 63(1):15–26, February 2022. ISSN 0004-8380, 1440-0960. doi: 10.1111/ajd.13695.
- [46] Guy Cox. *Optical Imaging Techniques in Cell Biology*. CRC Press, 2nd edition, 2012. ISBN 978-0-429-10551-7.
- [47] Euan McLeod and Aydogan Ozcan. Unconventional methods of imaging: computational microscopy and compact implementations. *Reports on Progress in Physics*, 79(7):076001, July 2016. ISSN 0034-4885, 1361-6633. doi: 10.1088/0034-4885/79/7/076001.

- [48] Mohendra Roy, Dongmin Seo, Sangwoo Oh, Ji-Woon Yang, and Sungkyu Seo. A review of recent progress in lens-free imaging and sensing. *Biosensors and Bioelectronics*, 88: 130–143, February 2017. ISSN 09565663. doi: 10.1016/j.bios.2016.07.115.
- [49] Yichen Wu and Aydogan Ozcan. Lensless digital holographic microscopy and its applications in biomedicine and environmental monitoring. *Methods*, 136:4–16, March 2018. ISSN 10462023. doi: 10.1016/j.ymeth.2017.08.013.
- [50] Peng Gao and Caojin Yuan. Resolution enhancement of digital holographic microscopy via synthetic aperture: a review. *Light: Advanced Manufacturing*, 3(1):105, 2022. ISSN 2831-4093. doi: 10.37188/lam.2022.006.
- [51] Duofang Chen, Lin Wang, Xixin Luo, Hui Xie, and Xueli Chen. Resolution and Contrast Enhancement for Lensless Digital Holographic Microscopy and Its Application in Biomedicine. *Photonics*, 9(5):358, May 2022. ISSN 2304-6732. doi: 10.3390/photonics9050358.
- [52] Tianjiao Zeng, Yanmin Zhu, and Edmund Y. Lam. Deep learning for digital holography: a review. *Optics Express*, 29(24):40572, November 2021. ISSN 1094-4087. doi: 10.1364/OE.443367.
- [53] Wenhui Zhang, Liangcai Cao, David J. Brady, Hua Zhang, Ji Cang, Hao Zhang, and Guofan Jin. Twin-Image-Free Holography: A Compressive Sensing Approach. *Physical Review Letters*, 121(9):093902, August 2018. ISSN 0031-9007, 1079-7114. doi: 10.1103/PhysRevLett.121.093902.
- [54] D. Gabor. A New Microscopic Principle. *Nature*, 161(4098):777–778, May 1948. ISSN 0028-0836, 1476-4687. doi: 10.1038/161777a0.
- [55] A. Adinda-Ougba, N. Koukourakis, N. C. Gerhardt, and M. R. Hofmann. Simple concept for a wide-field lensless digital holographic microscope using a laser diode. *Current Directions in Biomedical Engineering*, 1(1):261–264, September 2015. ISSN 2364-5504. doi: 10.1515/cdbme-2015-0065.
- [56] Onur Mudanyali, Derek Tseng, Chulwoo Oh, Serhan O. Isikman, Ikbal Sencan, Wahab Bishara, Cetin Oztoprak, Sungkyu Seo, Bahar Khademhosseini, and Aydogan Ozcan. Compact, light-weight and cost-effective microscope based on lensless incoherent holography for telemedicine applications. *Lab on a Chip*, 10(11):1417, 2010. ISSN 1473-0197, 1473-0189. doi: 10.1039/c000453g.
- [57] Zhen Xiong, Jeffrey E. Melzer, Jacob Garan, and Euan McLeod. Optimized sensing of sparse and small targets using lens-free holographic microscopy. *Optics Express*, 26(20):25676, October 2018. ISSN 1094-4087. doi: 10.1364/OE.26.025676.
- [58] Qingshan Wei, Euan McLeod, Hangfei Qi, Zhe Wan, Ren Sun, and Aydogan Ozcan. On-Chip Cytometry using Plasmonic Nanoparticle Enhanced Lensfree Holography. *Scientific Reports*, 3(1):1699, December 2013. ISSN 2045-2322. doi: 10.1038/srep01699.

- [59] Ting-Wei Su, Liang Xue, and Aydogan Ozcan. High-throughput lensfree 3D tracking of human sperms reveals rare statistics of helical trajectories. *Proceedings of the National Academy of Sciences*, 109(40):16018–16022, October 2012. ISSN 0027-8424, 1091-6490. doi: 10.1073/pnas.1212506109.
- [60] Sungkyu Seo, Serhan O. Isikman, Ikbal Sencan, Onur Mudanyali, Ting-Wei Su, Waheb Bishara, Anthony Erlinger, and Aydogan Ozcan. High-Throughput Lens-Free Blood Analysis on a Chip. *Analytical Chemistry*, 82(11):4621–4627, June 2010. ISSN 0003-2700, 1520-6882. doi: 10.1021/ac1007915.
- [61] Joseph W Goodman. *Introduction to Fourier Optics*. The McGraw-Hill Companies, 2nd edition, 2005.
- [62] Serhan O. Isikman, Ikbal Sencan, Onur Mudanyali, Waheb Bishara, Cetin Oztoprak, and Aydogan Ozcan. Color and monochrome lensless on-chip imaging of *Caenorhabditis elegans* over a wide field-of-view. *Lab on a Chip*, 10(9):1109, 2010. ISSN 1473-0197, 1473-0189. doi: 10.1039/c001200a.
- [63] Diane Coyle and Lucy Hampton. 21st century progress in computing. *Telecommunications Policy*, 48(1):102649, February 2024. ISSN 03085961. doi: 10.1016/j.telpol.2023.102649.
- [64] Waheb Bishara, Ting-Wei Su, Ahmet F. Coskun, and Aydogan Ozcan. Lensfree on-chip microscopy over a wide field-of-view using pixel super-resolution. *Optics Express*, 18(11):11181, May 2010. ISSN 1094-4087. doi: 10.1364/OE.18.011181.
- [65] C. Fournier, F. Jolivet, L. Denis, N. Verrier, E. Thiebaut, C. Allier, and T. Fournel. Pixel super-resolution in digital holography by regularized reconstruction. *Applied Optics*, 56(1):69, January 2017. ISSN 0003-6935, 1539-4522. doi: 10.1364/AO.56.000069.
- [66] Wei Luo, Alon Greenbaum, Yibo Zhang, and Aydogan Ozcan. Synthetic aperture-based on-chip microscopy. *Light: Science & Applications*, 4(3):e261–e261, March 2015. ISSN 2047-7538. doi: 10.1038/lisa.2015.34.
- [67] Maryam Baker, Weilin Liu, and Euan McLeod. Accurate and fast modeling of scattering from random arrays of nanoparticles using the discrete dipole approximation and angular spectrum method. *Optics Express*, 29(14):22761, July 2021. ISSN 1094-4087. doi: 10.1364/OE.431754.
- [68] Emilio Sánchez-Ortiga, Ana Doblas, Genaro Saavedra, Manuel Martínez-Corral, and Jorge Garcia-Sucerquia. Off-axis digital holographic microscopy: practical design parameters for operating at diffraction limit. *Applied Optics*, 53(10):2058, April 2014. ISSN 1559-128X, 2155-3165. doi: 10.1364/AO.53.002058.
- [69] Zhengzhong Huang, Pasquale Memmolo, Pietro Ferraro, and Liangcai Cao. Dual-plane coupled phase retrieval for non-prior holographic imaging. *Photonix*, 3(1):3, January 2022. ISSN 2662-1991. doi: 10.1186/s43074-021-00046-w.

- [70] Xuejuan Wu, Jiasong Sun, Jialin Zhang, Linpeng Lu, Rong Chen, Qian Chen, and Chao Zuo. Wavelength-scanning lensfree on-chip microscopy for wide-field pixel-super-resolved quantitative phase imaging. *Optics Letters*, 46(9):2023, May 2021. ISSN 0146-9592, 1539-4794. doi: 10.1364/OL.421869.
- [71] Onur Mudanyali, Cetin Oztoprak, Derek Tseng, Anthony Erlinger, and Aydogan Ozcan. Detection of waterborne parasites using field-portable and cost-effective lensfree microscopy. *Lab on a Chip*, 10(18):2419, 2010. ISSN 1473-0197, 1473-0189. doi: 10.1039/c004829a.
- [72] Manon Rostykus, Ferréol Soulez, Michael Unser, and Christophe Moser. Compact in-line lensfree digital holographic microscope. *Methods*, 136:17–23, March 2018. ISSN 10462023. doi: 10.1016/j.ymeth.2017.11.008.
- [73] Nassir Navab, Joachim Hornegger, William M. Wells, and Alejandro F. Frangi, editors. *Medical Image Computing and Computer-Assisted Intervention – MICCAI 2015: 18th International Conference, Munich, Germany, October 5-9, 2015, Proceedings, Part III*, volume 9351 of *Lecture Notes in Computer Science*. Springer International Publishing, Cham, 2015. ISBN 978-3-319-24573-7 978-3-319-24574-4. doi: 10.1007/978-3-319-24574-4.
- [74] Tomi Pitkäaho, Aki Manninen, and Thomas J. Naughton. Focus prediction in digital holographic microscopy using deep convolutional neural networks. *Applied Optics*, 58(5):A202, February 2019. ISSN 1559-128X, 2155-3165. doi: 10.1364/AO.58.00A202.
- [75] Colin J. Potter, Yanmei Hu, Zhen Xiong, Jun Wang, and Euan McLeod. Point-of-care SARS-CoV-2 sensing using lens-free imaging and a deep learning-assisted quantitative agglutination assay. *Lab on a Chip*, 22(19):3744–3754, 2022. ISSN 1473-0197, 1473-0189. doi: 10.1039/D2LC00289B.
- [76] Rajkumar Vaghashiya, Sanghoon Shin, Varun Chauhan, Kaushal Kapadiya, Smit Sanghavi, Sungkyu Seo, and Mohendra Roy. Machine Learning Based Lens-Free Shadow Imaging Technique for Field-Portable Cytometry. *Biosensors*, 12(3):144, February 2022. ISSN 2079-6374. doi: 10.3390/bios12030144.
- [77] Olaf Ronneberger, Philipp Fischer, and Thomas Brox. U-Net: Convolutional Networks for Biomedical Image Segmentation, May 2015. arXiv:1505.04597 [cs].
- [78] Zhenxiang Luo, Abdulkadir Yurt, Richard Stahl, Andy Lambrechts, Veerle Reumers, Dries Braeken, and Liesbet Lagae. Pixel super-resolution for lens-free holographic microscopy using deep learning neural networks. *Optics Express*, 27(10):13581, May 2019. ISSN 1094-4087. doi: 10.1364/OE.27.013581.
- [79] Luzhe Huang, Tairan Liu, Xilin Yang, Yi Luo, Yair Rivenson, and Aydogan Ozcan. Holographic Image Reconstruction with Phase Recovery and Autofocusing Using Recurrent Neural Networks. *ACS Photonics*, 8(6):1763–1774, June 2021. ISSN 2330-4022, 2330-4022. doi: 10.1021/acsphotonics.1c00337.

- [80] Yair Rivenson, Tairan Liu, Zhensong Wei, Yibo Zhang, Kevin De Haan, and Aydogan Ozcan. PhaseStain: the digital staining of label-free quantitative phase microscopy images using deep learning. *Light: Science & Applications*, 8(1):23, February 2019. ISSN 2047-7538. doi: 10.1038/s41377-019-0129-y.
- [81] Muhammed Ali Pala, Murat Erhan Çimen, Akif Akgül, Mustafa Zahid Yıldız, and Ali Fuat Boz. Fractal dimension-based viability analysis of cancer cell lines in lens-free holographic microscopy via machine learning. *The European Physical Journal Special Topics*, 231(5):1023–1034, June 2022. ISSN 1951-6355, 1951-6401. doi: 10.1140/epjs/s11734-021-00342-3.
- [82] Cédric Allier, Lionel Hervé, Chiara Paviolo, Ondrej Mandula, Olivier Cioni, William Pierré, Francesca Andriani, Kiran Padmanabhan, and Sophie Morales. CNN-Based Cell Analysis: From Image to Quantitative Representation. *Frontiers in Physics*, 9: 776805, January 2022. ISSN 2296-424X. doi: 10.3389/fphy.2021.776805.
- [83] Hongying Zhu, Oguzhan Yaglidere, Ting-Wei Su, Derek Tseng, and Aydogan Ozcan. Cost-effective and compact wide-field fluorescent imaging on a cell-phone. *Lab Chip*, 11(2):315–322, 2011. ISSN 1473-0197, 1473-0189. doi: 10.1039/C0LC00358A.
- [84] Jose C. Contreras-Naranjo, Qingshan Wei, and Aydogan Ozcan. Mobile Phone-Based Microscopy, Sensing, and Diagnostics. *IEEE Journal of Selected Topics in Quantum Electronics*, 22(3):1–14, May 2016. ISSN 1077-260X, 1558-4542. doi: 10.1109/JSTQE.2015.2478657.
- [85] Weiqiang Zheng, Juan Wang, Yunhong Zhou, Qiang Zeng, Cheng Zhang, Li Liu, Hui Yu, and Yuting Yang. Lensless holographic microscope with a time and memory-saving algorithm for large-volume imaging of organoids. *Optics Letters*, 48(3):771, February 2023. ISSN 0146-9592, 1539-4794. doi: 10.1364/OL.481627.
- [86] Alon Greenbaum, Yibo Zhang, Alborz Feizi, Ping-Luen Chung, Wei Luo, Shivani R. Kandukuri, and Aydogan Ozcan. Wide-field computational imaging of pathology slides using lens-free on-chip microscopy. *Science Translational Medicine*, 6(267), December 2014. ISSN 1946-6234, 1946-6242. doi: 10.1126/scitranslmed.3009850.
- [87] Yibo Zhang, Tairan Liu, Yujia Huang, Da Teng, Yinxu Bian, Yichen Wu, Yair Rivenson, Alborz Feizi, and Aydogan Ozcan. Accurate color imaging of pathology slides using holography and absorbance spectrum estimation of histochemical stains. *Journal of Biophotonics*, 12(3):e201800335, March 2019. ISSN 1864-063X, 1864-0648. doi: 10.1002/jbio.201800335.
- [88] Guang Zeng, Jiahui He, and Wenjian Qin. Wide-Field Pixel Super-Resolution Colour Lensfree Microscope for Digital Pathology. *Frontiers in Oncology*, 11:751223, October 2021. ISSN 2234-943X. doi: 10.3389/fonc.2021.751223.
- [89] Tairan Liu, Zhensong Wei, Yair Rivenson, Kevin De Haan, Yibo Zhang, Yichen Wu, and Aydogan Ozcan. Deep learning-based color holographic microscopy. *Journal of*

- Biophotonics*, 12(11):e201900107, November 2019. ISSN 1864-063X, 1864-0648. doi: 10.1002/jbio.201900107.
- [90] Hua Shen and Jinming Gao. Deep learning virtual colorful lens-free on-chip microscopy. *Chinese Optics Letters*, 18(12):121705, 2020. ISSN 1671-7694. doi: 10.3788/COL202018.121705.
- [91] Cheng Guo, Xianming Liu, Xingchi Kan, Feilong Zhang, Jiubin Tan, Shutian Liu, and Zhengjun Liu. Lensfree on-chip microscopy based on dual-plane phase retrieval. *Optics Express*, 27(24):35216, November 2019. ISSN 1094-4087. doi: 10.1364/OE.27.035216.
- [92] Cheng Guo, Xianming Liu, Xingchi Kan, Feilong Zhang, Jiubin Tan, Shutian Liu, Cuimei Tan, and Zhengjun Liu. Artifactless, lens-free coherent microscopy with quasi-3D scanning. *Measurement Science and Technology*, 31(4):045402, April 2020. ISSN 0957-0233, 1361-6501. doi: 10.1088/1361-6501/ab5757.
- [93] Cheng Guo, Feilong Zhang, Xiaoqing Zhang, Xingchi Kan, Jiubin Tan, Shutian Liu, and Zhengjun Liu. Lensfree super-resolved imaging based on adaptive Wiener filter and guided phase retrieval algorithm. *Journal of Optics*, 22(5):055703, May 2020. ISSN 2040-8978, 2040-8986. doi: 10.1088/2040-8986/ab8287.
- [94] Yibo Zhang, Hongda Wang, Yichen Wu, Miu Tamamitsu, and Aydogan Ozcan. Edge sparsity criterion for robust holographic autofocusing. *Optics Letters*, 42(19):3824, October 2017. ISSN 0146-9592, 1539-4794. doi: 10.1364/OL.42.003824.
- [95] Yichen Wu, Yair Rivenson, Yibo Zhang, Zhensong Wei, Harun Günaydin, Xing Lin, and Aydogan Ozcan. Extended depth-of-field in holographic imaging using deep-learning-based autofocusing and phase recovery. *Optica*, 5(6):704, June 2018. ISSN 2334-2536. doi: 10.1364/OPTICA.5.000704.
- [96] Yair Rivenson, Yibo Zhang, Harun Günaydin, Da Teng, and Aydogan Ozcan. Phase recovery and holographic image reconstruction using deep learning in neural networks. *Light: Science & Applications*, 7(2):17141–17141, February 2018. ISSN 2047-7538. doi: 10.1038/lsa.2017.141.
- [97] Hanlong Chen, Luzhe Huang, Tairan Liu, and Aydogan Ozcan. Fourier Imager Network (FIN): A deep neural network for hologram reconstruction with superior external generalization. *Light: Science & Applications*, 11(1):254, August 2022. ISSN 2047-7538. doi: 10.1038/s41377-022-00949-8.
- [98] Tairan Liu, Kevin De Haan, Yair Rivenson, Zhensong Wei, Xin Zeng, Yibo Zhang, and Aydogan Ozcan. Deep learning-based super-resolution in coherent imaging systems. *Scientific Reports*, 9(1):3926, March 2019. ISSN 2045-2322. doi: 10.1038/s41598-019-40554-1.
- [99] F. Momey, A. Berdeu, T. Bordy, J.-M. Dinten, F. Kermarrec Marcel, N. Picollet-D’ahan, X. Gidrol, and C. Allier. Lensfree diffractive tomography for the imaging of 3D cell cultures. *Biomedical Optics Express*, 7(3):949, March 2016. ISSN 2156-7085, 2156-7085. doi: 10.1364/BOE.7.000949.

- [100] Yibo Zhang, Yoonjung Shin, Kevin Sung, Sam Yang, Harrison Chen, Hongda Wang, Da Teng, Yair Rivenson, Rajan P. Kulkarni, and Aydogan Ozcan. 3D imaging of optically cleared tissue using a simplified CLARITY method and on-chip microscopy. *Science Advances*, 3(8):e1700553, August 2017. ISSN 2375-2548. doi: 10.1126/sciadv.1700553.
- [101] Jose Angel Picazo-Bueno, Karina Trindade, Martin Sanz, and Vicente Micó. Design, Calibration, and Application of a Robust, Cost-Effective, and High-Resolution Lensless Holographic Microscope. *Sensors*, 22(2):553, January 2022. ISSN 1424-8220. doi: 10.3390/s22020553.
- [102] Maria J. Lopera and Carlos Trujillo. Linear diattenuation imaging of biological samples with digital lensless holographic microscopy. *Applied Optics*, 61(5):B77, February 2022. ISSN 1559-128X, 2155-3165. doi: 10.1364/AO.440376.
- [103] Yibo Zhang, Seung Yoon Celine Lee, Yun Zhang, Daniel Furst, John Fitzgerald, and Aydogan Ozcan. Wide-field imaging of birefringent synovial fluid crystals using lens-free polarized microscopy for gout diagnosis. *Scientific Reports*, 6(1):28793, June 2016. ISSN 2045-2322. doi: 10.1038/srep28793.
- [104] Tairan Liu, Kevin de Haan, Bijie Bai, Yair Rivenson, Yi Luo, Hongda Wang, David Karalli, Hongxiang Fu, Yibo Zhang, John FitzGerald, and Aydogan Ozcan. Deep Learning-Based Holographic Polarization Microscopy. *ACS Photonics*, 7(11):3023–3034, November 2020. ISSN 2330-4022, 2330-4022. doi: 10.1021/acsp Photonics.0c01051.
- [105] Jessica Kun, Marek Smieja, Bo Xiong, Leyla Soleymani, and Qiyin Fang. The Use of Motion Analysis as Particle Biomarkers in Lensless Optofluidic Projection Imaging for Point of Care Urine Analysis. *Scientific Reports*, 9(1):17255, November 2019. ISSN 2045-2322. doi: 10.1038/s41598-019-53477-8.
- [106] Carolina Pacheco, Gregory N. McKay, Anisha Oommen, Nicholas J. Durr, René Vidal, and Benjamin D. Haeffele. Adaptive sparse reconstruction for lensless digital holography via PSF estimation and phase retrieval. *Optics Express*, 30(19):33433, September 2022. ISSN 1094-4087. doi: 10.1364/OE.458360.
- [107] Gregory N. McKay, Anisha Oommen, Carolina Pacheco, Mason T. Chen, Stuart C. Ray, Rene Vidal, Benjamin D. Haeffele, and Nicholas J. Durr. Lens Free Holographic Imaging for Urinary Tract Infection Screening. *IEEE Transactions on Biomedical Engineering*, 70(3):1053–1061, March 2023. ISSN 0018-9294, 1558-2531. doi: 10.1109/TBME.2022.3208220.
- [108] Robin Delacroix, Sophie Nhu An Morel, Lionel Hervé, Thomas Bordy, Jean-Marc Dinten, Michel Drancourt, and Cédric Allier. Cerebrospinal fluid lens-free microscopy: a new tool for the laboratory diagnosis of meningitis. *Scientific Reports*, 7(1):39893, January 2017. ISSN 2045-2322. doi: 10.1038/srep39893.
- [109] Morteza Khaleghi, Cosme Furlong, Mike Ravicz, Jeffrey Tao Cheng, and John J. Rosowski. Three-dimensional vibrometry of the human eardrum with stroboscopic

- lensless digital holography. *Journal of Biomedical Optics*, 20(5):051028, February 2015. ISSN 1083-3668. doi: 10.1117/1.JBO.20.5.051028.
- [110] Maryam Baker, Florian Gollier, Jeffrey E. Melzer, and Euan McLeod. Lensfree Air-Quality Monitoring of Fine and Ultrafine Particulate Matter Using Vapor-Condensed Nanolenses. *ACS Applied Nano Materials*, 6(13):11166–11174, July 2023. ISSN 2574-0970, 2574-0970. doi: 10.1021/acsanm.3c01154.
- [111] Piotr Arcab, Mikołaj Rogalski, and Maciej Trusiak. Single-shot experimental-numerical twin-image removal in lensless digital holographic microscopy. *Optics and Lasers in Engineering*, 172:107878, January 2024. ISSN 01438166. doi: 10.1016/j.optlaseng.2023.107878.
- [112] Yuqian Li, Bruno Cornelis, Alexandra Dusa, Geert Vanmeerbeeck, Dries Vercruysse, Erik Sohn, Kamil Blaszkiewicz, Dimitar Prodanov, Peter Schelkens, and Liesbet Lagae. Accurate label-free 3-part leukocyte recognition with single cell lens-free imaging flow cytometry. *Computers in Biology and Medicine*, 96:147–156, May 2018. ISSN 00104825. doi: 10.1016/j.compbiomed.2018.03.008.
- [113] Stephan Amann, Max Von Witzleben, and Stefan Breuer. 3D-printable portable open-source platform for low-cost lens-less holographic cellular imaging. *Scientific Reports*, 9(1):11260, August 2019. ISSN 2045-2322. doi: 10.1038/s41598-019-47689-1.
- [114] Heberley Tobon-Maya, Samuel Zapata-Valencia, Erick Zora-Guzmán, Carlos Buitrago-Duque, and Jorge Garcia-Sucerquia. Open-source, cost-effective, portable, 3D-printed digital lensless holographic microscope. *Applied Optics*, 60(4):A205, February 2021. ISSN 1559-128X, 2155-3165. doi: 10.1364/AO.405605.
- [115] Carlos Buitrago-Duque, Brayán Patiño-Jurado, and Jorge Garcia-Sucerquia. Robust and compact digital Lensless Holographic microscope for Label-Free blood smear imaging. *HardwareX*, 13:e00408, March 2023. ISSN 24680672. doi: 10.1016/j.ohx.2023.e00408.
- [116] Brayán Patiño-Jurado, Juan F. Botero-Cadavid, and Jorge Garcia-Sucerquia. Cone-shaped optical fiber tip for cost-effective digital lensless holographic microscopy. *Applied Optics*, 59(10):2969, April 2020. ISSN 1559-128X, 2155-3165. doi: 10.1364/AO.384208.
- [117] Maria J. Lopera and Carlos Trujillo. Holographic point source for digital lensless holographic microscopy. *Optics Letters*, 47(11):2862, June 2022. ISSN 0146-9592, 1539-4794. doi: 10.1364/OL.459146.
- [118] Antonio C Sobieranski, Fatih Inci, H Cumhur Tekin, Mehmet Yuksekkaya, Eros Comunello, Daniel Cobra, Aldo Von Wangenheim, and Utkan Demirci. Portable lensless wide-field microscopy imaging platform based on digital inline holography and multi-frame pixel super-resolution. *Light: Science & Applications*, 4(10):e346–e346, October 2015. ISSN 2047-7538. doi: 10.1038/lssa.2015.119.

- [119] Waheb Bishara, Uzair Sikora, Onur Mudanyali, Ting-Wei Su, Oguzhan Yaglidere, Shirley Luckhart, and Aydogan Ozcan. Holographic pixel super-resolution in portable lensless on-chip microscopy using a fiber-optic array. *Lab on a Chip*, 11(7):1276, 2011. ISSN 1473-0197, 1473-0189. doi: 10.1039/c0lc00684j.
- [120] Yuan Fang, Ningmei Yu, and Yuquan Jiang. Super-Resolution Lensless Imaging of Cells Using Brownian Motion. *Applied Sciences*, 9(10):2080, May 2019. ISSN 2076-3417. doi: 10.3390/app9102080.
- [121] Hanu Phani Ram Gurram, Ashwini S. Galande, and Renu John. Nanometric depth phase imaging using low-cost on-chip lensless inline holographic microscopy. *Optical Engineering*, 59(10), October 2020. ISSN 0091-3286. doi: 10.1117/1.OE.59.10.104105.
- [122] Yuncong Huang, Miaomiao Zhu, Lihong Ma, and Wen Zhang. Accurate and fast registration algorithm for multi-height lensless in-line on-chip holographic microscopy. *Optics Communications*, 526:128898, January 2023. ISSN 00304018. doi: 10.1016/j.optcom.2022.128898.
- [123] Martín Sanz, José Angel Picazo-Bueno, Javier García, and Vicente Micó. Improved quantitative phase imaging in lensless microscopy by single-shot multi-wavelength illumination using a fast convergence algorithm. *Optics Express*, 23(16):21352, August 2015. ISSN 1094-4087. doi: 10.1364/OE.23.021352.
- [124] Martín Sanz, José Ángel Picazo-Bueno, Luis Granero, Javier García, and Vicente Micó. Compact, cost-effective and field-portable microscope prototype based on MISHELF microscopy. *Scientific Reports*, 7(1):43291, February 2017. ISSN 2045-2322. doi: 10.1038/srep43291.
- [125] M. Sanz, J. A. Picazo-Bueno, J. García, and V. Micó. Dual-mode holographic microscopy imaging platform. *Lab on a Chip*, 18(7):1105–1112, 2018. ISSN 1473-0197, 1473-0189. doi: 10.1039/C7LC01304C.
- [126] Yuan Fang, Ningmei Yu, Yuquan Jiang, and Chaoliang Dang. High-Precision Lensless Flow Cytometer on a Chip. *Micromachines*, 9(5):227, May 2018. ISSN 2072-666X. doi: 10.3390/mi9050227.
- [127] Bruno Cornelis, David Blinder, Bart Jansen, Liesbet Lagae, and Peter Schelkens. Fast and robust Fourier domain-based classification for on-chip lens-free flow cytometry. *Optics Express*, 26(11):14329, May 2018. ISSN 1094-4087. doi: 10.1364/OE.26.014329.
- [128] DaeHan Ahn, JiYeong Lee, SangJun Moon, and Taejoon Park. Human-level blood cell counting on lens-free shadow images exploiting deep neural networks. *The Analyst*, 143(22):5380–5387, 2018. ISSN 0003-2654, 1364-5528. doi: 10.1039/C8AN01056K.
- [129] Xiwei Huang, Yangbo Li, Xuefeng Xu, Renjie Wang, Jiangfan Yao, Wentao Han, Maoyu Wei, Jin Chen, Weipeng Xuan, and Lingling Sun. High-Precision Lensless Microscope on a Chip Based on In-Line Holographic Imaging. *Sensors*, 21(3):720, January 2021. ISSN 1424-8220. doi: 10.3390/s21030720.

- [130] Timothy O'Connor, Christopher Hawxhurst, Leslie M. Shor, and Bahram Javidi. Red blood cell classification in lensless single random phase encoding using convolutional neural networks. *Optics Express*, 28(22):33504, October 2020. ISSN 1094-4087. doi: 10.1364/OE.405563.
- [131] Yibo Zhang, Mengxing Ouyang, Aniruddha Ray, Tairan Liu, Janay Kong, Bijie Bai, Donghyuk Kim, Alexander Guziak, Yi Luo, Alborz Feizi, Katherine Tsai, Zhuoran Duan, Xuewei Liu, Danny Kim, Chloe Cheung, Sener Yalcin, Hatice Ceylan Koydemir, Omai B. Garner, Dino Di Carlo, and Aydogan Ozcan. Computational cytometer based on magnetically modulated coherent imaging and deep learning. *Light: Science & Applications*, 8(1):91, October 2019. ISSN 2047-7538. doi: 10.1038/s41377-019-0203-5.
- [132] Dries Vercruyssen, Alexandra Dusa, Richard Stahl, Geert Vanmeerbeeck, Koen De Wijs, Chengxun Liu, Dimitar Prodanov, Peter Peumans, and Liesbet Lagae. Three-part differential of unlabeled leukocytes with a compact lens-free imaging flow cytometer. *Lab on a Chip*, 15(4):1123–1132, 2015. ISSN 1473-0197, 1473-0189. doi: 10.1039/C4LC01131G.
- [133] Dongmin Seo, Sangwoo Oh, Moonjin Lee, Yongha Hwang, and Sungkyu Seo. A Field-Portable Cell Analyzer without a Microscope and Reagents. *Sensors*, 18(2):85, December 2017. ISSN 1424-8220. doi: 10.3390/s18010085.
- [134] Gao Huang, Zhuang Liu, Geoff Pleiss, Laurens Van Der Maaten, and Kilian Q. Weinberger. Convolutional Networks with Dense Connectivity. *IEEE Transactions on Pattern Analysis and Machine Intelligence*, 44(12):8704–8716, May 2019. ISSN 0162-8828, 2160-9292, 1939-3539. doi: 10.1109/TPAMI.2019.2918284.
- [135] Tairan Liu, Yuzhu Li, Hatice Ceylan Koydemir, Yijie Zhang, Ethan Yang, Merve Eryilmaz, Hongda Wang, Jingxi Li, Bijie Bai, Guangdong Ma, and Aydogan Ozcan. Rapid and stain-free quantification of viral plaque via lens-free holography and deep learning. *Nature Biomedical Engineering*, 7(8):1040–1052, June 2023. ISSN 2157-846X. doi: 10.1038/s41551-023-01057-7.
- [136] Sungkyu Seo, Ting-Wei Su, Derek K. Tseng, Anthony Erlinger, and Aydogan Ozcan. Lensfree holographic imaging for on-chip cytometry and diagnostics. *Lab Chip*, 9(6):777–787, 2009. ISSN 1473-0197, 1473-0189. doi: 10.1039/B813943A.
- [137] Temitope E. Agbana, Hai Gong, Abena S. Amoah, Vitaly Bezzubik, Michel Verhaegen, and Gleb Vdovin. Aliasing, coherence, and resolution in a lensless holographic microscope. *Optics Letters*, 42(12):2271, June 2017. ISSN 0146-9592, 1539-4794. doi: 10.1364/OL.42.002271.
- [138] Yibo Zhang, Hatice Ceylan Koydemir, Michelle M. Shimogawa, Sener Yalcin, Alexander Guziak, Tairan Liu, Ilker Oguz, Yujia Huang, Bijie Bai, Yilin Luo, Yi Luo, Zhen-song Wei, Hongda Wang, Vittorio Bianco, Bohan Zhang, Rohan Nadkarni, Kent Hill, and Aydogan Ozcan. Motility-based label-free detection of parasites in bodily fluids using holographic speckle analysis and deep learning. *Light: Science & Applications*, 7(1):108, December 2018. ISSN 2047-7538. doi: 10.1038/s41377-018-0110-1.

- [139] Camila De Paula DAlmeida, Kamila Jessie Sammarro Silva, Lyda Patricia Sabogal-Paz, and Sebastião Pratavieira. Label-free detection and quantification of *Giardia duodenalis* cysts using a lens-free microscope. *Journal of Environmental Chemical Engineering*, 11(5):110932, October 2023. ISSN 22133437. doi: 10.1016/j.jece.2023.110932.
- [140] Eugene Serabyn, Kurt Liewer, Chris Lindensmith, Kent Wallace, and Jay Nadeau. Compact, lensless digital holographic microscope for remote microbiology. *Optics Express*, 24(25):28540, December 2016. ISSN 1094-4087. doi: 10.1364/OE.24.028540.
- [141] Samira Ebrahimi and Masoomeh Dashtdar. Lens-free digital holographic microscopy for cell imaging and tracking by Fresnel diffraction from a phase discontinuity. *Optics Letters*, 46(15):3516, August 2021. ISSN 0146-9592, 1539-4794. doi: 10.1364/OL.426588.
- [142] Manon Rostykus and Christophe Moser. Compact lensless off-axis transmission digital holographic microscope. *Optics Express*, 25(14):16652, July 2017. ISSN 1094-4087. doi: 10.1364/OE.25.016652.
- [143] Aniruddha Ray, Mustafa Ugur Daloglu, Joslynn Ho, Avee Torres, Euan Mcleod, and Aydogan Ozcan. Computational sensing of herpes simplex virus using a cost-effective on-chip microscope. *Scientific Reports*, 7(1):4856, December 2017. ISSN 2045-2322. doi: 10.1038/s41598-017-05124-3.
- [144] Onur Mudanyali, Euan McLeod, Wei Luo, Alon Greenbaum, Ahmet F. Coskun, Yves Hennequin, Cédric P. Allier, and Aydogan Ozcan. Wide-field optical detection of nanoparticles using on-chip microscopy and self-assembled nanolenses. *Nature Photonics*, 7(3):247–254, March 2013. ISSN 1749-4885, 1749-4893. doi: 10.1038/nphoton.2012.337.
- [145] Aniruddha Ray, Muhammad Arslan Khalid, Andriejus Demčenko, Mustafa Daloglu, Derek Tseng, Julien Reboud, Jonathan M. Cooper, and Aydogan Ozcan. Holographic detection of nanoparticles using acoustically actuated nanolenses. *Nature Communications*, 11(1):171, December 2020. ISSN 2041-1723. doi: 10.1038/s41467-019-13802-1.
- [146] Hongda Wang, Hatice Ceylan Koydemir, Yunzhe Qiu, Bijie Bai, Yibo Zhang, Yiyin Jin, Sabiha Tok, Enis Cagatay Yilmaz, Esin Gumustekin, Yair Rivenson, and Aydogan Ozcan. Early detection and classification of live bacteria using time-lapse coherent imaging and deep learning. *Light: Science & Applications*, 9(1):118, December 2020. ISSN 2047-7538. doi: 10.1038/s41377-020-00358-9.
- [147] Prisca Perlemino, Pierre R. Marcoux, Emmanuel Picard, Emmanuel Hadji, Marc Zelsmann, Grégoire Mugnier, Aurélie Marchet, Grégoire Resch, Larry O’Connell, and Eric Lacot. Phage susceptibility testing and infectious titer determination through wide-field lensless monitoring of phage plaque growth. *PLOS ONE*, 16(3):e0248917, March 2021. ISSN 1932-6203. doi: 10.1371/journal.pone.0248917.

- [148] Muhammed Veli and Aydogan Ozcan. Computational Sensing of *Staphylococcus aureus* on Contact Lenses Using 3D Imaging of Curved Surfaces and Machine Learning. *ACS Nano*, 12(3):2554–2559, March 2018. ISSN 1936-0851, 1936-086X. doi: 10.1021/acsnano.7b08375.
- [149] Yichen Wu, Aniruddha Ray, Qingshan Wei, Alborz Feizi, Xin Tong, Eva Chen, Yi Luo, and Aydogan Ozcan. Deep Learning Enables High-Throughput Analysis of Particle-Aggregation-Based Biosensors Imaged Using Holography. *ACS Photonics*, 6(2):294–301, February 2019. ISSN 2330-4022, 2330-4022. doi: 10.1021/acsp Photonics.8b01479.
- [150] Frederik Colle, Dries Vercruyssen, Sara Peeters, Chengxun Liu, Tim Stakenborg, Liesbet Lagae, and Jurgen Del-Favero. Lens-free imaging of magnetic particles in DNA assays. *Lab on a Chip*, 13(21):4257, 2013. ISSN 1473-0197, 1473-0189. doi: 10.1039/c3lc50707f.
- [151] Anthony Berdeu, Bastien Laperrousaz, Thomas Bordy, Ondrej Mandula, Sophie Morales, Xavier Gidrol, Nathalie Picollet-D’hahan, and Cédric Allier. Lens-free microscopy for 3D + time acquisitions of 3D cell culture. *Scientific Reports*, 8(1):16135, October 2018. ISSN 2045-2322. doi: 10.1038/s41598-018-34253-6.
- [152] Anthony Berdeu, Fabien Momey, Bastien Laperrousaz, Thomas Bordy, Xavier Gidrol, Jean-Marc Dinten, Nathalie Picollet-D’hahan, and Cédric Allier. Comparative study of fully three-dimensional reconstruction algorithms for lens-free microscopy. *Applied Optics*, 56(13):3939, May 2017. ISSN 0003-6935, 1539-4522. doi: 10.1364/AO.56.003939.
- [153] Gregor Scholz, Shinta Mariana, Agus Dharmawan, Iqbal Syamsu, Philipp Hörmann, Carsten Reuse, Jana Hartmann, Karsten Hiller, Joan Prades, Hutomo Wasisto, and Andreas Waag. Continuous Live-Cell Culture Imaging and Single-Cell Tracking by Computational Lensfree LED Microscopy. *Sensors*, 19(5):1234, March 2019. ISSN 1424-8220. doi: 10.3390/s19051234.
- [154] Lamya Ghenim, Cédric Allier, Patricia Obeid, Lionel Hervé, Jean-Yves Fortin, Maxim Balakirev, and Xavier Gidrol. A new ultradian rhythm in mammalian cell dry mass observed by holography. *Scientific Reports*, 11(1):1290, January 2021. ISSN 2045-2322. doi: 10.1038/s41598-020-79661-9.
- [155] Srikanth V. Kesavan, Fabrice P. Navarro Y Garcia, Mathilde Menneteau, Frédérique Mittler, Brigitte David-Watine, Nelly Dubrulle, Spencer L. Shorte, Bernard Chalmond, Jean-Marc Dinten, and Cédric P. Allier. Real-time label-free detection of dividing cells by means of lensfree video-microscopy. *Journal of Biomedical Optics*, 19(03):1, March 2014. ISSN 1083-3668. doi: 10.1117/1.JBO.19.3.036004.
- [156] Agus Budi Dharmawan, Shinta Mariana, Gregor Scholz, Philipp Hörmann, Torben Schulze, Kuwat Triyana, Mayra Garcés-Schröder, Ingo Rustenbeck, Karsten Hiller, Hutomo Suryo Wasisto, and Andreas Waag. Nonmechanical parfocal and autofocus features based on wave propagation distribution in lensfree holographic microscopy. *Scientific Reports*, 11(1):3213, February 2021. ISSN 2045-2322. doi: 10.1038/s41598-021-81098-7.

- [157] Ivan Pushkarsky, Yunbo Liu, Westbrook Weaver, Ting-Wei Su, Onur Mudanyali, Aydogan Ozcan, and Dino Di Carlo. Automated single-cell motility analysis on a chip using lensfree microscopy. *Scientific Reports*, 4(1):4717, April 2014. ISSN 2045-2322. doi: 10.1038/srep04717.
- [158] C. Allier, S. Morel, R. Vincent, L. Ghenim, F. Navarro, M. Menneteau, T. Bordy, L. Hervé, O. Cioni, X. Gidrol, Y. Usson, and J.-M. Dinten. Imaging of dense cell cultures by multiwavelength lens-free video microscopy: Cell Cultures by Lens-Free Microscopy. *Cytometry Part A*, 91(5):433–442, May 2017. ISSN 15524922. doi: 10.1002/cyto.a.23079.
- [159] Cedric Allier, Romaric Vincent, Fabrice Navarro, Mathilde Menneteau, Lamya Ghenim, Xavier Gidrol, Thomas Bordy, Lionel Hervé, Olivier Cioni, Sabine Bardin, Michel Bornens, Yves Usson, and Sophie Morales. Lens-free Video Microscopy for the Dynamic and Quantitative Analysis of Adherent Cell Culture. *Journal of Visualized Experiments*, (132):56580, February 2018. ISSN 1940-087X. doi: 10.3791/56580.
- [160] Bartosz Mirecki, Mikołaj Rogalski, Piotr Arcab, Piotr Rogujski, Luiza Stanaszek, Michał Józwiak, and Maciej Trusiak. Low-intensity illumination for lensless digital holographic microscopy with minimized sample interaction. *Biomedical Optics Express*, 13(11):5667, November 2022. ISSN 2156-7085, 2156-7085. doi: 10.1364/BOE.464367.
- [161] Guoxiao Li, Rongbiao Zhang, Ning Yang, Changsheng Yin, Mingji Wei, Yecheng Zhang, and Jian Sun. An approach for cell viability online detection based on the characteristics of lensfree cell diffraction fingerprint. *Biosensors and Bioelectronics*, 107:163–169, June 2018. ISSN 09565663. doi: 10.1016/j.bios.2018.01.047.
- [162] Md Alamgir Kabir, Ashish Kharel, Saloni Malla, Zachary Joseph Kreis, Peuli Nath, Jared Neil Wolfe, Marwa Hassan, Devinder Kaur, Hamed Sari-Sarraf, Amit K. Tiwari, and Aniruddha Ray. Automated detection of apoptotic versus nonapoptotic cell death using label-free computational microscopy. *Journal of Biophotonics*, 15(4), April 2022. ISSN 1864-063X, 1864-0648. doi: 10.1002/jbio.202100310.
- [163] Maria Falek Miniotis, Anthony Mukwaya, and Anette Gjørloff Wingren. Digital Holographic Microscopy for Non-Invasive Monitoring of Cell Cycle Arrest in L929 Cells. *PLoS ONE*, 9(9):e106546, September 2014. ISSN 1932-6203. doi: 10.1371/journal.pone.0106546.
- [164] Rostislav Boltyanskiy, Mary Ann Odete, Fook Chiong Cheong, and Laura A. Philips. Label-free viability assay using in-line holographic video microscopy. *Scientific Reports*, 12(1):12746, July 2022. ISSN 2045-2322. doi: 10.1038/s41598-022-17098-y.
- [165] Kerem Delikoyun, Sena Yaman, Esra Yilmaz, Oyku Sarigil, Muge Anil-Inevi, Kubra Telli, Ozden Yalcin-Ozuysal, Engin Ozcivici, and H. Cumhuri Tekin. HologLev: A Hybrid Magnetic Levitation Platform Integrated with Lensless Holographic Microscopy for Density-Based Cell Analysis. *ACS Sensors*, 6(6):2191–2201, June 2021. ISSN 2379-3694, 2379-3694. doi: 10.1021/acssensors.0c02587.

- [166] Mingjun Wang, Shaodong Feng, and Jigang Wu. Multilayer pixel super-resolution lensless in-line holographic microscope with random sample movement. *Scientific Reports*, 7(1):12791, October 2017. ISSN 2045-2322. doi: 10.1038/s41598-017-13134-4.
- [167] Serhan O. Isikman, Alon Greenbaum, Wei Luo, Ahmet F. Coskun, and Aydogan Ozcan. Giga-Pixel Lensfree Holographic Microscopy and Tomography Using Color Image Sensors. *PLoS ONE*, 7(9):e45044, September 2012. ISSN 1932-6203. doi: 10.1371/journal.pone.0045044.
- [168] Samuel I. Zapata-Valencia, Heberley Tobon-Maya, and Jorge Garcia-Sucerquia. Image enhancement and field of view enlargement in digital lensless holographic microscopy by multi-shot imaging. *Journal of the Optical Society of America A*, 40(4):C150, April 2023. ISSN 1084-7529, 1520-8532. doi: 10.1364/JOSAA.482496.
- [169] Heberley Tobon, Carlos Trujillo, and Jorge Garcia-Sucerquia. Preprocessing in digital lensless holographic microscopy for intensity reconstructions with enhanced contrast. *Applied Optics*, 60(4):A215, February 2021. ISSN 1559-128X, 2155-3165. doi: 10.1364/AO.404297.
- [170] Carlos A. Trujillo and Jorge Garcia-Sucerquia. Automatic method for focusing biological specimens in digital lensless holographic microscopy. *Optics Letters*, 39(9):2569, May 2014. ISSN 0146-9592, 1539-4794. doi: 10.1364/OL.39.002569.
- [171] Donghun Ryu, Zihao Wang, Kuan He, Guoan Zheng, Roarke Horstmeyer, and Oliver Cossairt. Subsampled phase retrieval for temporal resolution enhancement in lensless on-chip holographic video. *Biomedical Optics Express*, 8(3):1981, March 2017. ISSN 2156-7085, 2156-7085. doi: 10.1364/BOE.8.001981.
- [172] Matthias Ugele, Markus Weniger, Manfred Stanzel, Michael Bassler, Stefan W. Krause, Oliver Friedrich, Oliver Hayden, and Lukas Richter. Label-Free High-Throughput Leukemia Detection by Holographic Microscopy. *Advanced Science*, 5(12):1800761, December 2018. ISSN 2198-3844, 2198-3844. doi: 10.1002/advs.201800761.
- [173] Pasquale Memmolo, Genny Aprea, Vittorio Bianco, Roberta Russo, Immacolata Andolfo, Martina Mugnano, Francesco Merola, Lisa Miccio, Achille Iolascon, and Pietro Ferraro. Differential diagnosis of hereditary anemias from a fraction of blood drop by digital holography and hierarchical machine learning. *Biosensors and Bioelectronics*, 201:113945, April 2022. ISSN 09565663. doi: 10.1016/j.bios.2021.113945.
- [174] Matthias Ugele, Markus Weniger, Maria Leidenberger, Yiwei Huang, Michael Bassler, Oliver Friedrich, Barbara Kappes, Oliver Hayden, and Lukas Richter. Label-free, high-throughput detection of *P. falciparum* infection in sphered erythrocytes with digital holographic microscopy. *Lab on a Chip*, 18(12):1704–1712, 2018. ISSN 1473-0197, 1473-0189. doi: 10.1039/C8LC00350E.
- [175] Pierre Marquet, Christian Depeursinge, and Pierre J. Magistretti. Review of quantitative phase-digital holographic microscopy: promising novel imaging technique to resolve neuronal network activity and identify cellular biomarkers of psychiatric

- disorders. *Neurophotonics*, 1(2):020901, September 2014. ISSN 2329-423X. doi: 10.1117/1.NPh.1.2.020901.
- [176] Chen Wang, Xiao Zhong, David B. Ruffner, Alexandra Stutt, Laura A. Philips, Michael D. Ward, and David G. Grier. Holographic Characterization of Protein Aggregates. *Journal of Pharmaceutical Sciences*, 105(3):1074–1085, March 2016. ISSN 00223549. doi: 10.1016/j.xphs.2015.12.018.
- [177] Chen Wang, Fook Chiong Cheong, David B. Ruffner, Xiao Zhong, Michael D. Ward, and David G. Grier. Holographic characterization of colloidal fractal aggregates. *Soft Matter*, 12(42):8774–8780, 2016. ISSN 1744-683X, 1744-6848. doi: 10.1039/C6SM01790H.
- [178] Anna Wang, Jos W. Zwanikken, David M. Kaz, Ryan McGorty, Aaron M. Goldfain, W. Benjamin Rogers, and Vinothan N. Manoharan. Before the breach: Interactions between colloidal particles and liquid interfaces at nanoscale separations. *Physical Review E*, 100(4):042605, October 2019. ISSN 2470-0045, 2470-0053. doi: 10.1103/PhysRevE.100.042605.
- [179] Lauren E. Altman and David G. Grier. CATCH: Characterizing and Tracking Colloids Holographically Using Deep Neural Networks. *The Journal of Physical Chemistry B*, page acs.jp cb.9b10463, February 2020. ISSN 1520-6106, 1520-5207. doi: 10.1021/acs.jp cb.9b10463.
- [180] Mark D. Hannel, Aidan Abdulali, Michael O’Brien, and David G. Grier. Machine-learning techniques for fast and accurate feature localization in holograms of colloidal particles. *Optics Express*, 26(12):15221, June 2018. ISSN 1094-4087. doi: 10.1364/OE.26.015221.
- [181] Fook Chiong Cheong, Simone Duarte, Sang-Hyuk Lee, and David G. Grier. Holographic microrheology of polysaccharides from *Streptococcus mutans* biofilms. *Rheologica Acta*, 48(1):109–115, January 2009. ISSN 0035-4511, 1435-1528. doi: 10.1007/s00397-008-0320-1.
- [182] Siqing Dai, Tongyao Yu, Jiwei Zhang, Hua Lu, Jiazhen Dou, Mengmeng Zhang, Chen Dong, Jianglei Di, and Jianlin Zhao. Real-time and wide-field mapping of cell-substrate adhesion gap and its evolution via surface plasmon resonance holographic microscopy. *Biosensors and Bioelectronics*, 174:112826, February 2021. ISSN 09565663. doi: 10.1016/j.bios.2020.112826.
- [183] Wen Xiao, Lu Xin, Runyu Cao, Xintong Wu, Ran Tian, Leiping Che, Lianwen Sun, Pietro Ferraro, and Feng Pan. Sensing morphogenesis of bone cells under microfluidic shear stress by holographic microscopy and automatic aberration compensation with deep learning. *Lab on a Chip*, 21(7):1385–1394, 2021. ISSN 1473-0197, 1473-0189. doi: 10.1039/D0LC01113D.
- [184] Sanket Desai, Sonal Rashmi, Aishwarya Rane, Bhasker Dharavath, Aniket Sawant, and Amit Dutt. An integrated approach to determine the abundance, mutation rate and

- phylogeny of the SARS-CoV-2 genome. *Briefings in Bioinformatics*, 22(2):1065–1075, March 2021. ISSN 1467-5463, 1477-4054. doi: 10.1093/bib/bbaa437.
- [185] Olivier Vandenberg, Delphine Martiny, Olivier Rochas, Alex van Belkum, and Zisis Kozlakidis. Considerations for diagnostic COVID-19 tests. *Nature Reviews Microbiology*, 19(3):171–183, March 2021. ISSN 1740-1526, 1740-1534. doi: 10.1038/s41579-020-00461-z.
- [186] Beatriz Böger, Mariana M. Fachi, Raquel O. Vilhena, Alexandre F. Cobre, Fernanda S. Tonin, and Roberto Pontarolo. Systematic review with meta-analysis of the accuracy of diagnostic tests for COVID-19. *American Journal of Infection Control*, 49(1):21–29, January 2021. ISSN 01966553. doi: 10.1016/j.ajic.2020.07.011.
- [187] Nandini Sethuraman, Sundararaj Stanleyraj Jeremiah, and Akihide Ryo. Interpreting Diagnostic Tests for SARS-CoV-2. *JAMA*, 323(22):2249, June 2020. ISSN 0098-7484. doi: 10.1001/jama.2020.8259.
- [188] Tim Peto, Rishab Balaji, Ella Baldwin, Sophie Barraclough, Tracy Benford, Susan Bird, Marina Bishop, Richard Body, Rosie Boulton, Abbie Bown, Carla Bratten, Chris Bridgeman, Dominic Britton, Tim Brooks, Margaret Broughton-Smith, Beverley Buck, Elaine Butcher, Wendy Byrne, Gloria Calderon, Siobhan Campbell, Olivia Carr, Daniel Carter, Megan Cathrall, Matthew Catton, Jim Chadwick, David Chapman, Tanzina Chaudary, Shaolin Chidavaenzi, Samatha Chilcott, Bea Choi, Hannah Claasen, Richard Clarke, Dawn Clarke, Richard Clayton, Rima Colston, James Connolly, Eloïse Cook, Ben Corley, Laura Costello, Caroline Coulson, Ant Crook, Derrick W. Crook, Mary-Anne Darby, John Davis, Rosaline de Koning, Pauline Derbyshire, Mark Dolman, Natalie Draper, Mark Driver, Sarah Dyas, Emily Eaton, Joy Edwards, Ruth Elderfield, Kate Ellis, Graham Ellis, Sue Elwell, Rachel Evans, Becky Evans, Ranoromanana Evans, David Eyre, Vanessa Fenech, Janet Field, Tom Foord, Tom Fowler, Mollie French, Hannah Fuchs, Jasmine Gan, Joseph Gernon, Geeta Ghadiali, Kerry Gibbons, Kate Gilmour, Anika Goel, Sally Gordon, Alexander Grassam-Rowe, David Green, Anna Gronert, Tegan Gumsley-Read, Claire Hall, Bassam Hallis, Sally Hammond, Peter Hammond, Beth Hanney, Gabriella Harker, Andrew Harris, May Havinden-Williams, Elena Hazell, Joanne Henry, Kim Hicklin, Kelly Hollier, Ben Holloway, Sarah J. Hoosdally, Susan Hopkins, Steve Hurdowar, Sally-Anne Hurford, Harriet Jackson, Ruth Johns, Susan Johnston, Tinashe Kanyowa, Katie Keating-Fedders, Sharon Kempson, Iftikhar Khan, Thomas Knight, Anuradha Krishna, Patrick Lahert, Zoe Lampshire, Daniel Lasserson, Kirsten Lee, Lennard Y.W. Lee, Arabella Legard, Cristina Leggio, Teresa Lockett, Christopher Logue, Vanessa Lucas, Sheila F. Lumley, Des Markham, Philippa C. Matthews, Sarah Mckee, Deborah F. McKee, Neil McLeod, Antoinette McNulty, Freddie Mellor, Rachel Michel, Alex Mighiu, Zarina Mirza, Heena Mistry, Jane Mitchell, Mika Erik Moeser, Sophie Moore, Akhila Muthuswamy, Daniel Myers, Gemma Nanson, Mike Newbury, Scott Nicol, Harry Nuttall, Jewel Jones Nwanaforo, Wendy Osbourne, Jake Osbourne, Ashley Otter, Jodie Owen, Dimitris Papoulidis, Juan Dobaldo Pavon, Arro Peace, Karen Pearson, Ashley Pegg, Suzannah Pegler, Helen Permain, Prem Perumal, Leon Peto,

- Tim E.A. Peto, Thanh Pham, Hayleah L. Pickford, Mark Pinkerton, Michelle Platon, Ashley Price, Hellen Purnell, Lottie Rawden, Sara Read, Charles Reynard, Susan Ridge, Tom G. Ritter, James Robinson, Patrick Robinson, Gillian Rodger, Cathy Rowe, Alexandra Rowlands, Sarah Sampson, Kathryn Saunders, Rachel Sayers, Jackie Sears, Richard Sedgewick, Laura Seeney, Amanda Selassie, Jane Shallcross, Lucy Shepard, Anna Sherkat, Shelha Siddiqui, Alex Sienkiewicz, Lavanya Sinha, Jennifer Smith, Ella Smith, Emma Stanton, Thomas Starkey, Aleksander Stawiarski, Amelia Sterry, Joe Stevens, Mark Stockbridge, Anila Sukumaran, Angela Sweed, Sami Tatar, Hema Thomas, Carly Tibbins, Sian Tiley, Julie Timmins, Cara Tomas-Smith, Elena Turek, Toi Neibler, Kate Trigg-Hogarth, Elizabeth Truelove, Chris Turnbull, David Tyrrell, Alison Vaughan, John Vertannes, Richard Vipond, Linda Wagstaff, Joanne Waldron, Philip Walker, Ann Sarah Walker, Mary Walters, Jenny Y Wang, Ellie Watson, Kate Webberley, Kimberley Webster, Grace Westland, Ian Wickens, Jane Willcocks, Herika Willis, Stephen Wilson, Barbara Wilson, Louise Woodhead, Deborah Wright, Bindhu Xavier, Fiona Yelnoorkar, Lisa Zeidan, and Rangeni Zinyama. COVID-19: Rapid antigen detection for SARS-CoV-2 by lateral flow assay: A national systematic evaluation of sensitivity and specificity for mass-testing. *EClinicalMedicine*, 36:100924, June 2021. ISSN 25895370. doi: 10.1016/j.eclinm.2021.100924.
- [189] Benjamin D. Grant, Caitlin E. Anderson, John R. Williford, Luis F. Alonzo, Veronika A. Glukhova, David S. Boyle, Bernhard H. Weigl, and Kevin P. Nichols. SARS-CoV-2 Coronavirus Nucleocapsid Antigen-Detecting Half-Strip Lateral Flow Assay Toward the Development of Point of Care Tests Using Commercially Available Reagents. *Analytical Chemistry*, 92(16):11305–11309, August 2020. ISSN 0003-2700, 1520-6882. doi: 10.1021/acs.analchem.0c01975.
- [190] Suzanne Pickering, Rahul Batra, Blair Merrick, Luke B Snell, Gaia Nebbia, Sam Douthwaite, Fiona Reid, Amita Patel, Mark Tan Kia Ik, Bindi Patel, Themoula Charalampous, Adela Alcolea-Medina, Maria Jose Lista, Penelope R Cliff, Emma Cunningham, Jane Mullen, Katie J Doores, Jonathan D Edgeworth, Michael H Malim, Stuart J D Neil, and Rui Pedro Galão. Comparative performance of SARS-CoV-2 lateral flow antigen tests and association with detection of infectious virus in clinical specimens: a single-centre laboratory evaluation study. *The Lancet Microbe*, 2(9): e461–e471, September 2021. ISSN 26665247. doi: 10.1016/S2666-5247(21)00143-9.
- [191] Jasper Fuk-Woo Chan, Cyril Chik-Yan Yip, Kelvin Kai-Wang To, Tommy Hing-Cheung Tang, Sally Cheuk-Ying Wong, Kit-Hang Leung, Agnes Yim-Fong Fung, Anthony Chin-Ki Ng, Zijiao Zou, Hoi-Wah Tsoi, Garnet Kwan-Yue Choi, Anthony Raymond Tam, Vincent Chi-Chung Cheng, Kwok-Hung Chan, Owen Tak-Yin Tsang, and Kwok-Yung Yuen. Improved Molecular Diagnosis of COVID-19 by the Novel, Highly Sensitive and Specific COVID-19-RdRp/Hel Real-Time Reverse Transcription-PCR Assay Validated *In Vitro* and with Clinical Specimens. *Journal of Clinical Microbiology*, 58(5):e00310–20, April 2020. ISSN 0095-1137, 1098-660X. doi: 10.1128/JCM.00310-20.
- [192] Liting Chen, Gaoxiang Wang, Xiaolu Long, Hongyan Hou, Jia Wei, Yang Cao, Jiaqi

- Tan, Weiyong Liu, Liang Huang, Fankai Meng, Lifang Huang, Na Wang, Jianping Zhao, Gang Huang, Ziyong Sun, Wei Wang, and Jianfeng Zhou. Dynamics of Blood Viral Load Is Strongly Associated with Clinical Outcomes in Coronavirus Disease 2019 (COVID-19) Patients. *The Journal of Molecular Diagnostics*, 23(1):10–18, January 2021. ISSN 15251578. doi: 10.1016/j.jmoldx.2020.10.007.
- [193] J. A. Molina-Bolívar and F. Galisteo-González. Latex Immunoagglutination Assays. *Journal of Macromolecular Science, Part C: Polymer Reviews*, 45(1):59–98, January 2005. ISSN 1532-1797, 1520-5746. doi: 10.1081/MC-200045819.
- [194] Christina M. Marra, Clare L. Maxwell, Shelia B. Dunaway, Sharon K. Sahi, and Lauren C. Tantalo. Cerebrospinal Fluid *Treponema pallidum* Particle Agglutination Assay for Neurosyphilis Diagnosis. *Journal of Clinical Microbiology*, 55(6):1865–1870, June 2017. ISSN 0095-1137, 1098-660X. doi: 10.1128/JCM.00310-17.
- [195] RM Saldanha Dominic, H V Prashanth, Shalini Shenoy, and Shrikala Baliga. Diagnostic Value of Latex Agglutination in Cryptococcal Meningitis. *Journal of Laboratory Physicians*, 1(02):067–068, July 2009. ISSN 0974-2727, 0974-7826. doi: 10.4103/0974-2727.59702.
- [196] L. De la fuente, P. Anda, I. Rodriguez, K. E. Hechemy, D. Raoult, and J. Casal. Evaluation of a latex agglutination test for *Rickettsia conorii* antibodies in seropositive patients. *Journal of Medical Microbiology*, 28(1):69–72, January 1989. ISSN 0022-2615, 1473-5644. doi: 10.1099/00222615-28-1-69.
- [197] Charles A. Friedman, David F. Wender, and John E. Rawson. Rapid Diagnosis of Group B Streptococcal Infection Utilizing a Commercially Available Latex Agglutination Assay. *Pediatrics*, 73(1):27–30, January 1984. ISSN 0031-4005, 1098-4275. doi: 10.1542/peds.73.1.27.
- [198] Xiaojuan Xu, Meilin Jin, Zhengjun Yu, Hongchao Li, Dexin Qiu, Yadi Tan, and Huanchun Chen. Latex Agglutination Test for Monitoring Antibodies to Avian Influenza Virus Subtype H5N1. *Journal of Clinical Microbiology*, 43(4):1953–1955, April 2005. ISSN 0095-1137, 1098-660X. doi: 10.1128/JCM.43.4.1953-1955.2005.
- [199] David J. You, Kenneth J. Geshell, and Jeong-Yeol Yoon. Direct and sensitive detection of foodborne pathogens within fresh produce samples using a field-deployable handheld device. *Biosensors and Bioelectronics*, 28(1):399–406, October 2011. ISSN 09565663. doi: 10.1016/j.bios.2011.07.055.
- [200] Christopher F. Fronczek, David J. You, and Jeong-Yeol Yoon. Single-pipetting microfluidic assay device for rapid detection of *Salmonella* from poultry package. *Biosensors and Bioelectronics*, 40(1):342–349, February 2013. ISSN 09565663. doi: 10.1016/j.bios.2012.07.076.
- [201] Euan McLeod, T. Umut Dincer, Muhammed Veli, Yavuz N. Ertas, Chau Nguyen, Wei Luo, Alon Greenbaum, Alborz Feizi, and Aydogan Ozcan. High-Throughput and Label-Free Single Nanoparticle Sizing Based on Time-Resolved On-Chip Microscopy.

- ACS Nano*, 9(3):3265–3273, March 2015. ISSN 1936-0851, 1936-086X. doi: 10.1021/acsnano.5b00388.
- [202] Aydogan Ozcan and Euan McLeod. Lensless Imaging and Sensing. *Annual Review of Biomedical Engineering*, 18(1):77–102, July 2016. ISSN 1523-9829, 1545-4274. doi: 10.1146/annurev-bioeng-092515-010849.
- [203] Lobelia Samavati and Bruce D. Uhal. ACE2, Much More Than Just a Receptor for SARS-COV-2. *Frontiers in Cellular and Infection Microbiology*, 10:317, June 2020. ISSN 2235-2988. doi: 10.3389/fcimb.2020.00317.
- [204] Katharine H. D. Crawford, Rachel Eguia, Adam S. Dingens, Andrea N. Loes, Keara D. Malone, Caitlin R. Wolf, Helen Y. Chu, M. Alejandra Tortorici, David Veessler, Michael Murphy, Deleah Pettie, Neil P. King, Alejandro B. Balazs, and Jesse D. Bloom. Protocol and Reagents for Pseudotyping Lentiviral Particles with SARS-CoV-2 Spike Protein for Neutralization Assays. *Viruses*, 12(5):513, May 2020. ISSN 1999-4915. doi: 10.3390/v12050513.
- [205] Yanmei Hu, Xiangzhi Meng, Fushun Zhang, Yan Xiang, and Jun Wang. The *in vitro* antiviral activity of lactoferrin against common human coronaviruses and SARS-CoV-2 is mediated by targeting the heparan sulfate co-receptor. *Emerging Microbes & Infections*, 10(1):317–330, January 2021. ISSN 2222-1751. doi: 10.1080/22221751.2021.1888660.
- [206] Serhan O. Isikman, Waheb Bishara, Sam Mavandadi, Frank W. Yu, Steve Feng, Randy Lau, and Aydogan Ozcan. Lens-free optical tomographic microscope with a large imaging volume on a chip. *Proceedings of the National Academy of Sciences*, 108(18):7296–7301, May 2011. ISSN 0027-8424, 1091-6490. doi: 10.1073/pnas.1015638108.
- [207] Alon Greenbaum, Wei Luo, Ting-Wei Su, Zoltán Göröcs, Liang Xue, Serhan O Isikman, Ahmet F Coskun, Onur Mudanyali, and Aydogan Ozcan. Imaging without lenses: achievements and remaining challenges of wide-field on-chip microscopy. *Nature Methods*, 9(9):889–895, September 2012. ISSN 1548-7091, 1548-7105. doi: 10.1038/nmeth.2114.
- [208] Dan Hendrycks and Kevin Gimpel. A Baseline for Detecting Misclassified and Out-of-Distribution Examples in Neural Networks, October 2018. arXiv:1610.02136 [cs].
- [209] Yi-Chen Wu, Ashutosh Shiledar, Yi-Cheng Li, Jeffrey Wong, Steve Feng, Xuan Chen, Christine Chen, Kevin Jin, Saba Janamian, Zhe Yang, Zachary Scott Ballard, Zoltán Göröcs, Alborz Feizi, and Aydogan Ozcan. Air quality monitoring using mobile microscopy and machine learning. *Light: Science & Applications*, 6(9):e17046–e17046, March 2017. ISSN 2047-7538. doi: 10.1038/lsa.2017.46.
- [210] Yi Luo, Yichen Wu, Liqiao Li, Yuening Guo, Ege Çetintaş, Yifang Zhu, and Aydogan Ozcan. Dynamic Imaging and Characterization of Volatile Aerosols in E-Cigarette Emissions Using Deep Learning-Based Holographic Microscopy. *ACS Sensors*, 6(6):2403–2410, June 2021. ISSN 2379-3694, 2379-3694. doi: 10.1021/acssensors.1c00628.

- [211] Yi Luo, Yijie Zhang, Tairan Liu, Alan Yu, Yichen Wu, and Aydogan Ozcan. Virtual Impactor-Based Label-Free Pollen Detection using Holography and Deep Learning. *ACS Sensors*, 7(12):3885–3894, December 2022. ISSN 2379-3694, 2379-3694. doi: 10.1021/acssensors.2c01890.
- [212] Yannik Bourquin, Julien Reboud, Rab Wilson, Yi Zhang, and Jonathan M. Cooper. Integrated immunoassay using tuneable surface acoustic waves and lensfree detection. *Lab on a Chip*, 11(16):2725, 2011. ISSN 1473-0197, 1473-0189. doi: 10.1039/c1lc20320g.
- [213] Waseem Rawat and Zenghui Wang. Deep Convolutional Neural Networks for Image Classification: A Comprehensive Review. *Neural computation*, 29:2352–2449, 2017. doi: doi:10.1162/NECO_a_00990.
- [214] Zewen Li, Fan Liu, Wenjie Yang, Shouheng Peng, and Jun Zhou. A Survey of Convolutional Neural Networks: Analysis, Applications, and Prospects. *IEEE Transactions on Neural Networks and Learning Systems*, 33(12):6999–7019, December 2022. ISSN 2162-237X, 2162-2388. doi: 10.1109/TNNLS.2021.3084827.
- [215] Amjad Rehman, Muhammad Attique Khan, Tanzila Saba, Zahid Mehmood, Usman Tariq, and Noor Ayesha. Microscopic brain tumor detection and classification using 3D CNN and feature selection architecture. *Microscopy Research and Technique*, 84(1):133–149, January 2021. ISSN 1059-910X, 1097-0029. doi: 10.1002/jemt.23597.
- [216] Zabit Hameed, Sofia Zahia, Begonya Garcia-Zapirain, José Javier Aguirre, and Ana María Vanegas. Breast Cancer Histopathology Image Classification Using an Ensemble of Deep Learning Models. *Sensors*, 20(16):4373, August 2020. ISSN 1424-8220. doi: 10.3390/s20164373.
- [217] Steven Diamond, Vincent Sitzmann, Frank Julca-Aguilar, Stephen Boyd, Gordon Wetstein, and Felix Heide. Dirty Pixels: Towards End-to-end Image Processing and Perception. *ACM Transactions on Graphics*, 40(3):1–15, June 2021. ISSN 0730-0301, 1557-7368. doi: 10.1145/3446918.
- [218] Jürgen Schmidhuber. Deep learning in neural networks: An overview. *Neural Networks*, 61:85–117, January 2015. ISSN 08936080. doi: 10.1016/j.neunet.2014.09.003.
- [219] Md. Ferdous Wahid, Tasnim Ahmed, and Md. Ahsan Habib. Classification of Microscopic Images of Bacteria Using Deep Convolutional Neural Network. In *2018 10th International Conference on Electrical and Computer Engineering (ICECE)*, pages 217–220, Dhaka, Bangladesh, December 2018. IEEE. ISBN 978-1-5386-7482-6. doi: 10.1109/ICECE.2018.8636750.
- [220] Hyeokjun Byeon, Taesik Go, and Sang Joon Lee. Deep learning-based digital in-line holographic microscopy for high resolution with extended field of view. *Optics & Laser Technology*, 113:77–86, May 2019. ISSN 00303992. doi: 10.1016/j.optlastec.2018.12.014.

- [221] Zhenbo Ren, Hayden K.-H. So, and Edmund Y. Lam. Fringe Pattern Improvement and Super-Resolution Using Deep Learning in Digital Holography. *IEEE Transactions on Industrial Informatics*, 15(11):6179–6186, November 2019. ISSN 1551-3203, 1941-0050. doi: 10.1109/TII.2019.2913853.
- [222] Shuteng Niu, Yongxin Liu, Jian Wang, and Houbing Song. A Decade Survey of Transfer Learning (2010–2020). *IEEE Transactions on Artificial Intelligence*, 1(2), 2020.
- [223] Karl Weiss, Taghi M. Khoshgoftaar, and DingDing Wang. A survey of transfer learning. *Journal of Big Data*, 3(1):9, December 2016. ISSN 2196-1115. doi: 10.1186/s40537-016-0043-6.
- [224] Yanmin Zhu, Chok Hang Yeung, and Edmund Y. Lam. Digital holographic imaging and classification of microplastics using deep transfer learning. *Applied Optics*, 60(4): A38, February 2021. ISSN 1559-128X, 2155-3165. doi: 10.1364/AO.403366.
- [225] Sung-Jin Kim, Chuangqi Wang, Bing Zhao, Hyungsoon Im, Jouha Min, Hee June Choi, Joseph Tadros, Nu Ri Choi, Cesar M. Castro, Ralph Weissleder, Hakho Lee, and Kwonmoo Lee. Deep transfer learning-based hologram classification for molecular diagnostics. *Scientific Reports*, 8(1):17003, November 2018. ISSN 2045-2322. doi: 10.1038/s41598-018-35274-x.
- [226] Fangyuan Lei, Xun Liu, Qingyun Dai, and Bingo Wing-Kuen Ling. Shallow convolutional neural network for image classification. *SN Applied Sciences*, 2(1):97, January 2020. ISSN 2523-3963, 2523-3971. doi: 10.1007/s42452-019-1903-4.
- [227] Sergey Ioffe and Christian Szegedy. Batch Normalization: Accelerating Deep Network Training by Reducing Internal Covariate Shift. *arXiv:1502.03167v3 [cs]*, March 2015. doi: <https://doi.org/10.48550/arXiv.1502.03167>.
- [228] Arun Kumar Dubey and Vanita Jain. Comparative Study of Convolution Neural Network’s Relu and Leaky-Relu Activation Functions. In Sukumar Mishra, Yog Raj Sood, and Anuradha Tomar, editors, *Applications of Computing, Automation and Wireless Systems in Electrical Engineering*, volume 553, pages 873–880. Springer Singapore, Singapore, 2019. ISBN 9789811367717 9789811367724. doi: 10.1007/978-981-13-6772-4_76. Series Title: Lecture Notes in Electrical Engineering.
- [229] Yuesheng Xu and Haizhang Zhang. Convergence of Deep ReLU Networks. *arXiv:2107.12530v3 [cs]*, January 2023.
- [230] Bing Xu, Naiyan Wang, Tianqi Chen, and Mu Li. Empirical Evaluation of Rectified Activations in Convolution Network. *arXiv:1505.00853v2 [cs]*, pages 211–252, November 2015. doi: <https://doi.org/10.48550/arXiv.1505.00853>.
- [231] Jin Xu, Zishan Li, Bowen Du, Miaomiao Zhang, and Jing Liu. Reluplex made more practical: Leaky ReLU. In *2020 IEEE Symposium on Computers and Communications (ISCC)*, 2020. doi: <https://doi.org/10.1109/ISCC50000.2020.9219587>.

- [232] Sungheon Park and Nojun Kwak. Analysis on the Dropout Effect in Convolutional Neural Networks. In Shang-Hong Lai, Vincent Lepetit, Ko Nishino, and Yoichi Sato, editors, *Computer Vision – ACCV 2016*, volume 10112, pages 189–204. Springer International Publishing, Cham, 2017. ISBN 978-3-319-54183-9 978-3-319-54184-6. doi: 10.1007/978-3-319-54184-6_12. Series Title: Lecture Notes in Computer Science.
- [233] Siddharth Sharma, Simone Sharma, and Anidhya Athaiya. ACTIVATION FUNCTIONS IN NEURAL NETWORKS. *International Journal of Engineering Applied Sciences and Technology*, 04(12):310–316, May 2020. ISSN 24552143. doi: 10.33564/IJEAST.2020.v04i12.054.
- [234] Zheng Hu, Jiaojiao Zhang, and Yun Ge. Handling Vanishing Gradient Problem Using Artificial Derivative. *IEEE Access*, 9:22371–22377, 2021. ISSN 2169-3536. doi: 10.1109/ACCESS.2021.3054915.
- [235] Jialin Zhang, Jiasong Sun, Qian Chen, and Chao Zuo. Resolution Analysis in a Lens-Free On-Chip Digital Holographic Microscope. *IEEE Transactions on Computational Imaging*, 6:697–710, 2020. ISSN 2333-9403, 2334-0118, 2573-0436. doi: 10.1109/TCI.2020.2964247.
- [236] Shigeru Deguchi and Kaoru Tsujii. Supercritical water: a fascinating medium for soft matter. *Soft Matter*, 3(7):797, 2007. ISSN 1744-683X, 1744-6848. doi: 10.1039/b611584e.
- [237] Francisco E. Berger Bioucas, Cornelia Damm, Wolfgang Peukert, Michael H. Rausch, Thomas M. Koller, Cédric Giraudet, and Andreas P. Fröba. Translational and Rotational Diffusion Coefficients of Gold Nanorods Dispersed in Mixtures of Water and Glycerol by Polarized Dynamic Light Scattering. *The Journal of Physical Chemistry B*, 123(44):9491–9502, November 2019. ISSN 1520-6106, 1520-5207. doi: 10.1021/acs.jpcc.9b08274.